The Measurement of the Inclusive Triple Differential Dijet Cross Section at DØ

by

Freedy Nang

B.A., Rutgers University, 1988

M.S., Brown University, 1990

FERMILAB
LIBRARY

Thesis

Submitted in partial fulfillment of the requirements
for the Degree of Doctor of Philosophy
in the Department of Physics
at Brown University

May 1996

bitt Thesis AAE8168

This dissertation by Freedy Nang

is accepted in its present form by the Department of Physics

as satisfying the dissertation requirements for

the degree of Doctor of Philosophy

Date 4/15/96 .....

Richard Partridge

Recommended to the Graduate Council

Date 4/15/96 .....

Robert Brandenberger

Date 4/15/96 .....

Dave Cutts

Approved by the Graduate Council

Date ....

Abstract of "The Measurement of the Inclusive Triple Differential Dijet Cross Section at DØ", by Freedy Nang, Ph.D., Brown University, May 1996

Measurement of the inclusive triple differential dijet cross section, $d^3\sigma/dE_T d\eta_1 d\eta_2$, is described. The data were collected at the Fermilab Tevatron $p\bar{p}$ collider at a center of mass energy $\sqrt{s} = 1.8$ TeV with the DØ detector during the 1992-1993 run.

After selecting dijet events and correcting for inefficiencies, the triple differential dijet cross section is obtained. The cross section has also been unfolded by removing detector effects from the data and the corrected cross section is presented. The cross section is plotted as a function of the leading jet E_T for fixed ranges of pseudorapidity for the two leading jets. Comparing these distributions with theoretical predictions amounts to a test of Quantum Chromodynamics (QCD). Furthermore, when comparing the distributions for the cases of large η, the data are clearly in better agreement with the Next-to-Leading Order (NLO) predictions than the Leading Order (LO) predictions. The triple differential dijet cross section is sensitive to the distributions (pdf's) of parton momenta in the proton. In particular, the triple differential dijet cross section is sensitive to the gluon distribution function, which is not well determined. A comparison of the data to NLO theory using several pdf's is performed and resulted in no good fits. The comparisons were redone by testing different regions in the parton momentum fractions and still resulted in no good fits. We conclude that either there is an unaccounted source of point-to-point errors in the theory or experiment, or there is a need for a different gluon content in the proton than is predicted by current parton distribution sets.

ACKNOWLEDGEMENTS

First, I thank my advisor, Richard Partridge, who has been helpful in many ways, including his knowledge in physics and his detailed comments of my thesis. I would also like to thank the Brown HEP group at DØ for its active support for my research. I thank Professors Dave Cutts and Robert Brandenberger in my committee for their time and valuable comments.

During this long adventure, I have had the pleasure of meeting many great people, without their friendship life would have been less enjoyable. There are too many names, but just to cite a few: Jan and Joan Guida, Gene Alvarez, Jim Cochran, Thorsten Huehn, Kathy Fatyga, Tacy Joffe-Minor, Bob Kehoe, Cary Yoshikawa, Richard Astur, Daniel Elvira, Lynn Bagby, Chip Stewart, Jae Yu, Kaushik De, ... Thanks to Terry Geld for proof reading my thesis.

Special thanks to my office mates David Cullen Vidal, who with Eneida, have offered me great moments of hospitality. To Tom Fahland, whose "Applications of Probability and Statistics beyond High Energy Physics" I have found quite enjoyable. And to Haowei Xu, who answered many of my stupid questions. It was treat building the Level Ø detector with Haowei.

Special thanks to Harry Weerts, from whom a have learned a great deal of Physics and was always available. I am indebted to him for his support and encouragement. I also owe special gratitude to Walter Giele, a physicist from the Fermilab theory

division, for taking the time to discuss many issues related to my analysis.

Jerry Blazey was the true advisor of many students shipped to Fermilab in the QCD group, myself included. In my particular case, Jerry was more than a mentor, he was also a very good friend, taking time to help not just in Physics related matters but in personal matters as well. He rescued me every time I got lost in that dark and seemingly endless tunnel. My most heartfelt gratitude goes to Jerry.

I would also like to thank Angel Lin, who despite the long distance, has always been there for me and helped me keep my sanity during hard times. Last but not least, to my parents, for letting me pursue my dreams, and whose love, support, and sacrifices enable what I have accomplished.

This dissertation is dedicated to my Mother and to the memory of my Father.

獻給母親

慈母手中線遊子身上衣
臨行密密縫意恐遲遲歸
誰言寸草心報得三春暉

兒 惠強

一九九六年五月

TABLE OF CONTENTS

ABSTRACT iii

ACKNOWLEDGEMENTS iv

LIST OF TABLES xi

LIST OF FIGURES xv

LIST OF APPENDICES xix

CHAPTER

1. Introduction 1

2. Theoretical Motivation 2

2.1 Introduction 2
2.2 The Standard Model 3
2.3 The Parton Model 5
2.4 Theory of Strong Interactions 7
2.4.1 Running Coupling Constant 7
2.4.2 Leading and Next to Leading Order diagrams 8
2.4.3 Hadronization 11
2.4.4 Jets 11
2.5 Parton Distribution Functions 12
2.6 Choice of Variables for Differential Cross Section 14
2.7 Theoretical Calculations 15

3. Apparatus 18

3.1 Overview 18
3.2 Accelerator 20
3.3 Particle Detection 21
3.3.1 Principles of Wire Drift Chambers 21
3.3.2 Scintillation Counters and Photomultipliers 22
3.3.3 Transition Radiation Detectors 22
3.3.4 Calorimeters 22
3.4 The DØ Central Detector 23
3.4.1 Vertex Detector 24
3.4.2 Transition Radiation Detector 26

3.4.3 Central Drift Chamber 26
3.4.4 Forward Drift Chamber 27
3.5 Muon Detectors 28
3.6 Calorimeter 29
3.6.1 Central Calorimeter (CC) 32
3.6.2 End Calorimeter (EC) 35
3.6.3 Massless Gaps and Intercryostat Detector (ICD) . . . 36
3.7 Data Acquisition system (DAQ) 38
3.7.1 Level Ø Trigger (LØ) 38
3.7.2 Level 1 Trigger (L1) 42
3.7.3 Level 1.5 Trigger (L1.5) 42
3.7.4 Level 2 Trigger (L2) 42
3.8 Offline Reconstruction 44

4. Data Selection 46

4.1 Online Event Selection 46
4.1.1 Level Ø Trigger Selection 47
4.1.2 Level 1 Trigger Selection 47
4.1.3 Level 2 Trigger Selection 49
4.2 Offline Jet Reconstruction 51
4.3 Background Elimination 53
4.3.1 Standard Jet Quality Cuts 54
4.3.2 Missing E_T Cut 55
4.4 Final Event Selection 57

5. Data Correction 59

5.1 Jet Energy Scale 59
5.1.1 Underlying Event and Zero Suppression 60
5.1.2 Response 61
5.1.3 Out-of-Cone Showering 63
5.2 Jet E_T Resolution 65
5.3 Jet η Bias and Resolution 65
5.4 Efficiencies 70
5.4.1 Standard Jets Cuts and Missing E_T Cut 70
5.4.2 Multiple Interaction Cut 73
5.4.3 Derivation of Trigger Efficiencies 75
5.4.4 Measuring Trigger Efficiencies 83

6. Experimental Results 101

6.1 Two-Dimensional Cross Sections 102
6.2 E_T Distributions 107
6.3 Signed-η Distributions 111
6.4 Unsmearing 121
6.4.1 Inclusive Jet Cross Section Case 121
6.4.2 Inclusive Dijet Cross Section Case 122
6.5 Unsmeared Results 130

6.5.1 Unsmeared E_T cross sections 130
6.5.2 Unsmeared Signed-η cross sections 135

7. Comparisons to Parton Distribution Functions 145

7.1 χ^2 Fits of Data and Theory 145
7.2 Conclusions 161

APPENDICES 162

REFERENCES 182

LIST OF TABLES

Table		
2.1	The three generations of quarks.	3
2.2	The three generations of leptons.	3
2.3	The four fundamental forces.	4
2.4	The gauge bosons.	4
2.5	Squared matrix elements for $2 \rightarrow 2$ subprocesses in QCD (averaged over spin and color): q and q' denote distinct flavors of quark, $g_s^2 = 4\pi\alpha_s$ is the coupling squared.	9
3.1	Vertex chamber parameters.	26
3.2	Central Drift Chamber parameters.	29
3.3	Forward Drift Chamber parameters.	30
3.4	Muon system parameters.	31
3.5	Central calorimeter parameters.	35
3.6	End calorimeter parameters.	37
4.1	QCD L1 trigger bits and respective requirements. The z-vertex measurement is from the LØ trigger.	49
4.2	QCD L2 trigger bits and their respective requirements.	51
4.3	Number of QCD events and integrated luminosity for each trigger after the Standard Jet Quality and $\not{E}_T$ cuts.	57
5.1	Parametrization of the fractional transverse energy resolution as a function of the scale corrected jet E_T. It includes low E_T γ−jet data points.	68
5.2	Parametrization of the jet η resolution as a function of parton jet energy for different η_d bins.	69
5.3	Multiple interaction cut efficiencies for different QCD trigger bits.	75
5.4	QCD triggers and respective L1 and L2 requirements.	79
5.5	Logic table for a three jet event requiring one tower to satisfy the trigger condition where 0 represents the jet having no towers and | one or more towers above m GeV. Note that the event fails the L1 requirement with a probability of $q_1 * q_2 * q_3$.	80
5.6	Logic Table for a one jet event requiring two towers to satisfy the trigger condition where 0 represents no towers, | one and only one tower, and || two or more towers above m GeV.	81
5.7	Logic Table for a three jet event. Two towers above threshold are required to satisfy the trigger condition where 0 represents no towers, | one and only one tower, and || two or more towers above m GeV.	82

5.8 L1 trigger turn on parametrizations as a function of uncorrected RECO E_T. 96
5.9 L2 trigger turn on parametrizations as a function of uncorrected RECO E_T. 97
6.1 Parton momentum fractions, x_1 and x_2, for various transverse energies and outgoing parton pseudorapidities. 106
6.2 Jet cross section, $d^3\sigma/dE_T d\eta_1 d\eta_2$, as a function of the central jet E_T when the second jet is in the region $0.0 \leq |\eta| < 1.0$. 109
6.3 Jet cross section, $d^3\sigma/dE_T d\eta_1 d\eta_2$, as a function of the central jet E_T when the second jet is in the region $1.0 \leq |\eta| < 2.0$. 110
6.4 Jet cross section, $d^3\sigma/dE_T d\eta_1 d\eta_2$, as a function of the central jet E_T when the second jet is in the region $2.0 \leq |\eta| < 3.0$. 110
6.5 Jet cross section, $d^3\sigma/dE_T d\eta_1 d\eta_2$, as a function of the central jet E_T when the second jet is in the region $3.0 \leq |\eta| < 4.0$. 111
6.6 Jet cross section, $d^3\sigma/dE_T d\eta_1 d\eta_2$, as a function of $\eta_2 \times sign(\eta_1)$ for $0.0 \leq |\eta_1| < 0.5$. 118
6.7 Jet cross section, $d^3\sigma/dE_T d\eta_1 d\eta_2$, as a function of $\eta_2 \times sign(\eta_1)$ for $0.5 \leq |\eta_1| < 1.0$. 118
6.8 Jet cross section, $d^3\sigma/dE_T d\eta_1 d\eta_2$, as a function of $\eta_2 \times sign(\eta_1)$ for $1.0 \leq |\eta_1| < 1.5$. 119
6.9 Jet cross section, $d^3\sigma/dE_T d\eta_1 d\eta_2$, as a function of $\eta_2 \times sign(\eta_1)$ for $1.5 \leq |\eta_1| < 2.0$. 119
6.10 Jet cross section, $d^3\sigma/dE_T d\eta_1 d\eta_2$, as a function of $\eta_2 \times sign(\eta_1)$ for $2.0 \leq |\eta_1| < 2.5$. 120
6.11 Jet cross section, $d^3\sigma/dE_T d\eta_1 d\eta_2$, as a function of $\eta_2 \times sign(\eta_1)$ for $2.5 \leq |\eta_1| < 3.0$. 120
6.12 Point-by-point fractional errors between the CTEQ2M and AVERAGE unsmearing factors for each individual η_1 slice. 124
6.13 Point-by-point fractional errors between the $\mu = E_T$ and AVERAGE unsmearing factors for each individual η_1 slice. 128
6.14 Changes in the cross section normalization for the different $|\eta_1|$ slices due to the variation of the resolution parameters. The second column represents the overall normalization ratio for a fit over the range $-4.0 < \eta_2 \times Sign(\eta_1) < 4.0$. The third column gives the goodness of the fit. 129
6.15 Changes in the cross section normalization for the different $|\eta_1|$ slices due to the variation of the resolution parameters. The second column represents the overall normalization ratio for a fit over the range $-3.0 < \eta_2 \times Sign(\eta_1) < 3.0$. The third column gives the goodness of the fit. 130
6.16 Unsmeared jet cross section, $d^3\sigma/dE_T d\eta_1 d\eta_2$, as a function of the central jet E_T when the second jet is at $0.0 \leq |\eta| < 1.0$. . . 131
6.17 Unsmeared jet cross section, $d^3\sigma/dE_T d\eta_1 d\eta_2$, as a function of the central jet E_T when the second jet is at $1.0 \leq |\eta| < 2.0$. . . 134
6.18 Unsmeared jet cross section, $d^3\sigma/dE_T d\eta_1 d\eta_2$, as a function of the central jet E_T when the second jet is at $2.0 \leq |\eta| < 3.0$. . . 134
6.19 Unsmeared jet cross section, $d^3\sigma/dE_T d\eta_1 d\eta_2$, as a function of the central jet E_T when the second jet is at $3.0 \leq |\eta| < 4.0$. . . 135

6.20 Unsmeared cross section as a function of $\eta_2 \times sign(\eta_1)$ for $0.0 \leq |\eta_1| < 0.5$. 135
6.21 Unsmeared cross section as a function of $\eta_2 \times sign(\eta_1)$ for $0.5 \leq |\eta_1| < 1.0$. 142
6.22 Unsmeared cross section as a function of $\eta_2 \times sign(\eta_1)$ for $1.0 \leq |\eta_1| < 1.5$. 142
6.23 Unsmeared cross section as a function of $\eta_2 \times sign(\eta_1)$ for $1.5 \leq |\eta_1| < 2.0$. 143
6.24 Unsmeared cross section as a function of $\eta_2 \times sign(\eta_1)$ for $2.0 \leq |\eta_1| < 2.5$. 143
6.25 Unsmeared cross section as a function of $\eta_2 \times sign(\eta_1)$ for $2.5 \leq |\eta_1| < 3.0$. 144
7.1 Unsmeared cross section and statistical error as a function of $\eta_2 \times sign(\eta_1)$ for $0.0 \leq |\eta_1| < 0.5$ and $45 \leq E_T < 55$ GeV for the three choices of jet energy scale correction: HIGH, NOMINAL, and LOW. 147
7.2 Unsmeared cross section and statistical error as a function of $\eta_2 \times sign(\eta_1)$ for $0.5 \leq |\eta_1| < 1.0$ and $45 \leq E_T < 55$ GeV for the three choices of jet energy scale correction: HIGH, NOMINAL, and LOW. 148
7.3 Unsmeared cross section and statistical error as a function of $\eta_2 \times sign(\eta_1)$ for $1.0 \leq |\eta_1| < 1.5$ and $45 \leq E_T < 55$ GeV for the three choices of jet energy scale correction: HIGH, NOMINAL, and LOW. 148
7.4 Unsmeared cross section and statistical error as a function of $\eta_2 \times sign(\eta_1)$ for $1.5 \leq |\eta_1| < 2.0$ and $45 \leq E_T < 55$ GeV for the three choices of jet energy scale correction: HIGH, NOMINAL, and LOW. 149
7.5 Unsmeared cross section and statistical error as a function of $\eta_2 \times sign(\eta_1)$ for $2.0 \leq |\eta_1| < 2.5$ and $45 \leq E_T < 55$ GeV for the three choices of jet energy scale correction: HIGH, NOMINAL, and LOW. 149
7.6 Unsmeared cross section and statistical error as a function of $\eta_2 \times sign(\eta_1)$ for $2.5 \leq |\eta_1| < 3.0$ and $45 \leq E_T < 55$ GeV for the three choices of jet energy scale correction: HIGH, NOMINAL, and LOW. 150
7.7 Total χ^2 and fit parameters for the two families for pdf's tested. The number of data points used was 72. 150
7.8 Data points where both partons have $x < 0.1$. 158
7.9 Total χ^2 and fit parameters where both partons have $x < 0.1$. The number of data points is 11. 159
7.10 Data points where both partons have $x \geq 0.1$. 159
7.11 Total χ^2 and fit parameters where both partons have $x \geq 0.1$. The number of data points is 16. 160
7.12 Total χ^2 and fit parameters where one parton has $x \geq 0.1$ and the other parton has $x < 0.1$. The number of data points is 45. 160
A.1 First set of combinations for the case of requiring 3 towers above m GeV. 164

A.2 Second set of combinations for the case of requiring 3 towers above m GeV. 164
A.3 Third set of combinations for the case of requiring 3 towers above m GeV. 165
A.4 Last set of combinations for the case of requiring 3 towers above m GeV. 165
A.5 First set of combinations for the case of requiring 4 towers above m GeV. 167
A.6 Second set of combinations for the case of requiring 4 towers above m GeV. 168
A.7 Third set of combinations for the case of requiring 4 towers above m GeV. 169
A.8 Fourth set of combinations for the case of requiring 4 towers above m GeV. 170
A.9 Last set of combinations for the case of requiring 4 towers above m GeV. 171
B.1 Unsmearing factors for the dijet E_T spectra when the second jet is in the range $0.0 \leq |\eta| < 1.0$. 173
B.2 Unsmearing factors for the dijet E_T spectra when the second jet is in the range $1.0 \leq |\eta| < 2.0$. 174
B.3 Unsmearing factors for the dijet E_T spectra when the second jet is in the range $2.0 \leq |\eta| < 3.0$. 175
B.4 Unsmearing factors for the dijet E_T spectra when the second jet is in the range $3.0 \leq |\eta| < 4.0$. 175
B.5 Unsmearing factors for the signed η distribution when the leading jet is in the range $0.0 \leq |\eta| < 0.5$. 176
B.6 Unsmearing factors for the signed η distribution when the leading jet is in the range $0.5 \leq |\eta| < 1.0$. 177
B.7 Unsmearing factors for the signed η distribution when the leading jet is in the range $1.0 \leq |\eta| < 1.5$. 178
B.8 Unsmearing factors for the signed η distribution when the leading jet is in the range $1.5 \leq |\eta| < 2.0$. 179
B.9 Unsmearing factors for the signed η distribution when the leading jet is in the range $2.0 \leq |\eta| < 2.5$. 180
B.10 Unsmearing factors for the signed η distribution when the leading jet is in the range $2.5 \leq |\eta| < 3.0$. 181

LIST OF FIGURES

Figure		
2.1	The Leading Order Cross Section.	6
2.2	The Leading Order Feynman diagrams.	9
2.3	Some Next-to-Leading Order Feynman diagrams.	10
2.4	Cross Section with Higher Order Corrections.	10
2.5	Distributions of different partons in the proton as a function of x at Q=50 GeV for CTEQ2M.	14
2.6	The gluon distribution as a function of x at Q=50 GeV for several pdf's. The dashed line shows the minimum x-value that can be probed at the Tevatron using dijets. The dotted line shows the x-value that the CTEQ pdf's have roughly the same gluon content.	16
2.7	The gluon distribution as a function of x at Q=50 GeV for several pdf's at relatively "high" x-values.	16
2.8	The gluon distribution as a function of x at Q=50 GeV for several pdf's at relatively "low" x-values.	17
2.9	Examples of Two-to-Three Tree level and Two-to-Two one-loop diagrams.	17
3.1	The DØ detector consists of three subsystems: the Muon system, the Calorimeters, and the Central Tracking System.	19
3.2	The DØ Tracking System can be subdivided into the Vertex detector, the Transition Radiation Detector, the Central Drift Chamber, and the Forward Drift Chambers.	24
3.3	End view of a quadrant of the Vertex detector.	25
3.4	View of a section of the Transition Radiation Detector.	27
3.5	End view of a section of the Central Drift Chamber.	28
3.6	The Φ module sandwiched by the two Θ modules in the FDC.	31
3.7	The DØ calorimetry, consisting of the Central Calorimeter with two End Calorimeters. The Inter-Cryostat Detector is mounted on the face of each End Calorimeter.	33
3.8	Quarter view of the calorimeter with constant lines in η.	34
3.9	The DØ multilevel triggering system.	39
3.10	Layout of the Level Ø detector. The shaded regions are scintillators.	40
3.11	Level 1 trigger processing stages.	43
3.12	Overview of the Level 2 trigger and its relationship with the Data Acquisition system.	45
4.1	(a) Z-Vertex distribution for trigger bits with the LØ vertex cut, and (b) with no vertex requirement.	48

4.2 Standard Jet Quality Cuts: (a) Coarse Hadronic Fraction, (b) Hot Cell Fraction, (c) Electromagnetic Fraction. Also shown is (d) the missing E_T cut. 56
5.1 Jet energy scale correction factors for two different η_d regions as a function of the jet E_T. The dash lines show the scale correction uncertainty. 64
5.2 Parametrization of the fractional transverse energy resolution in the central and intercryostat regions as a function of the scale corrected jet E_T. The dark circles are obtained from the $jet-jet$ sample and the open circles are associated with the $\gamma-jet$ events. The fit includes both sets of measurements. 66
5.3 Parametrization of the fractional transverse energy resolution in the forward region as a function of the scale corrected jet E_T. The dark circles are obtained from the $jet - jet$ sample and the open circles are associated with the $\gamma - jet$ events. The fit includes both sets of measurements. 67
5.4 σ_η(E,η_d) as a function of the parton energy using a HERWIG simulation. 69
5.5 EMFR distribution for different E_T bins with respective fits. . 71
5.6 HOTFR and $\not{E}_T$ distributions with respective fits. 72
5.7 Parametrization of efficiencies as a function of jet E_T for: (a) the standard jet quality cuts and (b) for the missing E_T cut. . . . 74
5.8 Multiple interaction cut efficiencies are shown for: (a) JET_LOW, (b) JET_MEDIUM, (c) JET_HIGH, and (d) JET_MAX. The arrows show where the trigger is fully efficient. 76
5.9 Event trigger turn-on for JET_LOW showing 100% efficiency at 40 GeV. 78
5.10 The top figure shows the RECO E_T requiring only one tower above 3 GeV in the solid lines and the RECO E_T requiring one tower above 3 GeV and one L2 JET above 20 GeV in dashed lines. The bottom figure shows the RECO E_T requiring only one tower above 3 GeV in the solid lines and the RECO E_T requiring one tower above 3 GeV and one tower above 7 GeV in dashed lines. 85
5.11 L1 single jet trigger efficiencies as a function of uncorrected RECO E_T. 86
5.12 L2 single jet trigger efficiencies as a function of uncorrected RECO E_T. 87
5.13 L1 single jet trigger efficiencies for JET_MIN in different η regions as a function of uncorrected RECO E_T. 88
5.14 L1 single jet trigger efficiencies for JET_LOW in different η regions as a function of uncorrected RECO E_T. 89
5.15 L1 single jet trigger efficiencies for JET_MEDIUM in different η regions as a function of uncorrected RECO E_T. 90
5.16 L1 single jet trigger efficiencies for JET_HIGH in different η regions as a function of uncorrected RECO E_T. 91
5.17 L2 single jet trigger efficiencies for JET_MIN in different η regions as a function of uncorrected RECO E_T. 92

5.18 L2 single jet trigger efficiencies for JET_LOW in different η regions as a function of uncorrected RECO E_T. 93
5.19 L2 single jet trigger efficiencies for JET_MEDIUM in different η regions as a function of uncorrected RECO E_T. 94
5.20 L2 single jet trigger efficiencies for JET_HIGH in different η regions as a function of uncorrected RECO E_T. 95
5.21 Tests of the corrections due to trigger efficiencies for: (a) for JET_LOW, and (b) for JET_MEDIUM. 99
5.22 Tests of the corrections due to trigger efficiencies for: (c) for JET_HIGH. 100
6.1 The inclusive triple differential dijet cross section, $d^3\sigma/dE_T d\eta_1 d\eta_2$, vs. η_1 and η_2 for $45 \leq E_{T1} < 55$ GeV. 103
6.2 The inclusive triple differential dijet cross section, $d^3\sigma/dE_T d\eta_1 d\eta_2$, vs. η_1 and η_2 for $55 \leq E_{T1} < 65$ GeV. 104
6.3 The inclusive triple differential dijet cross section, $d^3\sigma/dE_T d\eta_1 d\eta_2$, vs. η_1 and η_2 for $95 \leq E_{T1} < 105$ GeV. 105
6.4 The inclusive triple differential dijet cross section, $d^3\sigma/dE_T d\eta_1 d\eta_2$, as a function the leading jet E_T. The 5.4% uncertainty due to luminosity has not been included. 108
6.5 The uncorrected inclusive triple differential dijet cross section, $d^3\sigma/dE_T d\eta_1 d\eta_2$ vs. $\eta_2 \times sign(\eta_1)$ for $0.0 \leq |\eta_1| < 0.5$. The 5.4% uncertainty due to luminosity has not been included. 112
6.6 The uncorrected inclusive triple differential dijet cross section, $d^3\sigma/dE_T d\eta_1 d\eta_2$ vs. $\eta_2 \times sign(\eta_1)$ for $0.5 \leq |\eta_1| < 1.0$. The 5.4% uncertainty due to luminosity has not been included. 113
6.7 The uncorrected inclusive triple differential dijet cross section, $d^3\sigma/dE_T d\eta_1 d\eta_2$ vs. $\eta_2 \times sign(\eta_1)$ for $1.0 \leq |\eta_1| < 1.5$. The 5.4% uncertainty due to luminosity has not been included. 114
6.8 The uncorrected inclusive triple differential dijet cross section, $d^3\sigma/dE_T d\eta_1 d\eta_2$ vs. $\eta_2 \times sign(\eta_1)$ for $1.5 \leq |\eta_1| < 2.0$. The 5.4% uncertainty due to luminosity has not been included. 115
6.9 The uncorrected inclusive triple differential dijet cross section, $d^3\sigma/dE_T d\eta_1 d\eta_2$ vs. $\eta_2 \times sign(\eta_1)$ for $2.0 \leq |\eta_1| < 2.5$. The 5.4% uncertainty due to luminosity has not been included. 116
6.10 The uncorrected inclusive triple differential dijet cross section, $d^3\sigma/dE_T d\eta_1 d\eta_2$ vs. $\eta_2 \times sign(\eta_1)$ for $2.5 \leq |\eta_1| < 3.0$. The 5.4% uncertainty due to luminosity has not been included. 117
6.11 Unsmearing factors for three different pdf's and their average for the central slice $0.0 \leq |\eta_1| < 0.5$. 125
6.12 Unsmearing factors for three different renormalization scale, μ, and their average for the central slice, $0.0 \leq |\eta_1| < 0.5$. 127
6.13 DØ measurement of $d^3\sigma/dE_T d\eta_1 d\eta_2$ vs. E_{T1} for $|\eta_1| < 1.0$ and comparison to next-to-leading order pQCD prediction using CTEQ2M pdf's. 132
6.14 A comparison of JETRAD leading order and next-to-leading order pQCD predictions of $d^3\sigma/dE_T d\eta_1 d\eta_2$ vs. E_{T1} for $|\eta_1| < 1.0$ and the noted $|\eta_2|$ ranges. 133

6.15 The unsmeared inclusive triple differential dijet cross section, $d^3\sigma/dE_T d\eta_1 d\eta_2$ vs. $\eta_2 \times sign(\eta_1)$ for $0.0 \leq |\eta_1| < 0.5$. The 5.4% luminosity uncertainty has not been included. 136
6.16 The unsmeared inclusive triple differential dijet cross section, $d^3\sigma/dE_T d\eta_1 d\eta_2$ vs. $\eta_2 \times sign(\eta_1)$ for $0.5 \leq |\eta_1| < 1.0$. The 5.4% luminosity uncertainty has not been included. 137
6.17 The unsmeared inclusive triple differential dijet cross section, $d^3\sigma/dE_T d\eta_1 d\eta_2$ vs. $\eta_2 \times sign(\eta_1)$ for $1.0 \leq |\eta_1| < 1.5$. The 5.4% luminosity uncertainty has not been included. 138
6.18 The unsmeared inclusive triple differential dijet cross section, $d^3\sigma/dE_T d\eta_1 d\eta_2$ vs. $\eta_2 \times sign(\eta_1)$ for $1.5 \leq |\eta_1| < 2.0$. The 5.4% luminosity uncertainty has not been included. 139
6.19 The unsmeared inclusive triple differential dijet cross section, $d^3\sigma/dE_T d\eta_1 d\eta_2$ vs. $\eta_2 \times sign(\eta_1)$ for $2.0 \leq |\eta_1| < 2.5$. The 5.4% luminosity uncertainty has not been included. 140
6.20 The unsmeared inclusive triple differential dijet cross section, $d^3\sigma/dE_T d\eta_1 d\eta_2$ vs. $\eta_2 \times sign(\eta_1)$ for $2.5 \leq |\eta_1| < 3.0$. The 5.4% luminosity uncertainty has not been included. 141
7.1 The interpolated triple differential dijet cross section, $d^3\sigma/dE_T d\eta_1 d\eta_2$ vs. $\eta_2 \times sign(\eta_1)$ for $0.0 \leq |\eta_1| < 0.5$. The 5.4% luminosity uncertainty has not been included. 152
7.2 The interpolated triple differential dijet cross section, $d^3\sigma/dE_T d\eta_1 d\eta_2$ vs. $\eta_2 \times sign(\eta_1)$ for $0.5 \leq |\eta_1| < 1.0$. The 5.4% luminosity uncertainty has not been included. 153
7.3 The interpolated triple differential dijet cross section, $d^3\sigma/dE_T d\eta_1 d\eta_2$ vs. $\eta_2 \times sign(\eta_1)$ for $1.0 \leq |\eta_1| < 1.5$. The 5.4% luminosity uncertainty has not been included. 154
7.4 The interpolated triple differential dijet cross section, $d^3\sigma/dE_T d\eta_1 d\eta_2$ vs. $\eta_2 \times sign(\eta_1)$ for $1.5 \leq |\eta_1| < 2.0$. The 5.4% luminosity uncertainty has not been included. 155
7.5 The interpolated triple differential dijet cross section, $d^3\sigma/dE_T d\eta_1 d\eta_2$ vs. $\eta_2 \times sign(\eta_1)$ for $2.0 \leq |\eta_1| < 2.5$. The 5.4% luminosity uncertainty has been included. 156
7.6 The interpolated triple differential dijet cross section, $d^3\sigma/dE_T d\eta_1 d\eta_2$ vs. $\eta_2 \times sign(\eta_1)$ for $2.5 \leq |\eta_1| < 3.0$. The 5.4% luminosity uncertainty has not been included. 157

LIST OF APPENDICES

Appendix

A. Trigger Logic Tables 163

B. Unsmearing Factors 172

CHAPTER 1

Introduction

This dissertation will report on the measurement of the inclusive triple differential cross section, $d^3\sigma/dE_T d\eta_1 d\eta_2$. This chapter simply gives an outline and organization of the thesis.

Chapter 2 focuses on the theoretical framework and motivation for performing this analysis.

Chapter 3 describes the detector used to gather the data used for this analysis.

Chapter 4 explains the event selection criteria, including the online trigger selection and the offline cuts that were applied to select the data sample.

Chapter 5 shows the corrections applied to the data and the efficiencies for the cuts used in this analysis.

Chapter 6 shows the uncorrected cross sections. After describing the unfolding method used, the corrected cross sections are shown.

Chapter 7 explains the handling of the jet energy scale uncertainties and compares the data to the theoretical predictions using different parton distribution functions.

CHAPTER 2

Theoretical Motivation

2.1 Introduction

As early as 460 B.C., the Greek philosopher Democritus theorized that the world was made up of indivisible entities which he called "atoms". This idea still prevails; today we call the building blocks quarks, leptons, and bosons. The presently accepted theoretical framework, known as the *Standard Model*, has proven to be quite successful in describing fundamental particles and their interactions. Its most recent triumph is the discovery of the top quark [1]. Among the theoretical predictions in the Standard Model that describe the dynamics among the fundamental particles we find the theory of *Quantum Chromodynamics* which describes the strong interactions.

In this chapter, we start by describing how the basic particles are arranged and which are the gauge field quanta that are associated with their interactions. After describing briefly the parton model, we then proceed to describe the theory of the strong interactions. Within this section, we describe the perturbative nature of the theory and subsequent implications: running of the coupling constant, number of diagrams, hadronization, jets, etc. We continue by describing the parton distribution functions and the experimental variables used in the analysis. Finally, we describe the theoretical calculations that will be used to compare with the data.

2.2 The Standard Model

According to the Standard model, matter is divided into two groups of fundamental building blocks: fermions with half-integer spin and bosons with integer spin. The fermions are further divided into quarks and leptons. The quarks come in six flavors and grouped into three generations: up and down, charm and strange, and top and bottom. The leptons are the electron (e), muon (μ), and tau (τ), with their associated neutrinos (ν). Tables 2.1 and 2.2 list the leptons and quarks and some of their characteristics. By the same token, antimatter is made up of antiquarks and antileptons, which have the opposite quantum numbers of their matter counterpart.

Quark	Symbol	Generation	Rest Mass	Charge
up	u	1	2-8 MeV	2/3
down	d		5-15 MeV	−1/3
charm	c	2	1.0-1.6 GeV	2/3
strange	s		0.1-0.3 GeV	−1/3
top	t	3	170-190 GeV	2/3
bottom	b		4.1-4.5 GeV	−1/3

Table 2.1: The three generations of quarks.

Lepton	Symbol	Generation	Rest Mass (MeV)	Charge
Electron	e^-	1	0.511	−1
Electron Neutrino	ν_e		≤ 0.005	0
Muon	μ^-	2	105.7	−1
Muon Neutrino	ν_μ		≤ 0.27	0
Tau	τ	3	1777.1	−1
Tau Neutrino	ν_τ		≤ 31	0

Table 2.2: The three generations of leptons.

Fermions interact with one another through different forces: gravitational, weak, electromagnetic, and strong. The relative strength of the forces are shown in Table 2.3. The carriers of these forces are the second group of building blocks: the bosons, which are listed in Table 2.4. Even though the electromagnetic and weak forces appear to be very different, they are just different manifestations of the electroweak force becoming one force when the momentum transfer equals the mass of the W boson ($Q^2 = M_W^2$). Furthermore, it has been hypothesized that at much higher momentum transfers (at $Q \sim 10^{16}\ GeV$), the strong and the electroweak forces are unified. Theoretically, it has not been possible to incorporate the gravitational force into these Grand Unified Theories (GUTs).

Force	Range (cm)	Relative Strength
Strong	10^{-13}	1
Electromagnetic	infinite	10^{-2}
Weak	10^{-16}	10^{-6}
Gravitational	infinite	10^{-40}

Table 2.3: The four fundamental forces.

Force	Carrier	Rest Mass (GeV)	Spin	Charge
Strong	Gluons	0.	1	0
Electromagnetic	Photon	0.	1	0
Weak	W^+	80.2	1	+1
	Z^0	91.2	1	0
	W^-	80.2	1	−1
Gravitational	Graviton	0.	2	0

Table 2.4: The gauge bosons.

While leptons exist freely, quarks have only been found in bound states held together by the carriers of the strong force, the gluons. The strong force obeys an SU(3) symmetry which predicts eight distinct carriers. This property, called color,

tells us that the strong force is mediated by eight colored gluons that bind the quarks. The quarks come in three colors. Typically, the colors are named: Red (R), Green (G), and Blue (B), so the different gluons are: $R\overline{G}$, $G\overline{R}$, $R\overline{B}$, $B\overline{R}$, $G\overline{B}$, $B\overline{G}$, $\sqrt{\frac{1}{2}}(R\overline{R}-G\overline{G})$, and $\sqrt{\frac{1}{6}}(R\overline{R}+G\overline{G}-2B\overline{B})$. Color may or may not be changed when gluons are emitted. A $G\overline{R}$ gluon interacts with a Green quark and turns it into a Red quark or a $G\overline{B}$ gluon interacts with a Green quark and turns it into a Blue quark. When two quarks carrying identical colors interact, the color does not change. Say, two Blue quarks can only interact through the $\sqrt{\frac{1}{6}}(R\overline{R}+G\overline{G}-2B\overline{B})$ gluon.

So far, we have only observed quarks assembled in groups of two (mesons) and in groups of three (baryons). Mesons and baryons are collectively referred to as hadrons. The Standard Model tells us that hadrons must be colorless objects; *i.e.*, they must be color singlet states. The quark combinations of lowest energy are found to consist of the color singlet QQQ state for the case of baryons and the color singlet $Q\overline{Q}$ state for the case of mesons. The proton and neutron are baryons and are roughly made up of two up and a down quark; and two down and an up quark, respectively.

2.3 The Parton Model

The proton, as well as for the neutron and other hadrons, has a more complex substructure than just being made of quarks. In order to bind these quarks, the proton must also be made up of gluons. A successful description of the proton is given by the parton model [2].

This dissertation will focus on understanding the production of two jets, or sprays of highly collimated particles, in proton-antiproton collisions. In the parton model, the collision can be pictured as shown in Fig. 2.1. Most $\bar{p}p$ interactions involve low momentum transfers among the constituents. Occasionally, a parton from the proton collides with a parton from the antiproton in what is called a ***hard scattering*** because of the large momentum transfer Q. The outgoing partons are usually observed in the detector as jets. The partons that participate in the interaction come in different varieties. The probability of finding a parton of a given variety (i) inside the proton (p) is given by the ***parton distribution function*** f_i^p. Similarly, $f_j^{\overline{p}}$ is the probability of finding parton j inside the antiproton ($\overline{p}$). The hard scattering cross section between

parton i and j is denoted as $\hat{\sigma}(ij \to 12)$ and is called a *subprocess cross section* where 1 and 2 are the resulting outgoing partons. The remaining partons in both the proton and antiproton, called *spectator* partons, do not participate in the collision.

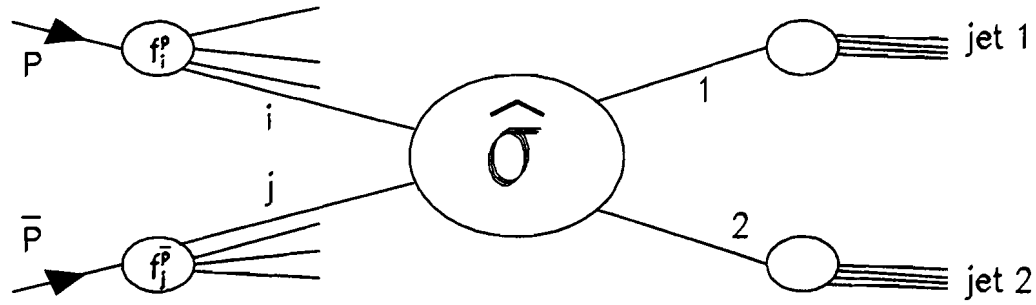

Figure 2.1: The Leading Order Cross Section.

At the Tevatron, protons and antiprotons are accelerated to 900 GeV and collided at a center of mass energy of $\sqrt{s} = 1800$ GeV. Even though both protons and antiprotons have fixed momenta, that is not the case for their constituent partons. The partons are assumed to be massless given that their masses are much smaller than the momentum transfer Q. Their longitudinal momentum ranges from zero to the proton momentum. A useful quantity is x_p ($x_{\bar{p}}$), which is defined as the fractional longitudinal momentum of a parton within the proton (antiproton); it ranges between zero and one. Thus, even though the lab frame is the center of mass frame for the interacting protons and antiprotons, it is not the center of mass frame for the interacting partons. To first order, the two jet cross section, σ, can be written in terms of the parton distribution functions and the subprocess cross section,

$$\sigma \sim \sum_{i,j} f_i^p f_j^{\bar{p}} \hat{\sigma}(ij \to 12). \tag{2.1}$$

In other words, thanks to a prescription known as *factorization*, by summing a series of integrals convoluting calculable fundamental cross-sections $\hat{\sigma}$ with universal parton distribution functions; and applying the QCD factorization theorems, one

obtains high energy hadron-hadron interaction cross sections σ [3]. The subprocesses are calculated via perturbative QCD and if the subprocesses are described appropriately, the pdf's can be derived from observed cross sections.

2.4 Theory of Strong Interactions

Perturbative QCD, pQCD, the theory of strong interactions between spin-1/2 quarks and spin-1 gluons, has proven to be very successful whenever the momentum transfer in a collision is high, hence short distances and short time. QCD was proposed following an analogy to the theory of electromagnetic interactions, QED. In the same manner that QED describes the interactions of electrons, QCD describes the interactions of quarks. The interactions are mediated in QED via quanta known as photons while in QCD they are known as gluons. The analogous charge characteristic that is associated with electrons, we have the property of color being associated with quarks. There are, however, fundamental differences between the two theories. In QED the photon does not carry charge while in QCD the gluon carries color. Due to this intrinsic nature, photons do not interact with themselves but gluons do.

2.4.1 Running Coupling Constant

In QED, electrons continuously emit and absorb photons with the photons converting into electron-positron pairs. The electron can then be viewed as surrounded by virtual electron-positron pairs. However, since opposite charges attract, the positrons will preferentially be nearer to the original electron. The vacuum surrounding the electron becomes polarized thus screening the real charge of the electron (*vacuum polarization*). Consequently, we measure that the charge of the electron increases as we get closer to the electron. This property of the vacuum polarization affects the effective coupling in QED:

$$\alpha(Q^2) = \frac{\alpha(Q_0^2)}{1 - \frac{\alpha(Q_0^2)}{3\pi} log(\frac{Q^2}{Q_0^2})}. \tag{2.2}$$

The change in the value of the effective coupling (α), as one goes from a process involving a typical momentum transfer Q_0^2 to one involving $Q^2 (> Q_0^2)$, depends logarithmically on the ratio $\frac{Q^2}{Q_0^2}$.

Similar to QED, QCD tells us that the quarks and gluons interact with each other with characteristic a coupling strength, α_s. However, unlike photons, gluons interact with themselves; in other words, the gluons self couple. Then, a gluon emitted from a quark can turn into a gluon pair resulting in an effect of antiscreening. As a result, unlike QED, the effective color charge decreases as one probes nearer the original quark. To leading order, the strong coupling constant is written as

$$\alpha_s(Q^2) = \frac{12\pi}{(33 - 2n_f)\log(Q^2/\Lambda^2_{QCD})} \tag{2.3}$$

where n_f is the number of quark flavors excited at a given Q, and Λ_{QCD} is a fundamental scale parameter of QCD obtained experimentally. This parameter, which has been measured at ~200 MeV, is roughly the energy scale that determines where perturbative calculations are accurate [4]. One must use phenomenological models for the non-perturbative calculations. From equation 2.3, one can see that as Q→ 0, (large distances), the coupling constant becomes very large and as Q→ ∞, (short distances), the constant goes to zero. Typical Q^2s for jet production at the Tevatron are large, so it is safe to use pQCD.

2.4.2 Leading and Next to Leading Order diagrams

For two jets final state, typical Feynman diagrams for the subprocess cross sections at Leading Order (LO) are shown in Fig. 2.2. The processes are shown in Table 2.5 with their respective cross sections expressed in terms of the Mandelstam variables. At LO, only these eight diagrams contribute and they are of the order $O(\alpha_s^2)$ because each diagram has two vertices. At Next-to-leading Order (NLO), the diagrams are of the order $O(\alpha_s^3)$. For NLO, one can have processes with two incoming partons and three outgoing partons or processes with two incoming partons and two outgoing partons but with a loop in between. Figure 2.3 shows several NLO diagrams. For the NLO calculations, all terms up to order $O(\alpha_s^3)$ are kept. Ideally, one would like to calculate the theory to all orders. At NLO, there are over one hundred distinct diagrams; for higher orders, the number of diagrams is even larger. So far, the theoretical calculation is available to NLO. Figure 2.4 shows a cartoon of a collision including higher order terms.

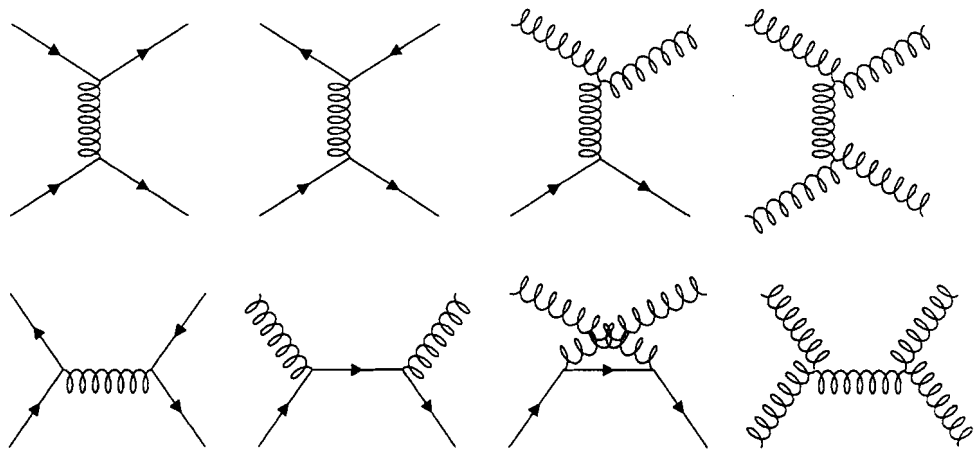

Figure 2.2: The Leading Order Feynman diagrams.

Subprocess	$\lvert\mathcal{M}\rvert/g_s^4$
$qq' \to qq'$	$\frac{4}{9}\frac{s^2+u^2}{t^2}$
$qq \to qq$	$\frac{4}{9}\left[\frac{s^2+u^2}{t^2}+\frac{s^2+t^2}{u^2}\right]-\frac{8}{27}\frac{s^2}{tu}$
$q\bar{q} \to q'\bar{q}'$	$\frac{4}{9}\frac{t^2+u^2}{s^2}$
$q\bar{q} \to q\bar{q}$	$\frac{4}{9}\left[\frac{s^2+u^2}{t^2}+\frac{u^2+t^2}{s^2}\right]-\frac{8}{27}\frac{u^2}{st}$
$gq \to gq$	$-\frac{4}{9}\left[\frac{s}{u}+\frac{u}{s}\right]+\frac{4}{9}\frac{s^2+u^2}{t^2}$
$q\bar{q} \to gg$	$\frac{32}{27}\left[\frac{t}{u}+\frac{u}{t}\right]-\frac{8}{3}\frac{t^2+u^2}{s^2}$
$gg \to q\bar{q}$	$\frac{1}{6}\left[\frac{t}{u}+\frac{u}{t}\right]-\frac{3}{8}\frac{t^2+u^2}{s^2}$
$gg \to gg$	$\frac{9}{2}\left[3-\frac{tu}{s^2}-\frac{su}{t^2}-\frac{st}{u^2}\right]$

Table 2.5: Squared matrix elements for $2 \to 2$ subprocesses in QCD (averaged over spin and color): q and q' denote distinct flavors of quark, $g_s^2 = 4\pi\alpha_s$ is the coupling squared.

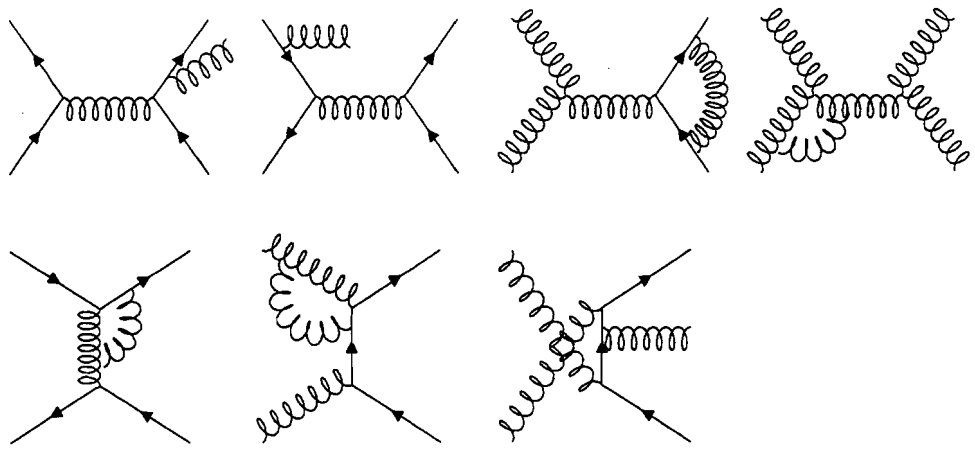

Figure 2.3: Some Next-to-Leading Order Feynman diagrams.

There are several improvements for NLO over LO:

- The NLO calculation includes higher order terms than the LO calculation making it less sensitive to the renormalization scale, which is introduced in QCD in order to handle the ultraviolet divergences. While LO calculations have a 30% normalization uncertainty, NLO calculations only have in general a 10% normalization uncertainty.

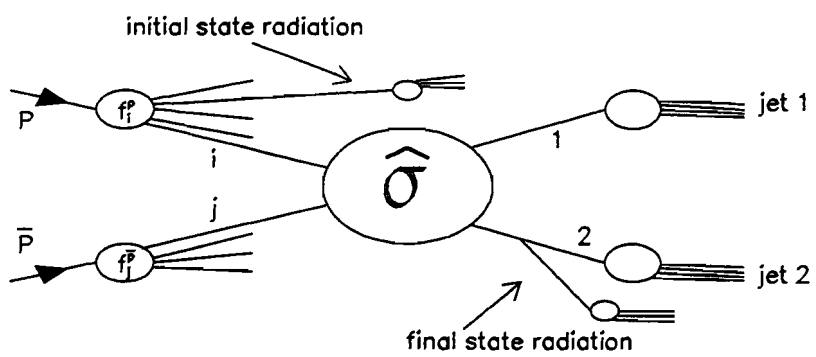

Figure 2.4: Cross Section with Higher Order Corrections.

- At LO, there are only two partons in the final state, so there is a one-to-one mapping with the outgoing jets. At NLO, we can have three partons in the final state. The possibility of having three jets in the final states is dependent on the jet clustering algorithm that one uses, so at NLO one introduces a jet clustering algorithm dependence.

- As we will see later, NLO relaxes some kinematic constraints. At LO, both jets must be balanced in p_T due to conservation of momentum. At NLO, the introduction of a possible third jet relaxes the requirement that the two leading jets must have the same p_T resulting in a larger cross section.

2.4.3 Hadronization

Given that quarks can never be free, how does one observe them? The resulting quarks from an interaction materialize into highly collimated sprays of particles moving in the directions of the initial quarks in a process known as *hadronization.* There are several models attempting to explain the hadronization process, the most successful of them is the so-called *string model* [5]. Intuitively, one starts with a quark-antiquark pair connected by color lines similar to the way two opposite charges are surrounded by an electric field. The difference is that in the case of the quarks, the lines of force are compressed into a *flux tube.* As they quark pair grows in separation, the energy also grows proportionally, but the flux tube cannot grow forever. When enough energy is available, a new quark pair is created out of the vacuum. This process continues, leading to a final state consisting of color singlet hadrons.

2.4.4 Jets

Experimentally, jets are made up of a collimated spray of particles originating from the hard scattering. Unlike an elementary particle, such as an electron or muon, the definition of a jet has a strong algorithm dependence. Theoretical calculations usually equate jets with partons, but at the experimental level, partons cannot be observed. We can only measure depositions of energy in the detector. A jet algorithm usually clusters together those energy depositions in an attempt to measure the original partons. This analysis will use the cone algorithm. The cone algorithm,

which clusters the energy contained in a fixed radius cone, will be described in detail in Chapter 4.

2.5 Parton Distribution Functions

According to QCD, the parton distribution functions depend both on x, the momentum fraction, and Q^2, the interaction momentum transfer squared. The slowly varying Q^2 dependence is predicted by QCD evolution through the Gribov-Lipatov-Altarelli-Parisi (GLAP) equations [6] and has been observed in *deep inelastic lepton scattering* (DIS) experiments [7].

A more complex picture of the proton tells us that the two up quarks and the down quark inside are valence quarks that are held together by exchanging gluons. In addition to these constituents, the proton also contains *sea* quarks and *sea* antiquarks originating from the Dirac sea of virtual quark-antiquark pairs. Hence the different varieties of partons are the six known quarks and antiquarks, and the gluons. Note that the gluon is its own antiparticle.

From charge conjugation invariance, the relationship between the parton distribution functions of the proton and antiproton is

$$f_i^p = f_{\bar{i}}^{\bar{p}} \tag{2.4}$$

where i runs over the six quarks, six antiquarks and the gluon.

Another useful quantity is the *parton structure function*, which is defined simply as the fractional momentum x times the parton distribution function f_i, where we have dropped the superscript for convenience. The quark and antiquark structure functions are usually written as

$$Q_i(x, Q^2) = x f_i(x, Q^2) \text{ with } i = u, \bar{u}, d, \bar{d}, ..., t, \bar{t} \tag{2.5}$$

and the gluon structure function is written as

$$G(x, Q^2) = x g_i(x, Q^2). \tag{2.6}$$

In the *single effective subprocess approximation* [8], where all parton-parton scattering cross sections are taken to be equal but weighted by color arguments, the

gluon-gluon, quark-gluon and quark-quark subprocesses have the ratio of $1{:}\frac{4}{9}{:}(\frac{4}{9})^2$ respectively. Thus, the *single effective parton density* is written as

$$F(x, Q^2) = G(x, Q^2) + \frac{4}{9}(Q(x, Q^2) + \overline{Q}(x, Q^2)) \tag{2.7}$$

where

$$Q(x, Q^2) = \sum_i Q_i(x, Q^2) \text{ with } i = u, d, c, s, t, b \tag{2.8}$$

$$\overline{Q}(x, Q^2) = \sum_i Q_i(x, Q^2) \text{ with } i = \overline{u}, \overline{d}, \overline{c}, \overline{s}, \overline{t}, \overline{b}. \tag{2.9}$$

The quark distributions have been extensively studied by deep inelastic scattering of muons and electrons off protons [7]. Since gluons do not have electroweak coupling, one must find other means to probe the gluon distribution. It can be accomplished by Drell-Yan pairs, by direct photons, or at the Tevatron, by jets given that at such high energies the main contributing diagrams are gluon-gluon and gluon-quark interactions. From Fig. 2.5, we see that the gluon distribution dominates at low values of x, while the quark distribution occupies the higher end of the spectrum.

There are many different methods for calculating the parton distribution functions; each using different experimental results, renormalization schemes, and fitting methods. Among the latest sets of pdf's we find the CTEQ [9], MRSD′ [10], and GRV sets [11].

The CTEQ collaboration has developed a family of curves fit to the latest available electron-proton scattering data from HERA [12]. They have different predictions depending on how the gluon distribution is extrapolated to low values of x (x$\sim$ 0.0001) in order to accommodate the upper and lower limits from the HERA gluon distribution results at these $x-$values. Their best fit is CTEQ2M. Assuming less gluons at x$\sim$ 0.0001, or a *flatter* gluon distribution, there is the CTEQ2MF prediction; for more gluons at x$\sim$ 0.0001, or a more *singular* gluon distribution, there is the CTEQ2MS prediction; and finally with Λ_{QCD} set at the LEP value, there is the CTEQ2ML prediction. Figures 2.6- 2.8 show the gluon distributions from the CTEQ collaboration over a wide range of x. The first figure shows the distribution over several decades of x-values indicating from which x-value Tevatron dijet production is sensitive to the gluon distribution and the latter two show the distributions near the value of $x = 0.1$.

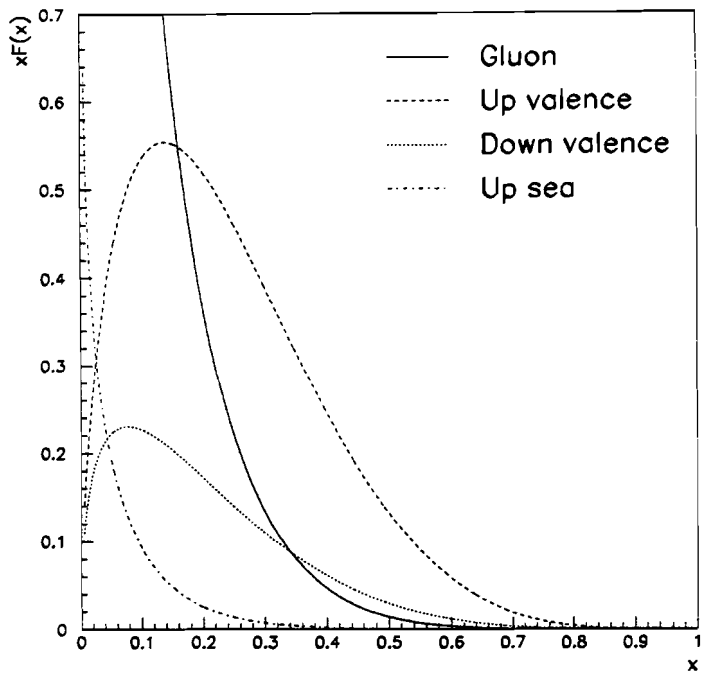

Figure 2.5: Distributions of different partons in the proton as a function of x at Q=50 GeV for CTEQ2M.

Martin, Stirling and Roberts [10] have also similar predictions: the MRSD$-'$ is the singular gluon prediction, the MRSD0$'$ is the flat gluon prediction and MRSA is their best fit.

2.6 Choice of Variables for Differential Cross Section

The two jet cross section can be described as

$$\frac{d^3\sigma}{dp_T dy_1 dy_2} \sim \sum_{i,j} f_i(x_1, Q^2) f_j(x_2, Q^2) \hat{\sigma}_{ij}(p_T, y_1, y_2) \tag{2.10}$$

where $x_{1(2)}$ is the momentum fraction of the proton (anti-proton) carried by the colliding parton; $f_{i,j}$ are the parton distribution functions (pdf) for the initial valence (u, $\bar{u}$, d, $\bar{d}$) or sea partons (u, d, s, ...), or gluons (g) evaluated at the energy scale of the hard scattering, Q^2; p_T is the transverse momentum; y_1 and y_2 are the rapidities of the outgoing partons; and $\hat{\sigma}_{ij}$ is the cross section for the scattering of partons i

and j. The rapidity is given by:

$$y = \frac{1}{2} \ln \frac{(\mathrm{E} + p_z)}{(\mathrm{E} - p_z)}. \tag{2.11}$$

However, for massless partons, y can be replaced by the pseudorapidity, η:

$$\eta = \ln \cot \frac{\theta}{2}. \tag{2.12}$$

For the leading order case, the momentum fractions, x_1 and x_2 of the incoming partons can be written in terms of the pseudorapidities of the final state partons:

$$x_1 = \frac{E_T}{\sqrt{s}}[\exp(\eta_1) + \exp(\eta_2)] \tag{2.13}$$

$$x_2 = \frac{E_T}{\sqrt{s}}[\exp(-\eta_1) + \exp(-\eta_2)] \tag{2.14}$$

where in addition to using $\eta = y$, we have set $E_T = p_T$ for massless partons. We have chosen these variables because we can measure them explicitly and because they are simple to transform to different reference frames. Hence, a cross section measured in terms of the transverse energy and the pseudorapidities of the outgoing jets is in essence a measurement of equation 2.10.

2.7 Theoretical Calculations

The experimental measurement will be compared to the theoretical predictions from JETRAD, which is a next-to-leading order (NLO) partonic generator written by Giele, Glover, and Kosower [13]. NLO diagrams are tree level $2 \rightarrow 3$ processes and 1-loop $2 \rightarrow 2$ processes such as the ones shown in Fig. 2.9. The output of JETRAD is the four-vectors for the two or three partons in the final state, which become two or three jets depending on the clustering algorithm. By partonic generator, we mean that there is a direct correlation between the jet and a parton; hence, there is no hadronization. The program is quite flexible by allowing several parameters to be changed by the user depending on the needs. The user could select whether to run LO or NLO; the η, E_T range of the outgoing jets; the jet cone size; different pdf's; and choice of renormalization/factorization scale.

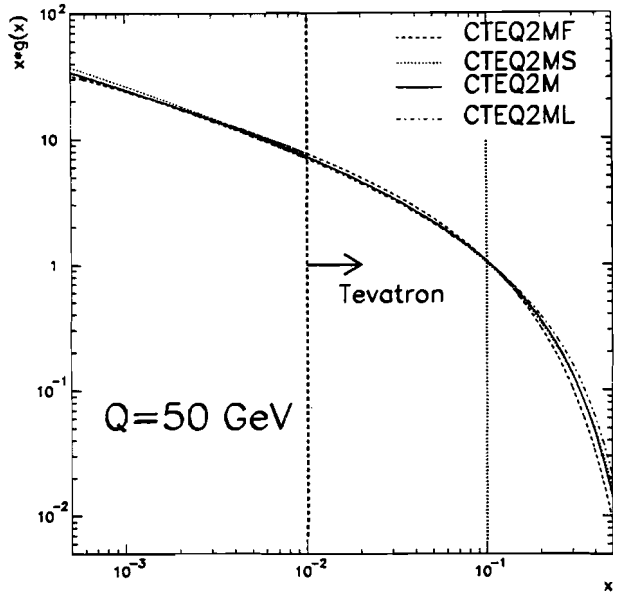

Figure 2.6: The gluon distribution as a function of x at Q=50 GeV for several pdf's. The dashed line shows the minimum x-value that can be probed at the Tevatron using dijets. The dotted line shows the x-value that the CTEQ pdf's have roughly the same gluon content.

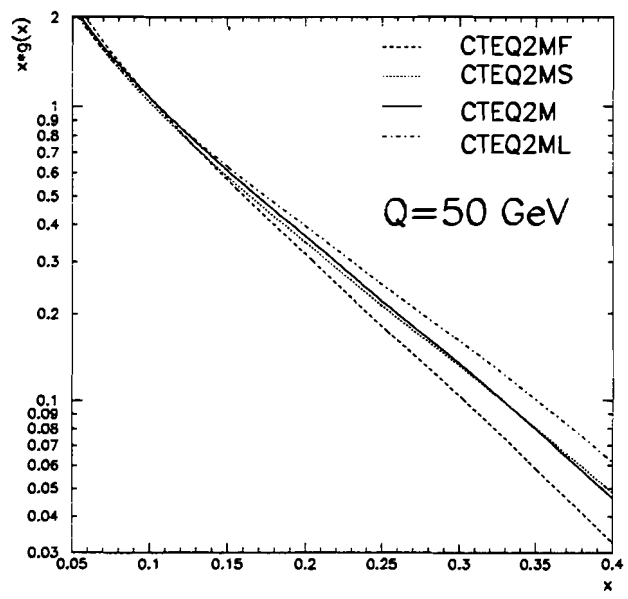

Figure 2.7: The gluon distribution as a function of x at Q=50 GeV for several pdf's at relatively "high" x-values.

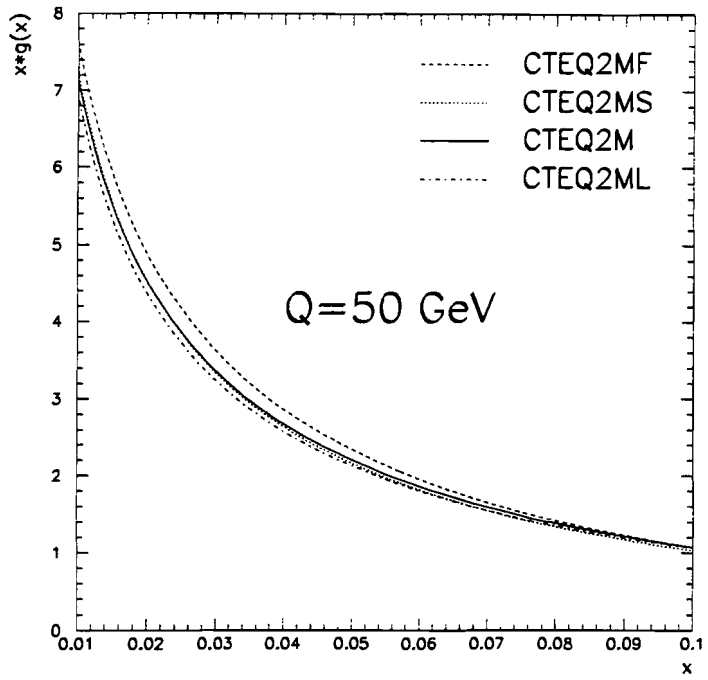

Figure 2.8: The gluon distribution as a function of x at Q=50 GeV for several pdf's at relatively "low" x-values.

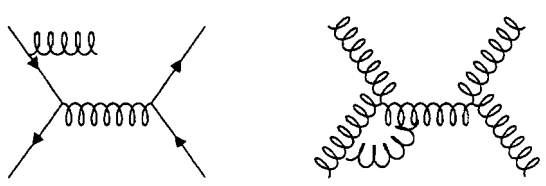

Figure 2.9: Examples of Two-to-Three Tree level and Two-to-Two one-loop diagrams.

CHAPTER 3

Apparatus

3.1 Overview

The DØ detector, shown in Fig. 3.1, is a general purpose particle detector designed to study $p\bar{p}$ interactions at the Fermilab Tevatron collider at a center-of-mass energy $\sqrt{s} = 1.8$ TeV.

The original DØ design report from 1984 [14] described the topics of interest to be studied. Among them were the study of electroweak physics (W, Z, γ), perturbative QCD, heavy quarks, and new physics. The detector was built with these topics in mind, and it is noteworthy that these topics are still relevant. Another design goal was that the detector would complement the strengths of the CDF [15] detector, also located at the Tevatron. This meant that DØ would not have a central magnetic field, following the spirit of the UA2 [16] detector, and would concentrate on identification and measurement of muons and electrons, reconstruction of jets, and identification of noninteracting particles (such as neutrinos) by measuring the missing transverse energy.

The DØ detector is composed of three types of subdetectors: tracking, calorimetry, and muon detectors. The tracking chambers lie closest to the interaction point and measure the trajectories of charged particles. Surrounding the tracking chambers are the calorimeters. The calorimeters are used to measure the energies of electrons, photons, and hadrons. These particles create showers in the calorimeters, which are built thick enough to completely absorb most showers. Only muons and neutrinos escape the calorimeter. Outside the calorimeters, drift chambers and magnetized

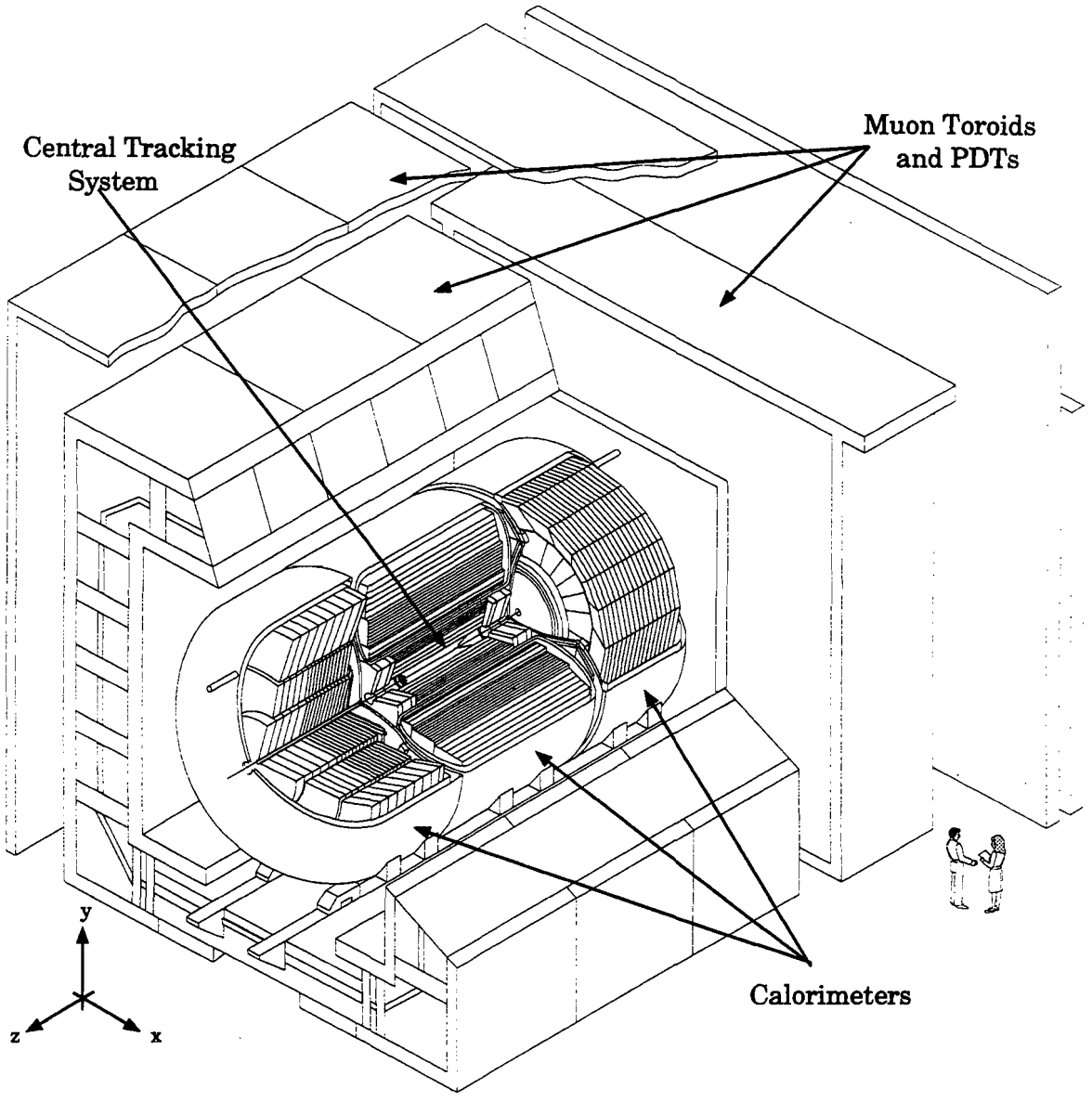

Figure 3.1: The DØ detector consists of three subsystems: the Muon system, the Calorimeters, and the Central Tracking System.

iron toroids are used to detect muons. Neutrinos are identified by a non-zero vector sum of the energy flow transverse to the beam. Note that we can only measure the neutrino momentum transverse to the beam because the DØ detector is not hermetic enough, (for example, near the beampipe), to accurately measure energy flow parallel to the beam.

In this chapter, we start with a brief description of the relevant accelerator parameters for high energy physics experiments. We then proceed to describe the physics principles behind the different detectors used for particle identification. We then describe the different detectors used by the DØ experiment including a description of the data acquisition system. We conclude by describing the data formats available from DØ in order to perform any kind of analyses.

3.2 Accelerator

In the study of elementary particles, there is an ongoing need to probe smaller distances. The spatial resolution that one can obtain by scattering particles from one another is inversely proportional to the momenta of the colliding particles. This implies that for smaller distances, we need higher energy in the center-of-mass reference frame.

The most important advantage of a colliding beam experiment over a fixed target experiment, where particles are accelerated and smashed against a fixed target, is the ability to achieve higher center-of-mass energy. The center-of-mass energy increases as $\sqrt{E_1}$ in the case of a fixed target experiment, while it increases as $\sqrt{E_1 \times E_2}$ for a colliding beam experiment where E_i is the energy of the accelerated beam of particles. However, the other crucial accelerator parameter is the luminosity and collider experiments have lower luminosity than fixed target experiments. Luminosity can be defined as the number of particles per second circulating in one beam multiplied by the average number of intercepted particles per square centimeter in the other. The event rate for the particular process is given by the product of the luminosity and cross section,

$$R = \sigma \mathcal{L} \tag{3.1}$$

where R is the event rate, σ is the cross section and $\mathcal{L}$ is the instantaneous luminosity

(in units of $cm^{-2}s^{-1}$).

In order to keep track of how much luminosity a machine has delivered, we use the term *integrated luminosity*, defined as the time integral of the instantaneous luminosity. Excellent descriptions of the Fermilab accelerator can be found in the literature [17, 18].

3.3 Particle Detection

The basic strategy to detect particles is by forcing them to interact and then trying to measure the product of their interaction. However, it is not enough just to detect them; one also hopes to determine physical quantities such as position, time, mass, energy, and momentum of the particle. The procedure is different for electromagnetic and hadronic particles. Charged particles can be detected by their electromagnetic interaction with the atomic electrons of the detector material, yielding ionization, scintillation, Čerenkov, and transition radiation. Photons interact via the photoelectric effect, Compton scattering, and pair creation, where the latter process dominates for photons with energies over 1 MeV. Electrons also interact electromagnetically losing energy through Bremsstrahlung and ionization processes. Hadrons can interact with detector nuclei producing a shower of short and long lived hadrons. For collider detectors, the presence of a neutrino is usually inferred by applying conservation of momentum. In this section, particle detection techniques used in DØ are described.

3.3.1 Principles of Wire Drift Chambers

Drift chambers [19, 20] allow accurate position measurement of charged particles. Drift chambers consist of planes of wires used to detect the ionization trail left by charged particles when they traverse the chamber, which is filled with a gas mixture.

An electric field is applied so that electrons and ions drift in separate directions. Ions, being heavier, tend to move much slower than the free electrons. The number of free electrons are not sufficient to provide a measurable signal. Under the influence of the electric field, as the electrons approach the positive electrode wire, the free electrons become energetic enough to start creating electron-ion pairs. The new free electrons can also become energetic enough to create even more electron-ion pairs

and so on. This process is called a cascade or avalanche and induces a signal on the wire. By measuring the electron drift time we can reconstruct the position of the charged particle as it traversed the chamber. Combining this information for the many wires in the chamber, we can reconstruct the track of the particle.

3.3.2 Scintillation Counters and Photomultipliers

A charged particle passing through a solid will excite electrons into higher energy states. In scintillating materials, the electron can be excited into a meta-stable state, which then decays by radiating a photon [21]. That light can be captured and transported to, for example, the photocathode of a photomultiplier tube (PMT), which liberates electrons from the photocathode by the photoelectric effect. These electrons are accelerated and focused onto the first dynode, which in turn creates more electrons. A PMT usually has 8 to 14 dynode stages producing a gain of up to 10^8. The timing of the PMT signal provides information about when the charged particle passed through the detector, while the amplitude measures the amount of scintillation light and hence the amount of energy deposited in the scintillator.

3.3.3 Transition Radiation Detectors

Transition radiation [22] occurs when a highly relativistic charged particle ($\beta\gamma \geq 500$) crosses the boundary between two materials with different dielectric constants. The particle must radiate photons in order to satisfy the boundary conditions at the transition point. The main purpose of a Transition radiation detector (TRD) is to discriminate between particles of different mass such as rejecting pions from electrons; or rejecting kaons from pions.

3.3.4 Calorimeters

Calorimeters [23] are used to measure the energy and direction of particles by forcing them to interact and deposit most of their energy in the subsequent "shower" of increasingly lower energy particles. In the case of electromagnetic particles (electrons and photons), these particles create showers of lower-energy photons, electrons and

positrons. The unit of measure for an electromagnetic shower is the radiation length, X_o, defined as the mean distance over which a high energy electron loses all but $1/e$ of its energy by bremsstrahlung. On the other hand, hadronic particles, such as $\pi^{\pm}$, $K^{\pm}$, p, interact with the nuclei of the detector atoms. The unit of measure for a hadronic shower is the nuclear interaction length, Λ, and is defined as the mean free path over which all but $1/e$ of the hadrons undergo nuclear interaction. Among the properties common to calorimeters, we have

- a) Calorimeters are sensitive to both neutral and charged particles.
- b) They can be used for particle identification based on the different shower patterns of electrons, photons, hadrons, and muons.
- c) Very fine segmentation can be achieved in order to provide accurate position measurements of particles.

Calorimeters can be classified as total absorbing or sampling. In a total absorbing calorimeter, the total energy of the shower is deposited in the active medium. This type of calorimeter generally has superior energy resolution. Among the disadvantages are expense and poor longitudinal segmentation. In sampling calorimeters, as the name indicates, only part of the total energy is deposited in the active medium. The major drawback is poorer energy resolution but the gains are low cost, compactness, and easy segmentation. Since sampling calorimeters only detect part of the energy loss, they must be corrected by the sampling fraction to reproduce the total energy lost. The sampling fraction is defined as

$$\frac{\mathrm{E_{live}}}{\mathrm{E_{live}} + \mathrm{E_{dead}}}.$$

3.4 The DØ Central Detector

The DØ central detector (CD) is made up of four major subdectectors as illustrated in Fig. 3.2. Three of them are tracking chambers and the fourth one is used for electron identification purposes. Following the trajectory of a particle produced at the interaction point, one meets the vertex detector (VTX), which is a drift chamber used for tracking and vertex finding. One then continues to the transition radiation detector (TRD), used for electron identification and then to the central drift chamber

(CDC), used for track finding. If the particle has a trajectory in the forward direction, it would meet the forward drift chambers (FDC) instead of the CDC. DØ's lack of a central magnet enables a very compact calorimeter. These four subdetectors are contained in a cylindrical tracking volume of radius r = 75 cm and length l=270 cm. A detailed description can be found in reference [24].

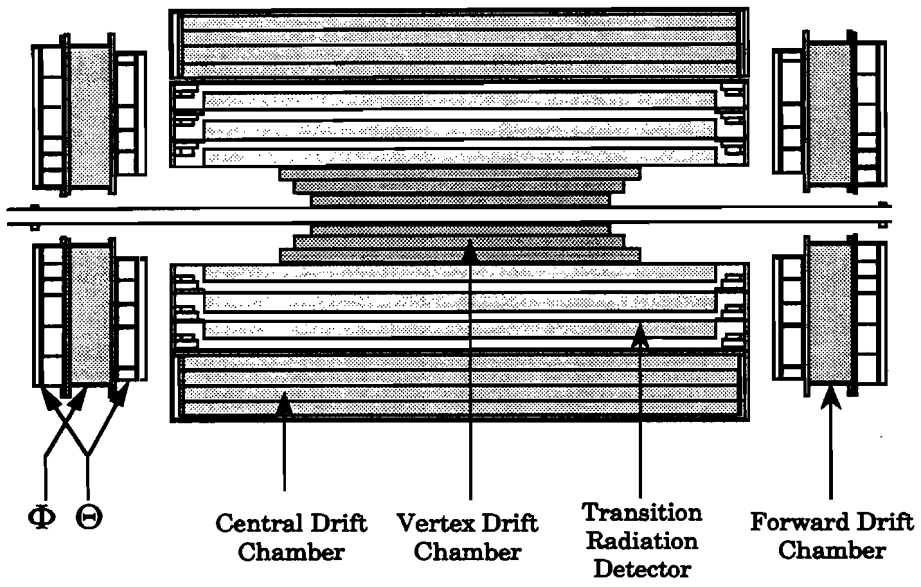

Figure 3.2: The DØ Tracking System can be subdivided into the Vertex detector, the Transition Radiation Detector, the Central Drift Chamber, and the Forward Drift Chambers.

3.4.1 Vertex Detector

The vertex chamber [25] surrounds the interaction point 2π in azimuth (ϕ) from an inner radius of 3.7 cm to an outer radius of 16.2 cm. The walls of the vertex detector were chosen to be carbon fiber, since it is low density, thereby minimizing the probability of photons converting into electron-positron pairs. An end view of a quadrant of the chamber is shown in Fig. 3.3. The inner layer is 97 cm long while each successive layer has an additional 10 cm, providing coverage for $|\eta| < 2.3$. The inner chamber is divided into 16 sectors in azimuth while the other two are divided into 32 sectors. Each sector consists of eight sense wires with readout at both ends

to measure the z position using the method of charge division. The r-ϕ position is obtained by measuring the drift time. In order to avoid left-right asymmetries, the wires are staggered by 100 microns. The layers are also rotated in ϕ to avoid dead regions. Wire sizes, composition, and other vital statistics may be found in Table 3.1

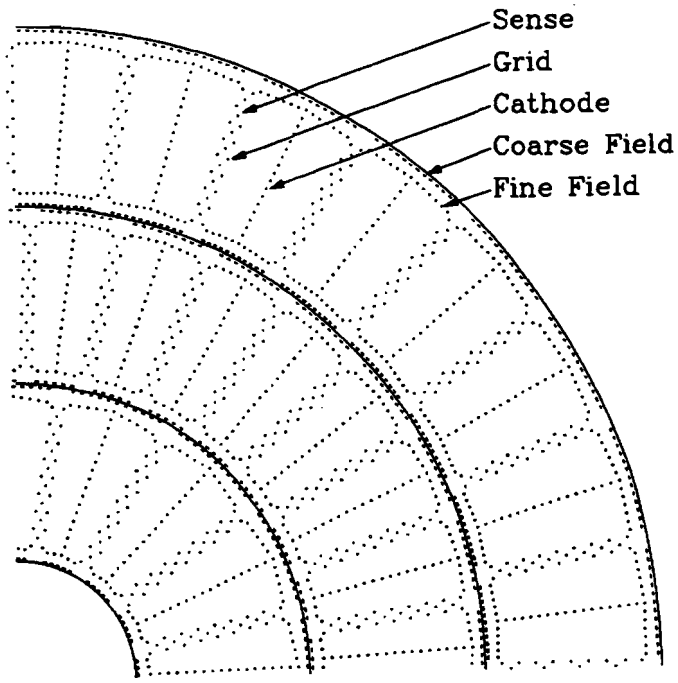

Figure 3.3: End view of a quadrant of the Vertex detector.

Length of active volume:	Layer 1	96.6 cm
	Layer 2	106.6 cm
	Layer 3	116.8 cm
Radial Interval (active)		3.7 - 16.2 cm
Number of layers		3
Radial wire interval		4.57 mm
Number of sense wires/cell		8
Number of sense wires		640
Type of Gas		CO_2(95%)-ethane(5%)-H_2O(0.5%)
Pressure of Gas		1 atm
Drift Field		1.0-1.6 kV/cm
Average Drift Velocity		7.6-12.8 μm/ns
Gas Gain at Sense Wires		$4x10^4$
Sense Wire Potential		+2.5 kV
Diameter of Sense wire		25 μm NiCoTin
Diameter of Guard wire		152 μm Au-plated Al

Table 3.1: Vertex chamber parameters.

3.4.2 Transition Radiation Detector

The TRD [26] is made of three concentric layers surrounding the VTX. Each layer has 393 layers of 18 micron polypropylene foil each separated by 150 microns. The detector is based on the principle that charged particles emit photons when crossing the boundary of two materials with different dielectric or magnetic properties. The energy of the photon is inversely proportional to the square root of the energy of the charged particle that crossed the media. Hence, if the particle is highly relativistic, it then emits X-rays, which are detected in a Xenon gas drift chamber. Since electrons are the only probable charged particles that can induce detectable radiation at the Tevatron, the TRD is used to help identify electrons. Figure 3.4 shows a view of the TRD.

3.4.3 Central Drift Chamber

The CDC [27] has a coverage of $|\eta| < 1$. It is made up of four cylindrical layers, each divided in ϕ into 32 cells. Each cell, in turn, has seven sense wires, staggered by

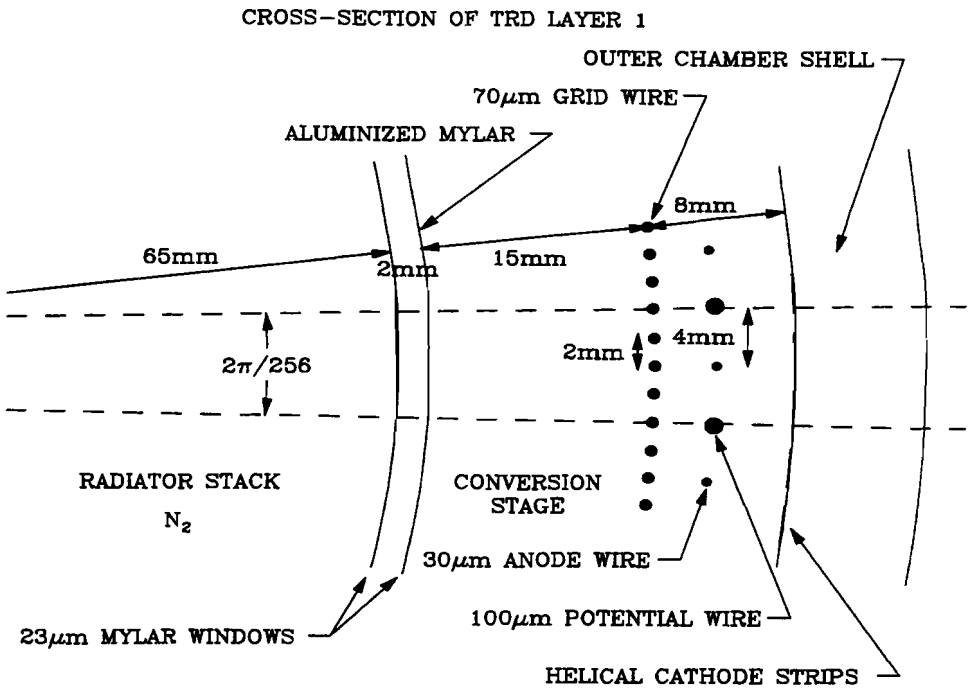

Figure 3.4: View of a section of the Transition Radiation Detector.

0.2 mm, running parallel to the beam pipe and two delay lines which are embedded in the outer and inner walls of each layer next to the sense wires. The delay lines provide a measurement of the z coordinate of the track. Similar to the VTX, the wires are staggered to resolve the left-right asymmetries. As can be seen from Fig. 3.5, the cells themselves are also staggered by one half cell to minimize dead regions and aid in track reconstruction. Table 3.2 shows the characteristics of the CDC.

3.4.4 Forward Drift Chamber

The FDC [28, 29] performs the same function as the CDC for $|\eta| > 1$ down to $|\eta| \sim 3.1 (\theta \sim 5°)$. There are two sets of three chambers taking care of the forward and backward tracking. The chambers are of two types: two of them were built to measure the θ coordinate (Θ module) and are rotated 45 degrees with respect to each other. The other type is the Φ module. It is placed in between the two Θ modules and measures the ϕ coordinate. Each Θ module consists of four mechanically separate quadrants, each one containing six rectangular cells at increasing radii. All the cells

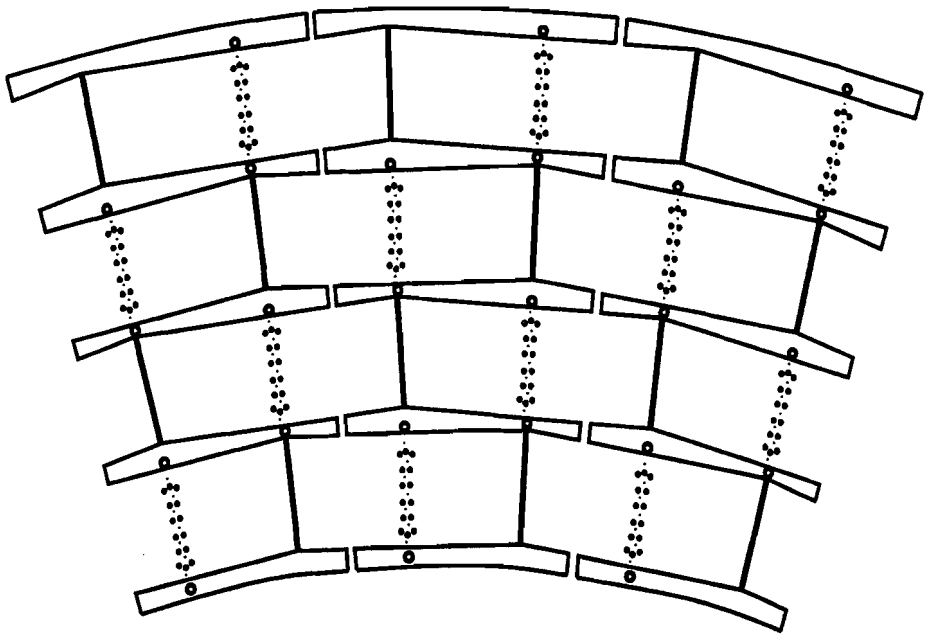

Figure 3.5: End view of a section of the Central Drift Chamber.

have eight anode wires (wireplane in $\phi - z$) and have one delay line to give a ϕ measurement. The Φ module consists of sixteen layers of 50 cm length radial sense wires. Each layer has 36 sense wires. Both types of chambers have a maximum drift distance of 5.3 cm and sense wire staggering of 0.2 mm. Figure 3.6 shows the three modules that make up the FDC and Table 3.3 shows the characteristics of the FDC.

3.5 Muon Detectors

The DØ muon system [30, 31] is divided in two subsystems: the Wide Angle Muon Spectrometer (WAMUS) and the Small Angle Muon Spectrometer (SAMUS). The WAMUS detector has an angular coverage of $10° \leq \theta \leq 170°$, and SAMUS has an angular coverage of $3.7° \leq \theta < 10°$. Since the DØ detector does not have a central magnet, the muon system has five separate solid-iron toroidal magnets that are used for momentum measurement. The muon drift chambers are placed in the following manner: one inside the iron (A layer), and two outside (B and C layers). Layers B and C are separated by an air gap of 1-3 m providing an accurate measurement of the muon direction after the iron toroid. The central toroid (CF) has an angular coverage

Length of active volume:	179.4 cm
Radial Interval (active)	51.8 - 71.9 cm
Number of layers	4
Radial wire interval	6.0 mm
Number of sense wires/cell	7
Number of sense wires	896
Number of delay lines	256
Type of Gas	Ar(93%)-CH_4(4%)-CO_2(3%)-H_2O
Pressure of Gas	1 atm
Drift Field	620 V/cm
Average Drift Velocity	34 μm/ns
Gas Gain at Sense Wires	$2,6 \times 10^4$
Sense Wire Potential	+1.5 kV
Diameter of Sense wire	30 μm Au-plated W
Diameter of Guard wire	125 μm Au-plated CuBe

Table 3.2: Central Drift Chamber parameters.

of $41° \leq \theta < 139°$, and the two end wall toroids (EF) have a coverage of $9° \leq \theta < 43°$. The CF iron has a thickness of approximately 110 cm, and the EF iron is around 150 cm thick. The field produced is about 2 Tesla. Multiple Coulomb scattering in the iron limits the relative momentum resolution to 18%. Characteristics of the muon system are described in Table 3.4.

3.6 Calorimeter

DØ's calorimetry is contained in three vessels: one central (CC) and two end cryostats (EC) [32]. DØ uses depleted uranium as the absorber in most of the calorimeter, but there are some outer sections made with copper or stainless steel absorber. The medium for detection is liquid argon. Charged particles that traverse the liquid argon ionize the normally liquid argon. An electric field causes the electrons to drift to the readout boards, inducing a charge on the readout pads which is measured by the calorimeter electronics. In the space between the central and endcap cryostats, there is a set of scintillators with associated photomultipliers called the Inter-Cryostat Detector (ICD). Right before the central cryostat and after the endcap cryostats, there are readout boards called Massless Gaps (MG). The ICD and MG are used to sample

	Θ *modules*	Φ *modules*
z interval	104.8-111.2 cm	113.0-127.0
	128.8-135.2 cm	
Radial Interval	11-62 cm	11-61.3 cm
Number of cells in radius	6	
Maximum Drift Distance	5.3 cm	5.3 cm
Sense Wire staggering	0.2 mm	0.2 mm
Sense Wire separation	8 mm	8 mm
Angular Interval/cell		10°
Number of Sense wires per cell	8	16
Number of Delay lines per cell	1	0
Number of Sense Wires per end	384	576
Number of Delay lines readout/end	96	
Type of Gas	$Ar(93\%)$-$CH_4(4\%)$-$CO_2(3\%)$	H_2O
Pressure of Gas	1 atm	1 atm
Drift Field	1.0 kV/cm	1.0 kV/cm
Average Drift Velocity	37 μm/ns	40 μm/ns
Gas Gain at Sense Wire	$2.3, 5.3 \times 10^4$	3.6×10^4
Sense Wire Potential	+1.5 kV	+1.5 kV
Sense Wire Diameter	30 μm Au-plated W	
Guard Wire Diameter	163 μm Au-plated Al(5056)	

Table 3.3: Forward Drift Chamber parameters.

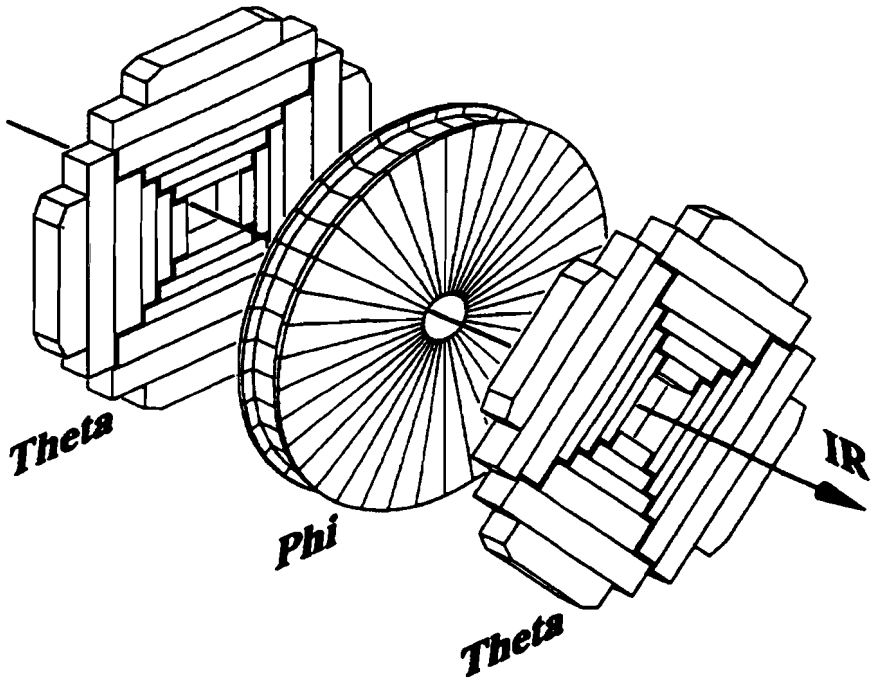

Figure 3.6: The Φ module sandwiched by the two Θ modules in the FDC.

	WAMUS	SAMUS
Rapidity coverage	$\lvert\eta\rvert \leq 1.7$	$1.7 \leq \lvert\eta\rvert \leq 3.6$
Magnetic Field	$2\ T$	$2\ T$
Number of Chambers	164	6
Interaction lengths	13.4	18.7
bend view resolution [a]	± 0.53 mm	± 0.35 mm
Non-bend resolution	± 3 mm	± 0.35 mm
$\delta P/P$ [b]	18%	18%
Gas	Ar(90%)-CF_4(5%)-CO_2(5%)	CF_4(90%)-CH_4(10%)
Avg. Drift Velocity	6.5 cm/μs	9.7 cm/μs
Anode Wire Voltage	$+4.56kV$	$+4.0kV$
Cathode Pad Voltage	$+2.3kV$	–
Number of cells	11,386	5308

Table 3.4: Muon system parameters.

[a] the diffusion limit is $0.2 - 0.3$ mm

[b] multiple scattering limit, assumes 100% chamber efficiency

the showers as many go through the cryostat walls in passing from the central to the end calorimeters. The combination of the ICD and MG improves the energy resolution from $\geq \frac{200\%}{\sqrt{E}}$ to $\frac{120\%}{\sqrt{E}}$ in the Inter-Cryostat Region (ICR).

Each calorimeter is divided into electromagnetic and hadronic layers; the former are optimized for the identification and measurement of electrons and photons whereas the latter are similarly optimized for hadronic jets. Figure 3.7 shows the three calorimeters and their subsections. Figure 3.8 shows a quadrant view of the full calorimeter. These figures show the transverse and longitudinal segmentation of the calorimeter and the relative locations of the tracking chambers. The beam pipe for the main ring accelerator, used to produce antiprotons, goes through the coarse hadronic section of all three calorimeters.

3.6.1 Central Calorimeter (CC)

The CC covers the region $|\eta| \leq 1.2$. It consists of three concentric rings of three kinds of modules. Closest to the interaction region, we find thirty-two CC Electromagnetic modules (CCEM), followed by sixteen CC Fine Hadronic modules (CCFH). Surrounding these, there are sixteen CC Coarse Hadronic modules (CCCH). The CCEM has four readout layers, while the CCFH has three and the CCCH has one. All layers have a fine transverse segmentation of 0.1×0.1 in $\eta \times \phi$ space except the third readout layer of the CCEM which is 0.05×0.05. The characteristics of the central calorimeter are in Table 3.5.

CC Electromagnetic Calorimeter (CCEM)

The thickness of the CCEM is 21 radiation lengths. All 32 modules cover the entire z-range and ≈ 0.2 radians in ϕ. The four readout layers are two, two, seven, and ten radiation lengths, respectively. The third layer, where the maximum of the EM shower is located, has a segmentation of 0.05×0.05 in $\eta - \phi$ space. This layer is finely segmented in order to optimize the position resolution and pattern recognition at the shower maximum for electrons and photons.

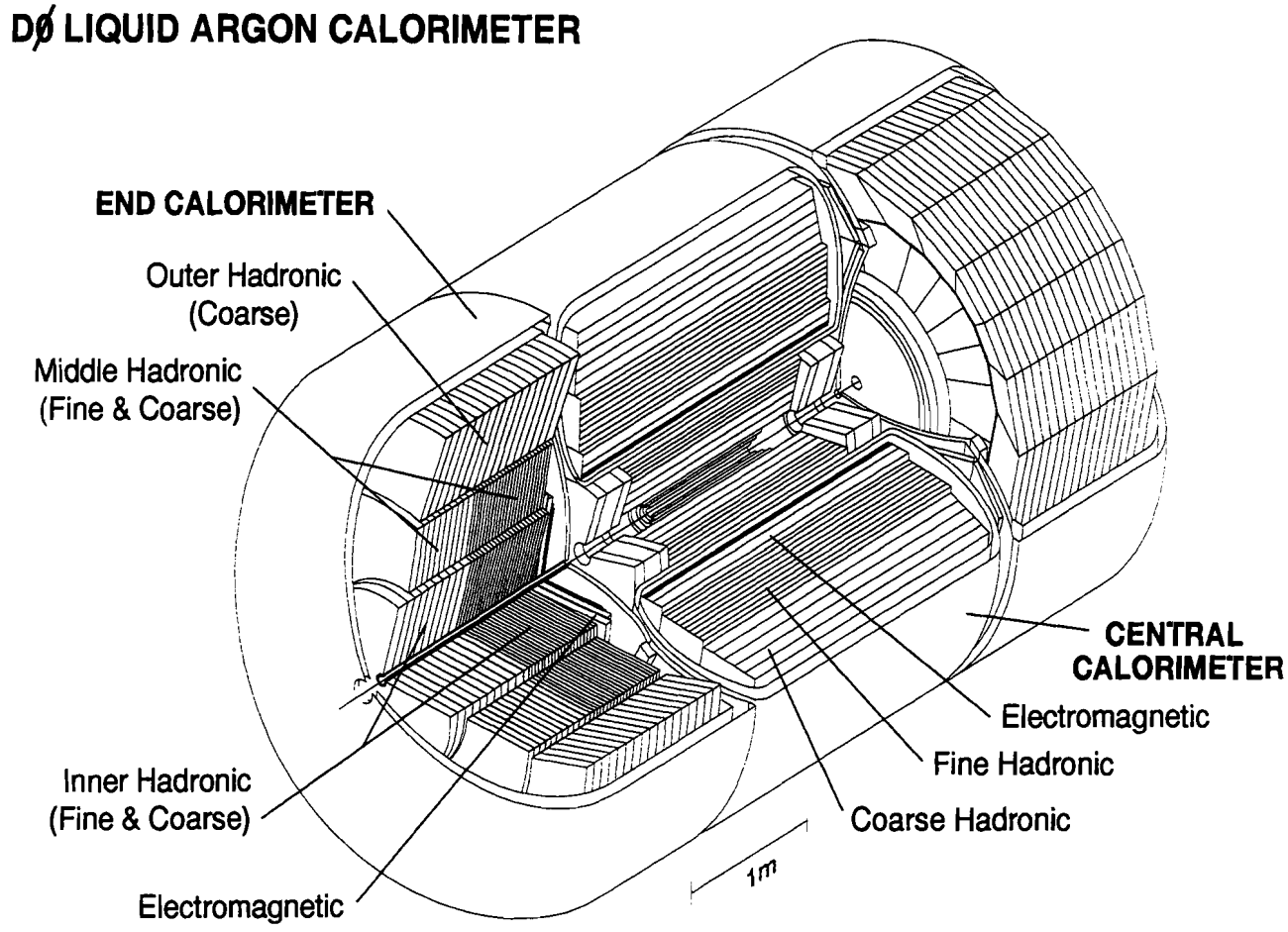

Figure 3.7: The DØ calorimetry, consisting of the Central Calorimeter with two End Calorimeters. The Inter-Cryostat Detector is mounted on the face of each End Calorimeter.

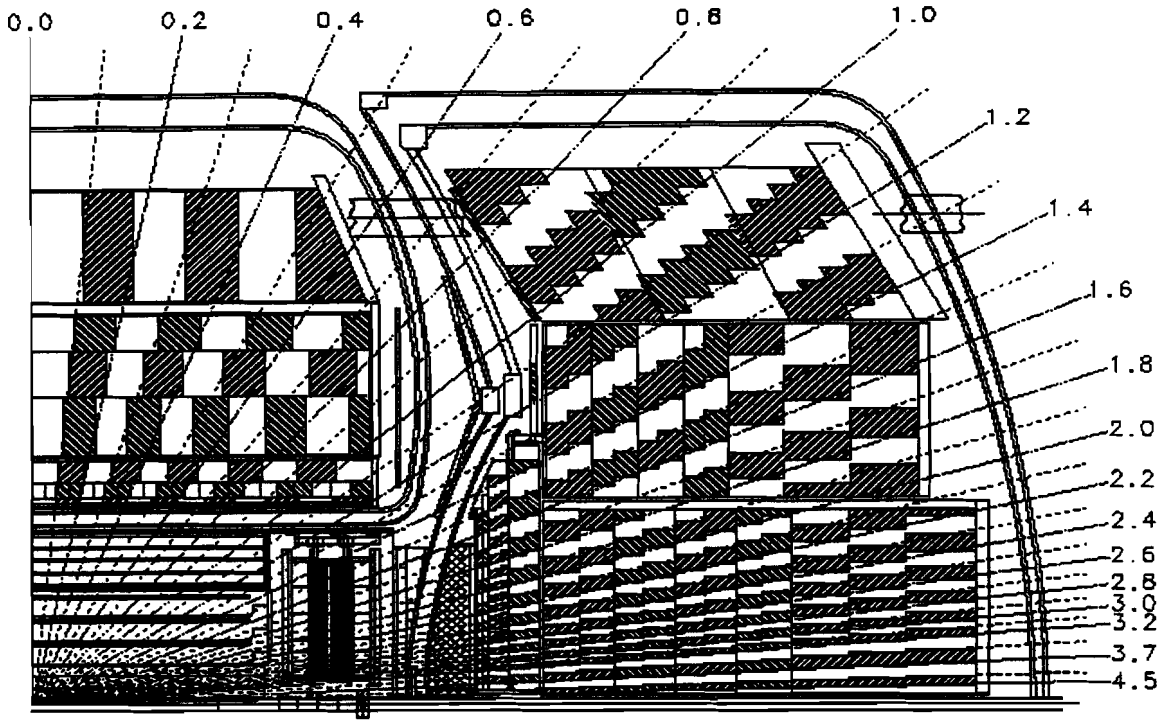

Figure 3.8: Quarter view of the calorimeter with constant lines in η.

CC Hadronic Calorimeter (CCFH and CCCH)

In order to identify and measure jets, the CCEM is followed by the hadronic portion of the calorimeter. Its 6.4 interaction lengths are added to the 0.8 interaction lengths from the CCEM to contain hadron showers. The full η coverage of the hadronic section goes roughly out to $|\eta| \leq 0.9$. The hadronic section is divided into Fine Hadronic (FH) and Coarse Hadronic (CH) sections, each containing 16 modules. The modules have a segmentation of 0.1×0.1 in $\eta \times \phi$. The CCFH modules use uranium as an absorber and are divided in three layers of 1.3, 1.0, and 0.9 interaction lengths, respectively. Given that hadronic showers have large fluctuations in longitudinal depth, the CCFH is backed up by the CCCH which uses copper instead of uranium as the absorber. It only has one readout layer of 3.2 interaction lengths. In order to avoid dead regions, the CCFH modules have been placed in such a way that the inter-module boundaries do not coincide with the CCEM intermodule boundaries. A similar philosophy was applied when placing the CCCH modules.

	EM	FH	CH
Rapidity coverage	±1.2	±1.0	±0.6
Number of Modules	32	16	16
Absorber [a]	uranium	uranium	Copper
Absorber Thickness (inches)	0.118	0.236	1.625
Argon Gap (inches)	0.09	0.09	0.09
Number of cells per module	21	50	9
Longitudinal depth	20.5 X_0	3.24 λ_0	2.93 λ_0
Number of readout layers	4	3	1
Cells per readout layer	2,2,7,10	20,16,14	9
Total Radiation lengths	20.5	96.0	32.9
Radiation length per cell	0.975	1.92	3.29
Total Absorption lengths (Λ)	0.76	3.2	3.2
Absorption length per cell	0.036	0.0645	0.317
Sampling Fraction (%)	11.79	6.79	1.45
Segmentation ($\Delta\phi \times \Delta\eta$) [b]	0.1×0.1	0.1×0.1	0.1×0.1
Total Number of readout cells	10,368	3000	1224

Table 3.5: Central calorimeter parameters.

[a] uranium is depleted and FH absorber contain 1.7% Niobium alloy

[b] Layer 3 of the EM has 0.05×0.05

3.6.2 End Calorimeter (EC)

The two End Calorimeters were built identically and have an η coverage of $0.7 \leq |\eta| \leq 4.45$. The $\eta - \phi$ segmentation is similar to the CC and each has an EM section, followed by hadronic coverage. The characteristics of the end calorimeters are in Table 3.6.

EC Electromagnetic Calorimeter (ECEM)

The ECEM has the distinction of being a single module in order to avoid dead regions. The module is a single disk centered on the Tevatron beampipe. Each module has a coverage of $1.4 \leq |\eta| \leq 4.0$ and has four longitudinal layers of 0.3, 2.6, 7.9, and 9.3 radiation lengths respectively. Each module has 0.1×0.1 in $\eta \times \phi$ segmentation, except the third layer which is 0.05×0.05. The absorber is uranium while the active medium is Liquid Argon. The segmentation decreases at $|\eta| \geq 3.2$ to 0.2×0.2.

EC Hadronic Calorimeter (ECIH, ECMH, and ECOH)

The Hadronic sections in the EC are divided based on their η coverage:

1) the EC Inner Hadronic module is situated behind the ECEM module and the η coverage is $1.6 \leq |\eta| \leq 4.45$. Similar to the ECEM, is centered around the Tevatron beampipe and is composed of a single module. Similar to the CC hadronic sections, it has a Fine Hadronic section (IFH) made of four readout layers of 1.1 total interaction lengths each and a Coarse Hadronic section (ICH) made of one readout layer of 4.1 interaction lengths. The absorber for the IFH is uranium and stainless steel for the ICH.

2) Surrounding the ECIH are the EC Middle Hadronic (ECMH) modules, also concentric to the Tevatron beampipe. The Fine Hadronic (EC-MFH) modules have four readout layers of 0.9 interaction lengths each with uranium absorber and the Coarse Hadronic (ECMCH) modules have one readout layer of 4.4 interaction length of stainless steel absorber. The ECMH section is divided into sixteen modules and cover $1.1 \leq |\eta| \leq 2.0$.

3) The EC Outer Hadronic section consists of sixteen modules, each with one readout layer of seven interaction lengths with stainless steel as the absorber. It is also concentric to the Tevatron beampipe and covers $0.7 \leq |\eta| \leq 1.4$ in $\eta - \phi$. The stainless steel plates are inclined at an angle of roughly 60° with respect to the beampipe.

3.6.3 Massless Gaps and Intercryostat Detector (ICD)

Showers that travel from the CC to the EC ($0.8 \leq |\eta| \leq 1.4$) must go through much dead material causing them to lose energy. In order to measure the showers in this region, and hence keep the energy resolution from degrading, there are two sets of detectors [33]:

1) Massless gaps are readout signal boards. They are placed on the surfaces of the CCFH, ECMH, and ECOH modules in order to sample the showers leaving the CC cryostat and entering the EC cryostat.

2) The Intercryostat Detector (ICD), a set of 384 scintillating tiles of size 0.1×0.1 in $\eta \times \phi$ space are placed in between the cryostats to sample the showers between the cryostats.

	EM	IFH	ICH	MFH	MCH	OH
Rapidity coverage	1.3-3.7	1.6-4.5	2.0-4.5	1.0-1.7	1.3-1.9	0.7-1.4
Number of Modules	1	1	1	16	16	16
Absorber [a]	U	U	SS [b]	U	SS	SS
Absorber Thickness (in)	0.118	0.236	0.236	0.236	1.83	1.83
Argon Gap (in)	0.09	0.082	0.082	0.087	0.087	0.087
No. of cells/module	18	64	12	60	14	24
Longitudinal depth	$20.5X_0$	$4.4\lambda_0$	$4.1\lambda_0$	$3.6\lambda_0$	$4.4\lambda_0$	$4.4\lambda_0$
No. of readout layers	4	4	1	4	1	3
Cells/readout layer	2,2,6,8	16	14	15	12	8
Tot. Rad. lengths	20.5	121.8	32.8	115.5	37.9	65.1
Tot. Absorp. len. (Λ)	0.95	4.9	3.6	4.0	4.1	7.0
Sampling Fraction (%)	11.9	5.7	1.5	6.7	1.6	1.6
$\Delta\phi$ Segmentation [c] [d]	0.1	0.1	0.1	0.1	0.1	0.1
$\Delta\eta$ Segmentation	0.1	0.1	0.1	0.1	0.1	0.1
No. of readout ch. [e]	7488	4288	928	1472	$384+64$	$896+64$

Table 3.6: End calorimeter parameters.

[a] uranium is depleted and FH (IFH and MFH) absorbers contain 1.7% Niobium alloy

[b] stainless steel

[c] Layer 3 of the EM has $\Delta\phi \times \Delta\eta = 0.05 \times 0.05$

[d] for $|\eta| > 3.2$, $\Delta\phi \times \Delta\eta = 0.2 \times 0.2$

[e] MCH and OH are summed together at $|\eta| \geq 1.4$

3.7 Data Acquisition system (DAQ)

At the Tevatron, there is a beam crossing every 3.5 μsec creating a potential data rate of 285 KHz. Most of the crossings yield no interesting events. In order to select events considered interesting, the DØ detector has a multilevel triggering system. At each level, a set of criteria is specified for a beam crossing to be considered interesting and hence accepted. The experiment has four different trigger levels, increasing in sophistication and time requirements at each level. The Level Ø (LØ) trigger is hardware based and determines that there is an inelastic collision. Level 1 (L1) is a hardware trigger which further reduces the rate to about 100 Hz. This is done by requiring a certain amount of energy deposited in the calorimeter compatible with jets, electrons, or photons, or tracks in the muon chambers compatible with muons. Certain L1 muon triggers must satisfy additional requirements (L1.5) before the event is accepted in order to further reduce the trigger rate. Events satisfying L1 undergo full detector readout and are passed to the software trigger, Level 2 (L2), which is composed of 48 Digital MicroVax 4000/60 microcomputers. Fast reconstruction of the event at L2 allows one to place further trigger requirements and reduce the rate to $\approx$ 2 Hz for tape recording. Figure 3.9 shows the different trigger levels through which the rate gets reduced to $\approx$ 2 Hz.

3.7.1 Level Ø Trigger (LØ)

The Level Ø detector [34] was designed to be the first trigger stage to provide rejection in the multilevel triggering scheme. It also provides the z-position of the event, identifies events with more than one interaction, and measures the instantaneous luminosity of the Tevatron. The Level Ø detector consists of two sets of scintillating hodoscopes, each mounted on the front surface of the end cryostats. It has partial coverage for $1.9 < |\eta| < 4.3$ and full coverage for $2.3 < |\eta| < 3.9$. Each hodoscope has 20 short (7 cm$\times$7 cm) scintillating pieces with a single PMT readout at one end and eight long (7 cm $\times$65 cm) scintillating pieces with PMT readout on both ends. Figure 3.10 shows the layout of the Level Ø detector.

The total cross section can be divided into the elastic and inelastic cross section. Given that elastic events are at very small angles, DØ does not "see" any of this cross

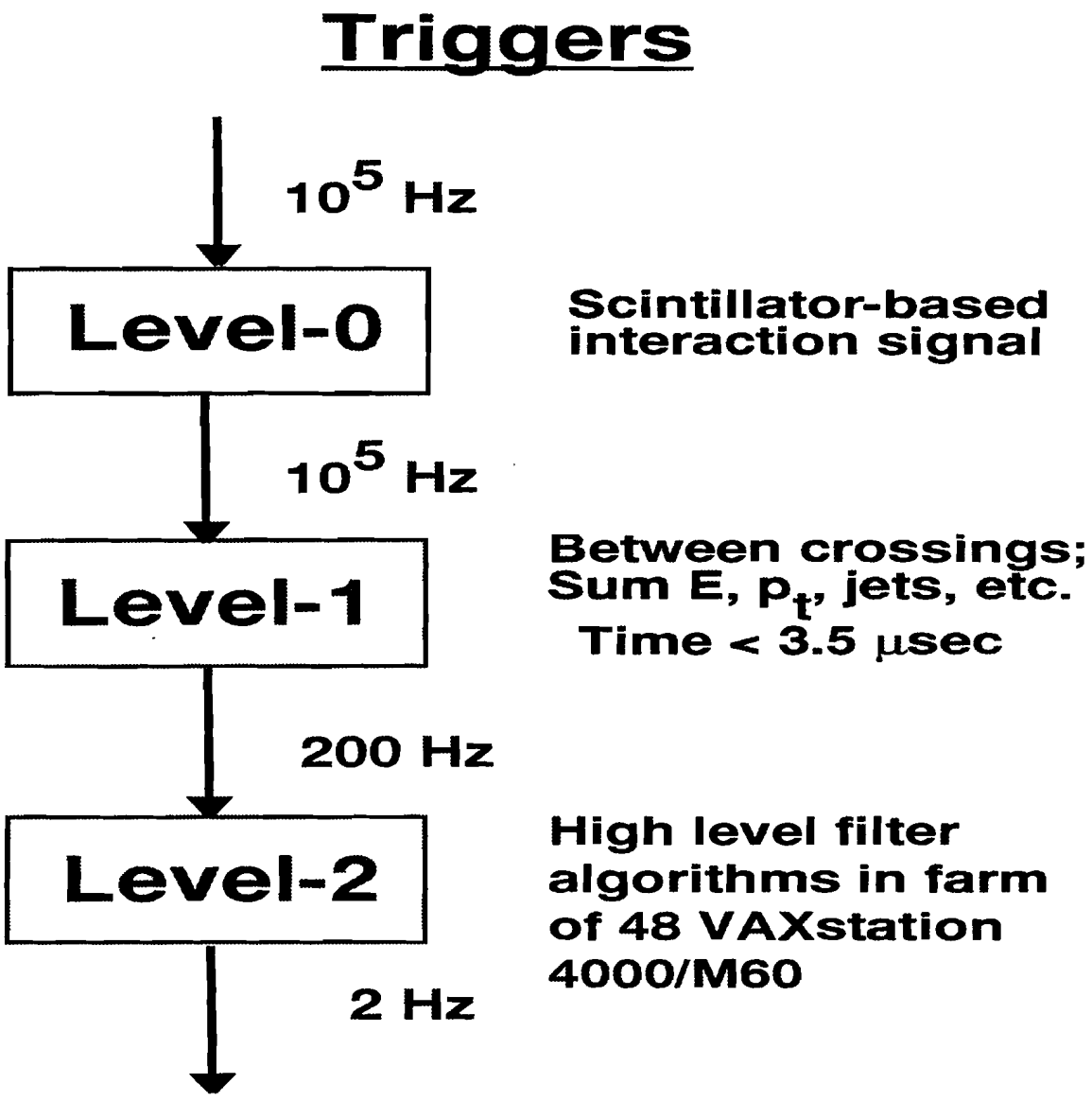

Figure 3.9: The DØ multilevel triggering system.

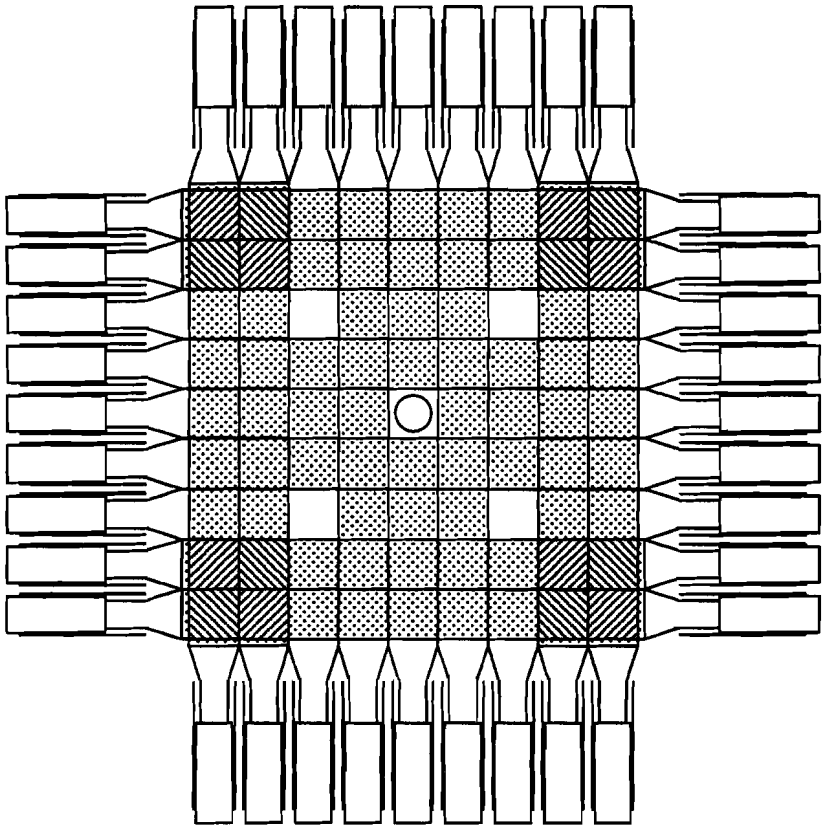

Figure 3.10: Layout of the Level Ø detector. The shaded regions are scintillators.

section. The inelastic cross section can be divided into diffractive and non-diffractive parts, with the diffractive part further subdivided into single diffractive and double diffractive. In a single diffractive event, one of the initial particles survives while the other one diffracts into a low mass ensemble of particles. Double diffractive is when both colliding particles diffract. By requiring a coincidence between both scintillator arrays, the Level Ø detector identifies $\geq 97\%$ of the inelastic non-diffractive beam-beam interactions. Single diffractive events cannot be observed with the Level Ø detector because the surviving initial particle escape detection because it is at a very small angle. Similarly, most double diffractive events cannot be identified because they are at small angles.

Timing measurements on the PMT signals in each array of counters allows a determination of the z-vertex position of the interaction. A z-vertex position with resolution of 3.5 cm is determined for beam crossings with a single $p\bar{p}$ interaction. As the luminosity increases, the probability of multiple interactions also rises, degrading the Level Ø position resolution.

Multiple $p\bar{p}$ interactions in a beam crossing can be identified by looking at the time distribution of the hits. If the hits came from one interaction, they would arrive at nearly the same time; otherwise the hits from the different interactions will in general arrive at different times. Obviously, interactions that occur at the same time and are together in z will not be resolved and the Level Ø detector will tag them as one interaction.

The probability for having m interactions in an event is given by a Poisson distribution:

$$P(m) = \frac{\bar{n}^m e^{-\bar{n}}}{m!} \tag{3.2}$$

with

$$\bar{n} = \mathcal{L}\sigma\tau \tag{3.3}$$

where τ is the time between beam crossings, $\mathcal{L}$ is the instantaneous luminosity and σ is the inelastic cross section to which the Level Ø is sensitive.

By calculating the geometric acceptance using the MBR (Appendix B of Ref. [35]) and DTUJET [36] event generators with full detector simulations, the Level Ø cross section, σ, was determined. The luminosity was then determined by measuring $P(0)$, the probability of 0 interactions, and applying formulas 3.2 and 3.3 [37, 38].

3.7.2 Level 1 Trigger (L1)

The outputs of the LØ trigger, the L1 Calorimeter trigger, and the L1 Muon trigger are fed into the L1 Trigger Framework. The L1 Calorimeter trigger identifies electron/photon or jet candidates and calculates the total energy, transverse energy, and missing transverse energy in the calorimeter. The calorimeter trigger uses trigger towers which are segmented in units of $\eta - \phi$ space of 0.2×0.2. The muon L1 trigger identifies the number of muon candidates, the p_T of each candidate and their locations [39].

The L1 Trigger Framework is a two-dimensional AND-OR network with 256 inputs and 32 outputs, also known as trigger bits. The L1 Framework passes an event that satisfies one or more of the 32 available trigger bits. This decision is made within 2.1 μsec ensuring that the system will be ready before the next interaction, (*i.e.*, no deadtime is incurred). Each of the trigger bits are programmed to require a logical combination of selected AND-OR input terms.

Due to the high rate of some trigger bits, it was necessary to "prescale" these trigger bits. This technique basically means choosing one event out of a fixed number chosen to be the prescale value. A prescale of p in trigger bit A means that for all the events that satisfy the L1 requirements of trigger bit A, every n-pth event is accepted where n is a positive integer. Figure 3.11 shows an overview of the L1 Framework.

3.7.3 Level 1.5 Trigger (L1.5)

Some of the L1 muon trigger bits require more sophisticated cuts in order to reduce the trigger rate and hence have a cleaner event sample. The L1 muon triggers only provide coarse momentum cuts on muon candidates. The L1.5 provides a more precise momentum cut on muon candidates, greatly reducing the trigger rate. Muon triggers were not used for this analysis.

3.7.4 Level 2 Trigger (L2)

All the previous trigger levels are hardware triggers. The L2 is a software trigger based on a farm of 48 microVAXes 4000-60's which receive and process the raw data,

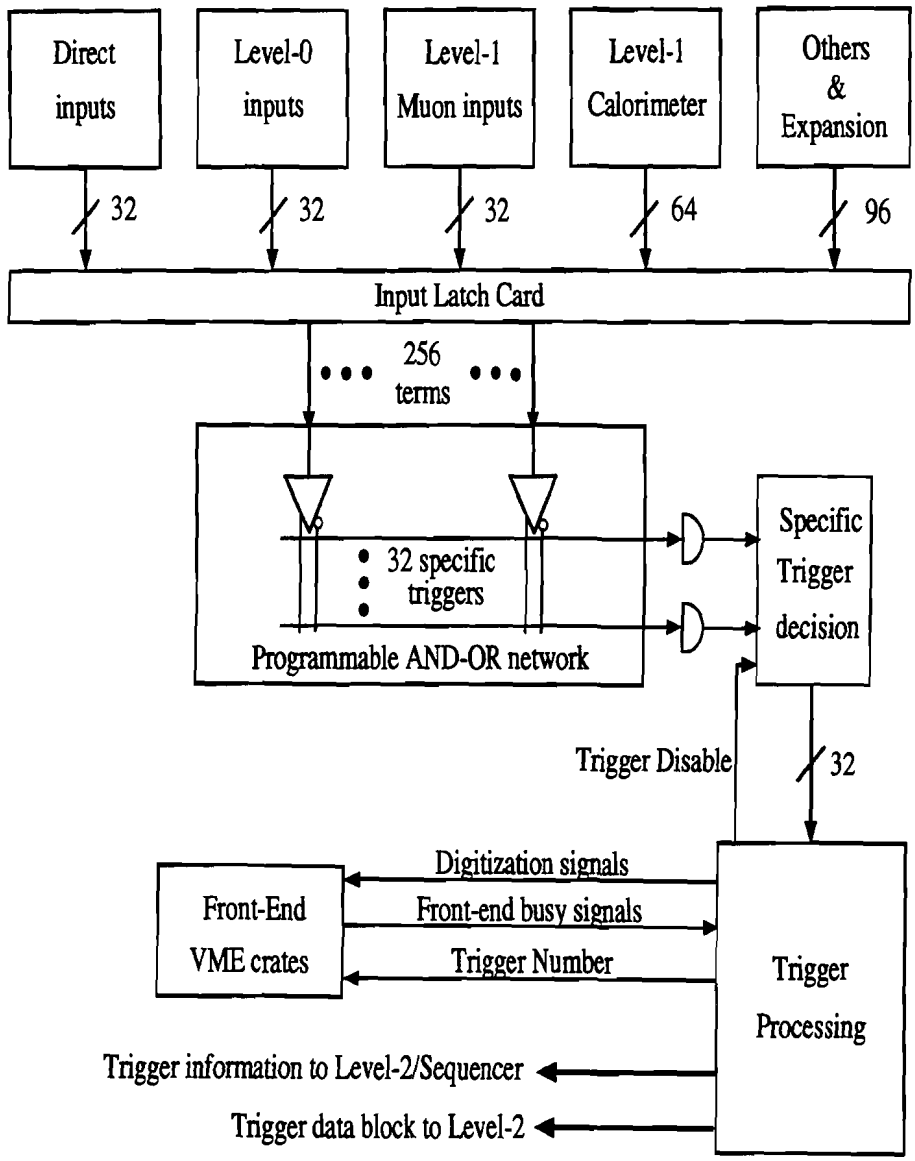

Figure 3.11: Level 1 trigger processing stages.

perform a quick reconstruction of objects such as jets, muons, electrons, etc., and decide whether or not to keep the event. There are 128 software filters connected to the 32 trigger bits. Similar to the L1, prescales can be set for the L2 filter bits. If an event passes the L2 requirements, it is accepted and recorded on 8 mm tapes. The tape writing rate is about 2 Hz. Figure 3.12 gives an overview of the L2 trigger and DAQ system.

3.8 Offline Reconstruction

All the data saved on tape were reprocessed with a more stringent code package called DØRECO to fully reconstruct each event. This was not possible online due to time constraints where we basically performed quick but rough reconstruction of objects. DØRECO uses a standard set of jet, electron, photon, and muon definitions to find all the objects in an event. The output format of DØRECO is known as STAndard (STA). For most analyses, the amount of information from the STA's is overwhelming, and in order to speed up the analysis, other formats were developed. The most important information from the STA's is saved onto Data Summary Tapes (DST's). An even more reduced set of information is saved in μDST's. For this analysis, we reduce the format size even further by creating NTUPLES from the μDST's. The data used for this analysis was processed using DØRECO version 10.

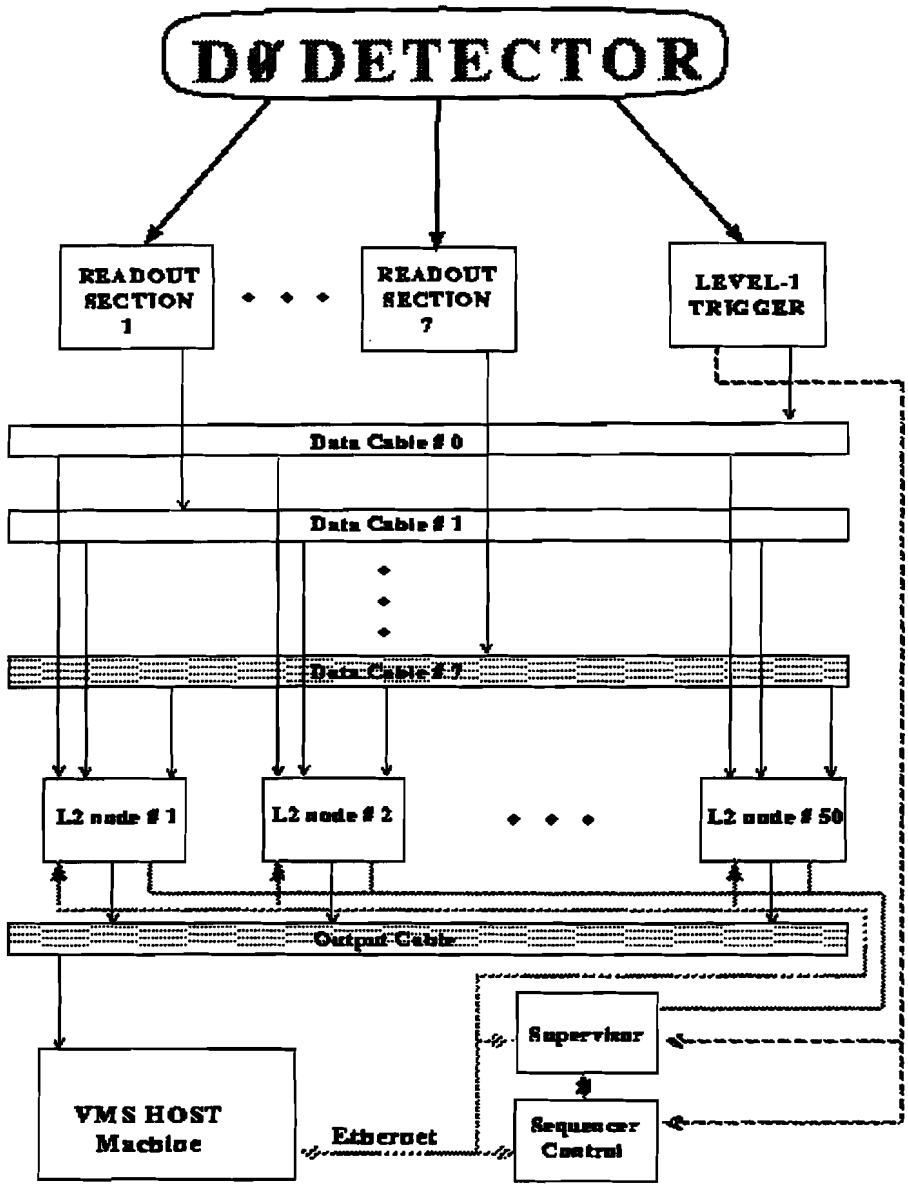

Figure 3.12: Overview of the Level 2 trigger and its relationship with the Data Acquisition system.

CHAPTER 4

Data Selection

Energetic jets are produced in $p\bar{p}$ collisions approximately one every thousand inelastic collisions. In order to collect these kind of events, they must be selected based on characteristics that are associated with jet events. One of these characteristics is large deposition of energy in the calorimeter. This chapter describes how jet data is triggered at the different online levels and selected at the offline level. It then describes how backgrounds are identified and removed from the sample. It concludes in describing the selection cuts used for this analysis. The data used in the analysis was collected from August 1992 to May 1993 for an integrated luminosity of $(13.3 \pm 0.7)\ \mathrm{pb}^{-1}$. This run, called Run Ia, was the first run taken with the DØ detector.

4.1 Online Event Selection

The DØ detector was exposed to $p\bar{p}$ collisions every 3.5 μsec corresponding to an approximate rate of 285 KHz. The DØ detector was able to record events at a rate of 3-4 Hz, so it was necessary to decide in a very small amount of time which events were of interest. The general online requirements for jet triggers were:

- There was a Level Ø (LØ) coincidence and the z-vertex position from the LØ trigger had to be within a preset fiducial region.
- At the Level 1 trigger (L1), there was a specified number of energy depositions in the calorimeter trigger towers above a prescribed threshold.

- At the Level 2 trigger (L2), the L1 energy depositions above threshold were clustered using a jet reconstruction algorithm and the resulting jets had to be above a prescribed threshold.

These requirements are described in more detail below.

4.1.1 Level Ø Trigger Selection

The LØ trigger provided two pieces of information relevant to the jet triggers: it signaled the presence of an inelastic collision and whenever that occurred it also provided a measurement of the z-vertex of the collision. Events where the LØ trigger indicated the presence of an inelastic collision within the prescribed fiducial region (see Table 4.1) were sent to the L1 trigger.

4.1.2 Level 1 Trigger Selection

The segmentation of the calorimeter readout towers in $\eta - \phi$ space is 0.1×0.1, providing excellent granularity. However, a coarser segmentation was used in the L1 trigger to reduce the number of trigger towers. The segmentation of the calorimeter trigger towers is $\Delta\eta \times \Delta\phi = 0.2 \times 0.2$. The calorimeter trigger towers summed the energy deposited in the Electromagnetic and Fine Hadronic sections of the calorimeter, but did not include energy deposited in the Coarse Hadronic, Massless Gaps, and ICD sections. In order to satisfy the L1 condition, the event had to have a specified number of trigger towers above a preset threshold. During run Ia, the calorimeter trigger towers were instrumented for $|\eta| \leq 3.2$.

The jet E_T spectrum falls rapidly as a function of increasing E_T [40, 41, 42]. Thus, there is an abundance of low E_T jets while high E_T jets are less frequent. In order to collect jets over a large E_T range, we used several triggers requiring that the calorimetric energy depositions were above different thresholds. A trigger with a high threshold will only collect high E_T jet events.

Most of the jet triggers, in particular those with low energy thresholds, were satisfied at a higher rate than the data acquisition system could handle. Two methods were used to reduce the rate for low E_T triggers. The first one was an additional

requirement that the triggers had to satisfy: since the calorimeter towers are projective, events with a primary vertex far away from $z = 0$ have a greater chance of having mismeasured jets. Given that not all the events that satisfied the trigger conditions could be kept, only events that satisfied the LØ z-vertex $|z_v| \leq 10.5$ cm requirement were kept. Figure 4.1 (a) shows the offline vertex distribution for a high rate, low E_T trigger (JET_1_HIGH) which imposed the vertex cut. The RMS of this distribution is 13.7 cm. Figure 4.1 (b) shows the offline vertex distribution of a low rate, high E_T trigger (JET_4_MED) which did not require the vertex cut. The RMS of this distribution is 27.3 cm, in agreement with the size of the colliding bunches.

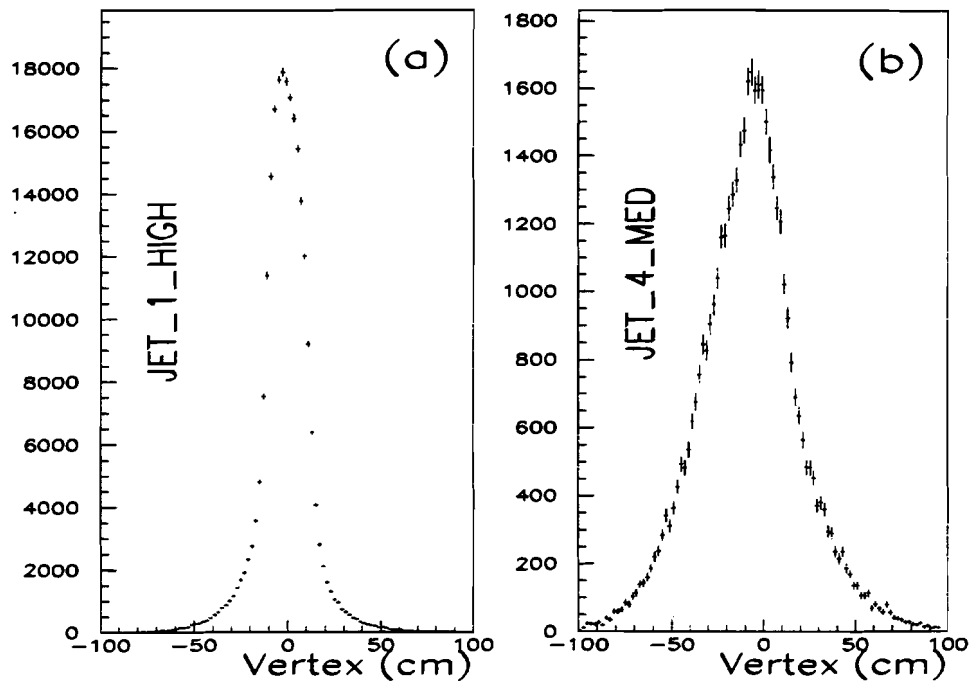

Figure 4.1: (a) Z-Vertex distribution for trigger bits with the LØ vertex cut, and (b) with no vertex requirement.

For several jet triggers, the vertex requirement was not sufficient to reduce the rate to an acceptable value, so those triggers had to be "prescaled". A trigger prescale of 200 indicates that one event is passed on to the next trigger level for every 200 that satisfied the trigger. Low E_T jet triggers were heavily prescaled while the highest E_T jet trigger did not need to be prescaled. Since the trigger rate grows as the instantaneous luminosity increases, different prescale values were used based

on the instantaneous luminosity.

Table 4.1 shows the different L1 jet triggers with their threshold requirements and LØ vertex requirement. The first three triggers had the tight vertex cut, JET_3_HIGH had it during the early stages of the run, and there was no tight vertex requirement for JET_4_MED.

L1 trigger	Requirement	Vertex Position
JET_1_LOW	1 tower$\geq$3 GeV	$\lvert z_v \rvert \leq$10 cm
JET_1_HIGH	1 tower$\geq$7 GeV	$\lvert z_v \rvert \leq$10 cm
JET_2_HIGH	2 towers$\geq$7 GeV	$\lvert z_v \rvert \leq$10 cm
JET_3_HIGH	3 towers$\geq$7 GeV	$\lvert z_v \rvert \leq$10 cm,97 cm
JET_4_MED	4 towers$\geq$5 GeV	$\lvert z_v \rvert \leq$97 cm

Table 4.1: QCD L1 trigger bits and respective requirements. The z-vertex measurement is from the LØ trigger.

4.1.3 Level 2 Trigger Selection

The third level of the online trigger is software based. The L2 computer farm receives complete detector information for the events that satisfied the L1 conditions and determines through event reconstruction whether the candidate events are of interest. As explained in the previous chapter, there are more L2 trigger bits than L1 trigger bits, meaning that more than one L2 trigger bit can hang off one L1 trigger bit. For the jet triggers, there is a one-to-one correspondence between L1 trigger bits and L2 trigger bits.

The L2 trigger requirements are more sophisticated than the L1 trigger in the sense that the L2 trigger uses a better algorithm, has access to the complete calorimeter information: the EM, FH, CH, MG, and ICD, and it also has more precise vertex information. Hence, the L2 trigger can calculate the E_T more accurately. For a particular trigger jet, the L2 trigger orders all the candidates that satisfied the L1 trigger in decreasing E_T value and tests them to determine which ones satisfy the

L2 conditions.

For example, an event that satisfied JET_1_HIGH at the L1 trigger must have had at least one tower$\geq$7 GeV. A list of all those L1 towers that exceeded 3 Gev in E_T, known as the L1 tower candidate list, was sent to the L2 trigger. The L2 algorithm then defined a jet with the following algorithm:

- Starting with the highest E_T L1 tower candidate, the L2 trigger drew a cone of radius 0.7 around the tower center.
- The L2 trigger then determined the jet E_T by adding up the cells for all the towers whose centers were within this cone using $E_T = E\sin(\theta)$ where θ was taken from the x, y, z position of the cells relative to the nominal vertex of $z_v = 0$. Other L1 tower candidates, which are 0.2×0.2, could be found inside the cone. If this was the case, they were dropped from the L1 tower candidate list.
- Besides determining the jet E_T, the L2 trigger also determined an E_T weighted average η and ϕ using:

$$\eta_j = \frac{\sum_i E_{Ti}\eta_i}{\sum_i E_{Ti}} \tag{4.1}$$

$$\phi_j = \frac{\sum_i E_{Ti}\phi_i}{\sum_i E_{Ti}} \tag{4.2}$$

  where i was the cell index.
- The above steps were repeated until the L2 trigger exhausted the input list of L1 tower candidates and had for output a list of L2 jet candidates. At this stage, all L2 jet candidates were defined.
- The L2 trigger then calculated the electromagnetic fraction (EMFR) and the energy weighted average ϕ and η deviation for each L2 jet candidate. The deviation is defined as the sum of the absolute value of the distance between the tower and the jet candidate and it was used to determine the jet width.
- The L2 trigger took the list of jet candidates and corrected the E_T, η, and the z-vertex position measured by the Level Ø trigger for each jet candidate.
- Finally, the L2 trigger determined whether the list of jet candidates satisfied a set of cuts particular to each trigger bit. The cuts were usually the number of jets and the minimum jet E_T. For all the QCD triggers, only one L2 jet

was required to be above a preset threshold in order to satisfy the L2 trigger condition. For example, JET_MIN required one jet greater or equal to 20 GeV in order to pass the L2 trigger condition.

Table 4.2 shows the L1 and L2 trigger bit requirements.

L2 Filter Bit	L1 Requirement	L2 Requirement
JET_MIN	JET_1_LOW	1 L2JET≥20 GeV
JET_LOW	JET_1_HIGH	1 L2JET≥30 GeV
JET_MEDIUM	JET_2_HIGH	1 L2JET≥50 GeV
JET_HIGH	JET_3_HIGH	1 L2JET≥85 GeV
JET_MAX	JET_4_MED	1 L2JET≥115 GeV

Table 4.2: QCD L2 trigger bits and their respective requirements.

4.2 Offline Jet Reconstruction

Objects of physics interest, such as electrons, muons, photons, and jets, are reconstructed online under a limited time budget. In order to gain in speed, one sacrifices in accuracy and completeness. Once the data had been collected, all the events were reconstructed again offline where more sophisticated and time consuming code was used to determine these objects. The offline jet reconstruction algorithm is described below.

There are several algorithms that have been used for jet reconstruction: JADE, nearest neighbor, fixed cone, etc [43]. We will concentrate on the fixed cone algorithm since it is the one used at DØ. The fixed cone algorithm sums up the energy contributions inside a cone of radius $R = \sqrt{(\Delta\eta)^2 + (\Delta\phi)^2}$ [44]. This is the method used for the L2 trigger. For this analysis, the fixed cone algorithm is also used offline. In addition, some of the jet variables can be defined in several ways. In order to allow different experiments and theories to compare their jet data, a group of theorists and experimentalists gathered in Snowmass, Colorado in 1990 and proposed a

set of standard definitions. These are known as the *Snowmass definitions* [45]. They defined the η and ϕ of jets as follows:

$$E_{Ti} = E_i sin\theta_i \tag{4.3}$$

$$\eta_j = \frac{\sum_i E_{Ti}\eta_i}{\sum_i E_{Ti}} \tag{4.4}$$

$$\phi_j = \frac{\sum_i E_{Ti}\phi_i}{\sum_i E_{Ti}} \tag{4.5}$$

where i is the tower or parton index. DØ followed these definitions to some extent as described below.

- The offline jet reconstruction started with a list of "seeds", which are readout towers (0.1×0.1 in $\eta - \phi$ space) above the E_T threshold of 1 GeV and ordered in decreasing E_T.
- The algorithm drew a cone of radius $R = \sqrt{(\Delta\eta)^2 + (\Delta\phi)^2} = 0.3$ around the highest E_T tower. Any seeds inside this cone were dropped from the candidate list.
- The algorithm proceeded to draw a 0.3 cone around the next highest seed in the list until all seeds were clustered in a process known as "preclustering". The purpose was to reduce the number of starting points used for jet formation. The η and ϕ for each precluster was taken from the seed tower from which the precluster was created.
- With the list of preclusters, the algorithm drew a cone of size R around the first precluster. The first precluster was the first one obtained by the preclustering process and it was not necessarily the highest E_T precluster. Depending on the analysis, one could choose different cone sizes of 0.3, 0.5, 0.7, or 1.0. This analysis used a cone size of R= 0.7. The algorithm calculated η and ϕ using the Snowmass definition from all the readout towers whose centers were inside the cone.
- With these new values of η and ϕ, a new cone of radius of 0.7 centered on the new η and ϕ was used to collect the tower energies. This process continued until stable values for η and ϕ were found. "Stable" is defined as $\Delta R = \sqrt{(\Delta\eta)^2 + (\Delta\phi)^2} \leq 0.01$ between iterations.
- Once the stable center had been found, the algorithm checked whether the E_T

was greater than the predetermined threshold to be considered as a jet, which was set at 8 GeV.

- As a final step, the algorithm recalculated the jet angular parameters using the following formulae:

$$\tan\phi_{jet} = \frac{E_y}{E_x} \tag{4.6}$$

$$\eta_{jet} = -\ln[\tan(\theta_{jet}/2)] \tag{4.7}$$

where

$$\tan\theta_{jet} = \frac{\sqrt{E_x^2 + E_y^2}}{E_z} \tag{4.8}$$

$$E_x = \sum_i E_i \sin\theta_i \cos\phi_i \tag{4.9}$$

$$E_y = \sum_i E_i \sin\theta_i \sin\phi_i \tag{4.10}$$

$$E_z = \sum_i E_i \cos\theta_i \tag{4.11}$$

where i is the tower index.

- The algorithm then moved on to the next precluster until it finished the list.
- Occasionally, preclusters would end up giving two jets that were very similar. When this occurred, one was dropped with the criteria that either $\Delta R \leq 0.0001$ in $\eta - \phi$ or the difference in E_T between the two jets was $\Delta\ E_T \leq 0.01$ GeV.
- There is also the possibility that two jets may overlap and a decision had to be made on whether to split or merge the jets. If the E_T of the overlapped region is more than 50% of the E_T of the lower E_T jet, the jets are merged. A vector sum of the two original jet quantities is performed in order to obtain the new jet quantities. If the ratio is less than 50%, then the jet is split into two jets. The cells in the overlapped region are assigned to the closest jet centroid. The E_T of the cells are added to or subtracted from the original jets, but the η and ϕ information remain unchanged.

4.3 Background Elimination

Once events have been selected based on the trigger, we must make sure to remove background events from the data. Backgrounds are usually divided into two categories: physics background consisting of other physical processes mimicking the

signal of interest and instrumental background mostly due to detector malfunctions. Given the large jet cross sections, there are no significant physics backgrounds. However, there are several instrumental backgrounds due to cosmic rays, calorimeter noise, and protons from the Main Ring entering into the detector. The DØ detector has the peculiarity of enclosing two accelerators. In addition to the Tevatron, the Main Ring, used to create antiprotons, passes through the detector. The instrumental background and noise from the Main Ring leave energy depositions in the calorimeter which are misidentified as jets. In order to remove these "fake" jets, we have devised a set of quality cuts based on characteristics corresponding to real jets. This group of cuts is called the *Standard Jet Quality Cuts* and is applied to every jet. There is a also missing E_T cut applied on an event-by-event basis.

4.3.1 Standard Jet Quality Cuts

The Standard Jet Quality Cuts are based on the following variables:

- CHFR, which is defined as the fraction of the jet's energy deposited in the Coarse Hadronic section of the calorimeter. This cut was instituted mainly to remove activity caused by the Main Ring. The Main Ring goes through the Coarse Hadronic section of the calorimeter and any energy deposition related to the Main Ring will be concentrated in this section of the calorimeter. It has been shown that fake jets due to the Main Ring tend to have more than 40% of the energy in the CH region [46] while real jets usually have roughly 10% of their energy in the coarse hadronic section as shown in Fig. 4.2 (a).
- HOTFR, which is defined as the ratio of the energy of the highest E_T cell over the energy of the second highest E_T cell within a jet. This cut is used to remove calorimeter noise. Occasionally a cell will start sparking and it will be misinterpreted as energy deposition. Since this occurs at random and usually without affecting neighboring cells, the HOTFR will be large. Energy deposition from a true jet is spread over many cells and several of these cells usually receive similar amounts of energy resulting in a small HOTFR as shown in Fig. 4.2 (b).
- EMFR, which is defined as the fraction of energy deposited in the electromagnetic portion of the calorimeter. This cut is designed to remove electrons

and/or photons from the jet sample, which by nature deposit nearly all their energy in the electromagnetic section of the calorimeter. As a result, they have a very high EMFR. Fake jets, caused by the Main Ring or by hot cells, do not have energy depositions in the electromagnetic section of the calorimeter resulting in a low EMFR. In general, jets leave energy in both the electromagnetic and hadronic sections of the calorimeter since they are a mixture of hadrons and photons from π^0 decays.

The threshold values for the Standard Quality cuts were set as follows:

$$CHFR < 0.4 \tag{4.12}$$

$$HOTFR < 10.0 \tag{4.13}$$

$$0.95 > EMFR > \begin{cases} 0.0 & \text{if } 1.0 \leq \eta_{det} \leq 1.6 \\ 0.05 & \text{otherwise.} \end{cases} \tag{4.14}$$

4.3.2 Missing E_T Cut

Neutrinos are identified by relying on momentum conservation since they rarely leave any traces as they traverse the detector ($\sim 10^{-9}$ for a 100 GeV neutrino and $\sim 10^{-11}$ for a 1 GeV neutrino). Conservation of momentum can only be applied in the transverse direction with respect to the beam direction as it is not possible to measure the momenta of particles escaping down the beampipe. The vector sum of the E_T of all the calorimeter cells is used to infer the transverse momentum due to the neutrinos, usually called Missing E_T and denoted as $\not{E}_T$. The vector components of $\not{E}_T$ are given by:

$$\not{E}_x = -\sum_i E_i \sin\theta_i \cos\phi_i \tag{4.15}$$

$$\not{E}_y = -\sum_i E_i \sin\theta_i \sin\phi_i \tag{4.16}$$

$$\not{E}_T = \sqrt{\not{E}_x^2 + \not{E}_y^2} \tag{4.17}$$

where i runs over all the calorimeter cells, E_i is the energy deposited in the ith cell, and θ_i and ϕ_i are the polar and azimuthal angle of the ith cell, respectively.

Even though there are no neutrinos expected in the final states for this analysis, the $\not{E}_T$ information was important as it provided a handle for removing undesired

events since not all fake jets were removed with the Standard Jet Quality cuts. If there is a fake jet, say due to a hot cell, it will result in a non-zero $\not{E}_T$ value since the energy from the cell did not come from the $p\bar{p}$ interaction. Studies have shown that the use of $\not{E}_T$ is good for removing events where the standard cuts failed to remove fake jets [46]. The requirement to keep the event was that the $\not{E}_T$ in the event had to be less than 70% of the the leading jet E_T. Figure 4.2 (d) shows the missing E_T cut.

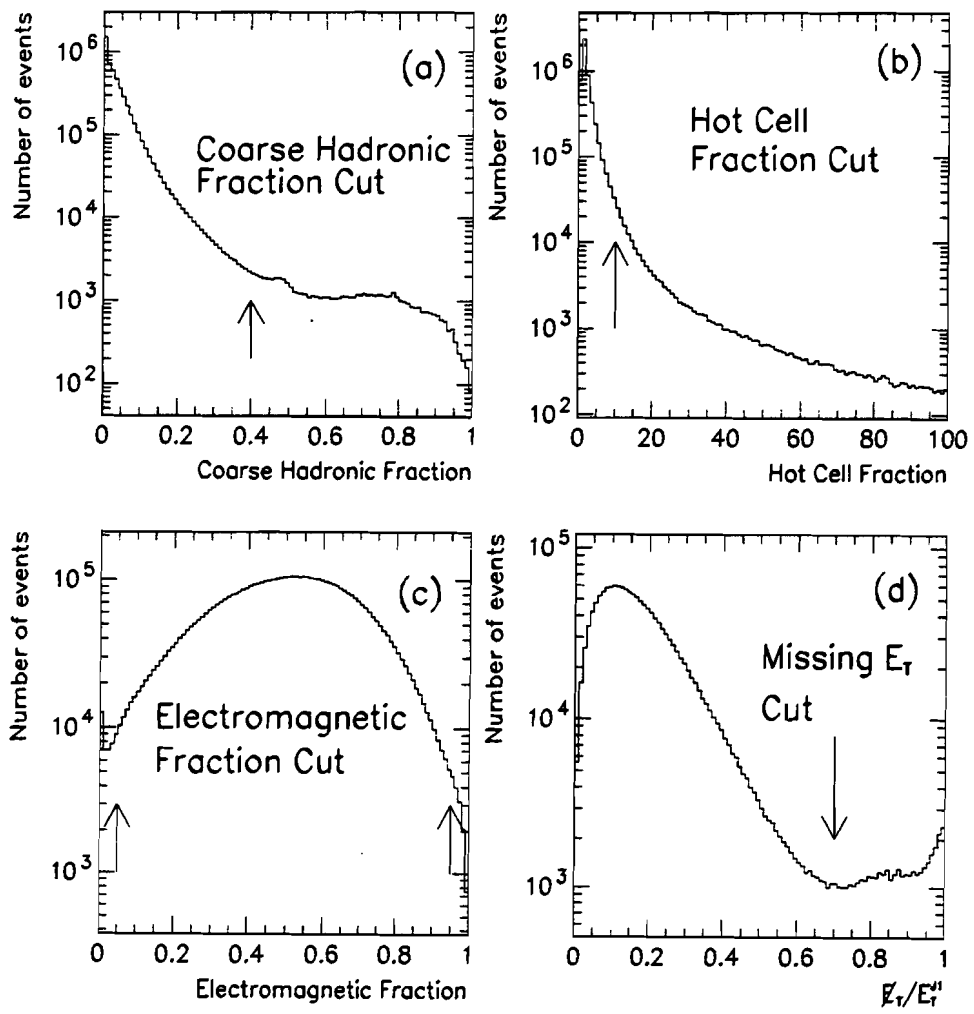

Figure 4.2: Standard Jet Quality Cuts: (a) Coarse Hadronic Fraction, (b) Hot Cell Fraction, (c) Electromagnetic Fraction. Also shown is (d) the missing E_T cut.

Table 4.3 shows the number of events that survive the Standard jet quality cuts and the $\not\!\!E_T$ cut and respective integrated luminosities for each of the jet triggers used in this analysis. The luminosity numbers were obtained from a database kept by the experiment.

Bit Number	Trigger Name	Number of Events	$\int \mathcal{L}dt\ (nb^{-1})$
18	JET_LOW	265,552	74.7
19	JET_MEDIUM	318,799	991.8
20	JET_HIGH	148,242	7762.7
21	JET_MAX	48,435	13321.0

Table 4.3: Number of QCD events and integrated luminosity for each trigger after the Standard Jet Quality and $\not\!\!E_T$ cuts.

4.4 Final Event Selection

The Standard Jet Quality Cuts and $\not\!\!E_T$ cut are applied for all QCD analyses. For this particular analysis, there are additional requirements such as a multiple interaction cut. In each beam crossing, there is a probability of having more than one $p\overline{p}$ interaction and some of the events that have been collected show the presence of a second interaction. Since it is difficult to determine the correct interaction vertex from the energy depositions in the calorimeter, we decided to use the LØ information to indicate that there was only one interaction in the event and only use these events. The LØ trigger assigns a value to a variable called MIFLAG depending on the likelihood that the event had a single or multiple interaction. The greatest possibility of having a single interaction corresponds to a value of MIFLAG=1.

For the final event selection, the following requirements were applied to the data:

- Remove all fake jets from an event using the Standard Jet Quality Cuts.
- Reject event if it failed the missing E_T cut.
- Require that the number of good jets be at least two. The analysis requires two or more jets in the final state.

- The two leading jets (jets are ordered by decreasing E_T) must pass the Standard Jet Quality Cuts. Due to inefficiencies of the standard jet quality cuts, good jets misidentified as fake jets get removed changing the topology of the event.
- Require $E_T^{J2} \geq 20$ GeV to ensure full reconstruction efficiency.
- Require the LØ trigger to flag that there was only one interaction (MIFLAG=1).
- Require that the E_T^{J1} is already fully trigger efficient to remove any trigger biases.

Before obtaining a cross section measurement from the sample obtained after these requirements, we must apply certain corrections to the data, such as efficiencies, energy scale corrections, etc. These corrections are described in the following chapter.

CHAPTER 5

Data Correction

Before calculating final cross sections, corrections for various inefficiencies must be applied. These are due to event selection and trigger biases. In addition, each jet must be corrected for contributions from the underlying event and zero suppression as well as energy scale errors. This chapter explains the various corrections to the jet energy scale, going through each component. It then proceeds to explain the corrections due to the selection cuts applied to the data: jet quality cut, missing E_T cut, and multiple interaction cut. And finally, it shows the efficiency calculations for the triggers used and their implementation.

5.1 Jet Energy Scale

In order to make accurate measurements of the jet E_T, it is imperative to understand how the response of the DØ calorimeter varies for different particle types (*e.g.* muons, electrons, hadrons). The response can be defined as the fraction of the input energy that the calorimeter detected for a given particle. DØ measured the calorimeter response to single charged pions and electrons using calorimeter modules in a test beam [47]. The response was measured to be linear as a function of the energy of the particles for energies above 10 GeV. However, jets are collimated sprays of hadrons and it is not uncommon to find more than half the energy of a jet to be carried by particles with less than a tenth of the total jet energy meaning that there are a lots of particles with less than 10 GeV so large corrections may be necessary to obtain the jet's true energy.

In a hard scattering, particles from the partons that do not take part in the interaction, known as *spectators*, can be detected in the calorimeter. The energy contribution from these particles is defined as the *underlying event*. In addition, DØ uses uranium as an absorber and the energy from particles from the uranium decay, referred to as *uranium noise*, can also be detected in the calorimeter. Since jets cover a wide area, they can be contaminated with energy from the the underlying event and uranium noise.

Another correction which is particular to the measurement of the jet itself is from the algorithm used to identify the jet. We define the jet energy in terms of particles within a fixed radius cone. As particles shower in the detector, they may deposit energy in the calorimeter that crosses the cone boundary.

The distortions of the jet E_T measurement can be expressed as:

$$E_{measured} = (1 - C)\mathcal{R}_{HAD}E_{true} + K \tag{5.1}$$

where $\mathcal{R}_{had}$ is the overall hadronic response dependent on the energy, pseudorapidity, and width of the jet; K is a constant offset from noise and particles unrelated to the hard interaction; and C is a correction for the energy that crosses the jet cone boundary due to particle showering in the detector.

The version of the jet energy scale correction used for this analysis was version 4 (CAFIX 4.0) and the overall correction was roughly 30%. It is the largest source of the systematic uncertainty in the measurement of the triple differential cross section.

5.1.1 Underlying Event and Zero Suppression

The underlying event (U) and the uranium noise (N) are regarded as the additive corrections to the jet energy escale. Both corrections were determined using a sample of minimum bias events. Minimum bias events, as the name indicates, are those events triggered with the least amount of trigger bias possible; that is, just requiring that the Level Ø trigger flags the event as an inelastic collision. Minimum bias events result from the soft scattering of the incoming partons and we expect them to mimic the behavior of the underlying event.

The amount of energy due to the underlying event was measured by taking the difference of the transverse energy density (in GeV) per unit area in $\eta - \phi$ space for

events with multiple interactions (which for run 1a meant on average two interactions) and events with single interactions:

$$U/rad/\eta = E_T/rad/\eta(multipleinteractions) - E_T/rad/\eta(singleinteraction). \quad (5.2)$$

A large number of the calorimeter cells have no energy deposition from the interaction and a scheme was implemented to ignore such cells. Each cell has a pedestal due to electronics offset with a unique mean and variance value, which is determined from special runs called "pedestal runs". For every event, if the pedestal subtracted contribution is less than two standard deviations, the cell is not read out but "suppressed". A pedestal due only to electronic noise is symmetric around its mean, but the energy depositions from the uranium noise changes the pedestal into an asymmetric distribution with a long positive tail. For those cells not zero suppressed, there is an excess of positive energy due to the uranium noise which must be removed. The amount of transverse energy density per unit area in $\eta - \phi$ space for single interaction minimum bias events contains both the underlying event and the uranium noise. Hence, in order to determine the uranium noise, one subtracts the underlying event obtained as above from the amount of transverse energy density per unit area in $\eta \cdot \phi$ from single interaction minimum bias events:

$$N/rad/\eta = E_T/rad/\eta(singleinteraction) - U/rad/\eta. \quad (5.3)$$

The average transverse energy correction density due to the underlying event was determined to be 0.6 GeV and due to uranium noise was $1.2 \sin\theta$ GeV. With $N/rad/\eta$ and $U/rad/\eta$ determined, one finds the U and N for each jet by multiplying the densities by the jets area in $\eta \times \phi$ space and subtracts them from the jets.

5.1.2 Response

The jet response, more precisely, the jet hadronic response is obtained with respect to the electromagnetic response, which is known to greater precision. The calorimeter response to electrons and photons is different from the response of hadrons. Additionally, since jets are broad objects compared to electrons or photons, it is not possible to exclude regions with large amounts of dead material, such as the intercryostat region. Finally, the electromagnetic response can be calibrated using known

resonances: the $\pi^{\pm}$, J/Ψ and Z^0 boson. The EM response has been calibrated using the mass of the Z^0 boson and checked with the mass of the π^0. In principle, one could calibrate the jet hadronic response using the invariant mass of the dijet system from the hadronic decay of the W and Z bosons, but the QCD dijet background makes it extremely difficult to select those jet pairs. The next best option was to study events such as leading order photon plus one jet production in which the final state consists of a photon and a gluon. The gluon (hence the outgoing jet) should balance the E_T of the photon. However, events do not occur only at leading order and there is a large QCD dijet background where one of the jets fragments into leading photons ($\pi^0 \rightarrow \gamma\gamma$). Even in the best case of just one photon and one jet, the jet E_T measurement is dependent on the jet algorithm. Thus, the $\not{E}_T$ was used to determine the jet hadronic response. The ratio of the hadronic response to the electromagnetic response is defined as follows:

$$\mathcal{R}_{HAD}(E^{JET}) \;=\; 1 + MPF \tag{5.4}$$

where

$$MPF \;=\; \frac{\not{E}_{\mathrm{T}} \cdot \hat{u}_{\gamma}}{E_T^{\gamma}}. \tag{5.5}$$

$\mathcal{R}_{HAD}$ is less than one when the $\not{E}_T$ vector is pointing in the opposite direction of the electromagnetic jet, indicating that the jet energy was undermeasured. The photons were required to be central ($|\eta^{\gamma}| \leq 0.9$) and the hadronic section searched was also central ($|\eta| \leq 0.7$). Both the E_T and the direction of the photon candidate are well measured. Note that photon candidates include real photons, electrons, and electromagnetic jets (with appropriate quality cuts). But since the energy of the jet can change greatly as a function of η, what was determined was a more stable quantity. The quantity $E_T^{\gamma}\cosh(\eta_{jet})$ is exactly equal to the jet energy, E^{JET}, in a $2 \rightarrow 2$ process. Since the electromagnetic jet E_T and the away-side jet position are well measured, whereas the jet energy is not as well measured. The expression was then rewritten as:

$$\mathcal{R}_{HAD}(E_T^{\gamma}\cosh(\eta_{jet})) \;=\; 1 + MPF. \tag{5.6}$$

In order to relate the equation to jets, we also determine the average jet energy as a function of $E_T^{\gamma}\cosh(\eta_{jet})$. The two equations are in terms of $E_T^{\gamma}\cosh(\eta_{jet})$ and

can be combined to give the average response as a function of the average jet energy. Jets are scaled by the reciprocal of this response.

The hadronic response for the forward region was determined after the central region was done. For this task, dijet events were used where one jet, referred to as the trigger jet, was required to be central and the hadronic response of the other jet was determined. The jets are not expected to balance each other for the same reasons that the away-side jet was not expected to balance the photon candidate. What was of interest was to determine the change of the hadronic response as a function of pseudorapidity. The equation is similar to the previous one, except that the trigger jet replaces the photon candidate:

$$\mathcal{R}_{eta} = 1 + \frac{\not{E}_{\mathrm{T}} \cdot \hat{u}_{trigger}}{E_T^{trigger}}. \tag{5.7}$$

It was found that the hadronic response is fairly uniform over a wide range of pseudorapidity.

5.1.3 Out-of-Cone Showering

There is one more correction that has to be applied for jets. Jets, unlike electrons or muons, are not definite objects. Identification of jets depend on the jet definition or algorithm that was used. This is particularly true for fixed cone algorithms which are defined at the parton level as well as in the detector. As mentioned previously, for this analysis jets were reconstructed using a fixed-cone algorithm with a cone size of 0.7. The out of cone showering correction compensates for the energy crossing the cone boundary due to particles showering in the detector. This was done by using data taken from subjecting test central calorimeter modules to calibration beams of fixed energy pions and electrons, yielding the transverse angular energy profile for these particles. This profile was then combined with Monte Carlo predictions on the particle makeup of a jet to predict what the showering losses would be. For jets of cone size of 0.7 the correction was determined to be 4%.

Figure 5.1 shows the jet energy scale correction for two different detector η regions as a function of the jet E_T for CAFIX 4.0. The band from the dashed lines show the correction uncertainty.

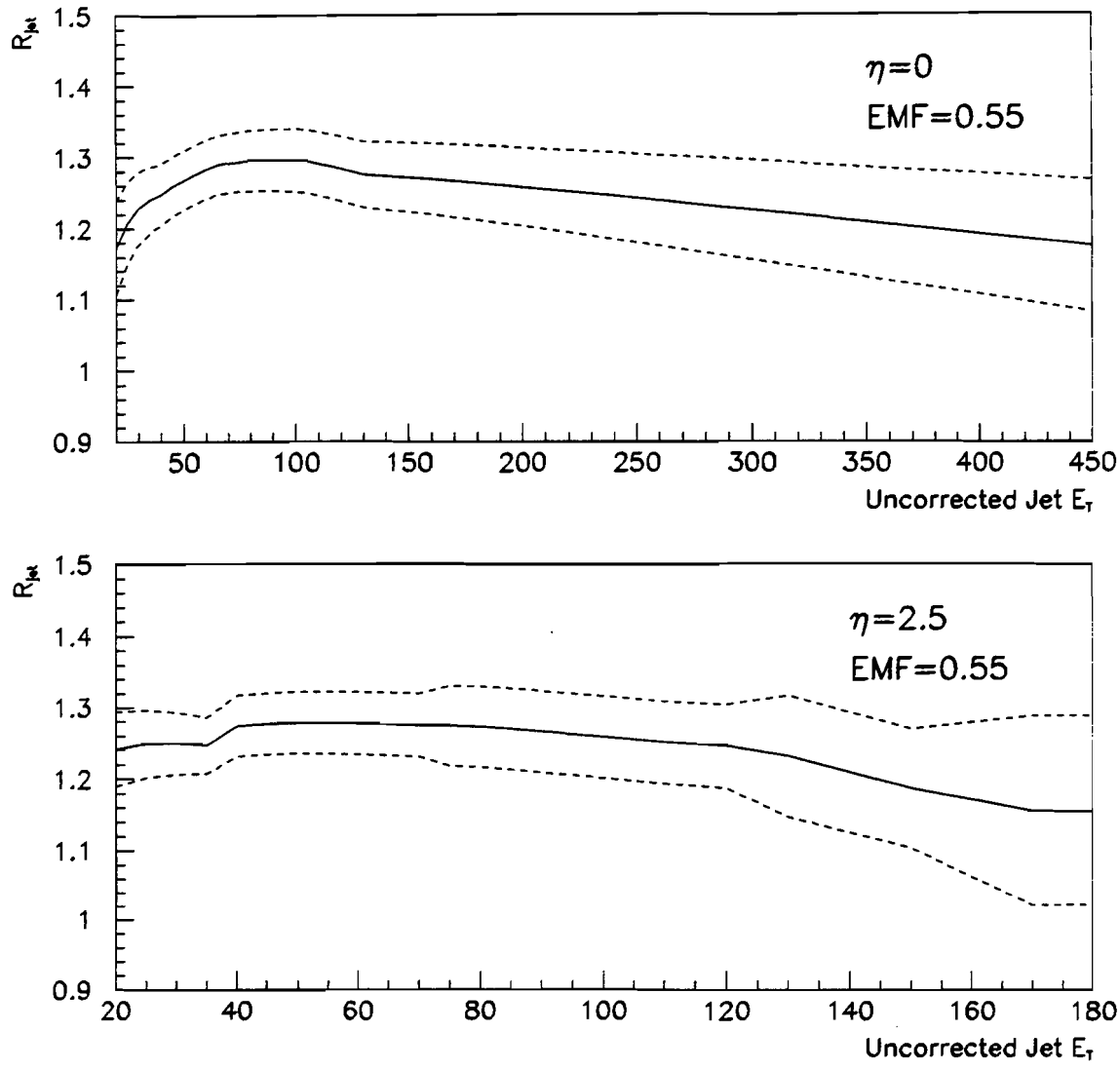

Figure 5.1: Jet energy scale correction factors for two different η_d regions as a function of the jet E_T. The dash lines show the scale correction uncertainty.

5.2 Jet E_T Resolution

In addition to the jet energy scale, we must also study the jet resolution [48]. The jet E_T resolution is a measure of the accuracy of the calorimeter in determining the E_T of jets. In other words, ideally, if we were able to measure 100 GeV jets, the mean value will provide the jet energy scale correction factor and the resolution will be given by the sigma. The jet E_T resolution was determined as a function of the jet physics η, which is different from the detector η if the event $z-$vertex is not at the center of the detector ($z_v = 0.$) We determined the E_T resolution by selecting a sample of dijet events and determine the asymmetry, which is defined as:

$$A \equiv \frac{E_{T_1} - E_{T_2}}{E_{T_1} + E_{T_2}} \tag{5.8}$$

where E_{T_1} and E_{T_2} are the transverse energies of the two leading jets. The variance of A is then:

$$\sigma_A^2 = \left|\frac{\partial A}{\partial E_{T_1}}\right|^2 \sigma_{E_{T_1}}^2 + \left|\frac{\partial A}{\partial E_{T_2}}\right|^2 \sigma_{E_{T_2}}^2. \tag{5.9}$$

Assuming $E_T \equiv E_{T_1} = E_{T_2}$ and $\sigma_{E_T} \equiv \sigma_{E_{T_1}} = \sigma_{E_{T_2}}$, the fractional transverse energy resolution is simplified to:

$$\left(\frac{\sigma_{E_T}}{E_T}\right) = \sqrt{2}\sigma_A. \tag{5.10}$$

The procedure was repeated using a a sample of photon-jet data in order to obtain the resolution at low E_T values.

The resolution was then parametrized as a function of energy scale corrected jet E_T and η for five η regions using the functional form:

$$\left(\frac{\sigma_{E_T}}{E_T}\right)^2 = \frac{N^2}{E_T^2} + \frac{S^2}{E_T} + C^2. \tag{5.11}$$

The parametrizations are shown in Figs. 5.2 and 5.3 and the values for the three parameters are shown in table 5.1 where the errors are just the errors due to the fit [48]. The theoretical predictions will be smeared with these E_T resolutions before comparing to the data.

5.3 Jet η Bias and Resolution

In addition to the E_T resolution, the detector also has a finite η resolution. It was found from Monte Carlo studies that jets are slightly mismeasured in η [49]. The

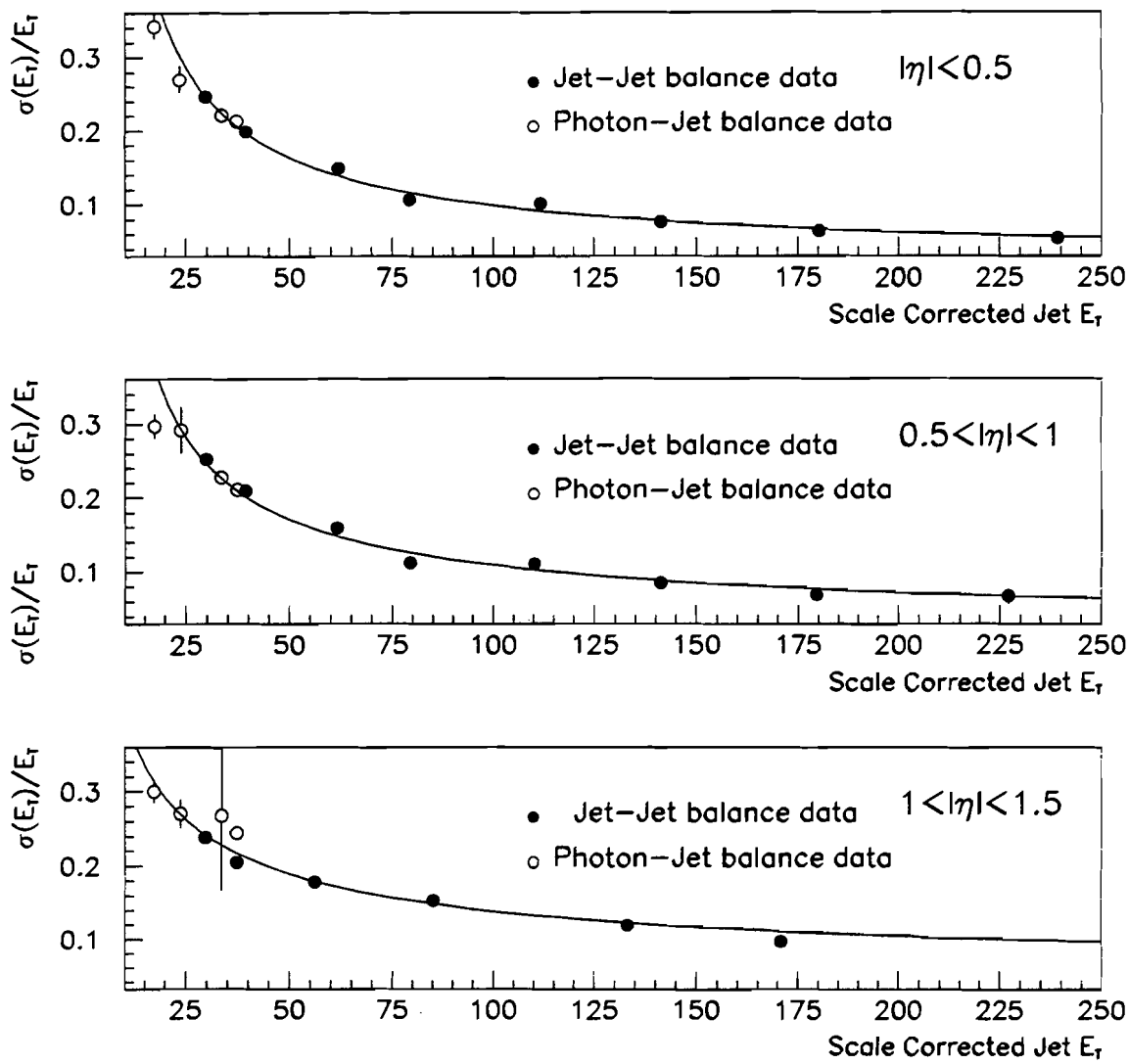

Figure 5.2: Parametrization of the fractional transverse energy resolution in the central and intercryostat regions as a function of the scale corrected jet E_T. The dark circles are obtained from the $jet - jet$ sample and the open circles are associated with the $\gamma - jet$ events. The fit includes both sets of measurements.

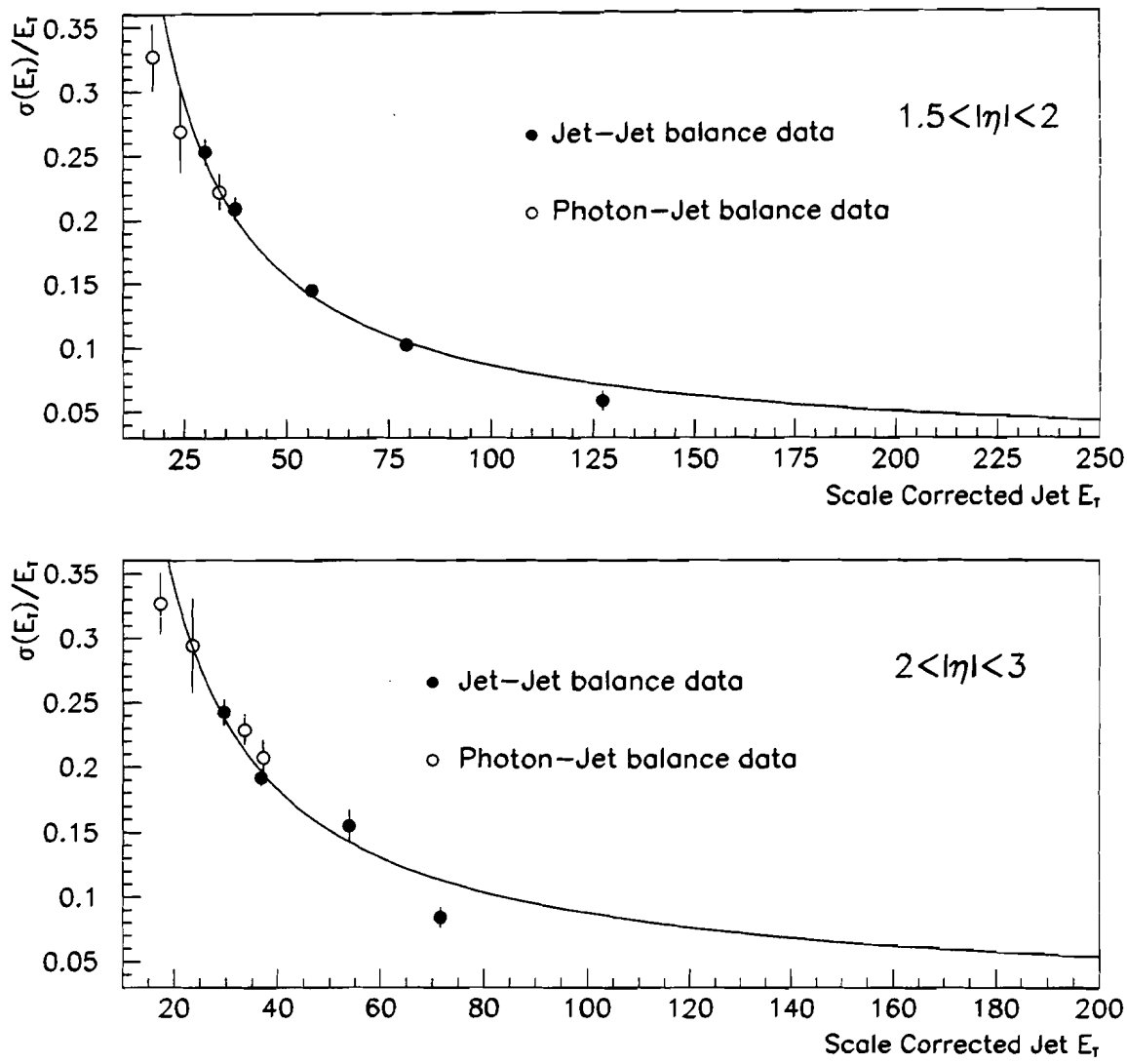

Figure 5.3: Parametrization of the fractional transverse energy resolution in the forward region as a function of the scale corrected jet E_T. The dark circles are obtained from the $jet - jet$ sample and the open circles are associated with the $\gamma - jet$ events. The fit includes both sets of measurements.

η	N(GeV^2)	S(GeV)	C
0.0 – 0.5	5.99 ± 0.18	0.80 ± 0.03	0.
0.5 – 1.0	5.15 ± 0.25	0.96 ± 0.03	0.
1.0 – 1.5	0.0011 ± 0.0001	1.29 ± 0.03	0.053 ± 0.010
1.5 – 2.0	6.80 ± 0.32	0.53 ± 0.08	0.
2.0 – 3.0	6.16 ± 0.37	0.62 ± 0.10	0.

Table 5.1: Parametrization of the fractional transverse energy resolution as a function of the scale corrected jet E_T. It includes low E_T γ–jet data points.

average difference between the parton η and the reconstructed jet η was non-zero, indicating a small bias in the way jets are reconstructed. The bias has been corrected in the data and it is a rather small effect for large bin sizes (η bin size of 0.5): 2% for central values of η and a 7% effect for $2.5 \leq |\eta| \leq 3.0$. The sigma of the average difference previously determined tells us the η resolution of the detector. The η resolution has been parametrized for six detector η regions, η_d, with the form:

$$\sigma_\eta(E, \eta_d) \;=\; \mathrm{A} + \frac{\mathrm{B}}{E} + \frac{\mathrm{C}}{E^2}. \tag{5.12}$$

The results are shown in Fig. 5.4 and in Table 5.2. Given the good η resolution for the detector, no η resolution correction is required in the triple differential cross section.

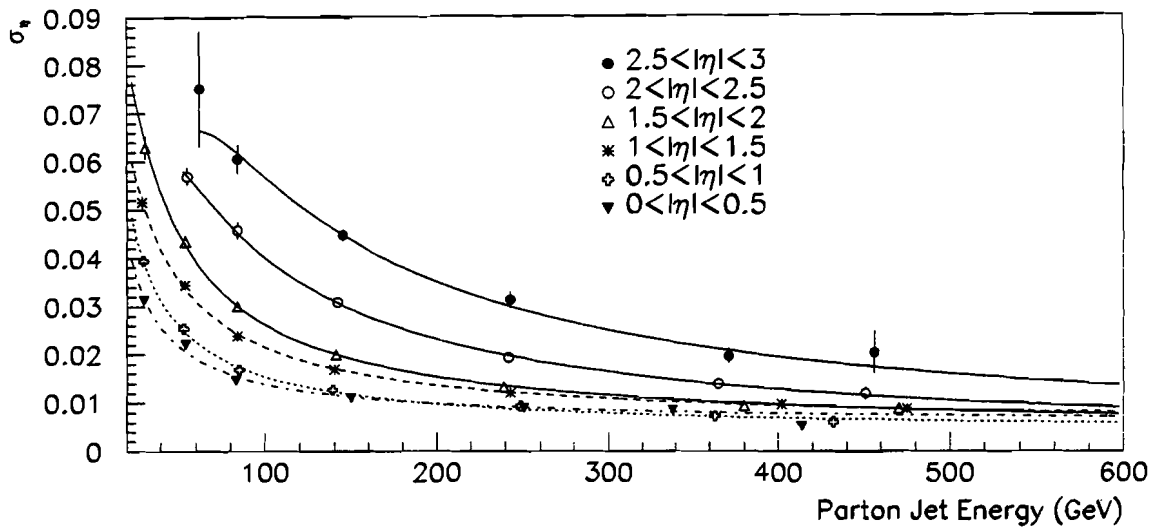

Figure 5.4: $\sigma_\eta(E,\eta_d)$ as a function of the parton energy using a HERWIG simulation.

η	A	B(GeV)	C(GeV^2)
0.0 – 0.5	0.0057	0.820	−0.960
0.5 – 1.0	0.0039	1.19	−3.860
1.0 – 1.5	0.0052	1.74	−10.98
1.5 – 2.0	0.0037	2.42	−17.10
2.0 – 2.5	0.0011	4.90	−100.3
2.5 – 3.0	0.00081	8.08	−248.9

Table 5.2: Parametrization of the jet η resolution as a function of parton jet energy for different η_d bins.

5.4 Efficiencies

We have applied several cuts to the data sample and must determine their efficiencies. Among the efficiencies that must be determined are the ones due to the jet quality cuts, the missing E_T cut, the trigger, the jet reconstruction algorithm, and the multiple interaction cut. They are discussed below.

5.4.1 Standard Jets Cuts and Missing E_T Cut

The efficiency of each jet quality cuts was calculated in a similar manner [50]. For example, the jet electromagnetic fraction (EMFR) was plotted for different E_T bins. For each E_T bin, the region of EMFR inside [0.2,0.85] is assumed to have no background and two gaussian functions are fit to its rising and falling edges. The curves are then extrapolated to EMFR= 0 and EMFR= 0.99 and the number of jets (N) under the fits are counted. N should be the total number of good jets. But given that only jets inside of EMFR=[0.05,0.95] are considered, by counting the number of jets (n) inside of EMFR=[0.05,0.95], the efficiency of the EMFR cut is simply the ratio of n over N:

$$\epsilon_{\rm emf} = \frac{n}{N}. \tag{5.13}$$

Figure 5.5 shows the EMFR distribution with respective fits for two different E_T bins.

Similar procedures were performed for the hot cell fraction cut, the coarse hadronic fraction cut and $\not{E}_T$ cut. Figure 5.6 shows the HOTFR and missing E_T distributions with respective fits. The method used to determine the EMFR efficiency is used here.

The efficiencies were then determined for each cut for different E_T bins. They were then parametrized as a function of the the mean E_T value of each of the E_T bins. For example, the $\not{E}_T$ cut was parametrized as a function of the leading jet E_T for the E_T range of 40 GeV through 500 GeV as:

$$\epsilon_{met} = -0.0085\text{GeV}^{-1} \times E_T^{\rm J1} + 100.3. \tag{5.14}$$

The three efficiencies for the Standard jet quality cuts (EMFR, HOTFR, and CHFR) were then multiplied for the different E_T points to obtain a global efficiency

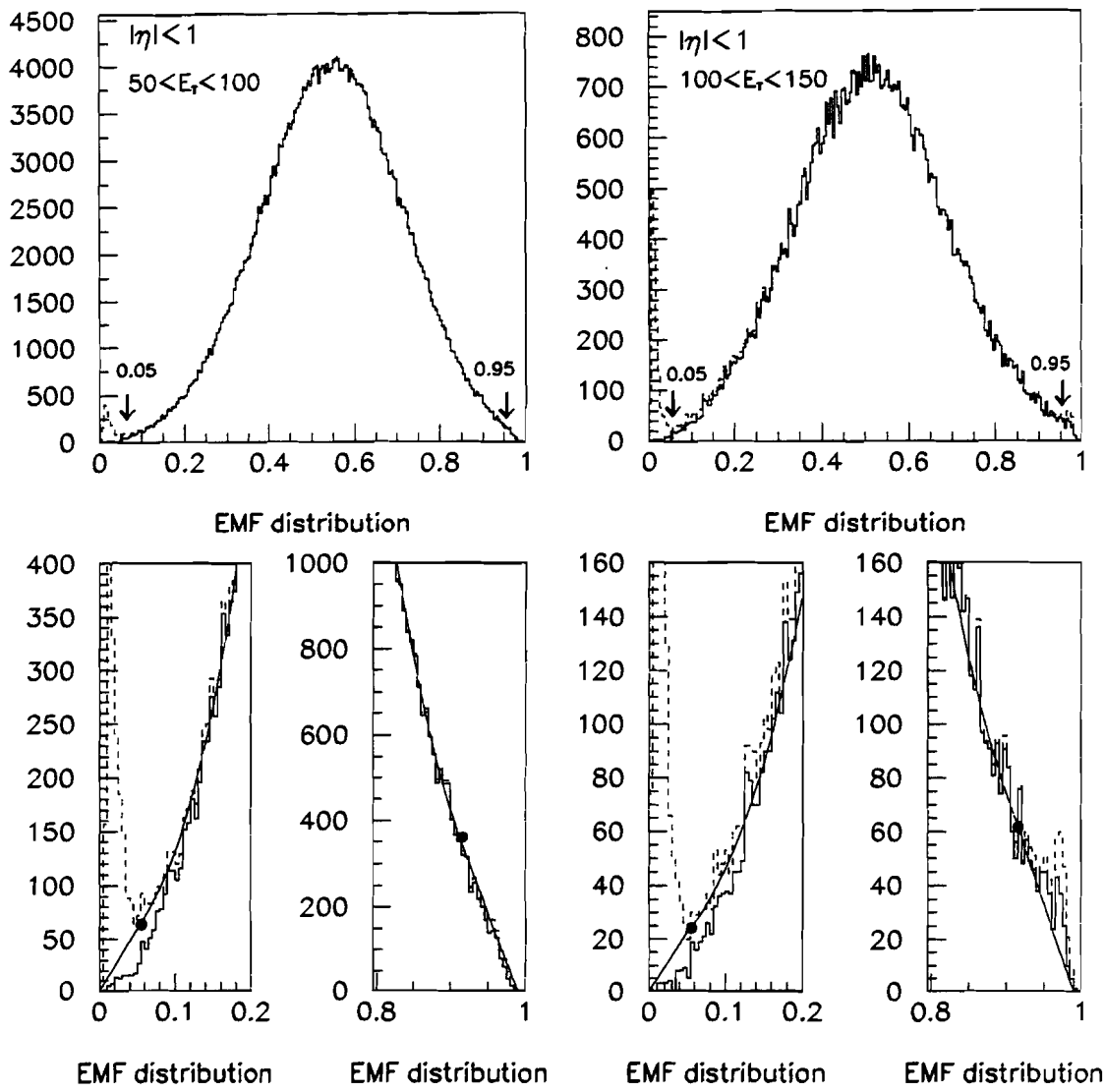

Figure 5.5: EMFR distribution for different E_T bins with respective fits.

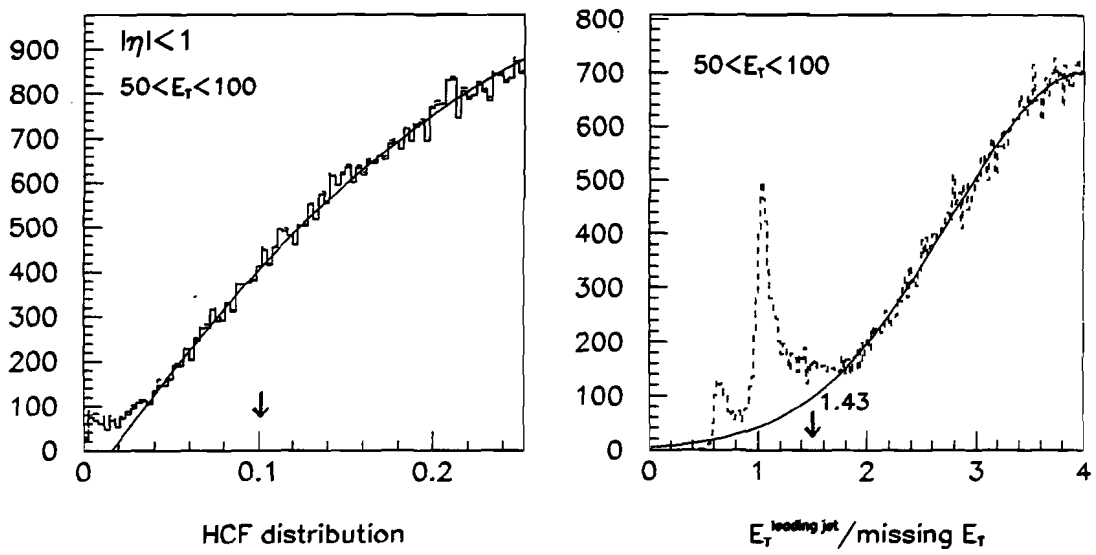

Figure 5.6: HOTFR and $\not{E}_T$ distributions with respective fits.

value:

$$\epsilon_{\text{quality-ji}} \equiv \epsilon_{\text{emf}} \times \epsilon_{\text{chf}} \times \epsilon_{\text{hcf}}. \tag{5.15}$$

Similar to the $\not{E}_T$ cut, the global efficiency values were parametrized as a function of the mean E_T value of each E_T bin:

$$\epsilon_{\text{quality-ji}} = -0.019 \times E_T + 97.85. \tag{5.16}$$

Since this analysis requires two leading jets to satisfy the standard jet quality cuts, the event efficiency for the standard jet quality cuts is:

$$\epsilon_{\text{event-quality}} = \epsilon_{\text{quality-j1}} \times \epsilon_{\text{quality-j2}}. \tag{5.17}$$

Figure 5.7(a) shows the standard jet quality cut efficiency as a function of jet E_T and Fig. 5.7(b) shows the missing E_T cut efficiency as a function of the leading jet E_T. Note that the standard jet quality cut efficiency should be used to correct individual jets but the missing E_T cut efficiency should be used to correct the event.

5.4.2 Multiple Interaction Cut

As described in the previous chapter, it is possible to have more than one hard $p\bar{p}$ interaction in a beam crossing. This possibility increases as the instantaneous luminosity increases. If there are two interactions in an event, it is very difficult to separate the contributions from each interaction, hence only those events with one interaction were selected. The efficiency of the multiple interaction cut was obtained for each trigger bit. For every trigger bit, the E_T spectrum above 50 GeV for central jets ($0.0 \leq |\eta| \leq 1.0$) is plotted. The spectrum is determined twice: first with the requirement of only one interaction in the event (MIFLAG=1), and second without any restrictions on the number of interactions. The ratio of the spectrum with the requirement over the one without gives the efficiency of the cut. Since the effect of this cut should be independent of the jet E_T for central leading jets, the ratio should be independent of the leading jet E_T.

Fig. 5.8 shows the ratios for the different QCD triggers. We fit the distributions to a straight horizontal line and the normalization parameter of the fit gives the multiple interaction cut efficiency. We only consider those events that have full

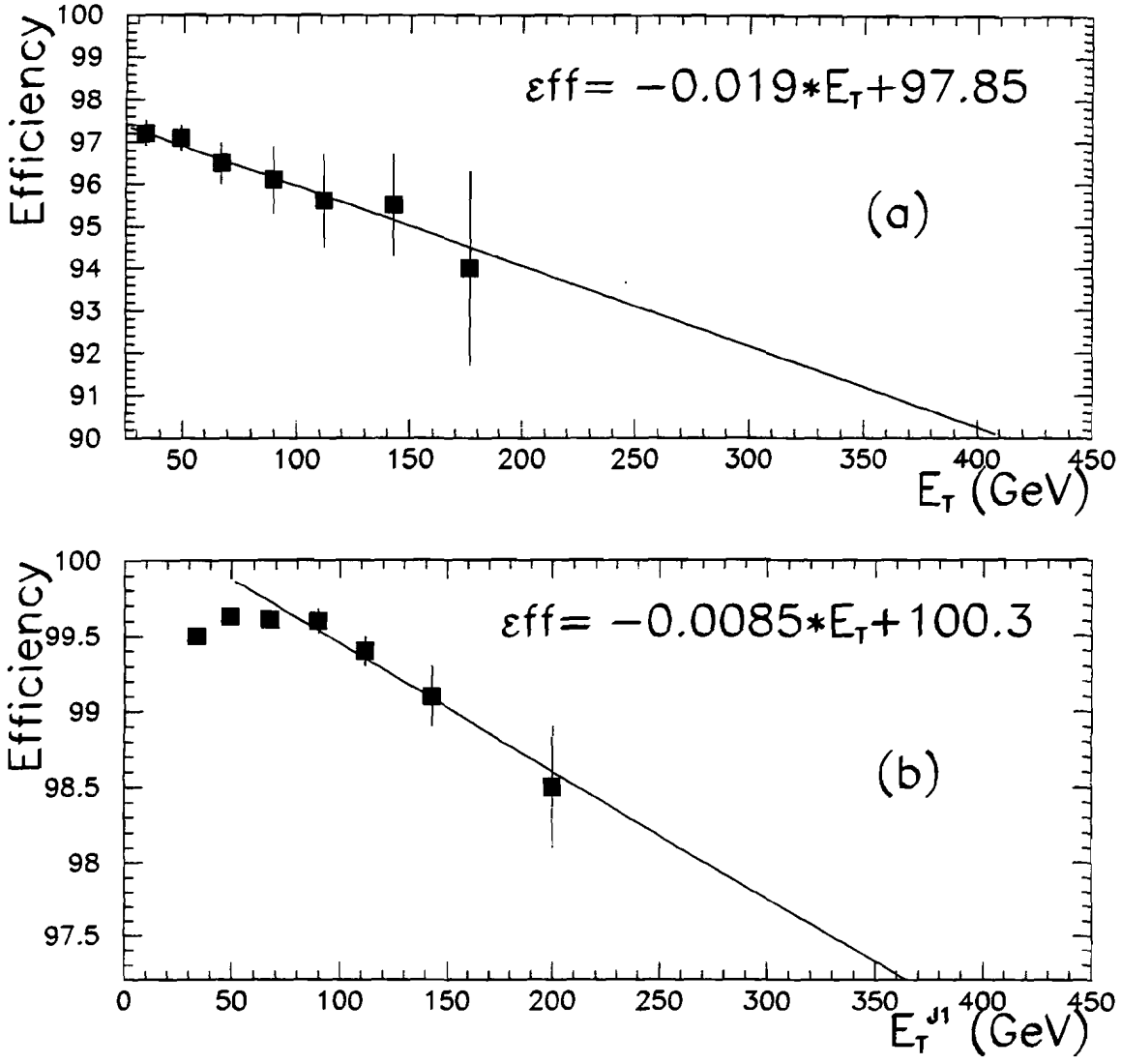

Figure 5.7: Parametrization of efficiencies as a function of jet E_T for: (a) the standard jet quality cuts and (b) for the missing E_T cut.

trigger efficiency. The multiple interaction cut efficiencies and the E_T values where the triggers are fully efficient are shown in Table 5.3.

TRIGGER BIT	EFFICIENCY	E_T CUT
JET_LOW	0.54	50 GeV
JET_MEDIUM	0.50	70 GeV
JET_HIGH	0.49	115 GeV
JET_MAX	0.47	150 GeV

Table 5.3: Multiple interaction cut efficiencies for different QCD trigger bits.

The multiple interaction cut efficiencies are roughly the same. JET_LOW has the highest efficiency because most of the JET_LOW data was obtained when the instantaneous luminosity was low, hence most events had a single interaction. Similarly, a large portion of the JET_MAX data was recorded at the highest luminosity when there is a greater probability for multiple interactions.

The overall cut efficiency on an event-by-event basis is the product of the event efficiency of the standard cuts, the efficiency of the $\not{E}_T$ cut, and the efficiency due to the multiple interaction cut:

$$\epsilon_{\text{event-cut}} = \epsilon_{event-quality} \times \epsilon_{met} \times \epsilon_{\text{miflag}}. \tag{5.18}$$

5.4.3 Derivation of Trigger Efficiencies

The inefficiencies due to the trigger must also be considered. The event trigger efficiency for a particular QCD filter bit can, in principle, be calculated from the single jet trigger efficiency. The single jet trigger efficiency is defined as the probability a single jet at a particular E_T, η, and ϕ would pass both the Level 1 (L1) and Level 2 (L2) requirements for the filter bit under study. The event trigger efficiency (ϵ_{event}) is defined as the probability that the event satisfied the filter bit. This could occur because any one jet or combination of jets passed the L1 and L2 requirements. For

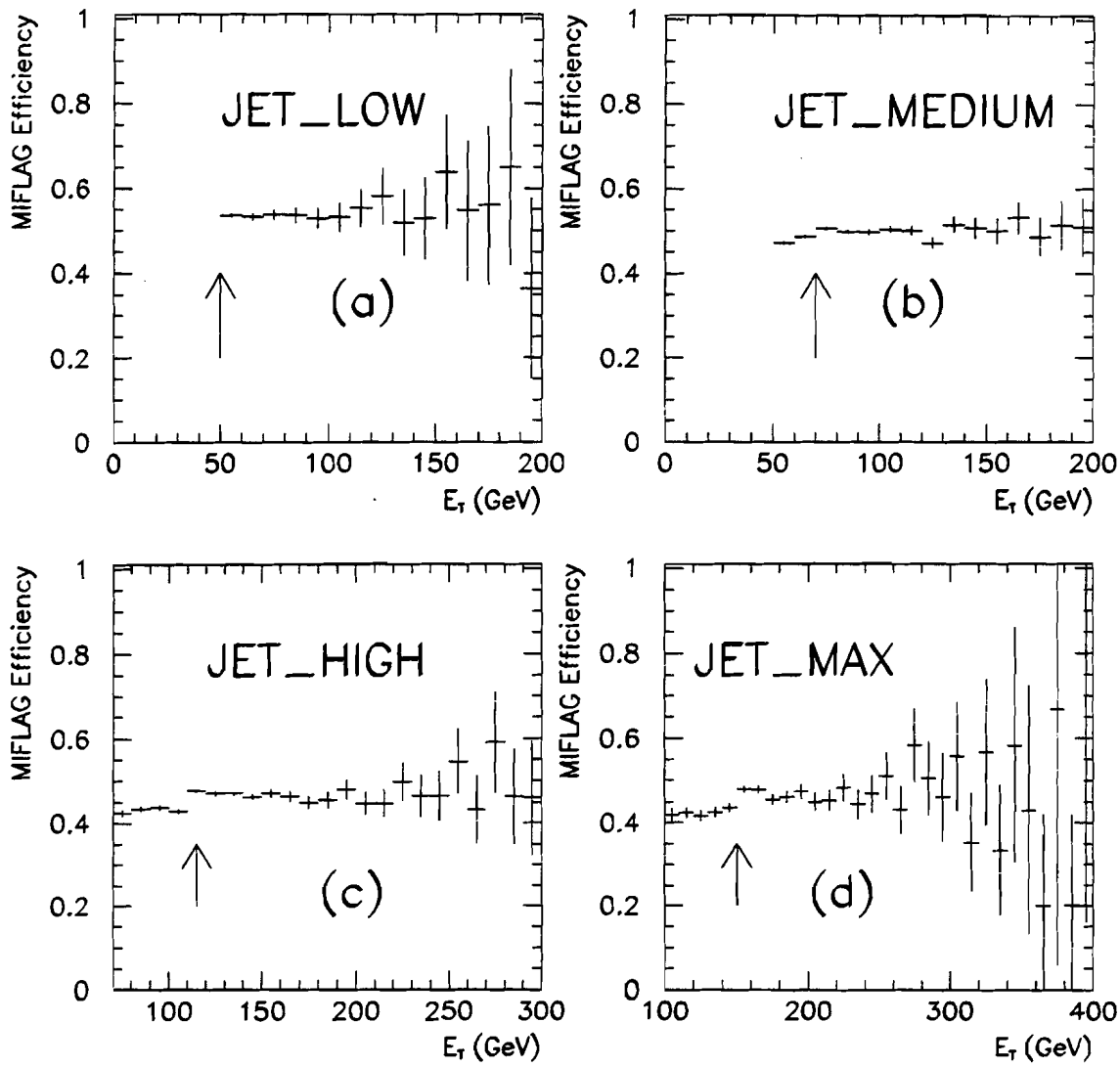

Figure 5.8: Multiple interaction cut efficiencies are shown for: (a) JET_LOW, (b) JET_MEDIUM, (c) JET_HIGH, and (d) JET_MAX. The arrows show where the trigger is fully efficient.

an event with N jets,

$$\epsilon_{event} = 1 - \prod_{n=i}^{N} q_i = 1 - \prod_{n=i}^{N}(1 - p_i) \tag{5.19}$$

where q_i is the probability that the *ith* jet fails and p_i=1 $-q_i$ is the probability of success for the *ith* jet.

There are several other ways of understanding event efficiencies but the results should be identical. This can be easily shown with an example: consider a 2 jet event. Using (5.54)

$$\begin{aligned} \epsilon_{event} &= 1 - q_1 * q_2 \\ &= 1 - (1 - p_1)(1 - p_2) \\ &= p_1 + p_2 - p_1 p_2. \end{aligned}$$

This agrees with the intuition that the event efficiency is the sum of the individual probabilities minus their overlap.

A simpler method to determine the trigger efficiencies for a particular trigger is to determine as a function of the E_T spectrum of the trigger of interest and the one for a less restrictive trigger. For example, we are interested in JET_LOW, so we determine the E_T spectra of JET_LOW and JET_MIN, which is a less restrictive trigger as shown in Fig. 5.9. We can see the turn-on behavior of JET_LOW and note that it is 100% efficient around 40 GeV, but this only shows where the trigger is fully efficient for the event parametrized as a function of E_T, averaging over other variables such as pseudorapidity. We are interested in determining the single jet trigger efficiency as a function of E_T and η and then determine from it the event efficiency.

To determine the single jet trigger efficiency p_i, we must start with an unbiased sample of jets, i.e., minimum bias events, and determine for each reconstructed (RECO) jet whether the jet satisfied the trigger requirements. This method does not take the reconstruction efficiency into account, which we assume to be 100%. The trigger was done in three stages: LØ, L1, and L2. The efficiency of LØ has been calculated to be 97%. The efficiency for L1 and L2 should be given to first order by

$$P(L1L2) = P(L1)P(L2|L1) \tag{5.20}$$

where P(L1) is the probability of a RECO jet passing L1 and P(L2|L1) is the probability of a RECO jet passing L2 given the jet satisfies the L1 trigger condition.

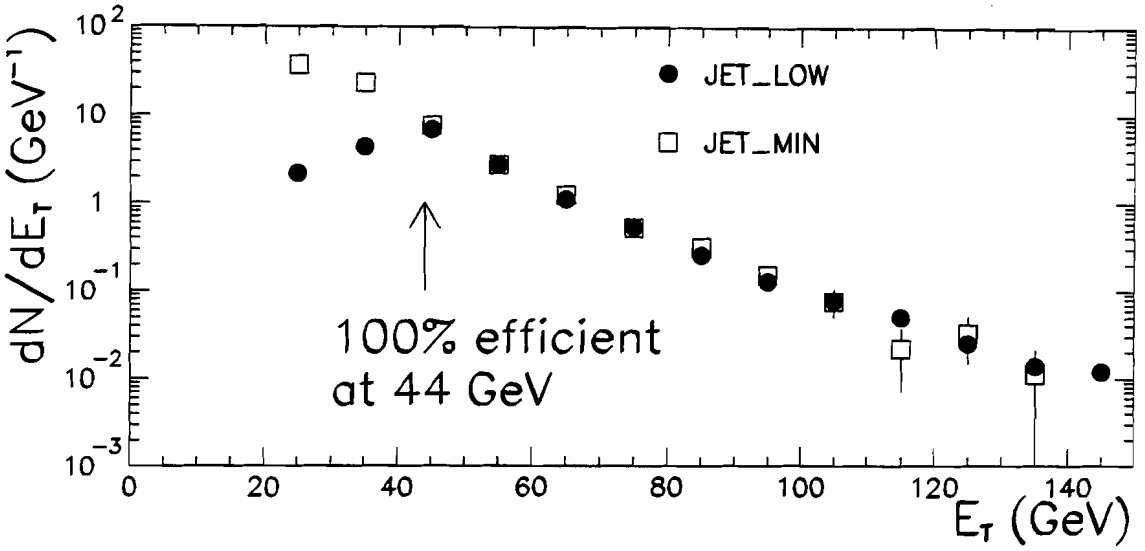

Figure 5.9: Event trigger turn-on for JET_LOW showing 100% efficiency at 40 GeV.

However, according to our triggering scheme, two jets could combine to satisfy the L1 and L2 requirements without being able to do so individually. Similarly, several jets could and do combine to satisfy some of the L1 triggers. We must, therefore, use a different scheme if we are to determine the overall event trigger efficiency. We must determine the L1 event efficiency due to single jets and then the L2 event efficiency due to single jets.

The probability for an event to pass plus the probability for the event to fail the trigger should add up to unity.

$$\epsilon_{trigger-pass} + \epsilon_{trigger-fail} = 1. \tag{5.21}$$

We show that it is easier to use the failure probabilities in the formulae. The probability that an event fails is given by two parts:

1) The probability that all jets or combination of jets failed the L1 requirement and

2) given that not all jets or combination of jets failed the L1 requirement, all jets failed the L2 requirement:

$$\epsilon_{trigger-fail} = \epsilon^{L1}_{fail} + [1 - \epsilon^{L1}_{fail}] * \epsilon^{L2}_{fail} \tag{5.22}$$

where ϵ^{L2}_{fail} is defined as the probability of the event failing to satisfy the L2 condition and ϵ^{L1}_{fail} is the probability of the event failing to satisfy the L1 condition. Combining the last two equations we get

$$\epsilon_{trigger-pass} = 1 - \epsilon_{trigger-fail} = (1 - \epsilon^{L1}_{fail}) \times (1 - \epsilon^{L2}_{fail}). \tag{5.23}$$

The definitions for ϵ^{L1}_{fail} and ϵ^{L2}_{fail} change depending on the QCD filter. Table 5.4 shows the L1 and L2 requirements associated with each QCD trigger.

FILTER	L1 REQUIREMENT	L2 REQUIREMENT
JET_MIN	1 tower≥3 GeV	1 L2JET≥20 GeV
JET_LOW	1 tower≥7 GeV	1 L2JET≥30 GeV
JET_MEDIUM	2 towers≥7 GeV	1 L2JET≥50 GeV
JET_HIGH	3 towers≥7 GeV	1 L2JET≥85 GeV
JET_MAX	4 towers≥5 GeV	1 L2JET≥115 GeV

Table 5.4: QCD triggers and respective L1 and L2 requirements.

To find the formula for ϵ^{L1}_{fail}, let us illustrate first with a three-jet event. Assume that the trigger requirement is one tower above m GeV. Define p_i as the probability of the *ith* jet passing that requirement and q_i as the probability of the jet failing, such that $p + q = 1$. Table 5.5 shows each possibility. The probability that the event fails the L1 requirement is $q_1 * q_2 * q_3$.

Consider now the case of a one-jet event where the trigger requirement is two towers above m GeV. Define s_i the probability the ith jet passes two towers or more, r_i the probability the ith jet passes one and ONLY one tower and q_i the probability of passing none ($s + r + q = 1$). The possibilities are shown in Table 5.6.

For this case, the event fails L1 with probability:

$$\epsilon^{L1}_{fail} = q_1 + r_1.$$

Let us extend our discussion to a three-jet event with the trigger requirement of two towers above m GeV. Define as before, s_i the probability the ith jet passes two

J1	J2	J3	TOPOLOGY	COMMENTS
|	|	|	$p_1 * p_2 * p_3$	event passes
|	|	0	$p_1 * p_2 * q_3$	event passes
|	0	|	$p_1 * q_2 * p_3$	event passes
|	0	0	$p_1 * q_2 * q_3$	event passes
0	|	|	$q_1 * p_2 * p_3$	event passes
0	|	0	$q_1 * p_2 * q_3$	event passes
0	0	|	$q_1 * q_2 * p_3$	event passes
0	0	0	$q_1 * q_2 * q_3$	event FAILS

Table 5.5: Logic table for a three jet event requiring one tower to satisfy the trigger condition where 0 represents the jet having no towers and | one or more towers above m GeV. Note that the event fails the L1 requirement with a probability of $q_1 * q_2 * q_3$.

towers or more, r_i the probability the ith jet passes one and ONLY one tower and q_i the probability of passing none ($s + r + q = 1$). The possible combinations are shown in Table 5.7.

For this case, the event fails L1 with probability:

$$\begin{aligned} \epsilon_{fail}^{L1} &= q_1 * q_2 * q_3 + \\ & \quad r_1 * q_2 * q_3 + r_2 * q_1 * q_3 + r_3 * q_1 * q_2. \end{aligned}$$

The cases for three and four L1 towers are shown in the appendix.

Guided by these examples, one can then write the general formula for N jets in the event. Let us start with a couple of definitions:

P_i(n,m) is the probability of the ith jet having n or MORE towers above m GeV.

$\tilde{P}_i$(n,m) is the probability for the ith jet to have n and ONLY n towers above m GeV. Note that

$$\tilde{P}_i(n,m) = P_i(n,m) - P_i(n+1,m) \tag{5.24}$$

Then, for the different QCD triggers, we have:

a) JET_MIN required one tower above 3 GeV at L1 hence

$$\epsilon_{fail}^{L1} = \prod_{i=1}^{N} \{1 - P_i(1,3)\} \tag{5.25}$$

J1	TOPOLOGY	COMMENTS
||	s_1	event passes
|	r_1	event FAILS
0	q_1	event FAILS

Table 5.6: Logic Table for a one jet event requiring two towers to satisfy the trigger condition where 0 represents no towers, | one and only one tower, and || two or more towers above m GeV.

where the summation is over all jets in the event.

b) JET_LOW required one tower above 7 GeV at L1, hence

$$\epsilon_{fail}^{L1} = \prod_{i=1}^{N}\{1 - P_i(1,7)\}. \tag{5.26}$$

c) JET_MEDIUM required two towers above 7 Gev, hence

$$\begin{aligned}\epsilon_{fail}^{L1} &= \prod_{i=1}^{N}\{1 - P_i(1,7)\} + \\ &\sum_{i=1}^{N}\tilde{P}_i(1,7) * \prod_{j\neq i}^{N}\{1 - P_j(1,7)\}.\end{aligned} \tag{5.27}$$

d) JET_HIGH required three towers above 7 Gev, so the contributing factors for failure are: no jet has a tower above threshold, only one jet has a tower above threshold, only one jet has two towers above threshold, and each of two jets has one tower above threshold:

$$\begin{aligned}\epsilon_{fail}^{L1} &= \prod_{i=1}^{N}\{1 - P_i(1,7)\} + \\ &[\sum_{i=1}^{N}\tilde{P}_i(1,7) + \sum_{i=1}^{N}\tilde{P}_i(2,7)] * \prod_{j\neq i}^{N}\{1 - P_j(1,7)\} + \\ &\sum_{i=1}^{N}\tilde{P}_i(1,7) * [\sum_{j>i}^{N}\tilde{P}_j(1,7) * \prod_{k\neq i,j}^{N}\{1 - P_k(1,7)\}].\end{aligned} \tag{5.28}$$

e) JET_MAX required four towers above 5 Gev, hence

$$\epsilon_{fail}^{L1} = \prod_{i=1}^{N}\{1 - P_i(1,5)\} +$$

J1	J2	J3	TOPOLOGY	COMMENTS
||	||	||	$s_1 * s_2 * s_3$	event passes
||	||	|	$s_1 * s_2 * r_3$	event passes
||	||	0	$s_1 * s_2 * q_3$	event passes
||	|	||	$s_1 * r_2 * s_3$	event passes
||	|	|	$s_1 * r_2 * r_3$	event passes
||	|	0	$s_1 * r_2 * q_3$	event passes
||	0	||	$s_1 * q_2 * s_3$	event passes
||	0	|	$s_1 * q_2 * r_3$	event passes
||	0	0	$s_1 * q_2 * q_3$	event passes
|	||	||	$r_1 * s_2 * s_3$	event passes
|	||	|	$r_1 * s_2 * r_3$	event passes
|	||	0	$r_1 * s_2 * q_3$	event passes
|	|	||	$r_1 * r_2 * s_3$	event passes
|	|	|	$r_1 * r_2 * r_3$	event passes
|	|	0	$r_1 * r_2 * q_3$	event passes
|	0	||	$r_1 * q_2 * s_3$	event passes
|	0	|	$r_1 * q_2 * r_3$	event passes
|	0	0	$r_1 * q_2 * q_3$	event FAILS
0	||	||	$q_1 * s_2 * s_3$	event passes
0	||	|	$q_1 * s_2 * r_3$	event passes
0	||	0	$q_1 * s_2 * q_3$	event passes
0	|	||	$q_1 * r_2 * s_3$	event passes
0	|	|	$q_1 * r_2 * r_3$	event passes
0	|	0	$q_1 * r_2 * q_3$	event FAILS
0	0	||	$q_1 * q_2 * s_3$	event passes
0	0	|	$q_1 * q_2 * r_3$	event FAILS
0	0	0	$q_1 * q_2 * q_3$	event FAILS

Table 5.7: Logic Table for a three jet event. Two towers above threshold are required to satisfy the trigger condition where 0 represents no towers, | one and only one tower, and || two or more towers above m GeV.

$$
\begin{aligned}
&[\sum_{i=1}^{N}\tilde{P}_i(1,5)+\sum_{i=1}^{N}\tilde{P}_i(2,5)+\sum_{i=1}^{N}\tilde{P}_i(3,5)]*\prod_{j\neq i}^{N}\{1-P_j(1,5)\}+\\
&\sum_{i=1}^{N}\tilde{P}_i(1,5)*[\sum_{j>i}^{N}\tilde{P}_j(1,5)*\prod_{k\neq i,j}^{N}\{1-P_k(1,5)\}]+\\
&\sum_{i=1}^{N}\tilde{P}_i(2,5)*[\sum_{j\neq i}^{N}\tilde{P}_j(1,5)*\prod_{k\neq i,j}^{N}\{1-P_k(1,5)\}]+\\
&\sum_{i=1}^{N}\tilde{P}_i(1,5)*\\
&[\sum_{j>i}^{N}\tilde{P}_j(1,5)*\sum_{k>i,j}^{N}\tilde{P}_k(1,5)*\prod_{l\neq i,j,k}^{N}\{1-P_l(1,5)\}].
\end{aligned}
\tag{5.29}
$$

It is evident that to get the L1 jet event efficiency, one needs to find only P_i(n,m) for different n and m.

The event efficiency for L2 is quite straightforward since it only required one object at different thresholds for the different filters. They are Υ(1,20) for JET_MIN, $\Upsilon(1,30)$ for JET_LOW, Υ(1,50) for JET_MEDIUM, Υ(1,85) for JET_HIGH, and Υ(1,115) for JET_MAX where Υ(n,m) is the probability for the jet to have n L2 jets above m GeV. Then,

$$
\epsilon_{fail}^{L2}=\prod_{i=1}^{N}\{1-\Upsilon_i(1,m)\} \tag{5.30}
$$

where ϵ_{fail}^{L2} is defined as the probability of the event failing to satisfy the L2 condition and $\Upsilon_i(1,m)$ is the probability for the ith jet to have one L2 jet above m GeV. Recall each jet must have a corresponding L1 tower above the 3 GeV threshold.

Summarizing, one must determine from L1 single jet trigger efficiencies the L1 event trigger efficiency and from L2 single jet trigger efficiencies the L2 event trigger efficiency.

5.4.4 Measuring Trigger Efficiencies

In order to determine the single jet trigger efficiencies for both L1 and L2 a series of special runs called *Mark and Pass* (QMP) runs were taken. These were taken with less restrictive conditions than the actual trigger conditions. For example, JET_MIN requires 1 tower above 3 GeV at L1 and one jet above 20 GeV at L2. We took a QMP run requiring simply 1 tower above 3 GeV as its trigger condition. We can plot the RECO E_T spectrum of all jets in the event with and without requiring the

jets to have a matching L2 jet above 20 GeV. The ratio of these two plots provides us with the L2 single jet efficiency.

We can plot the RECO E_T spectrum requiring also a matching tower above 7 GeV. This will provide us with the JET_LOW L1 single jet trigger efficiency. A run requiring the JET_LOW L1 trigger condition is used to determine the JET_MEDIUM L1 single jet trigger efficiency and the JET_LOW L2 single jet trigger efficiency. But note with JET_MIN, one determines the JET_LOW L1 single jet trigger efficiency with respect to one tower above 3 GeV. In order to determine the JET_MIN L1 single jet trigger efficiency, we used MIN_BIAS events as an unbiased sample. Hence, the absolute JET_LOW L1 single jet trigger efficiency is given by

$$\begin{aligned} \text{JET_LOW L1} &= \frac{P(1,7)}{P(1,3)} \times \frac{P(1,3)}{\text{MIN_BIAS}} \\ \text{or JET_HIGH L1} &= \frac{P(3,7)}{P(2,7)} \times \frac{P(2,7)}{P(1,7)} \times \frac{P(1,7)}{P(1,3)} \times \frac{P(1,3)}{\text{MIN_BIAS}} \end{aligned}$$

and so on.

Figure 5.10 shows the RECO E_T spectra for the the QMP run used to obtain the JET_MIN L2 single jet trigger efficiency and the JET_LOW L1 single jet trigger efficiency for $0.0 \leq \eta < 4.0$. Fig. 5.11 and 5.12 shows the the single jet L1 and L2 trigger efficiencies as a function of uncorrected RECO E_T for different QCD trigger bits.

We have determined the single jet trigger efficiencies for different η regions of the detector. We defined the central region as $0.0 \leq |\eta| < 0.6$, the intercryostat region $0.6 \leq |\eta| < 1.6$, and the end region $1.6 \leq |\eta| < 4.0$ where the η here is detector η. The motivation for this grouping is that the Intercryostat Detector (ICD) and the Massless Gaps (MG), which are in the Intercryostat Region (ICR), are not included in the L1 trigger. Figures 5.13- 5.16 show the L1 trigger turn on curves for the JET_MIN, JET_LOW, JET_MEDIUM, and JET_HIGH triggers for the different regions and all three regions combined. Figures 5.17- 5.20 are the same for L2.

For each of these three regions, we have fitted the curves with the parametrization $1.-\text{Exp}(\text{A}+\text{B}E_T+\text{C}E_T^2)$ where E_T is the RECO E_T. Table 5.8 and 5.9 show the best fit parameters for both the L1 and L2 single jet trigger efficiencies for the different QCD triggers. Due to lack of statistics, the trigger efficiency for JET_MAX could not be determined.

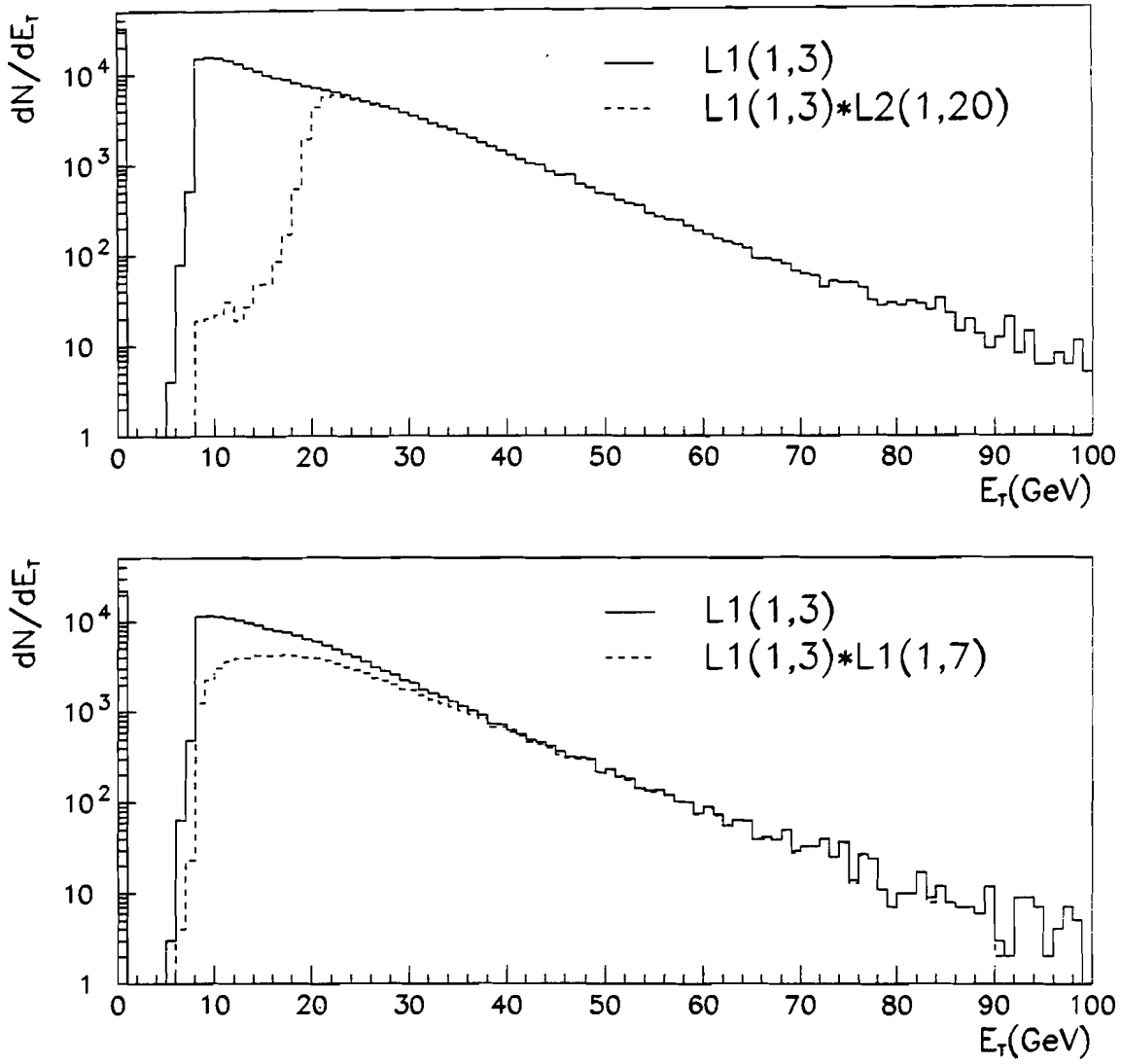

Figure 5.10: The top figure shows the RECO E_T requiring only one tower above 3 GeV in the solid lines and the RECO E_T requiring one tower above 3 GeV and one L2 JET above 20 GeV in dashed lines. The bottom figure shows the RECO E_T requiring only one tower above 3 GeV in the solid lines and the RECO E_T requiring one tower above 3 GeV and one tower above 7 GeV in dashed lines.

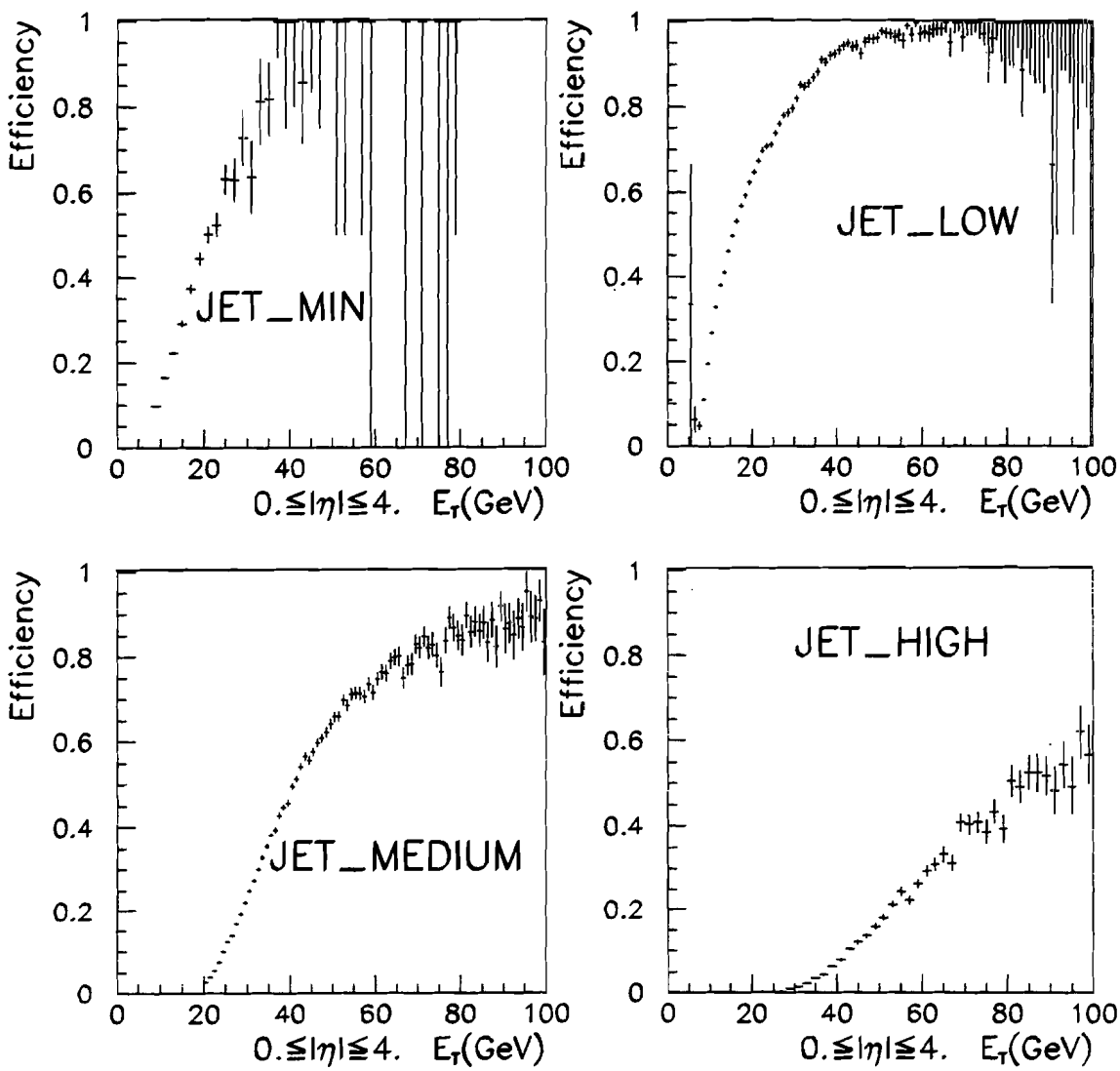

Figure 5.11: L1 single jet trigger efficiencies as a function of uncorrected RECO E_T.

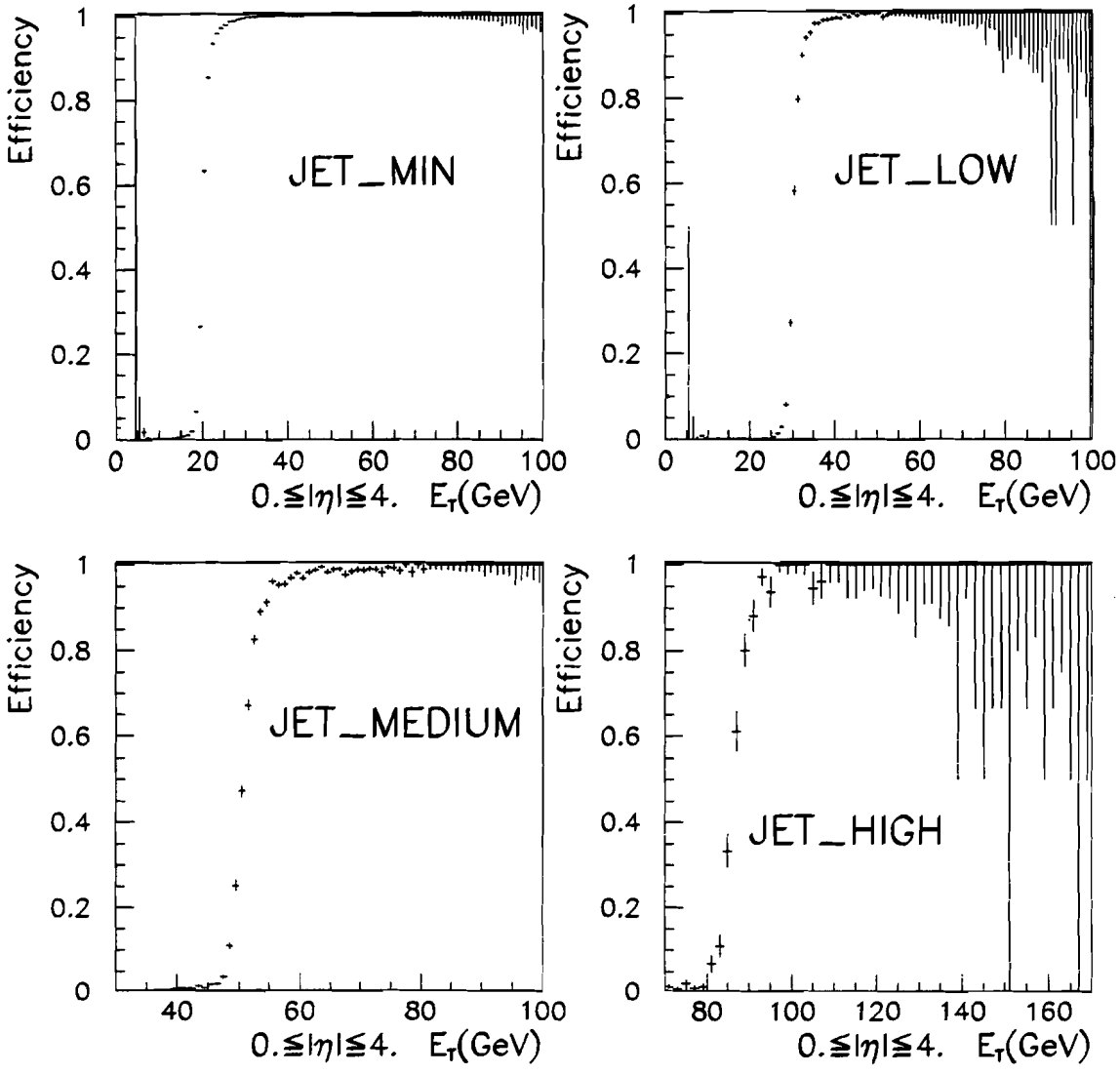

Figure 5.12: L2 single jet trigger efficiencies as a function of uncorrected RECO E_T.

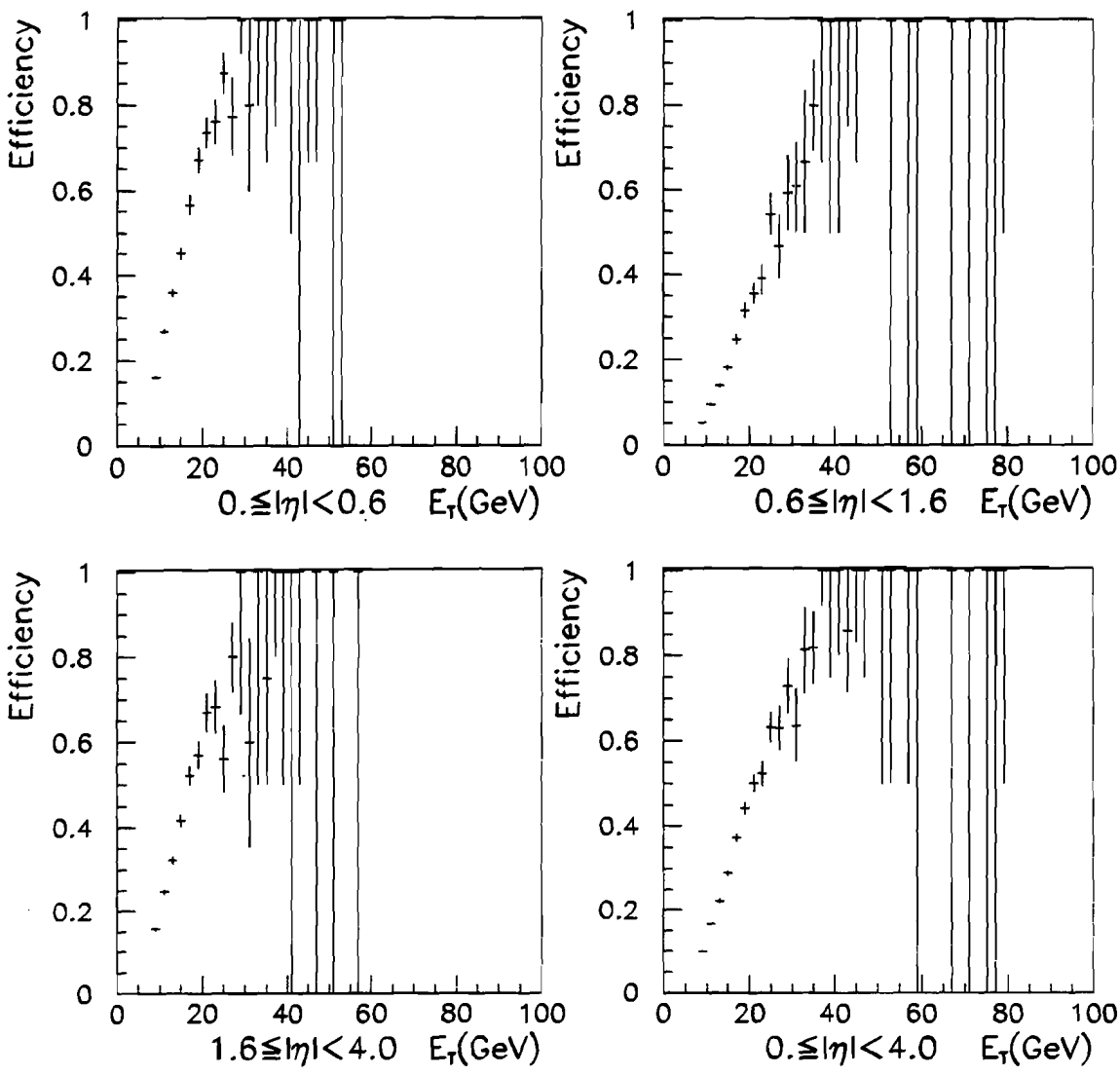

Figure 5.13: L1 single jet trigger efficiencies for JET_MIN in different η regions as a function of uncorrected RECO E_T.

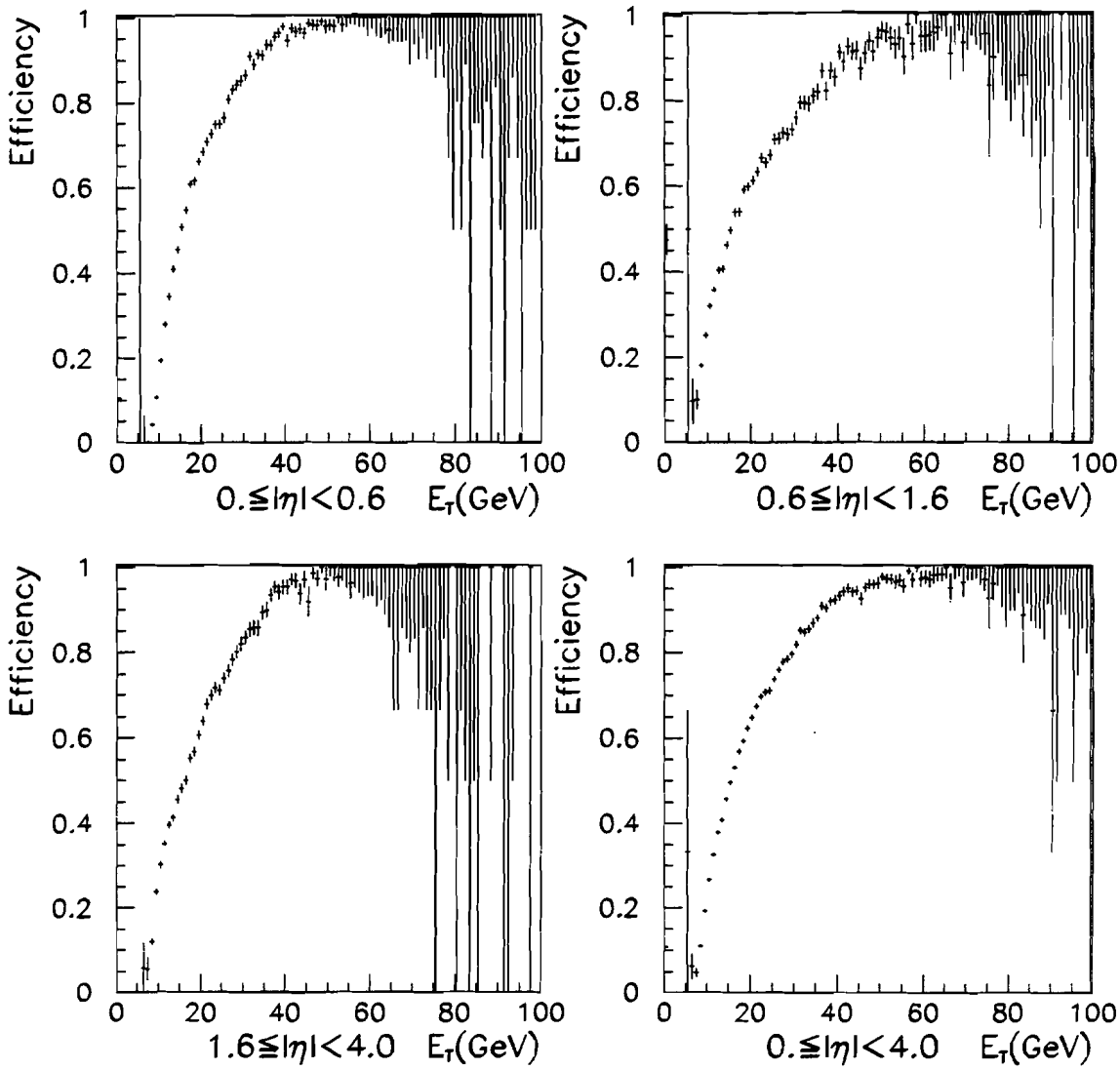

Figure 5.14: L1 single jet trigger efficiencies for JET_LOW in different η regions as a function of uncorrected RECO E_T.

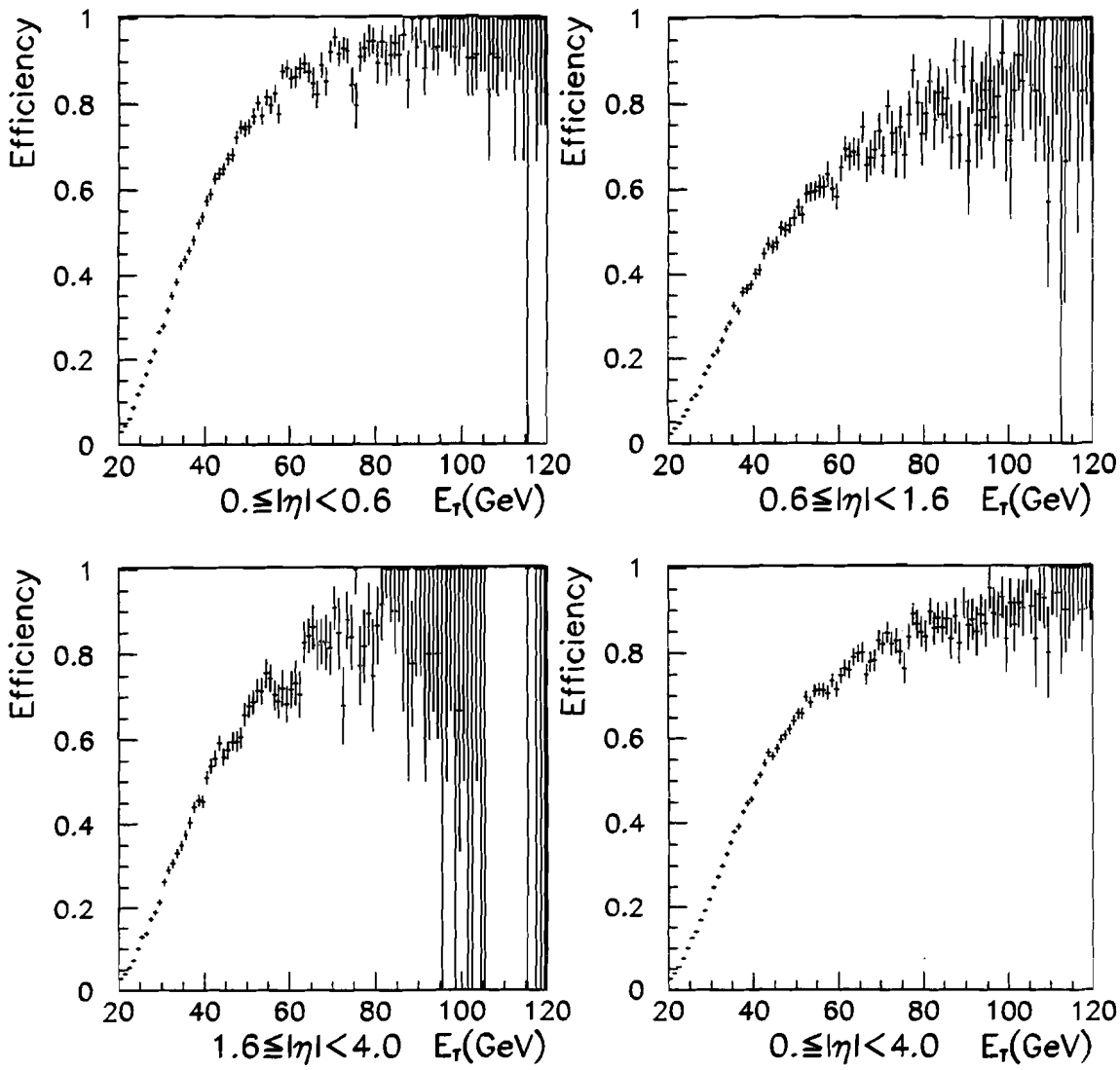

Figure 5.15: L1 single jet trigger efficiencies for JET_MEDIUM in different η regions as a function of uncorrected RECO E_T.

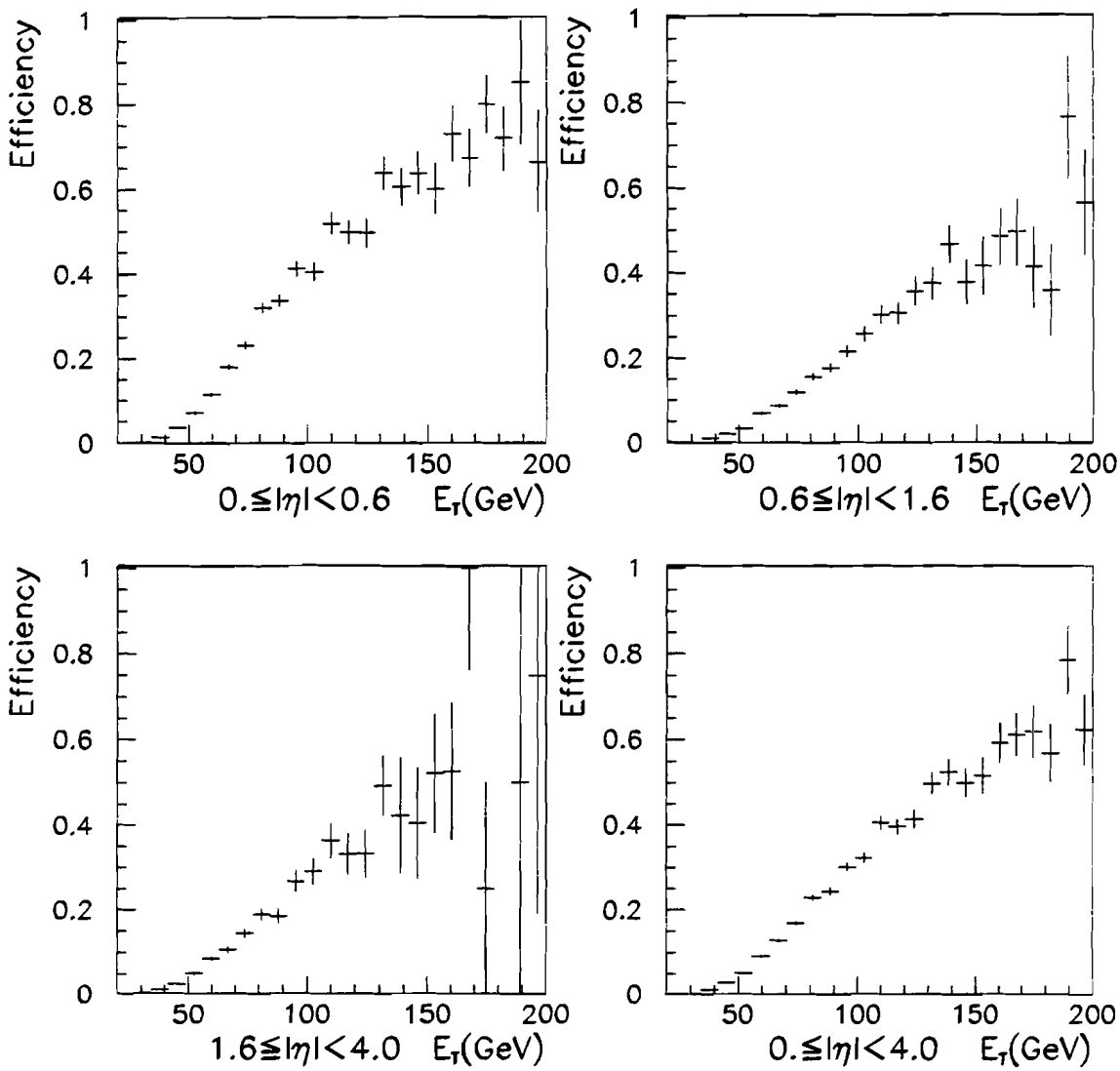

Figure 5.16: L1 single jet trigger efficiencies for JET_HIGH in different η regions as a function of uncorrected RECO E_T.

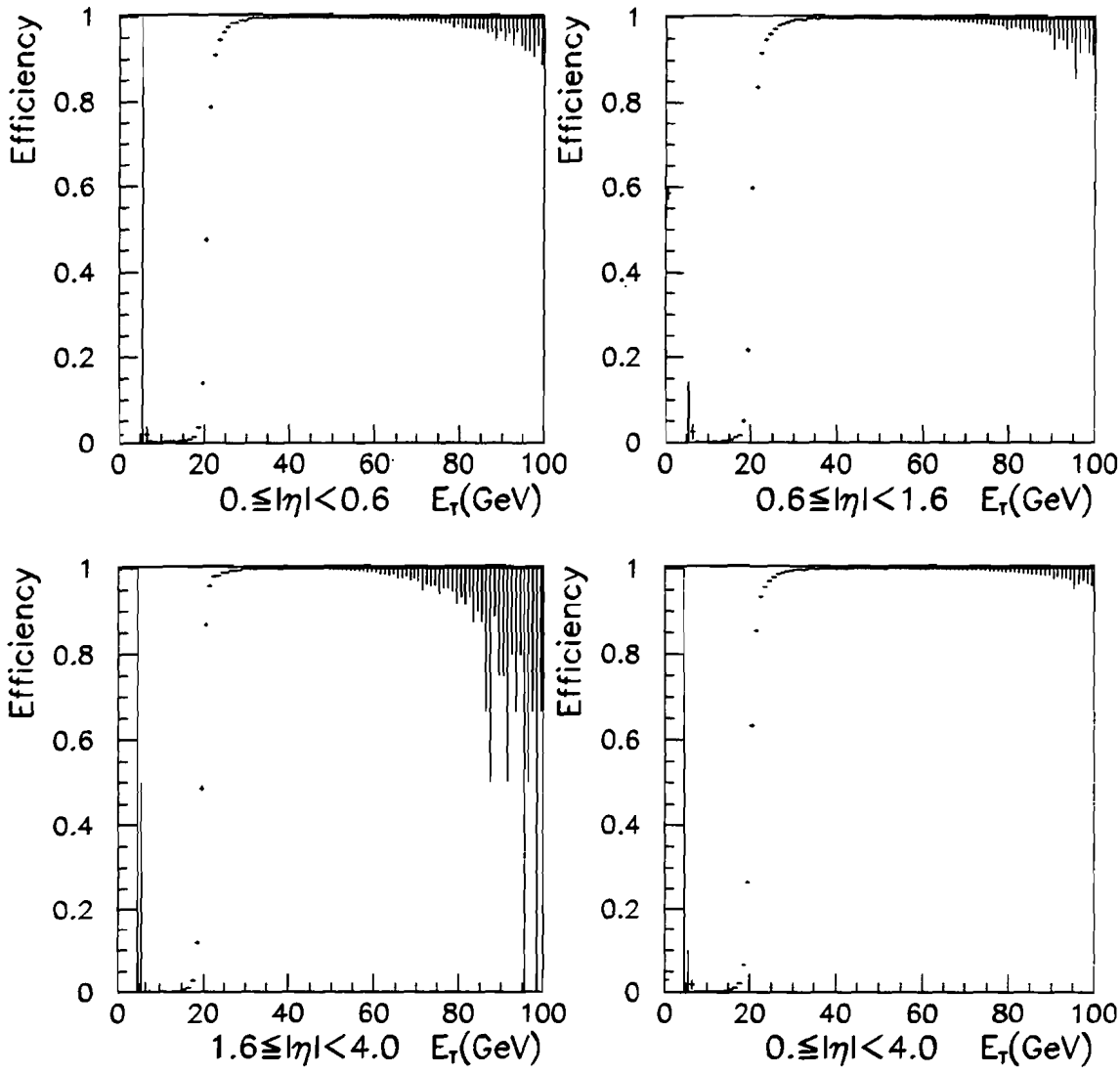

Figure 5.17: L2 single jet trigger efficiencies for JET_MIN in different η regions as a function of uncorrected RECO E_T.

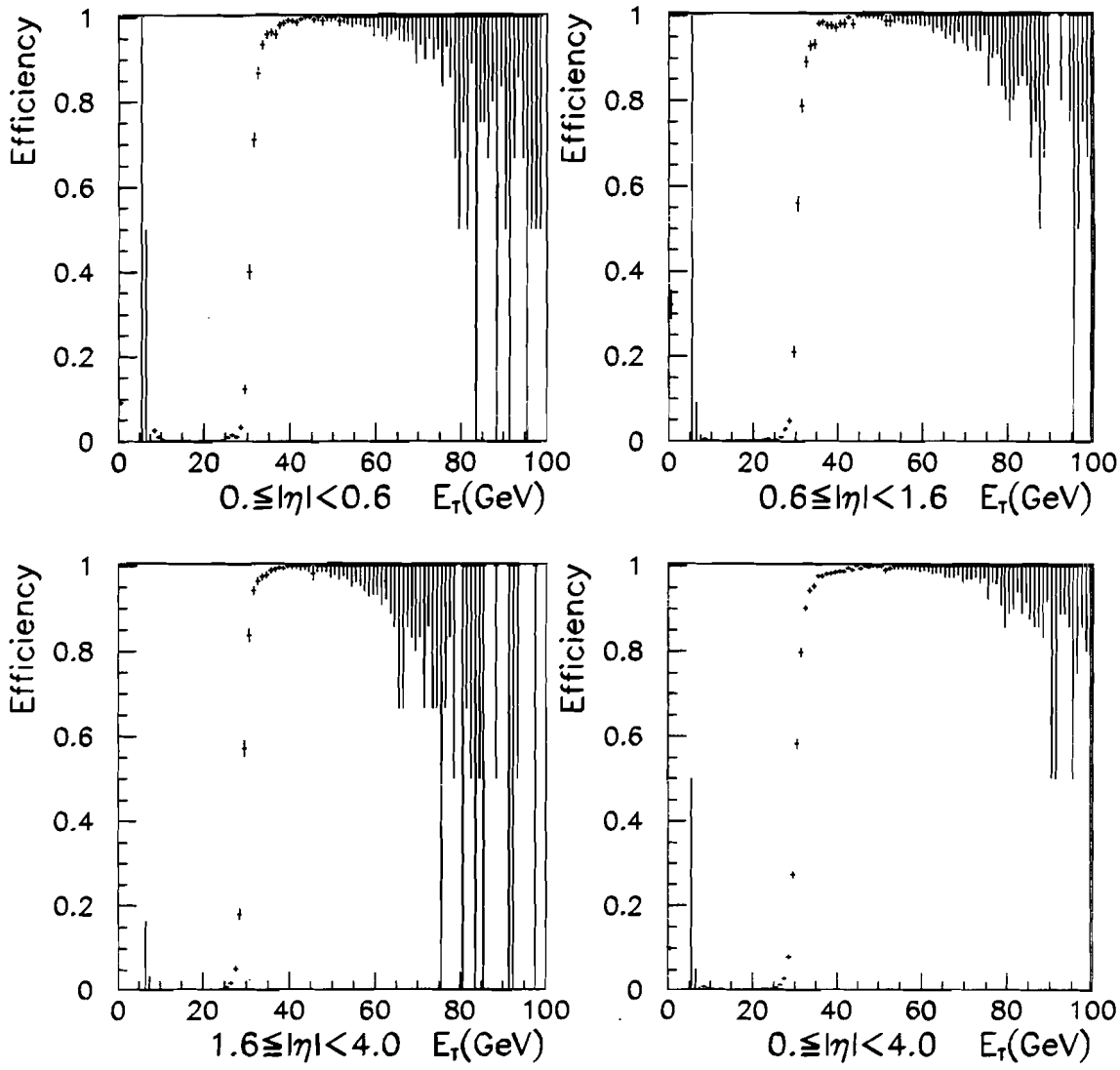

Figure 5.18: L2 single jet trigger efficiencies for JET_LOW in different η regions as a function of uncorrected RECO E_T.

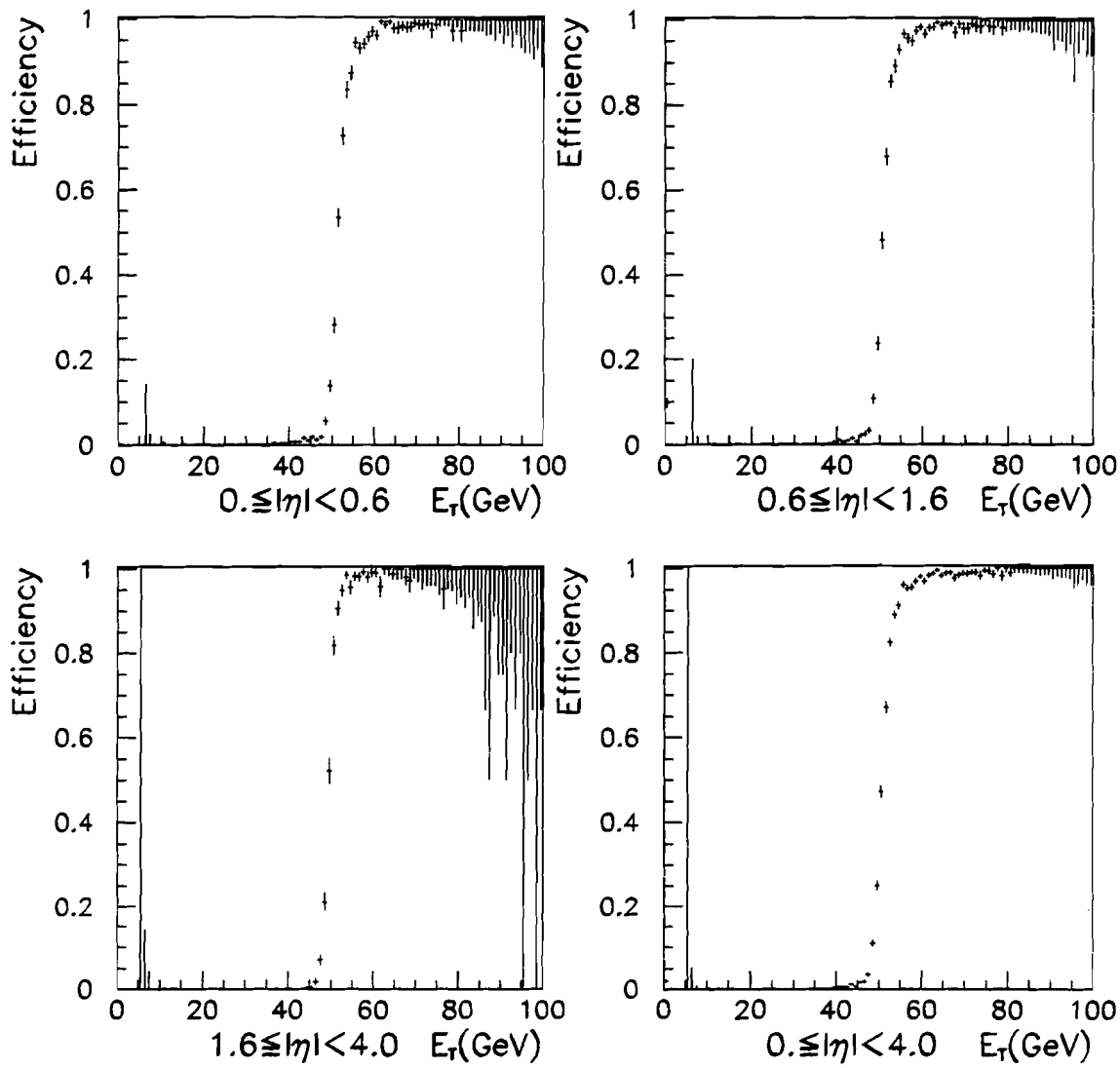

Figure 5.19: L2 single jet trigger efficiencies for JET_MEDIUM in different η regions as a function of uncorrected RECO E_T.

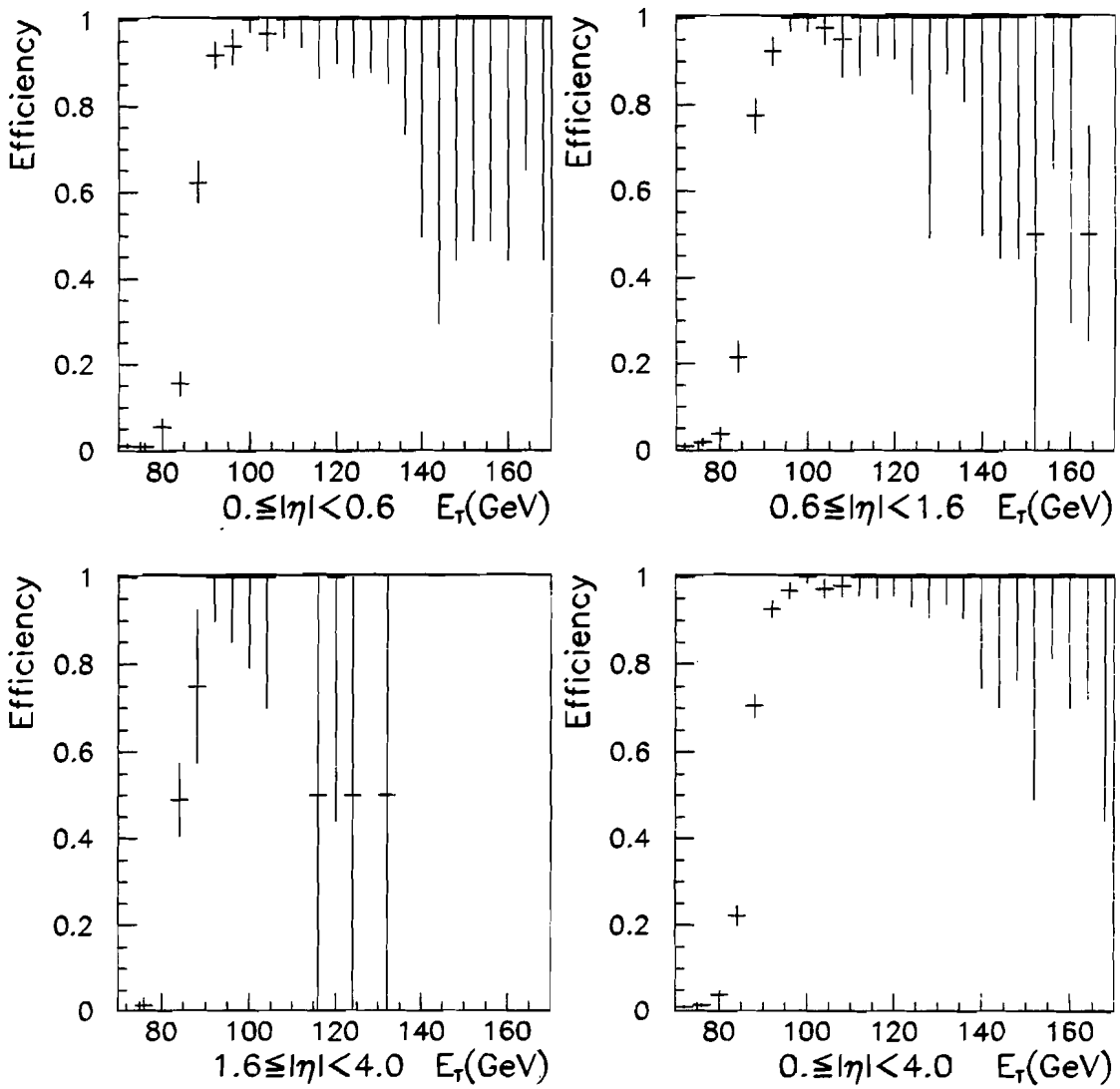

Figure 5.20: L2 single jet trigger efficiencies for JET_HIGH in different η regions as a function of uncorrected RECO E_T.

QCD BIT	$\lvert\eta_{det}\rvert$	A	B	C
JET_MIN	0.0-0.6	0.114	-0.006	-0.003
JET_MIN	0.6-1.6	0.034	0.0003	-0.001
JET_MIN	1.6-4.0	0.204	-0.030	-0.001
JET_LOW	0.0-0.6	0.702	-0.072	-0.001
JET_LOW	0.6-1.6	0.614	-0.078	0.0002
JET_LOW	1.6-4.0	0.634	-0.067	-0.0005
JET_MEDIUM	0.0-0.6	0.151	0.007	-0.0008
JET_MEDIUM	0.6-1.6	0.310	-0.012	-0.0002
JET_MEDIUM	1.6-4.0	0.207	-0.0005	-0.0005
JET_HIGH	0.0-0.6	-0.172	0.0150	-0.0003
JET_HIGH	0.6-1.6	-0.070	0.006	-0.0001
JET_HIGH	1.6-4.0	-0.090	0.008	-0.0002

Table 5.8: L1 trigger turn on parametrizations as a function of uncorrected RECO E_T.

QCD BIT	$\lvert\eta_{det}\rvert$	A	B	C
JET_MIN	0.0-0.6	20.543	-1.407	0.018
JET_MIN	0.6-1.6	20.7	-1.42	0.018
JET_MIN	1.6-4.0	26.1	-1.51	0.007
JET_LOW	0.0-0.6	44.5	-2.28	0.026
JET_LOW	0.6-1.6	44.5	-2.28	0.026
JET_LOW	1.6-4.0	44.5	-2.31	0.026
JET_MEDIUM	0.0-0.6	-4.784	0.450	-0.007
JET_MEDIUM	0.6-1.6	-2.508	0.441	-0.008
JET_MEDIUM	1.6-4.0	5.207	0.423	-0.011
JET_HIGH	0.0-0.6	-78.625	2.052	-0.013
JET_HIGH	0.6-1.6	-78.617	2.050	-0.013
JET_HIGH	1.6-4.0	-78.613	2.046	-0.013

Table 5.9: L2 trigger turn on parametrizations as a function of uncorrected RECO E_T.

Plugging these parameters into equation 5.19, we determine the event efficiencies for the L1 and L2 triggers separately. The overall event trigger efficiency is then determined using equation 5.21. We can check whether the efficiencies determined with this method are correct we showing distributions like the ones in Fig. 5.9. We simply replot the jet E_T distribution for the trigger of interest after applying the corrections due to the trigger inefficiencies. For example, we plotted the E_T distribution of JET_MIN, we then plotted the same distribution for the next more restrictive trigger, which is JET_LOW. The E_T value where the two distributions start to agree is the value for the more restrictive trigger is 100% efficient. We overlaid the E_T distribution for JET_LOW after correcting for trigger efficiencies obtained as described before. Figures 5.21 and 5.22 show these tests for JET_LOW, JET_MEDIUM, and JET_HIGH. We notice that there is agreement when this method indicates nearly 100% efficiency, but we usually are not able to accurately correct for lower efficiencies. We, therefore, have decided to only use events where the event trigger efficiency is at least 95% efficient.

Overall Efficiency

The data was corrected for every event with an overall efficiency defined as follows:

$$\epsilon_{\text{overall}} = \epsilon_{\text{event-cut}} \times \epsilon_{trigger-pass} \tag{5.31}$$

where $\epsilon_{trigger-pass}$ is the jet event trigger efficiency defined in equation 5.21, and $\epsilon_{\text{event-cut}}$ is defined in equation 5.18.

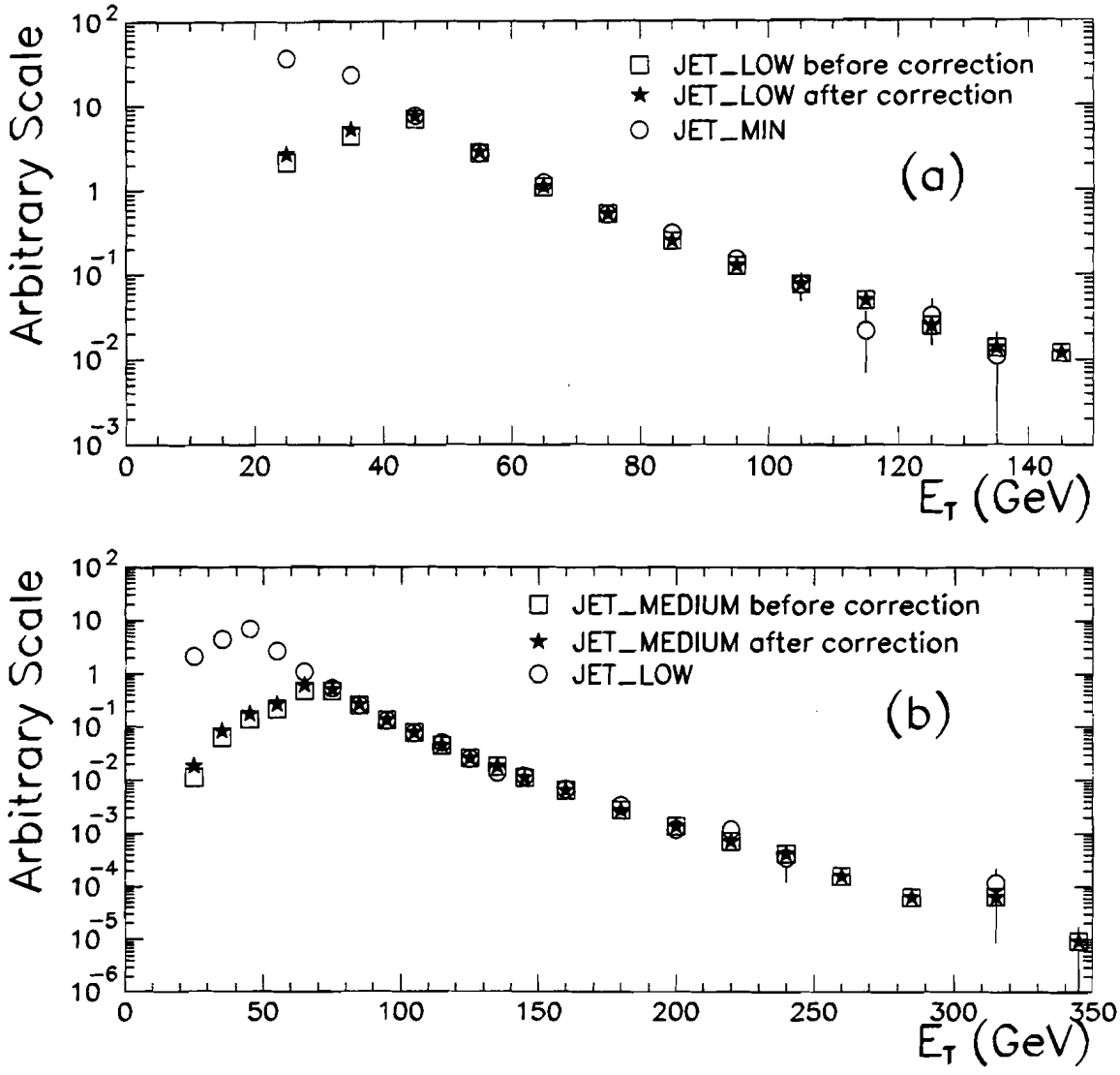

Figure 5.21: Tests of the corrections due to trigger efficiencies for: (a) for JET_LOW, and (b) for JET_MEDIUM.

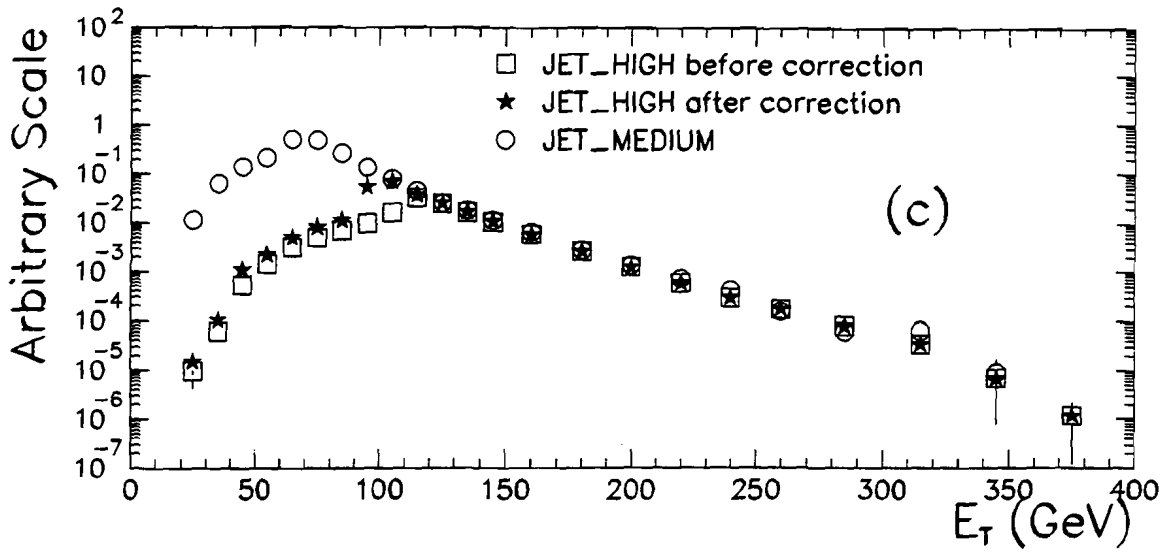

Figure 5.22: Tests of the corrections due to trigger efficiencies for: (c) for JET_HIGH.

CHAPTER 6

Experimental Results

After selecting jets, selecting events and applying the corrections described before, we can calculate the dijet triple differential cross section. This cross section is given by

$$\frac{d^3\sigma}{dE_T d\eta_1 d\eta_2} = \frac{1}{\int \mathcal{L}dt \Delta E_T \Delta\eta_1 \Delta\eta_2} \sum_{i=1}^{N} \frac{1}{\epsilon^i_{\text{event-cut}}\, \epsilon^i_{\text{trigger-pass}}} \tag{6.1}$$

where N is the number of events; $\int \mathcal{L}dt$ is the integrated luminosity; ΔE_T, $\Delta\eta_1$, and $\Delta\eta_2$ are the bin sizes for the E_T of the leading jet, η of the leading jet and η of the second leading jet respectively; $\epsilon^i_{\text{event-cut}}$ is the overall efficiency of several cuts as described in equation 5.18 and $\epsilon^i_{\text{trigger-pass}}$ is the event trigger efficiency as described in equation 5.21.

The triple differential cross section, $d^3\sigma/dE_T d\eta_1 d\eta_2$, needs four dimensions to be represented: one dimension for each of the variables and the fourth dimension for the cross section itself. In order to graphically display the cross section, we integrate one or more variables over a specific range. We first show a two-dimensional distribution where we have integrated over the transverse energy of the leading jet. This is referred to as the "lego" plot. We then show one-dimensional distributions of the cross section after having integrated over two of the three variables. They will be referred to as the "E_T" and the "signed-η" distributions. These distributions are shown without having removed the effects from the detector due to jet energy resolution. After explaining how we remove the detector effects from the data, we show the corrected cross sections.

6.1 Two-Dimensional Cross Sections

We first show the cross sections where we have integrated over a range of the transverse energy of the leading jet. We have done so for three E_T ranges: $45 \leq E_T < 55$ GeV, $55 \leq E_T < 65$ GeV, and $95 \leq E_T < 105$ GeV. Figures 6.1-6.3 show the cross sections as a function of η_1 and η_2, where η_1 and η_2 are the pseudorapidities of the highest and second highest E_T jets, respectively.

One of the first things we notice from these cross sections is that they fall rapidly at large pseudorapidities, as expected from kinematics constraints: a forward jet with a particular E_T value is more energetic than a central jet with a similar E_T value. It can also be seen that the events with $95 \leq E_T < 105$ GeV are concentrated at small η values while those with $45 \leq E_T < 55$ GeV populate a larger η region.

All the information available from two jet events are contained in these plots. In particular, at leading order (LO), η_1 and η_2 are directly related to the parton momentum fractions x_1, x_2 through:

$$x_1 = \frac{E_T}{\sqrt{s}}(\exp(\eta_1) + \exp(\eta_2)) \tag{6.2}$$

$$x_2 = \frac{E_T}{\sqrt{s}}(\exp(-\eta_1) + \exp(-\eta_2)) \tag{6.3}$$

where E_{Ti} and η_i (i =1,2) represent the transverse energies and pseudorapidities of the two partons ordered in decreasing E_T. Consequently, a measurement of the triple differential cross section $d^3\sigma/dE_T d\eta_1 d\eta_2$ is effectively a measurement of $d^2\sigma/dx_1 dx_2$. Table 6.1 shows the corresponding x values for different η_1, η_2 when held at a fixed E_T. Values were calculated using the formula shown above.

As can be seen from Table 6.1, for fixed values of η_1 and η_2, an increase in E_T translates into an increase in x_1 and x_2. Events where $\eta_1 = -\eta_2$ corresponds to events with jets in opposite η hemispheres and x_1 is always equal to x_2 ("back-to-back" or "opposite side" events). Events where $\eta_1 = \eta_2$ corresponds to the topology of a high-x with a low-x ("same side" events). This is more noticeable for large values of η. Finally, events with a particular η combination may not be allowed for high E_T values, as seen in the last entry of the table, because at LO the topology is kinematically forbidden.

A more subtle detail is the rather sharp cutoff of the cross sections for η_1 but not for η_2. The excess of events at large η_2 is a consequence of a relaxation of the

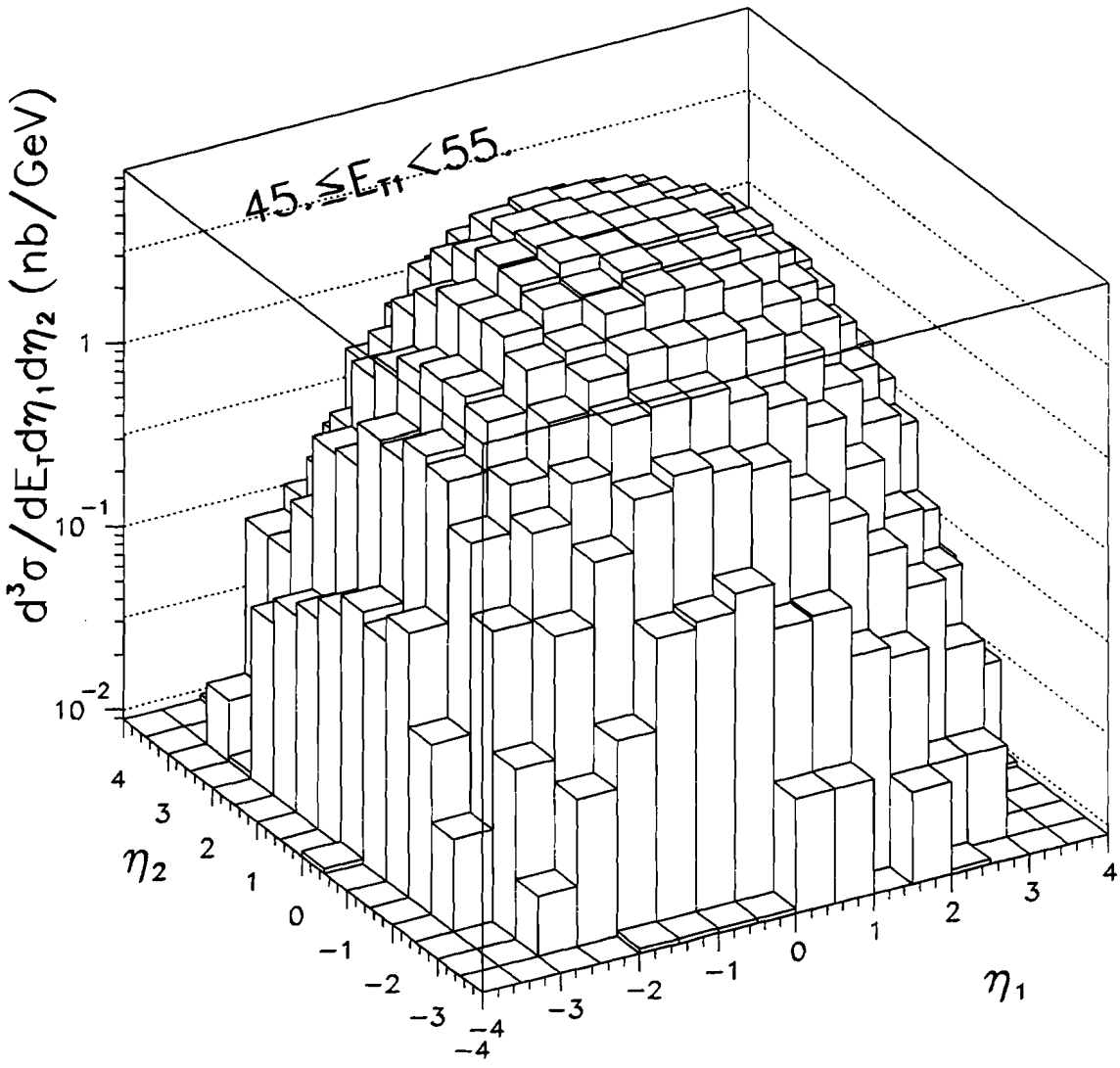

Figure 6.1: The inclusive triple differential dijet cross section, $d^3\sigma/dE_T d\eta_1 d\eta_2$, vs. η_1 and η_2 for $45 \leq E_{T1} < 55$ GeV.

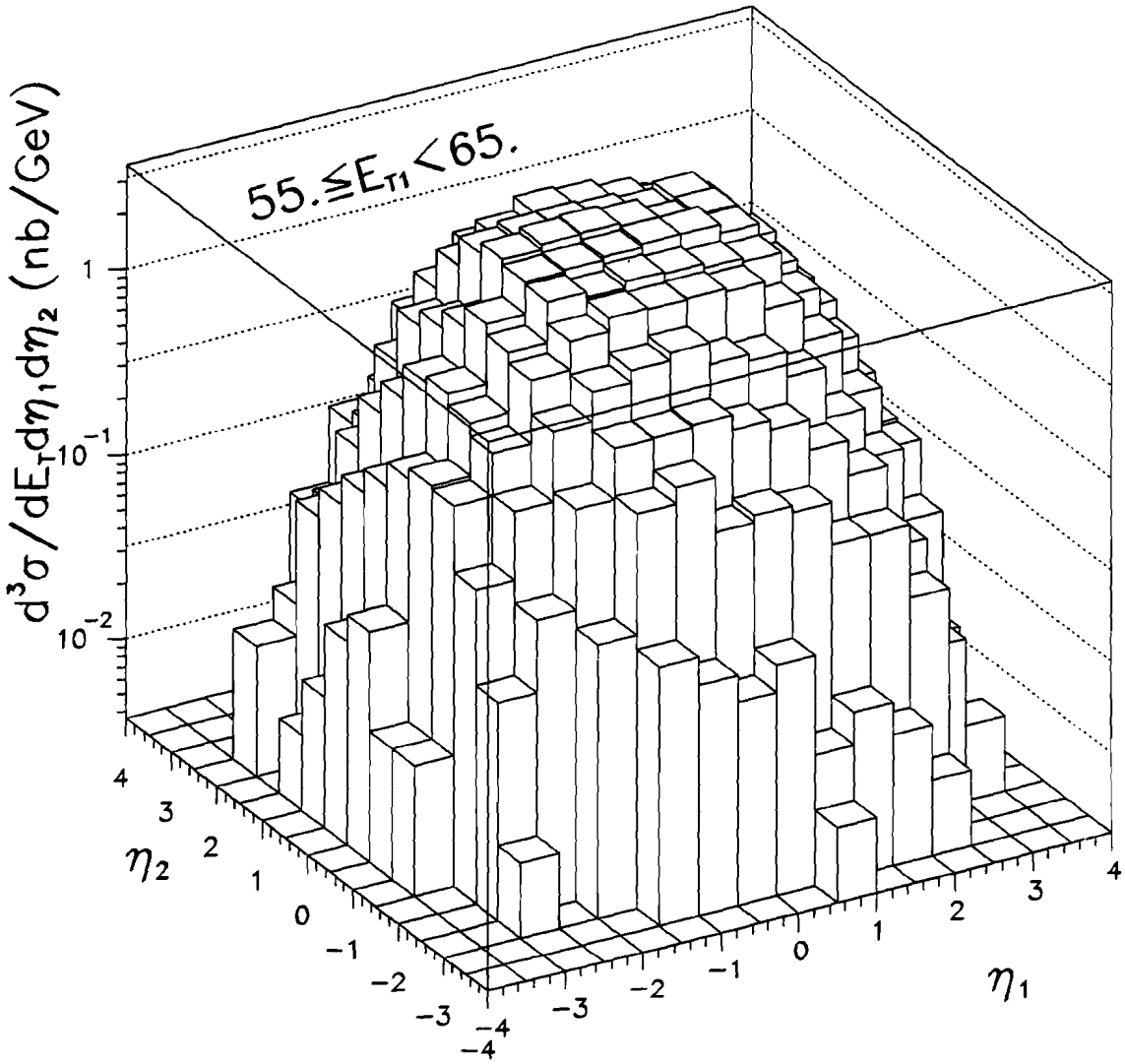

Figure 6.2: The inclusive triple differential dijet cross section, $d^3\sigma/dE_T d\eta_1 d\eta_2$, vs. η_1 and η_2 for $55 \leq E_{T1} < 65$ GeV.

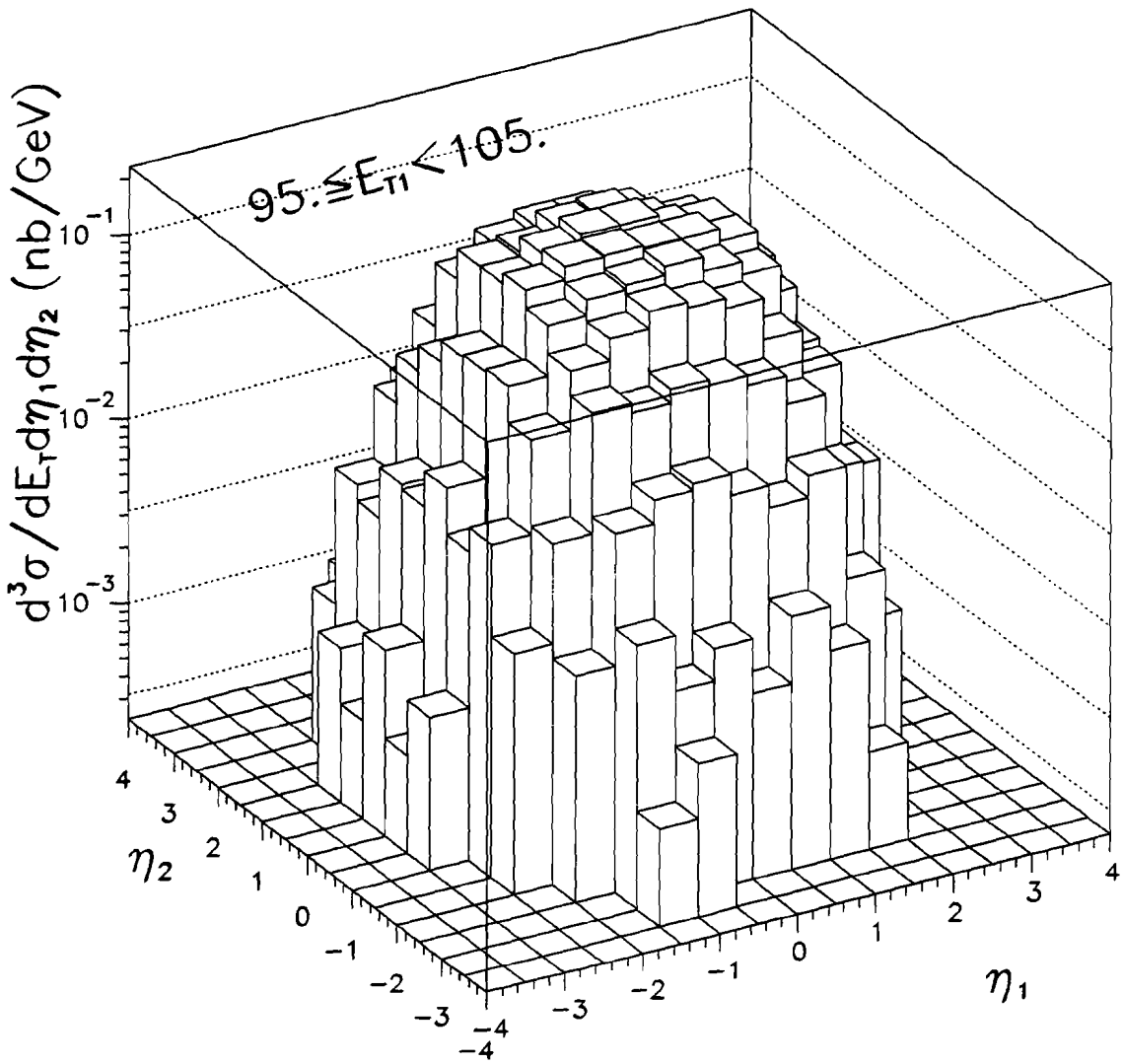

Figure 6.3: The inclusive triple differential dijet cross section, $d^3\sigma/dE_T d\eta_1 d\eta_2$, vs. η_1 and η_2 for $95 \leq E_{T1} < 105$ GeV.

E_{T1} (GeV)	η_1	η_2	x_1	x_2
50	0.0	0.0	0.056	0.056
50	0.0	2.5	0.366	0.030
50	1.0	1.0	0.151	0.020
50	-2.5	2.5	0.341	0.341
50	2.5	2.5	0.677	0.004
60	0.0	0.0	0.067	0.067
60	0.0	2.5	0.439	0.036
60	1.0	1.0	0.181	0.024
60	-2.5	2.5	0.409	0.409
60	2.5	2.5	0.812	0.005
100	0.0	0.0	0.111	0.111
100	0.0	2.5	0.732	0.060
100	1.0	1.0	0.302	0.041
100	-2.5	2.5	0.681	0.681
100	2.5	2.5	not allowed	not allowed

Table 6.1: Parton momentum fractions, x_1 and x_2, for various transverse energies and outgoing parton pseudorapidities.

kinematic constraints only possible at NLO [51]. At NLO, the equation relating momentum fractions to pseudorapidities and transverse energies is:

$$x_{1,2} = \frac{E_{T1}}{\sqrt{s}}[\exp(\pm\eta_1) + \frac{E_{T2}}{E_{T1}}\exp(\pm\eta_2) + \frac{E_{T3}}{E_{T1}}\exp(\pm\eta_3)] \tag{6.4}$$

where again E_{Ti} and η_i (i =1,2,3) represent the transverse energies and pseudorapidities of the three partons ordered in decreasing E_T. The LO case is given when $E_{T2} = E_{T1}$, but for NLO, the ratio $\frac{E_{T2}}{E_{T1}}$ decreases enabling $\exp(\pm\eta_2)$ to increase, allowing for more phase space in the pseudorapidity of the second jet.

Since it is difficult to make quantitative comparisons of three-dimensional distributions, it is more useful to integrate over two variables and reduce the cross sections to two-dimensional distributions.

6.2 E_T Distributions

One choice is to integrate over the pseudorapidity variables and plot the cross section as a function of the transverse energy of the leading jet. A comparison with theoretical predictions is in essence a test of QCD. Furthermore, since NLO predicts more cross section than LO in the high η regions, a comparison with the data will indicate whether the data favors NLO or LO. We select those events where the leading jet is central ($0.0 \leq |\eta_1| < 1.0$), and show the E_T spectrum of the leading jet when the second highest E_T jet is also central ($0.0 \leq |\eta_2| < 1.0$). We also show the E_T spectrum of the leading jet when the second highest E_T jet is in other η regions: $1.0 \leq |\eta_2| < 2.0$, $2.0 \leq |\eta_2| < 3.0$, and $3.0 \leq |\eta_2| < 4.0$. We have only studied events where the leading jet is in the region $0.0 \leq |\eta_1| < 1.0$ because this region has the highest statistics and the central region of the detector is the best understood area.

Figure 6.4 shows the E_T distributions for the different η_2 conditions. The inner error bars are statistical and the outer error bars are statistical added in quadrature with the systematic errors. The dominant systematic error is due to the jet energy scale correction and it is obtained as follows. There are three choices when applying the jet energy scale correction: the NOMINAL choice using the nominal correction value, the HIGH choice using the nominal plus the one-sigma error value, and the LOW choice using the nominal minus the one-sigma error value. We generated three cross sections corresponding to each choice and took the systematic error to be half

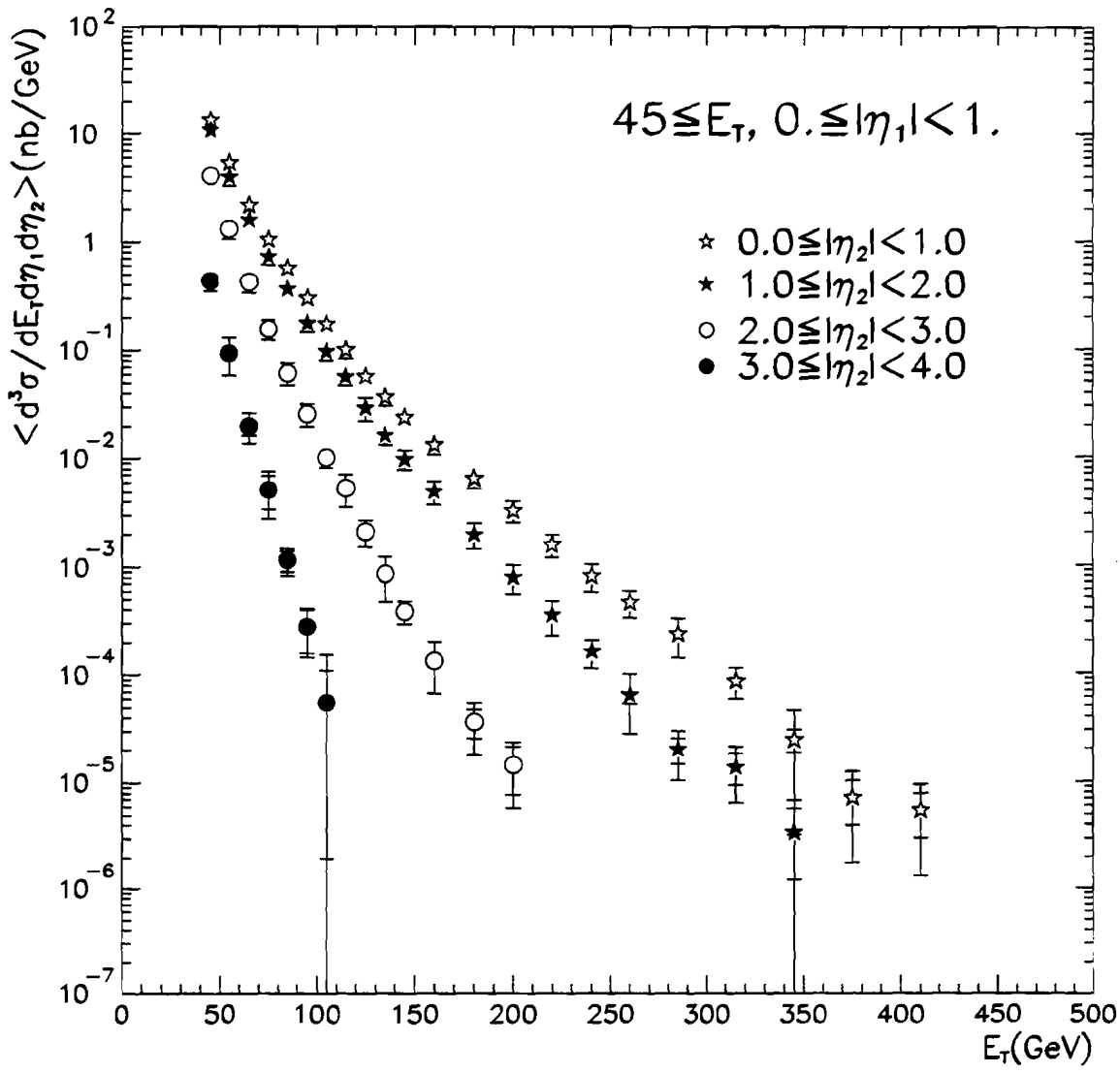

Figure 6.4: The inclusive triple differential dijet cross section, $d^3\sigma/dE_T d\eta_1 d\eta_2$, as a function the leading jet E_T. The 5.4% uncertainty due to luminosity has not been included.

the difference in cross section for the HIGH and LOW scales for a given E_T:

$$\epsilon_{sys} = \frac{\sigma_{HIGH} - \sigma_{LOW}}{2} \tag{6.5}$$

where ϵ_{sys} was assigned as the systematic error due to the jet energy scale uncertainty. There is an additional 5.4% normalization error due to the luminosity uncertainty that was not included. The E_T distributions are also shown in tabular form in Tables 6.2-6.5.

E_T (GeV)	Cross Section (nb/GeV)	Statistical Error (nb/GeV)	Systematic Error (nb/GeV)
40.- 50.	13.44	0.09	1.55
50.- 60.	5.39	0.06	0.87
60.- 70.	2.17	0.04	0.36
70.- 80.	1.05	0.03	0.17
80.- 90.	0.57	0.01	0.08
90.- 100.	0.30	0.39E-02	0.05
100.- 110.	0.17	0.30E-02	0.03
110.- 120.	0.10	0.23E-02	0.02
120.- 130.	0.06	0.17E-02	0.01
130.- 140.	0.04	0.49E-03	0.62E-02
140.- 150.	0.02	0.39E-03	0.38E-02
150.- 170.	0.01	0.21E-03	0.25E-02
170.- 190.	0.64E-02	0.12E-03	0.12E-02
190.- 210.	0.32E-02	0.83E-04	0.72E-03
210.- 230.	0.16E-02	0.58E-04	0.36E-03
230.- 250.	0.80E-03	0.41E-04	0.23E-03
250.- 270.	0.45E-03	0.31E-04	0.12E-03
270.- 300.	0.23E-03	0.18E-04	0.90E-04
300.- 330.	0.85E-04	0.11E-04	0.24E-04
330.- 360.	0.24E-04	0.59E-05	0.20E-04
360.- 390.	0.71E-05	0.32E-05	0.43E-05
390.- 430.	0.54E-05	0.24E-05	0.33E-05

Table 6.2: Jet cross section, $d^3\sigma/dE_T d\eta_1 d\eta_2$, as a function of the central jet E_T when the second jet is in the region $0.0 \leq |\eta| < 1.0$.

E_T (GeV)	Cross Section (nb/GeV)	Statistical Error (nb/GeV)	Systematic Error (nb/GeV)
40.- 50.	10.77	0.08	1.01
50.- 60.	3.96	0.05	0.68
60.- 70.	1.60	0.03	0.21
70.- 80.	0.73	0.02	0.12
80.- 90.	0.37	0.43E-02	0.57E-01
90.- 100.	0.18	0.30E-02	0.31E-01
100.- 110.	0.10	0.22E-02	0.17E-01
110.- 120.	0.06	0.17E-02	0.96E-02
120.- 130.	0.03	0.12E-02	0.68E-02
130.- 140.	0.02	0.33E-03	0.31E-02
140.- 150.	0.10	0.25E-03	0.20E-02
150.- 170.	0.49E-02	0.13E-03	0.11E-02
170.- 190.	0.20E-02	0.64E-04	0.52E-03
190.- 210.	0.79E-03	0.41E-04	0.23E-03
210.- 230.	0.35E-03	0.27E-04	0.12E-03
230.- 250.	0.16E-03	0.18E-04	0.43E-04
250.- 270.	0.64E-04	0.12E-04	0.34E-04
270.- 300.	0.20E-04	0.53E-05	0.80E-05
300.- 330.	0.14E-04	0.44E-05	0.59E-05
330.- 360.	0.34E-05	0.22E-05	0.26E-05

Table 6.3: Jet cross section, $d^3\sigma/dE_T d\eta_1 d\eta_2$, as a function of the central jet E_T when the second jet is in the region $1.0 \leq |\eta| < 2.0$.

E_T (GeV)	Cross Section (nb/GeV)	Statistical Error (nb/GeV)	Systematic Error (nb/GeV)
40.- 50.	4.09	0.05	0.52
50.- 60.	1.31	0.03	0.25
60.- 70.	0.42	0.02	0.08
70.- 80.	0.16	0.01	0.03
80.- 90.	0.06	0.18E-02	0.14E-01
90.- 100.	0.03	0.11E-02	0.59E-02
100.- 110.	0.01	0.72E-03	0.18E-02
110.- 120.	0.53E-02	0.52E-03	0.17E-02
120.- 130.	0.21E-02	0.33E-03	0.47E-03
130.- 140.	0.85E-03	0.74E-04	0.37E-03
140.- 150.	0.38E-03	0.50E-04	0.78E-04
150.- 170.	0.13E-03	0.21E-04	0.62E-04
170.- 190.	0.36E-04	0.11E-04	0.14E-04
190.- 210.	0.14E-04	0.69E-05	0.54E-05

Table 6.4: Jet cross section, $d^3\sigma/dE_T d\eta_1 d\eta_2$, as a function of the central jet E_T when the second jet is in the region $2.0 \leq |\eta| < 3.0$.

E_T (GeV)	Cross Section (nb/GeV)	Statistical Error (nb/GeV)	Systematic Error (nb/GeV)
40.- 50.	0.43	0.02	0.08
50.- 60.	0.09	0.01	0.03
60.- 70.	0.02	0.34E-02	0.51E-02
70.- 80.	0.01	0.17E-02	0.16E-02
80.- 90.	0.11E-02	0.24E-03	0.22E-03
90.- 100.	0.27E-03	0.12E-03	0.55E-04
100.- 110.	0.55E-04	0.53E-04	0.82E-04

Table 6.5: Jet cross section, $d^3\sigma/dE_T d\eta_1 d\eta_2$, as a function of the central jet E_T when the second jet is in the region $3.0 \leq |\eta| < 4.0$.

6.3 Signed-η Distributions

A different way of plotting two-dimensional distributions is by integrating over the E_T and η of the leading jet. We then show the cross section as a function of $\eta_2 \times Sign(\eta_1)$. The purpose of using this variable is that events where both jets are in the same η hemisphere ("Same Side") appear on the positive abscissa while events where the jets are in different η hemispheres ("Opposite Side") appear on the negative abscissa. As can be seen from Table 6.1, events with Opposite Side jets have similar x-values and those with Same Side jets probe a high x-value combined with a low x-value.

To maximize statistics, we take the first lego plot where $45 \leq E_T < 55$ GeV and plot the cross section for different ranges of η_1: from $|\eta_1| = 0.0$ to $|\eta_1| = 3.0$ in increments of half-units of η. Figures 6.5-6.10 show the signed cross sections as a function of $\eta_2 \times sign(\eta_1)$. Each plot corresponds to a different choice of the leading jet η: $0.0 \leq |\eta_1| < 0.5$, $0.5 \leq |\eta_1| < 1.0$, $1.0 \leq |\eta_1| < 1.5$, $1.5 \leq |\eta_1| < 2.0$, $2.0 \leq |\eta_1| < 2.5$, and $2.5 \leq |\eta_1| < 3.0$. Once again, the inner error bars are statistical and the outer error bars are statistical added in quadrature with the systematic error, where the systematic error is given by the jet energy scale uncertainty obtained as before. The 5.4% error due to the luminosity uncertainty was not included. The cross sections are also shown in tabular form in Tables 6.6-6.11.

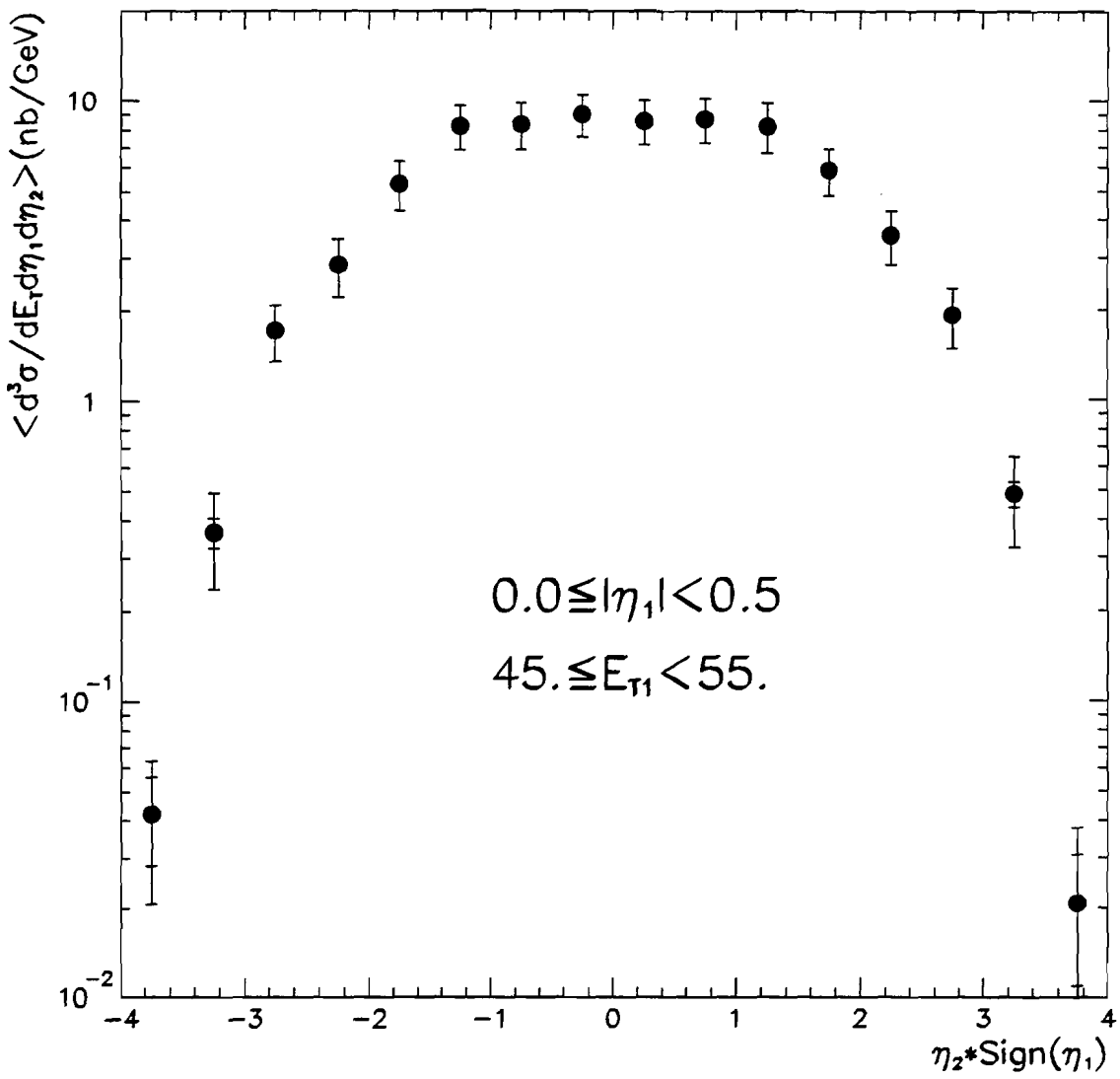

Figure 6.5: The uncorrected inclusive triple differential dijet cross section, $d^3\sigma/dE_T d\eta_1 d\eta_2$ vs. $\eta_2 \times sign(\eta_1)$ for $0.0 \leq |\eta_1| < 0.5$. The 5.4% uncertainty due to luminosity has not been included.

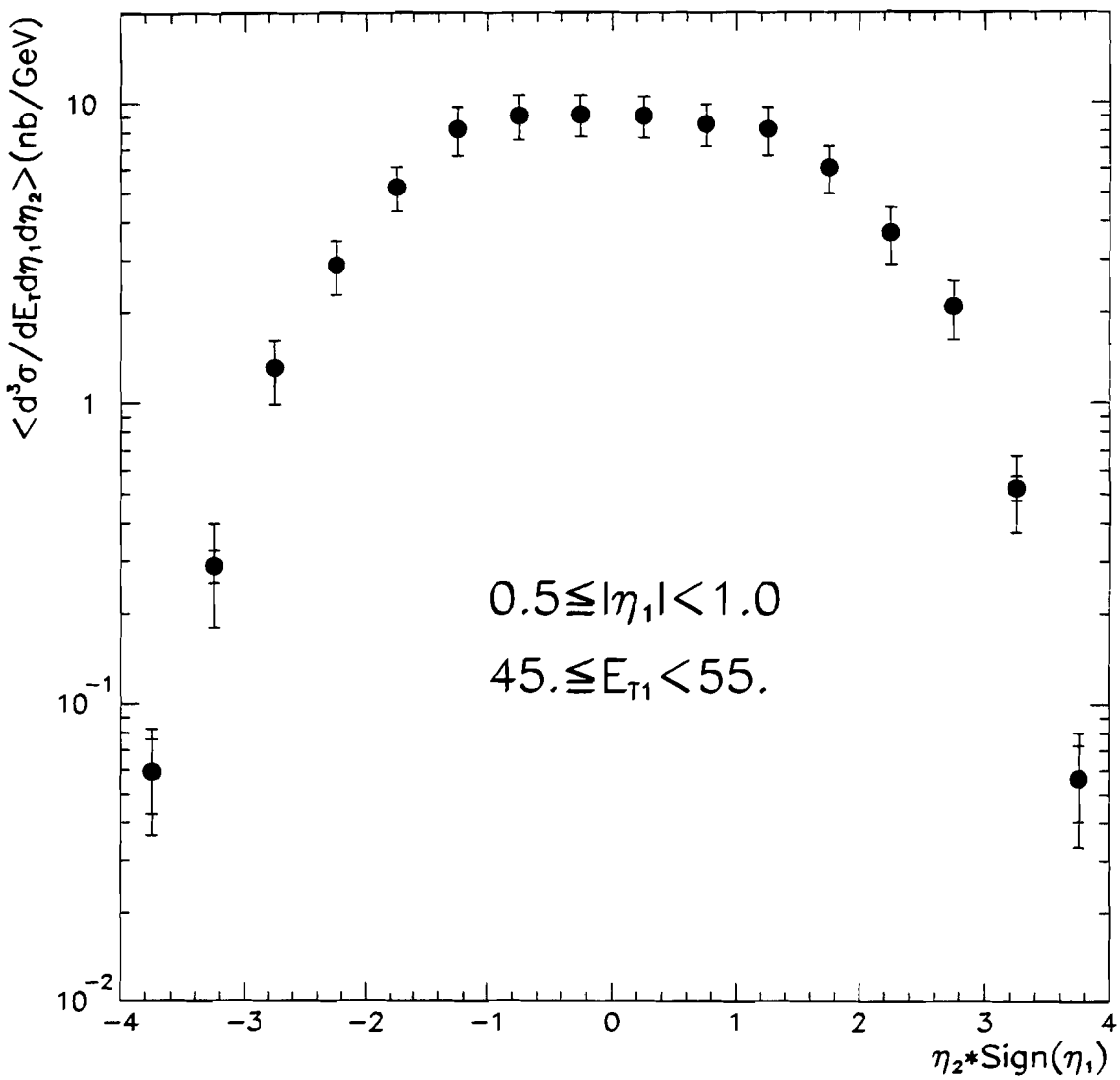

Figure 6.6: The uncorrected inclusive triple differential dijet cross section, $d^3\sigma/dE_T d\eta_1 d\eta_2$ vs. $\eta_2 \times sign(\eta_1)$ for $0.5 \leq |\eta_1| < 1.0$. The 5.4% uncertainty due to luminosity has not been included.

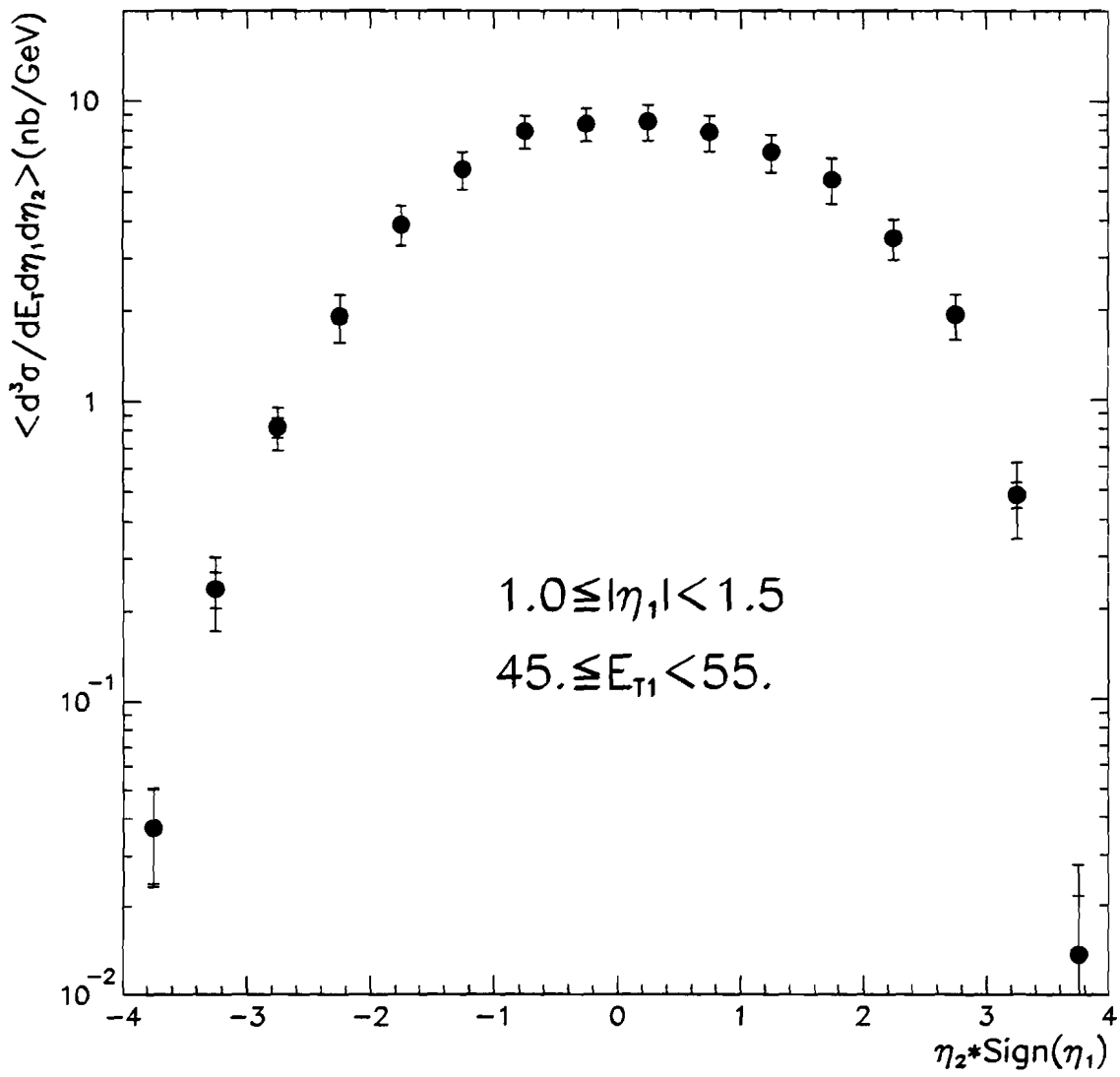

Figure 6.7: The uncorrected inclusive triple differential dijet cross section, $d^3\sigma/dE_T d\eta_1 d\eta_2$ vs. $\eta_2 \times sign(\eta_1)$ for $1.0 \leq |\eta_1| < 1.5$. The 5.4% uncertainty due to luminosity has not been included.

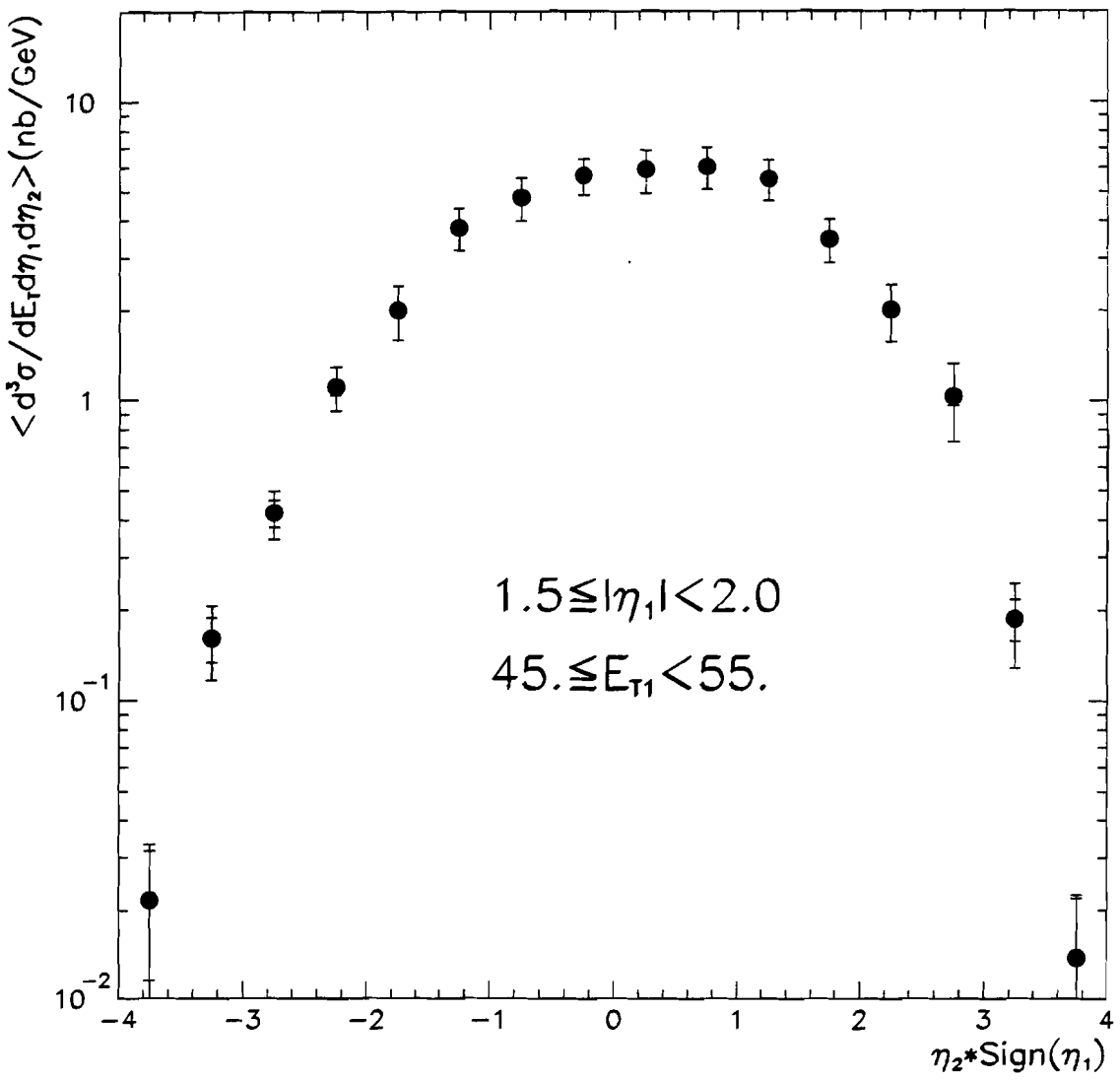

Figure 6.8: The uncorrected inclusive triple differential dijet cross section, $d^3\sigma/dE_T d\eta_1 d\eta_2$ vs. $\eta_2 \times sign(\eta_1)$ for $1.5 \leq |\eta_1| < 2.0$. The 5.4% uncertainty due to luminosity has not been included.

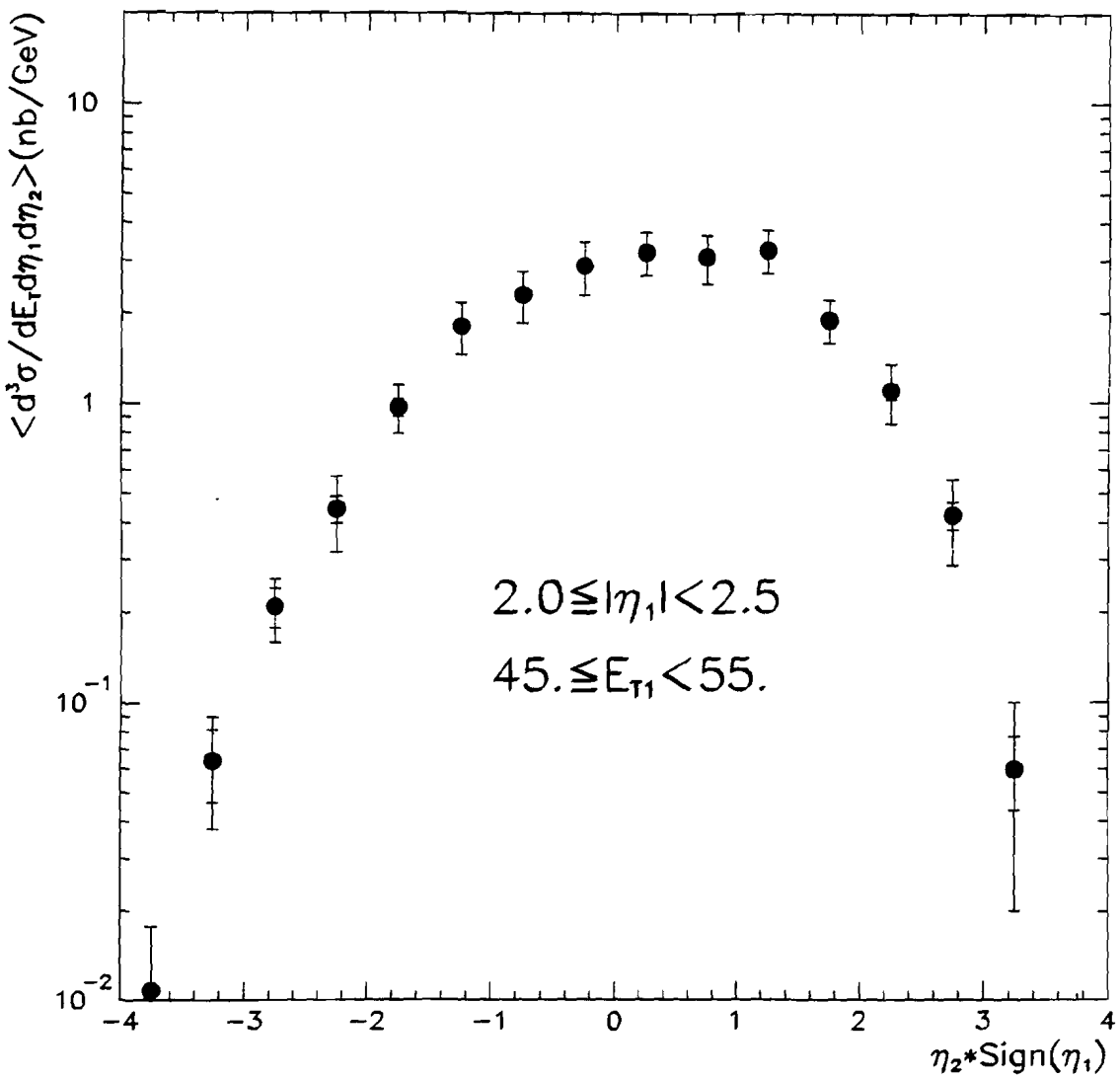

Figure 6.9: The uncorrected inclusive triple differential dijet cross section, $d^3\sigma/dE_T d\eta_1 d\eta_2$ vs. $\eta_2 \times sign(\eta_1)$ for $2.0 \leq |\eta_1| < 2.5$. The 5.4% uncertainty due to luminosity has not been included.

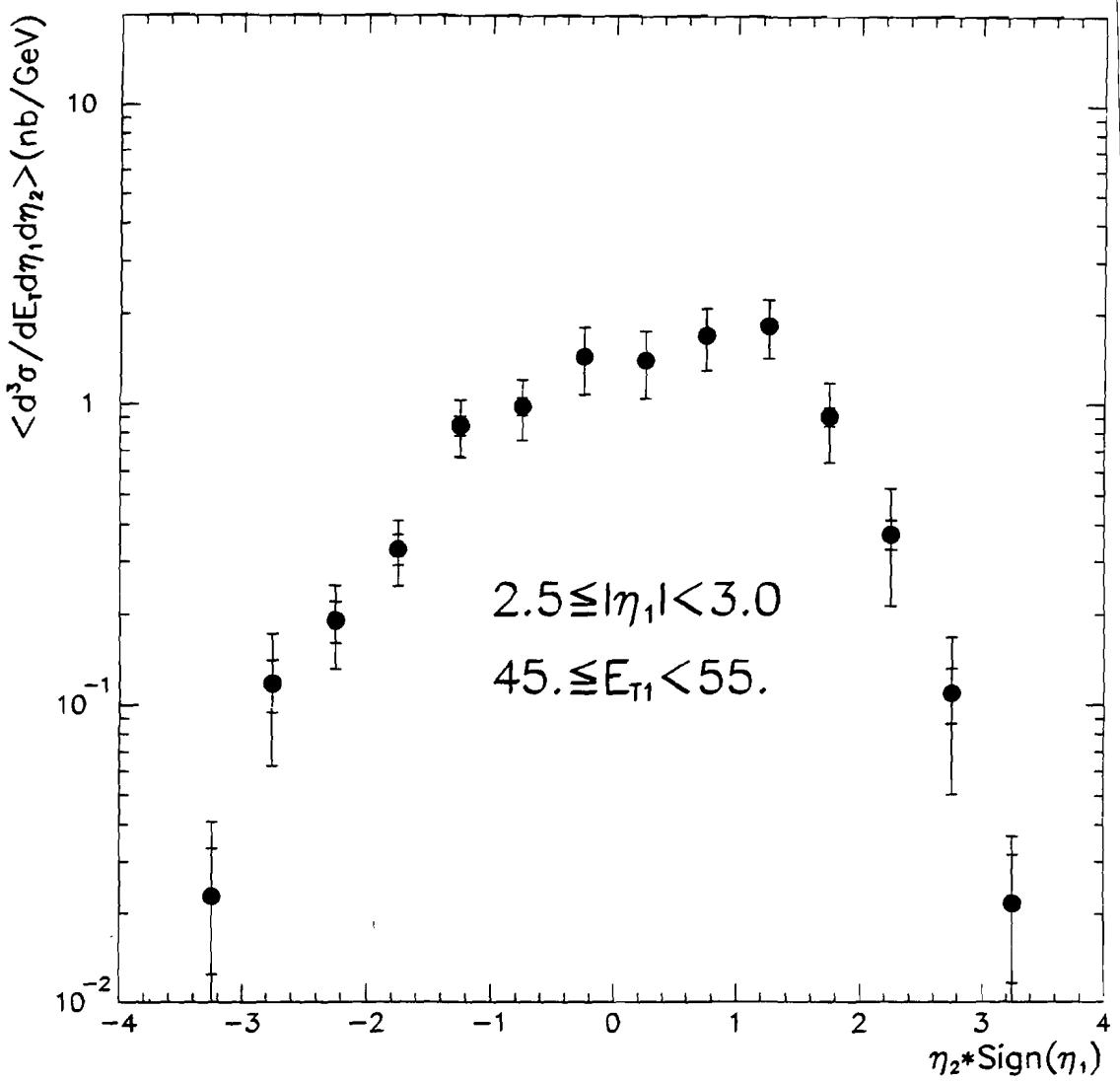

Figure 6.10: The uncorrected inclusive triple differential dijet cross section, $d^3\sigma/dE_T d\eta_1 d\eta_2$ vs. $\eta_2 \times sign(\eta_1)$ for $2.5 \leq |\eta_1| < 3.0$. The 5.4% uncertainty due to luminosity has not been included.

$\eta_2 \times sign(\eta_1)$	Cross Section (nb/GeV)	Statistical Error (nb/GeV)	Systematic Error (nb/GeV)
-3.75	0.04	0.01	0.02
-3.25	0.37	0.04	0.13
-2.75	1.72	0.09	0.37
-2.25	2.85	0.12	0.62
-1.75	5.30	0.16	0.99
-1.25	8.27	0.20	1.34
-0.75	8.36	0.20	1.45
-0.25	9.03	0.20	1.42
0.25	8.57	0.20	1.40
0.75	8.69	0.20	1.45
1.25	8.24	0.20	1.56
1.75	5.87	0.17	1.06
2.25	3.54	0.13	0.72
2.75	1.92	0.09	0.44
3.25	0.48	0.05	0.16
3.75	0.02	0.01	0.02

Table 6.6: Jet cross section, $d^3\sigma/dE_T d\eta_1 d\eta_2$, as a function of $\eta_2 \times sign(\eta_1)$ for $0.0 \leq |\eta_1| < 0.5$.

$\eta_2 \times sign(\eta_1)$	Cross Section (nb/GeV)	Statistical Error (nb/GeV)	Systematic Error (nb/GeV)
-3.75	0.06	0.02	0.02
-3.25	0.29	0.04	0.11
-2.75	1.30	0.08	0.31
-2.25	2.87	0.12	0.58
-1.75	5.23	0.16	0.90
-1.25	8.15	0.19	1.51
-0.75	9.05	0.21	1.54
-0.25	9.15	0.21	1.41
0.25	9.10	0.21	1.43
0.75	8.48	0.20	1.35
1.25	8.15	0.19	1.51
1.75	6.05	0.17	1.08
2.25	3.68	0.13	0.78
2.75	2.09	0.10	0.46
3.25	0.52	0.05	0.15
3.75	0.06	0.02	0.02

Table 6.7: Jet cross section, $d^3\sigma/dE_T d\eta_1 d\eta_2$, as a function of $\eta_2 \times sign(\eta_1)$ for $0.5 \leq |\eta_1| < 1.0$.

$\eta_2 \times sign(\eta_1)$	Cross Section (nb/GeV)	Statistical Error (nb/GeV)	Systematic Error (nb/GeV)
-3.75	0.04	0.01	0.01
-3.25	0.24	0.03	0.07
-2.75	0.82	0.06	0.13
-2.25	1.91	0.09	0.35
-1.75	3.87	0.13	0.58
-1.25	5.90	0.17	0.82
-0.75	7.92	0.19	1.04
-0.25	8.36	0.20	1.09
0.25	8.52	0.20	1.18
0.75	7.81	0.19	1.05
1.25	6.74	0.18	0.96
1.75	5.46	0.16	0.95
2.25	3.48	0.13	0.54
2.75	1.93	0.09	0.33
3.25	0.48	0.05	0.14
3.75	0.01	0.01	0.01

Table 6.8: Jet cross section, $d^3\sigma/dE_T d\eta_1 d\eta_2$, as a function of $\eta_2 \times sign(\eta_1)$ for $1.0 \leq |\eta_1| < 1.5$.

$\eta_2 \times sign(\eta_1)$	Cross Section (nb/GeV)	Statistical Error (nb/GeV)	Systematic Error (nb/GeV)
-3.75	0.02	0.01	0.01
-3.25	0.16	0.03	0.04
-2.75	0.42	0.04	0.08
-2.25	1.11	0.07	0.19
-1.75	2.00	0.10	0.41
-1.25	3.78	0.13	0.60
-0.75	4.77	0.15	0.78
-0.25	5.65	0.16	0.78
0.25	5.92	0.17	0.99
0.75	6.06	0.17	0.98
1.25	5.53	0.16	0.87
1.75	3.47	0.13	0.58
2.25	2.01	0.10	0.43
2.75	1.03	0.07	0.30
3.25	0.19	0.03	0.06
3.75	0.01	0.01	0.01

Table 6.9: Jet cross section, $d^3\sigma/dE_T d\eta_1 d\eta_2$, as a function of $\eta_2 \times sign(\eta_1)$ for $1.5 \leq |\eta_1| < 2.0$.

$\eta_2 \times sign(\eta_1)$	Cross Section (nb/GeV)	Statistical Error (nb/GeV)	Systematic Error (nb/GeV)
-3.75	0.01	0.01	0.01
-3.25	0.06	0.02	0.03
-2.75	0.21	0.03	0.05
-2.25	0.44	0.05	0.13
-1.75	0.97	0.07	0.18
-1.25	1.80	0.09	0.35
-0.75	2.30	0.10	0.45
-0.25	2.87	0.12	0.58
0.25	3.18	0.12	0.52
0.75	3.07	0.12	0.56
1.25	3.25	0.12	0.53
1.75	1.90	0.09	0.31
2.25	1.10	0.07	0.24
2.75	0.42	0.04	0.13
3.25	0.06	0.02	0.04
3.75	0.01	0.01	0.01

Table 6.10: Jet cross section, $d^3\sigma/dE_T d\eta_1 d\eta_2$, as a function of $\eta_2 \times sign(\eta_1)$ for $2.0 \leq |\eta_1| < 2.5$.

$\eta_2 \times sign(\eta_1)$	Cross Section (nb/GeV)	Statistical Error (nb/GeV)	Systematic Error (nb/GeV)
-3.75	0.01	0.01	0.01
-3.25	0.02	0.01	0.02
-2.75	0.12	0.02	0.05
-2.25	0.19	0.03	0.06
-1.75	0.33	0.04	0.08
-1.25	0.85	0.06	0.18
-0.75	0.98	0.07	0.22
-0.25	1.44	0.08	0.37
0.25	1.40	0.08	0.36
0.75	1.69	0.09	0.40
1.25	1.83	0.09	0.41
1.75	0.91	0.07	0.27
2.25	0.37	0.04	0.16
2.75	0.11	0.02	0.06
3.25	0.02	0.01	0.01
3.75	–	–	–

Table 6.11: Jet cross section, $d^3\sigma/dE_T d\eta_1 d\eta_2$, as a function of $\eta_2 \times sign(\eta_1)$ for $2.5 \leq |\eta_1| < 3.0$.

6.4 Unsmearing

The detector E_T resolution has a large effect on the uncorrected cross section, shown in sections 6.1-6.3. In order to compare the experimental measurement with theoretical parton-level predictions, one must either include detector resolution effects in the theoretical predictions (*i.e.*, "smear" the theory), or "unsmear" the data to remove these detector effects. The latter method is preferred since, after removing the detector effects, one obtains a true physical measurement which can be compared to any theory without specific knowledge of the DØ detector.

6.4.1 Inclusive Jet Cross Section Case

Let us start by considering the inclusive single jet cross section, $d^2\sigma/dE_T d\eta$. This cross section has been measured at DØ and the effects due to detector resolution have been studied in great detail [48, 52]. This cross section is very steeply falling as a function of E_T, $\sim E_T^{-5}$. Detector E_T resolution will tend to flatten out the overall E_T spectrum. Due to the steepness of the spectrum, there are more jets at lower E_T's which fluctuate to higher E_T's than there are jets at higher E_T's which fluctuate to lower E_T's, hence a net shift towards the higher jet E_T's occurs resulting in a flatter E_T spectrum.

The measured (smeared) cross section, f, can be written in terms of the true (unsmeared) cross section, F, the detector E_T resolution, G, and the detector η resolution, H:

$$f(E_T', \eta') = \int G(E_T' - E_T) H(\eta' - \eta) F(E_T, \eta) dE_T d\eta. \tag{6.6}$$

IF f, G, and H are known, we can in principle solve a system of inhomogeneous linear equations to extract the true, unsmeared cross section from the smeared data. However, in practice, the steeply falling cross section and statistical fluctuations cause unphysical oscillations in the resulting $F(E_T, \eta)$.

An alternate method of unsmearing was developed in which an arbitrary parameterization of the cross section was chosen:

$$f(E_T', A, B, C, D) = \int G(E_T' - E_T) F(E_T, A, B, C, D) dE_T \tag{6.7}$$

where we have ignored the effects due to η resolution. The detector η resolution is very good and has less than a 2.5% effect, mostly due to migration from one η bin to another, in the forward region ($2.5 < |\eta| < 3.0$) of the inclusive jet cross section and an even more negligible effect at smaller η [49, 52]. The parameterization, F, is a function of E_T and the parameters A, B, C, and D. It is smeared numerically using the above formula where $G(E_T' - E_T)$ is a Gaussian whose width is given by detector E_T resolution described in the previous chapter. The smeared function, f, is then fit to the data. The fit determines the parameters A, B, C, and D, which determine both F and f. To unsmear, the measured cross section as a function of the jet E_T, is divided by:

$$R_{res} = \frac{f(E_T', A, B, C, D)}{F(E_T, A, B, C, D)}. \tag{6.8}$$

The errors on the cross section due to this unsmearing procedure were determined to be between 0.5% and 5%, increasing as a function of E_T and η [52].

6.4.2 Inclusive Dijet Cross Section Case

For the case of the inclusive dijet cross section, $d^3\sigma/dE_T d\eta_1 d\eta_2$, the situation becomes much more complex. In the single jet cross section, the effect of energy resolution can move a jet from one E_T bin to another. Each jet in the event is entered into the cross section once. In the dijet cross section, as discussed before, each *event* enters into the cross section twice (with the double counting) and is binned according to either (E_{T1}, η_1, η_2), or (E_{T2}, η_2, η_1). Energy resolution can radically change where an event is binned. In events where there are two jets, a fluctuation in the energy of either can move the event from one E_T bin to another. More importantly, in events where there are three jets, energy fluctuations can cause *jet 2* and *jet 3* to change places, in terms of E_T ordering, and change the η bin where the event is entered. Thus, the energy resolution can significantly affect the *topology* of the event and hence, the dijet cross section.

Unsmearing the detector energy resolution effects from the measured cross section is also much more difficult in the dijet case than in the single jet inclusive cross section. In the single jet inclusive case, the cross section is based on the relevant jet variables, E_T and η, and all relevant information for unsmearing is saved in

the actual cross section measurement. In the dijet case, the triple differential cross section only has knowledge of the E_T of one of the jets; the E_T of *jet 2* and *jet 3* are not part of the cross section so energy resolution effects that change the event topology are difficult to unsmear. Hence, the unsmearing procedure used for the inclusive jet cross section cannot be applied.

The following procedure was used to unsmear the cross sections:

- Generate theoretical predictions for the E_T and signed-η cross sections. These distributions are called the "RAW" distributions.
- Generate theoretical predictions with the known DØ detector E_T resolution described in the previous chapter for the E_T and signed-η cross sections. These distributions are called the "SMEARED" distributions.
- The unsmearing factors are obtained from the ratio of "RAW" distributions over "SMEARED" distributions.

$$F_{unsmeared}(E_T, \eta_1, \eta_2) = \frac{RAW\ distribution}{SMEARED\ distribution}. \tag{6.9}$$

- Multiply measured cross sections with these unsmearing factors.

$$f_{true}(E_T, \eta_1, \eta_2) = F_{unsmeared}(E_T, \eta_1, \eta_2) \times f_{measured}(E_T, \eta_1, \eta_2). \tag{6.10}$$

The theoretical predictions were generated using JETRAD. This method is model-dependent since it assumes that JETRAD reproduces faithfully the true cross section. We have, therefore, studied the magnitude of the unsmearing differences by varying the different parameters to which JETRAD is dependent. These parameters are the choice on renormalization/factorization scale and the choice of parton distribution functions. In addition, we also studied the effects of varying the resolution functions within their one-sigma error. These variations are described below.

Variation of parton distribution functions

We have generated the dijet cross sections for three different choices of pdf's: CTEQ2M, CTEQ2ML, and GRV. These three pdf's give the greatest variance in cross section predictions. The cross sections (both RAW and SMEARED) were generated with

$\mu = E_T$ as the choice for the renormalization scale and the SMEARED cross sections were generated with nominal E_T resolution values. Once generated, we obtained the unsmearing values as described before. Figure 6.11 shows the unsmearing factors for the three pdf choices and their average for the case of the central slice ($0.0 \leq |\eta_1| < 0.5$).

We see from Fig. 6.11 that in the central region of η that the differences due to different pdf's are small. We have determined the fractional difference between the unsmearing functions from CTEQ2M and from the average for all the η slices and show them in Table 6.12. Since the differences are small, we will use the unsmearing values obtained with the CTEQ2M pdf.

$\eta_2 \times Sign(\eta_1)$	0.25	0.75	1.25	1.75	2.25	2.75
-3.75	0.07	0.12	0.18	-0.52	1.00	0.75
-3.25	0.04	0.06	-0.10	0.20	-0.13	0.86
-2.75	0.02	0.06	-0.03	-0.02	0.00	-0.01
-2.25	0.04	0.00	0.00	0.04	0.18	0.00
-1.75	0.01	-0.02	-0.02	-0.01	0.02	0.14
-1.25	0.01	0.03	0.00	-0.01	-0.06	0.01
-0.75	0.01	0.02	0.00	0.00	-0.02	0.00
-0.25	0.03	-0.02	0.02	-0.01	0.00	0.04
0.25	0.02	0.01	0.00	0.01	0.04	0.00
0.75	0.02	0.01	0.02	0.02	-0.02	0.03
1.25	-0.01	0.00	0.01	-0.02	0.00	0.02
1.75	-0.02	-0.01	-0.01	0.00	0.02	-0.01
2.25	0.00	-0.02	0.00	0.01	0.01	0.05
2.75	0.01	-0.01	0.02	0.00	0.02	0.04
3.25	0.02	0.09	0.05	0.00	0.20	0.15
3.75	0.11	-0.07	0.10	0.22	0.31	-0.25

Table 6.12: Point-by-point fractional errors between the CTEQ2M and AVERAGE unsmearing factors for each individual η_1 slice.

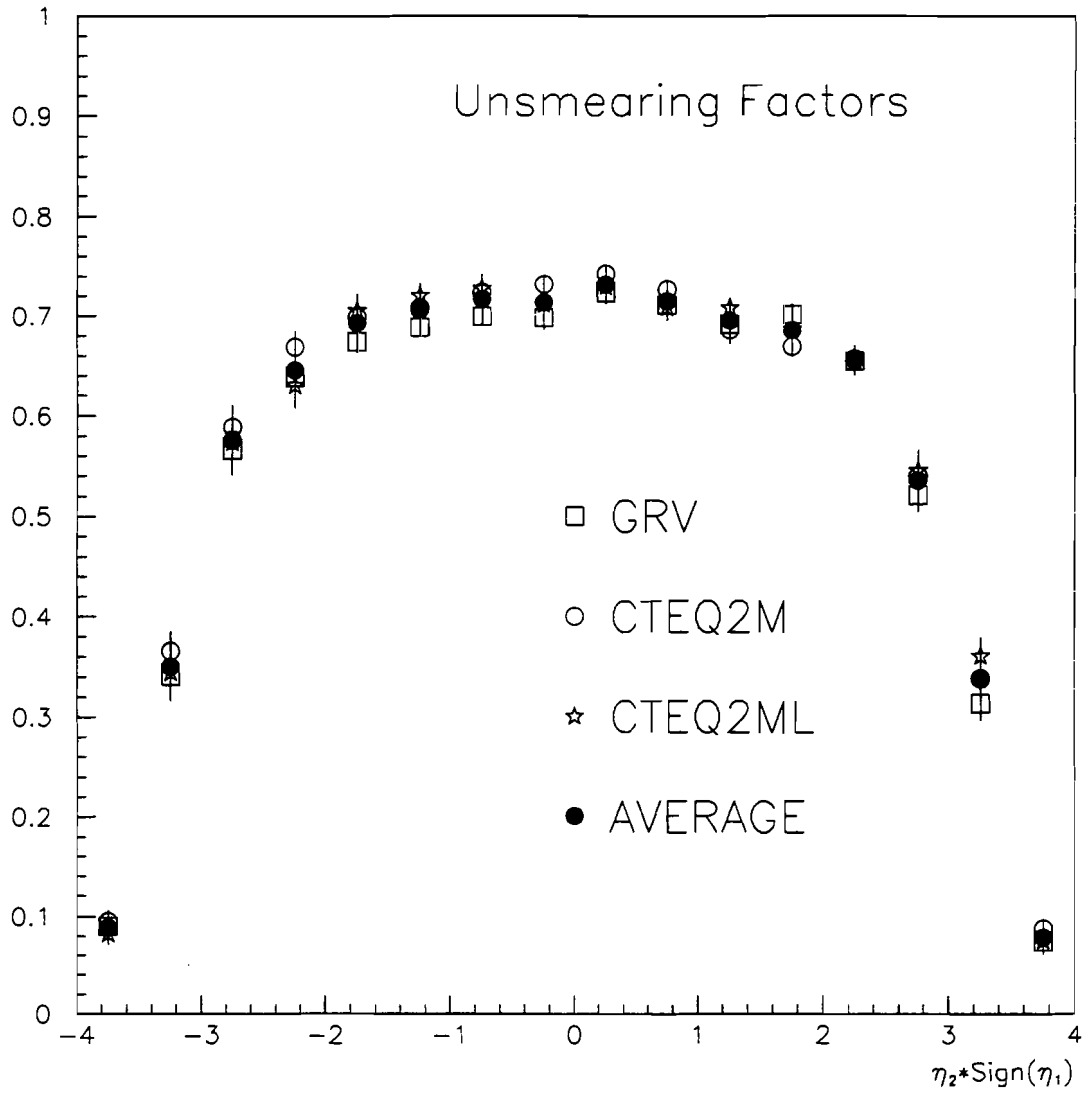

Figure 6.11: Unsmearing factors for three different pdf's and their average for the central slice $0.0 \leq |\eta_1| < 0.5$.

Variation of renormalization scale

A similar study was preformed with the renormalization scale parameter. The cross sections (both RAW and SMEARED) were generated with CTEQ2M as the choice of pdf and the SMEARED cross sections were generated with nominal E_T resolution values. Once generated, we obtained the unsmearing values as described before. Figure 6.12 shows the unsmearing factors for all three renormalization scale choices and their average value for the case of the central slice ($0.0 \leq |\eta_1| < 0.5$).

Similar to the pdf exercise, the unsmearing factors to be used are those with the choice of $\mu = E_T$ and the errors are obtained in a similar fashion to the pdf case. Table 6.13 shows the fractional error in the unsmearing factors from the $\mu = E_T$ choice calculated as described above for each $\eta_2 \times Sign(\eta_1)$ point and each η_1 slice. As seen in Fig. 6.12 and Table 6.13 the variations due to the different choices of renormalization/factorization scale are mostly negligible.

Variation of E_T resolution parameters

The last set of tests performed was the study of the E_T resolution parameters. The cross sections (both RAW and SMEARED) were generated with $\mu = E_T$ as the choice of renormalization scale and with CTEQ2M as the choice of pdf. Three SMEARED distributions were generated: one with the nominal resolution parameters, another with the nominal plus the one-sigma deviation, and the last one with the nominal minus the one-sigma deviation. To first order, we believe that the variation of the resolution parameters simply result in a shift in normalization; in other words, the cross section with the plus one-sigma deviation will be larger than the nominal one while the cross section with the minus one-sigma deviation will be smaller. We have taken a ratio of the cross sections and a good fit to a constant ratio confirms this hypothesis in most rapidity ranges. The offset coefficient indicates the magnitude of the normalization change resulting from the variation of the E_T resolution parameters. This technique was applied to each η_1 slice and the results are shown in Table 6.14.

From the table it is clear that the last two slices fit poorly to a constant normalization offset. They, however, can be fitted to a quadratic. For the 2.0-2.5 slice the parametrization is $1.06 + 0.004x + 0.01x^2$ with a χ^2/ndf of 12.79/13 and for the 2.5-3.0 slice the parametrization is $1.05 + 0.007x + 0.02x^2$ with a χ^2/ndf of 10.55/13

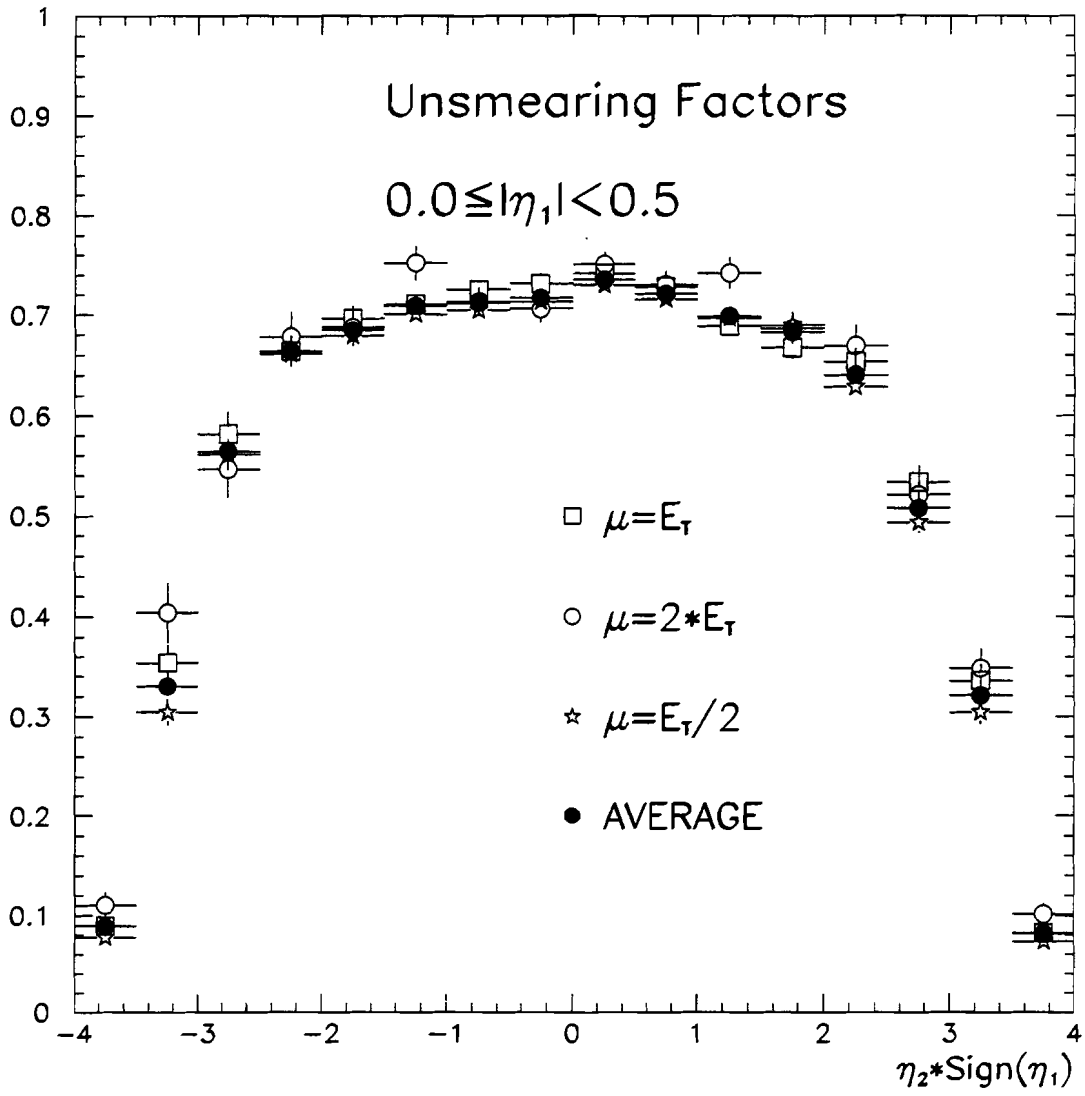

Figure 6.12: Unsmearing factors for three different renormalization scale, μ, and their average for the central slice, $0.0 \leq |\eta_1| < 0.5$.

$\eta_2 \times Sign(\eta_1)$	0.25	0.75	1.25	1.75	2.25	2.75
-3.75	0.01	0.15	-0.10	-0.71	0.85	0.55
-3.25	0.07	0.12	0.06	0.40	-0.06	0.40
-2.75	0.03	0.03	0.01	-0.01	0.02	0.29
-2.25	0.00	0.03	0.04	0.01	0.17	0.32
-1.75	0.02	0.00	-0.01	0.01	0.04	0.13
-1.25	0.00	0.03	-0.01	-0.01	-0.01	0.00
-0.75	0.02	0.00	-0.01	0.01	0.01	0.00
-0.25	0.02	-0.01	0.03	-0.01	-0.02	0.05
0.25	0.01	0.01	-0.01	0.00	0.03	0.00
0.75	0.01	0.01	0.01	0.03	0.00	0.03
1.25	-0.01	0.02	0.02	0.00	-0.01	0.03
1.75	-0.02	0.01	0.00	0.00	0.01	-0.02
2.25	0.02	0.00	0.01	0.02	0.00	0.04
2.75	0.05	-0.01	0.03	0.02	0.01	0.04
3.25	0.04	0.05	0.07	-0.02	0.11	0.18
3.75	0.01	0.05	0.14	0.26	0.03	0.88

Table 6.13: Point-by-point fractional errors between the $\mu = E_T$ and AVERAGE unsmearing factors for each individual η_1 slice.

$\|\eta_1\|$ slice	Offset (A_0)	χ^2/ndf
0.0-0.5	1.02	4.04/15
0.5-1.0	1.02	7.51/15
1.0-1.5	1.01	4.17/15
1.5-2.0	1.05	11.65/15
2.0-2.5	1.08	26.56/15
2.5-3.0	1.11	32.30/15

Table 6.14: Changes in the cross section normalization for the different $|\eta_1|$ slices due to the variation of the resolution parameters. The second column represents the overall normalization ratio for a fit over the range $-4.0 < \eta_2 \times Sign(\eta_1) < 4.0$. The third column gives the goodness of the fit.

where x is $\eta_2 \times Sign(\eta_1)$.

We have used all the data points from -4.0 to 4.0 in the previous fits; if we were to constrain ourselves from -3.0 to 3.0 and fit to a constant normalization offset, we obtained the results shown in Table 6.15.

We see that the overall normalization was consistent with being constant for each slice. From this study, we have shown that a variation of the E_T resolution parameters simply result in a shift in the overall normalization of the cross section. The overall normalization uncertainty can be assigned either as an error in the smearing or in the unsmearing.

In this subsection, we have studied in detail the resulting effects in unsmearing by varying different parameters and have shown that they are small compared to other uncertainties, for instance, the uncertainty due to the jet energy scale correction. Hence, it is safe to ignore these uncertainties.

$\|\eta_1\|$ slice	Offset (A_0)	χ^2/ndf
0.0-0.5	1.02	1.99/11
0.5-1.0	1.02	2.99/11
1.0-1.5	1.01	2.02/11
1.5-2.0	1.05	6.89/11
2.0-2.5	1.08	8.43/11
2.5-3.0	1.10	16.14/11

Table 6.15: Changes in the cross section normalization for the different $|\eta_1|$ slices due to the variation of the resolution parameters. The second column represents the overall normalization ratio for a fit over the range $-3.0 < \eta_2 \times Sign(\eta_1) < 3.0$. The third column gives the goodness of the fit.

6.5 Unsmeared Results

Using the procedure described above we unsmeared the cross sections for the E_T and signed-η distributions and have overlaid NLO theoretical predictions on them. The unsmearing factors will be shown in the appendix.

6.5.1 Unsmeared E_T cross sections

After unsmearing the data, we compare the cross sections to the theoretical predictions given by JETRAD. The DØ measurement of the E_T spectrum is shown in Fig. 6.13. As with the raw cross section, we plot the cross section as a function of the leading jet E_T with the leading jet central and the second jet rapidity varied from 0.0 to 4.0. The inner error bars indicate the statistical error and the outer error bars indicate the statistical error added in quadrature to the systematic. There is also an additional 5.4% error due to the luminosity not shown in the plot. The solid line represents the theoretical calculations from the JETRAD parton level event generator at NLO with the choice of CTEQ2M as the pdf and the renormalization scale set at $\mu = E_T$ [51]. In Fig. 6.14, the leading order and next-to-leading order theoretical cross sections with the choice of pdf's CTEQ2L (LO) and CTEQ2M (NLO) are

shown. As the second jet moves forward in $|\eta_2|$, NLO theory predicts higher cross sections. Our measurements are in agreement with NLO theory, given the current level of systematic errors, and favor the NLO prediction over the LO prediction. We also show the results in Tables 6.16-6.19.

E_T (GeV)	Cross Section (nb/GeV)	Statistical Error (nb/GeV)(%)	Systematic Error (nb/GeV) (%)
40.- 50.	10.15	0.07 (0.7)	0.91 (8.9)
50.- 60.	4.09	0.04 (1.1)	0.61 (15.0)
60.- 70.	1.73	0.03 (1.7)	0.25 (14.4)
70.- 80.	0.86	0.02 (2.4)	0.12 (13.8)
80.- 90.	0.48	0.45E-02 (0.9)	0.06 (13.2)
90.- 100.	0.26	0.34E-02 (1.3)	0.04 (15.2)
100.- 110.	0.15	0.26E-02 (1.7)	0.02 (14.7)
110.- 120.	0.09	0.20E-02 (2.3)	0.02 (17.2)
120.- 130.	0.05	0.15E-02 (3.0)	0.77E-02 (15.0)
130.- 140.	0.03	0.43E-03 (1.3)	0.55E-02 (16.9)
140.- 150.	0.02	0.36E-03 (1.7)	0.34E-02 (15.9)
150.- 170.	0.01	0.19E-03 (1.6)	0.22E-02 (18.6)
170.- 190.	0.59E-02	0.11E-03 (1.8)	0.11E-02 (18.9)
190.- 210.	0.30E-02	0.76E-04 (2.6)	0.66E-03 (22.2)
210.- 230.	0.14E-02	0.53E-04 (3.7)	0.33E-03 (23.1)
230.- 250.	0.72E-03	0.37E-04 (5.2)	0.21E-03 (28.4)
250.- 270.	0.41E-03	0.28E-04 (6.9)	0.11E-03 (27.4)
270.- 300.	0.21E-03	0.17E-04 (7.8)	0.82E-04 (38.8)
300.- 330.	0.77E-04	0.99E-05 (13.0)	0.22E-04 (28.2)
330.- 360.	0.22E-04	0.53E-05 (24.1)	0.18E-04 (83.1)
360.- 390.	0.63E-05	0.28E-05 (44.7)	0.38E-05 (60.8)
390.- 430.	0.48E-05	0.21E-05 (44.4)	0.29E-05 (61.5)

Table 6.16: Unsmeared jet cross section, $d^3\sigma/dE_T d\eta_1 d\eta_2$, as a function of the central jet E_T when the second jet is at $0.0 \leq |\eta| < 1.0$.

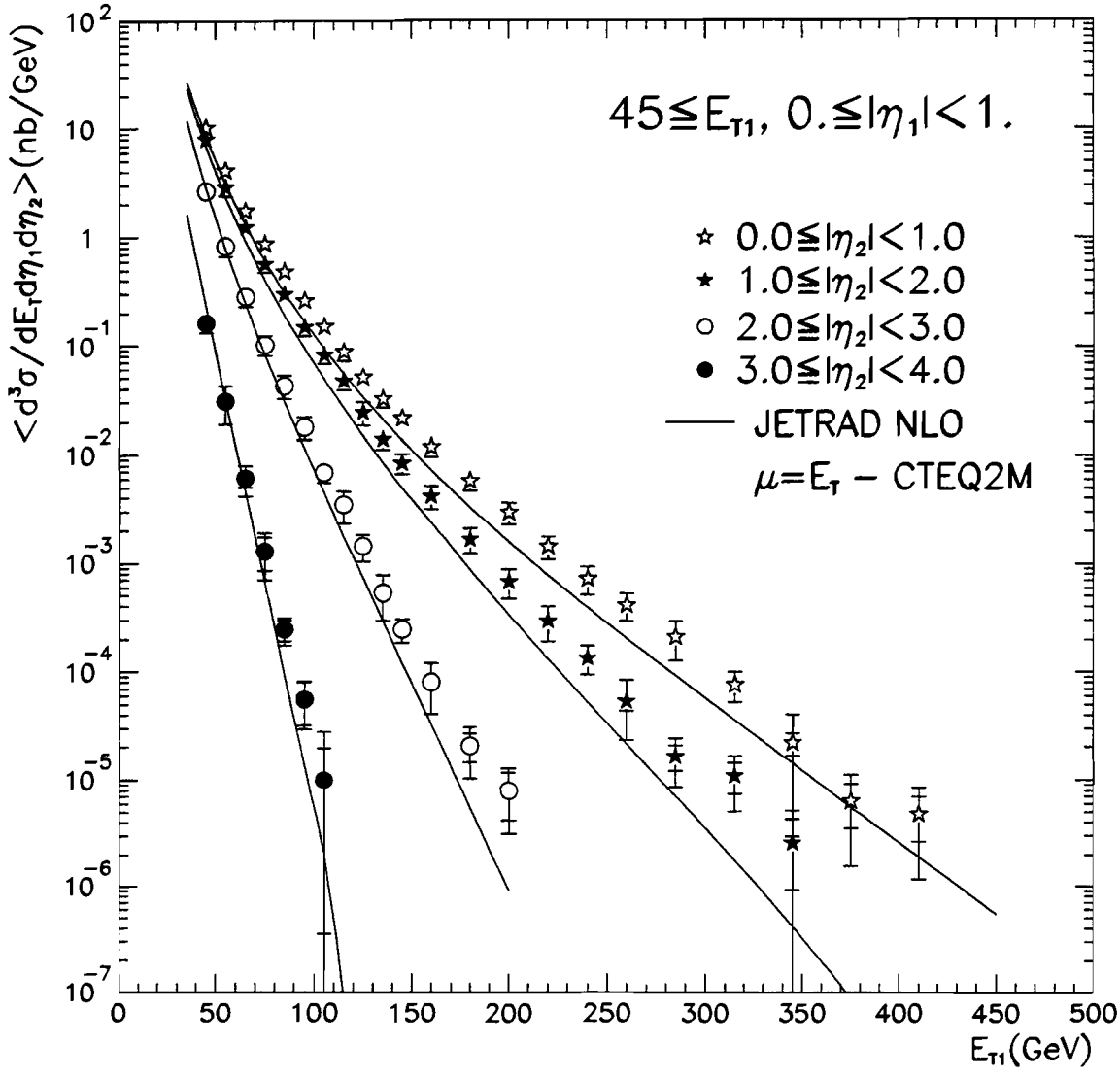

Figure 6.13: DØ measurement of $d^3\sigma/dE_T d\eta_1 d\eta_2$ vs. E_{T1} for $|\eta_1| < 1.0$ and comparison to next-to-leading order pQCD prediction using CTEQ2M pdf's.

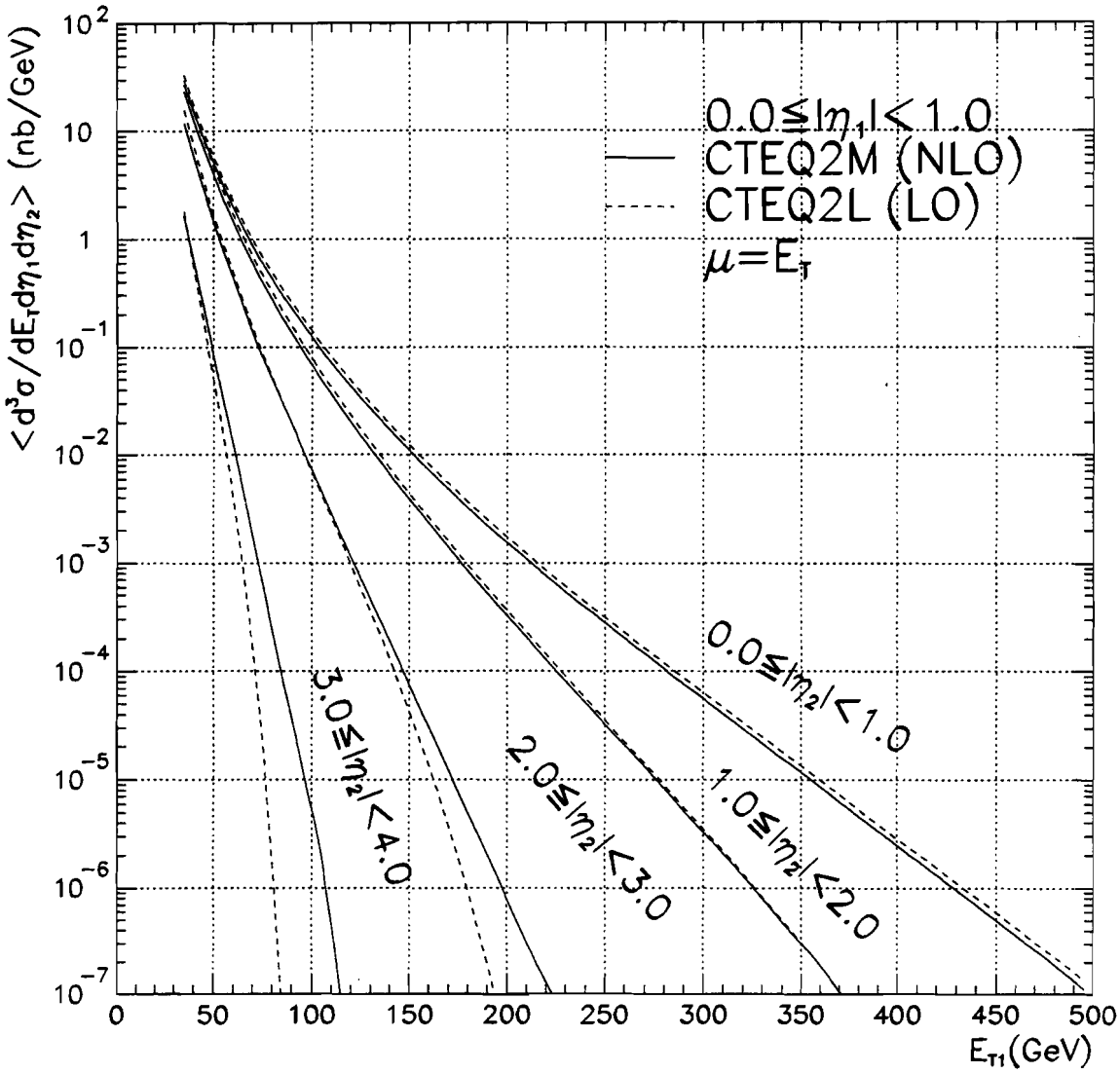

Figure 6.14: A comparison of JETRAD leading order and next-to-leading order pQCD predictions of $d^3\sigma/dE_T d\eta_1 d\eta_2$ vs. E_{T1} for $|\eta_1| < 1.0$ and the noted $|\eta_2|$ ranges.

E_T (GeV)	Cross Section (nb/GeV)	Statistical Error (nb/GeV)(%)	Systematic Error (nb/GeV) (%)
40.- 50.	7.93	0.06 (0.7)	0.74 (9.3)
50.- 60.	2.87	0.04 (1.2)	0.49 (17.0)
60.- 70.	1.23	0.02 (1.9)	0.16 (13.2)
70.- 80.	0.56	0.02 (2.9)	0.09 (16.7)
80.- 90.	0.30	0.35E-02 (1.2)	0.05 (15.3)
90.- 100.	0.15	0.25E-02 (1.7)	0.03 (17.3)
100.- 110.	0.08	0.19E-02 (2.3)	0.01 (17.2)
110.- 120.	0.05	0.14E-02 (3.0)	0.01 (17.0)
120.- 130.	0.02	0.10E-02 (4.2)	0.01 (23.5)
130.- 140.	0.01	0.28E-03 (2.0)	0.27E-02 (19.1)
140.- 150.	0.85E-02	0.22E-03 (2.6)	0.18E-02 (20.9)
150.- 170.	0.42E-02	0.11E-03 (2.6)	0.99E-03 (23.5)
170.- 190.	0.17E-02	0.55E-04 (3.3)	0.44E-03 (26.5)
190.- 210.	0.68E-03	0.35E-04 (5.2)	0.20E-03 (29.7)
210.- 230.	0.30E-03	0.23E-04 (7.8)	0.10E-03 (34.5)
230.- 250.	0.13E-03	0.16E-04 (11.6)	0.36E-04 (27.2)
250.- 270.	0.54E-04	0.98E-05 (18.3)	0.29E-04 (53.4)
270.- 300.	0.16E-04	0.44E-05 (26.6)	0.66E-05 (40.0)
300.- 330.	0.11E-04	0.35E-05 (32.2)	0.47E-05 (43.0)
330.- 360.	0.26E-05	0.17E-05 (64.8)	0.20E-05 (76.3)

Table 6.17: Unsmeared jet cross section, $d^3\sigma/dE_T d\eta_1 d\eta_2$, as a function of the central jet E_T when the second jet is at $1.0 \leq |\eta| < 2.0$.

E_T (GeV)	Cross Section (nb/GeV)	Statistical Error (nb/GeV)(%)	Systematic Error (nb/GeV) (%)
40.- 50.	2.65	0.03 (1.2)	0.33 (12.6)
50.- 60.	0.82	0.02 (2.1)	0.16 (19.0)
60.- 70.	0.28	0.01 (3.8)	0.05 (19.3)
70.- 80.	0.10	0.63E-02 (6.2)	0.02 (19.7)
80.- 90.	0.04	0.12E-02 (2.9)	0.01 (23.4)
90.- 100.	0.02	0.80E-03 (4.5)	0.41E-02 (23.0)
100.- 110.	0.69E-02	0.49E-03 (7.1)	0.13E-02 (18.1)
110.- 120.	0.35E-02	0.34E-03 (9.8)	0.11E-02 (31.2)
120.- 130.	0.15E-02	0.23E-03 (15.6)	0.32E-03 (22.3)
130.- 140.	0.54E-03	0.48E-04 (8.8)	0.24E-03 (44.1)
140.- 150.	0.24E-03	0.32E-04 (13.1)	0.50E-04 (20.6)
150.- 170.	0.80E-04	0.13E-04 (15.7)	0.38E-04 (47.0)
170.- 190.	0.21E-04	0.62E-05 (30.1)	0.82E-05 (39.9)
190.- 210.	0.79E-05	0.37E-05 (47.5)	0.30E-05 (37.5)

Table 6.18: Unsmeared jet cross section, $d^3\sigma/dE_T d\eta_1 d\eta_2$, as a function of the central jet E_T when the second jet is at $2.0 \leq |\eta| < 3.0$.

E_T (GeV)	Cross Section (nb/GeV)	Statistical Error (nb/GeV)(%)	Systematic Error (nb/GeV) (%)
40.- 50.	0.16	0.60E-02 (3.7)	0.03 (18.5)
50.- 60.	0.03	0.25E-02 (8.0)	0.01 (37.0)
60.- 70.	0.61E-02	0.11E-02 (17.3)	0.16E-02 (25.8)
70.- 80.	0.13E-02	0.44E-03 (34.1)	0.41E-03 (31.2)
80.- 90.	0.24E-03	0.52E-04 (21.0)	0.47E-04 (19.0)
90.- 100.	0.56E-04	0.24E-04 (43.1)	0.11E-04 (20.0)
100.- 110.	0.99E-05	0.95E-05 (96.4)	0.15E-04 (150.1)

Table 6.19: Unsmeared jet cross section, $d^3\sigma/dE_T d\eta_1 d\eta_2$, as a function of the central jet E_T when the second jet is at $3.0 \leq |\eta| < 4.0$.

6.5.2 Unsmeared Signed-η cross sections

We have also unsmeared the signed-η distributions, $d^3\sigma/dE_T d\eta_1 d\eta_2$, as a function of $\eta_2 \times sign(\eta_1)$ for $45 \leq E_T < 55$ GeV. The inner error bars are statistical and the outer error bars are statistical added in quadrature to the systematic error. Figures 6.15-6.20 show the cross sections, the 5.4% error due to the luminosity uncertainty was not included. The results are also shown in tabular form in Tables 6.20-6.25.

$\eta_2 \times sign(\eta_1)$	Cross Section (nb/GeV)	Statistical Error (nb/GeV)(%)	Systematic Error (nb/GeV)(%)
-3.75	0.01	0.26E-02 (33.2)	0.30E-02 (38.5)
-3.25	0.15	0.02 (11.3)	0.05 (33.5)
-2.75	0.91	0.05 (5.2)	0.19 (20.7)
-2.25	1.85	0.07 (4.0)	0.40 (21.5)
-1.75	3.69	0.11 (3.0)	0.68 (18.4)
-1.25	5.91	0.14 (2.4)	0.95 (16.0)
-0.75	6.10	0.14 (2.4)	1.05 (17.2)
-0.25	6.61	0.15 (2.3)	1.03 (15.6)
0.25	6.28	0.15 (2.3)	1.02 (16.2)
0.75	6.37	0.15 (2.3)	1.05 (16.5)
1.25	5.82	0.14 (2.4)	1.09 (18.7)
1.75	4.07	0.11 (2.8)	0.73 (17.9)
2.25	2.25	0.08 (3.6)	0.45 (20.0)
2.75	1.09	0.05 (4.9)	0.24 (22.1)
3.25	0.18	0.02 (9.8)	0.06 (32.0)
3.75	0.24E-02	0.24E-02 (47.3)	0.16E-02 (66.3)

Table 6.20: Unsmeared cross section as a function of $\eta_2 \times sign(\eta_1)$ for $0.0 \leq |\eta_1| < 0.5$.

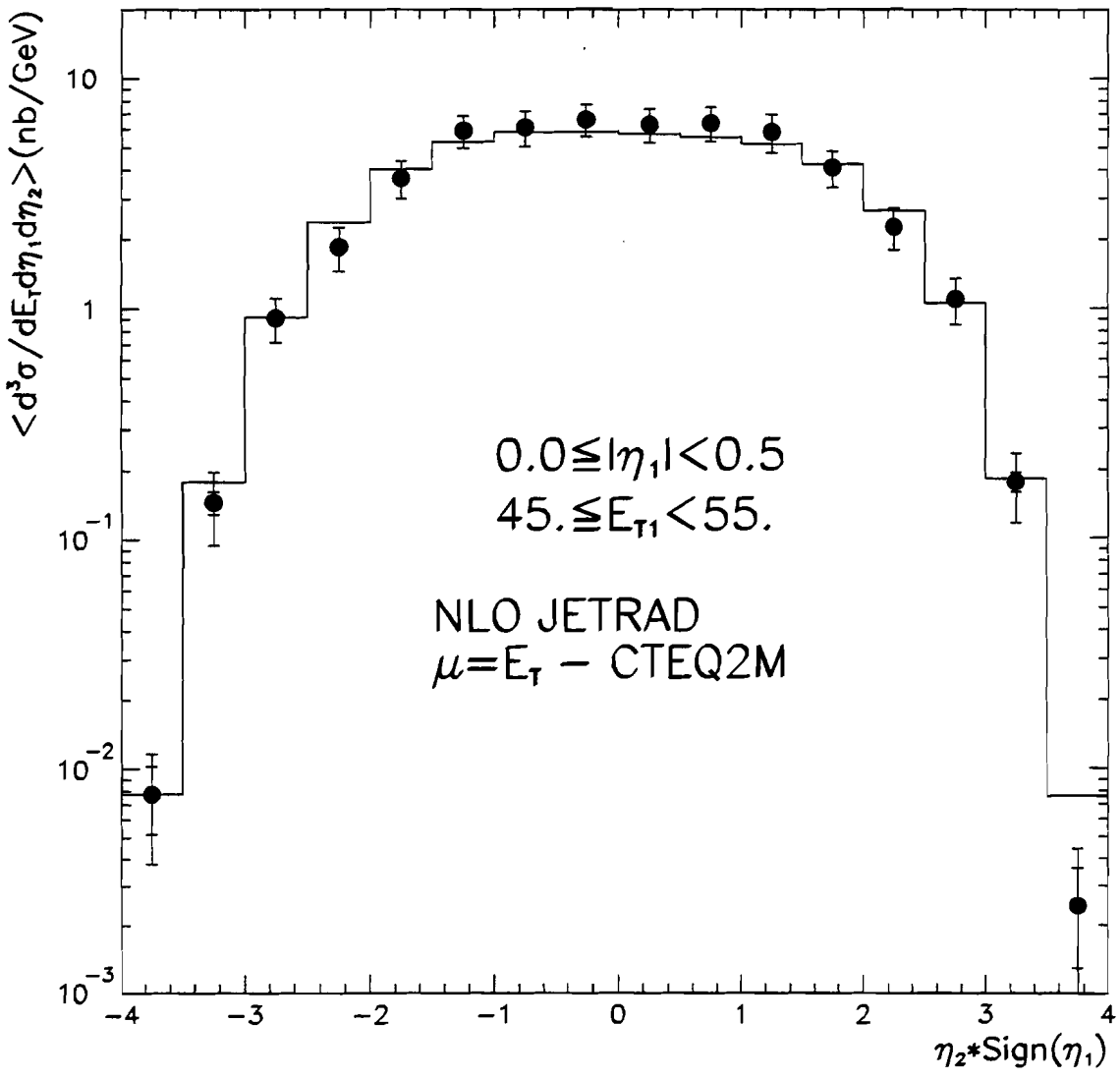

Figure 6.15: The unsmeared inclusive triple differential dijet cross section, $d^3\sigma/dE_T d\eta_1 d\eta_2$ vs. $\eta_2 \times sign(\eta_1)$ for $0.0 \leq |\eta_1| < 0.5$. The 5.4% luminosity uncertainty has not been included.

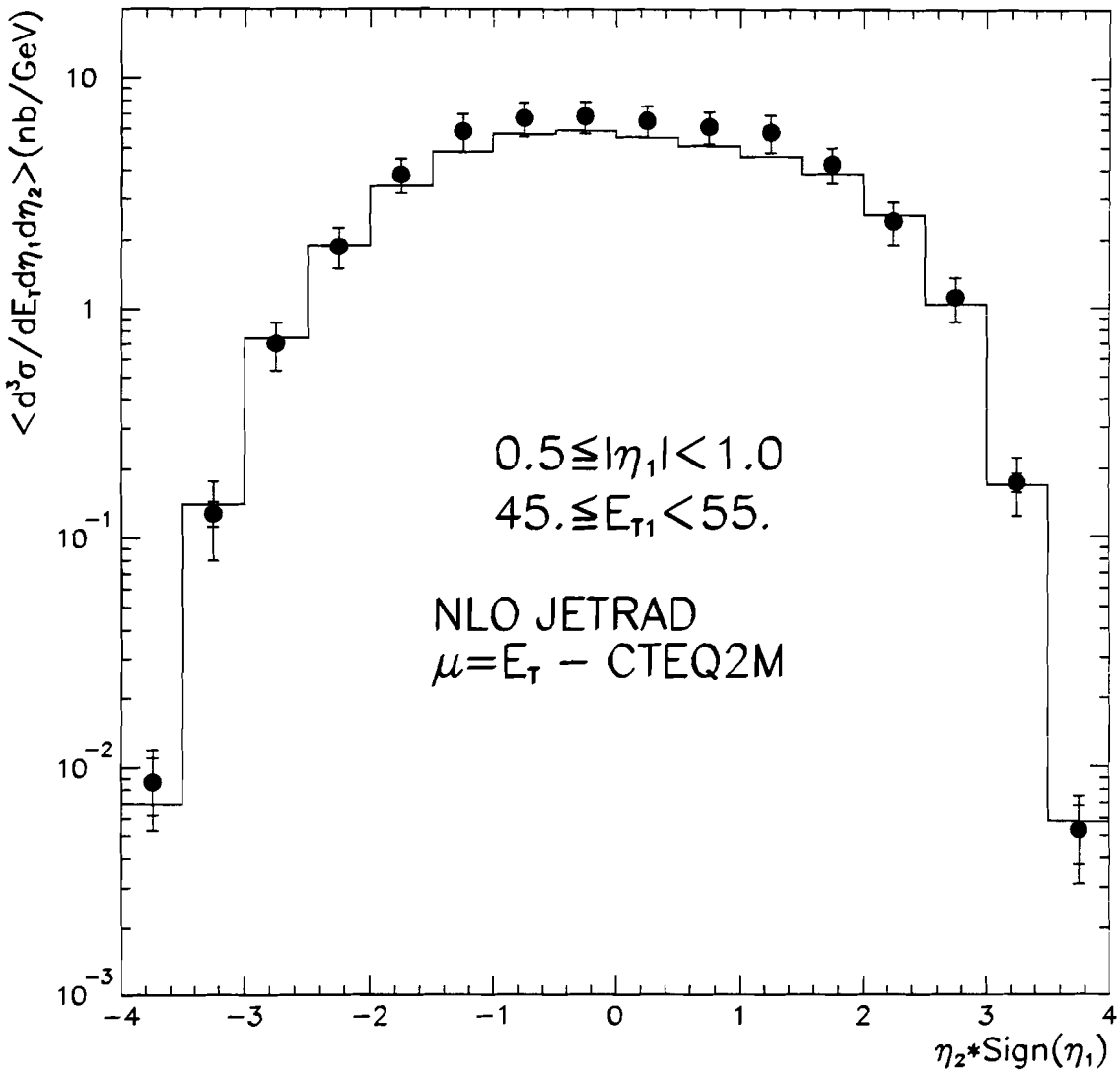

Figure 6.16: The unsmeared inclusive triple differential dijet cross section, $d^3\sigma/dE_T d\eta_1 d\eta_2$ vs. $\eta_2 \times sign(\eta_1)$ for $0.5 \leq |\eta_1| < 1.0$. The 5.4% luminosity uncertainty has not been included.

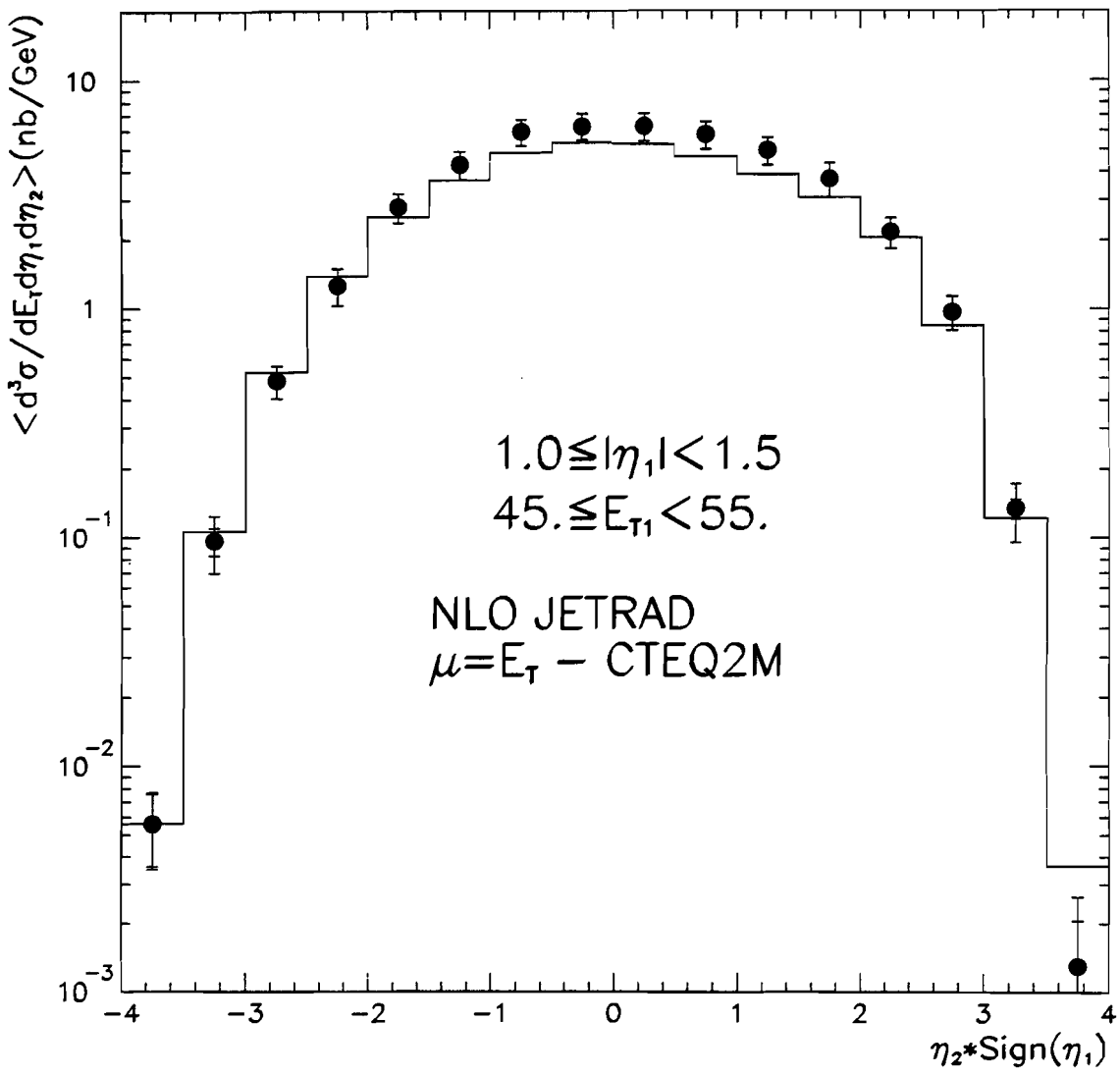

Figure 6.17: The unsmeared inclusive triple differential dijet cross section, $d^3\sigma/dE_T d\eta_1 d\eta_2$ vs. $\eta_2 \times sign(\eta_1)$ for $1.0 \leq |\eta_1| < 1.5$. The 5.4% luminosity uncertainty has not been included.

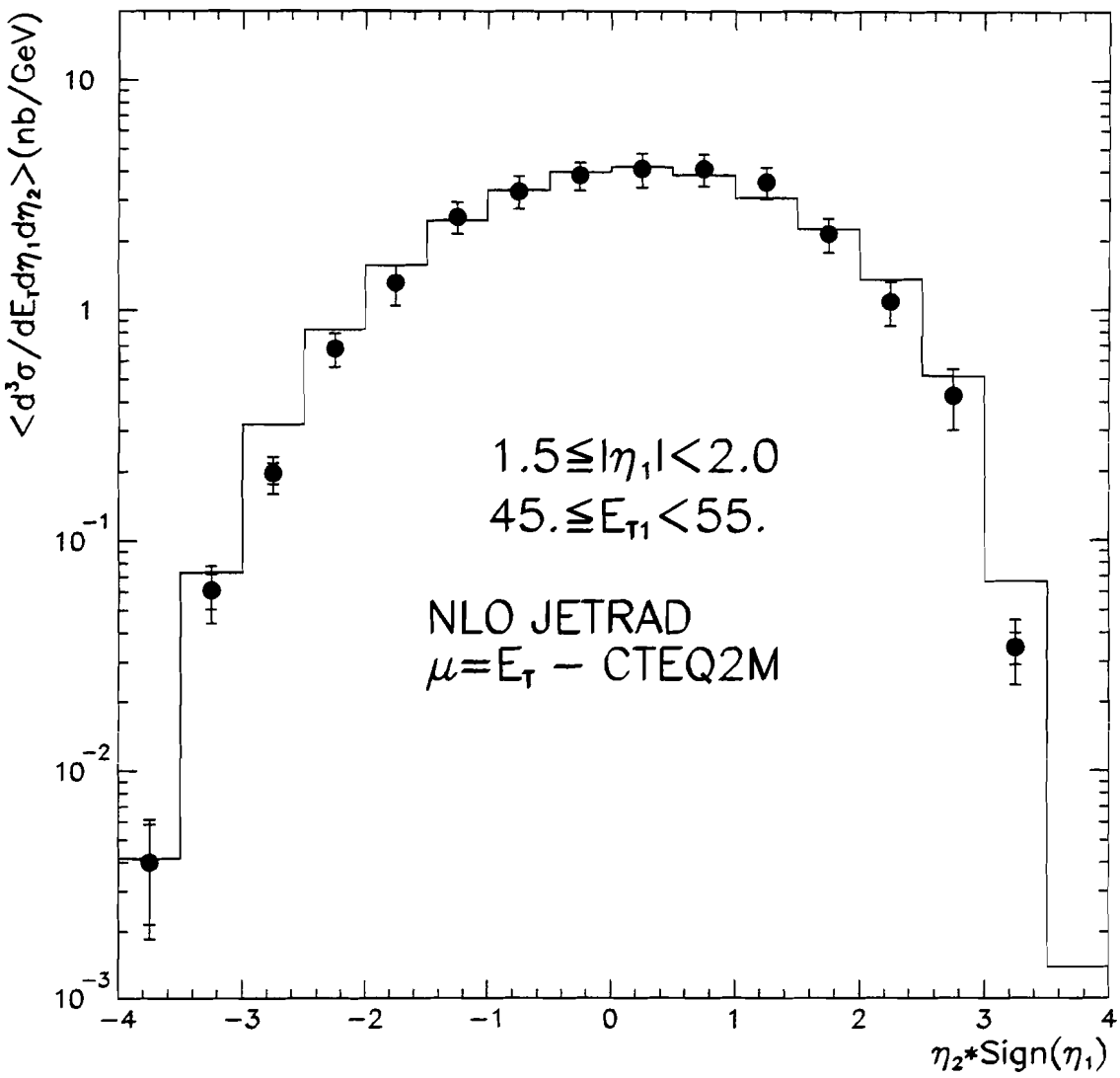

Figure 6.18: The unsmeared inclusive triple differential dijet cross section, $d^3\sigma/dE_T d\eta_1 d\eta_2$ vs. $\eta_2 \times sign(\eta_1)$ for $1.5 \leq |\eta_1| < 2.0$. The 5.4% luminosity uncertainty has not been included.

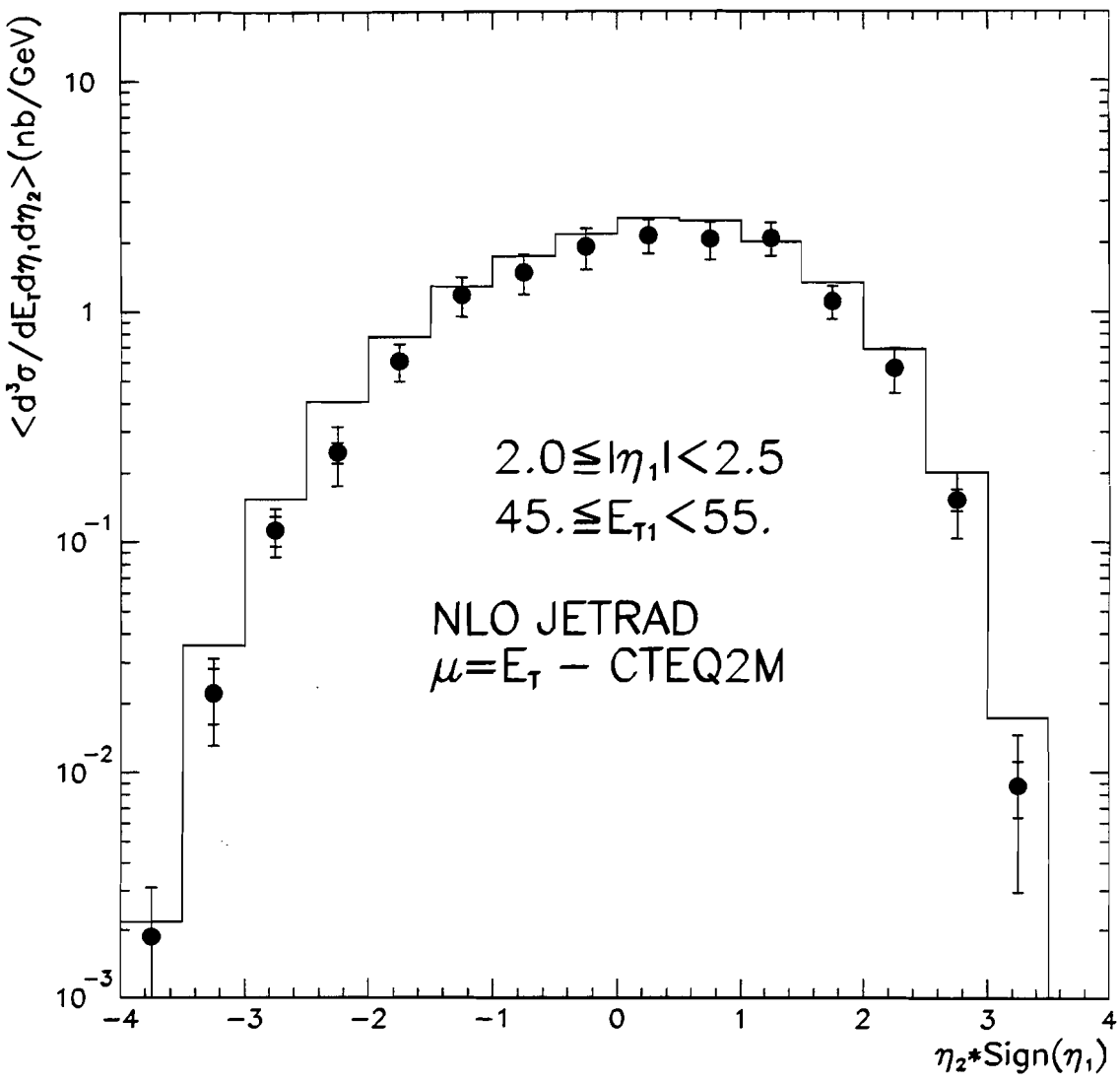

Figure 6.19: The unsmeared inclusive triple differential dijet cross section, $d^3\sigma/dE_T d\eta_1 d\eta_2$ vs. $\eta_2 \times sign(\eta_1)$ for $2.0 \leq |\eta_1| < 2.5$. The 5.4% luminosity uncertainty has not been included.

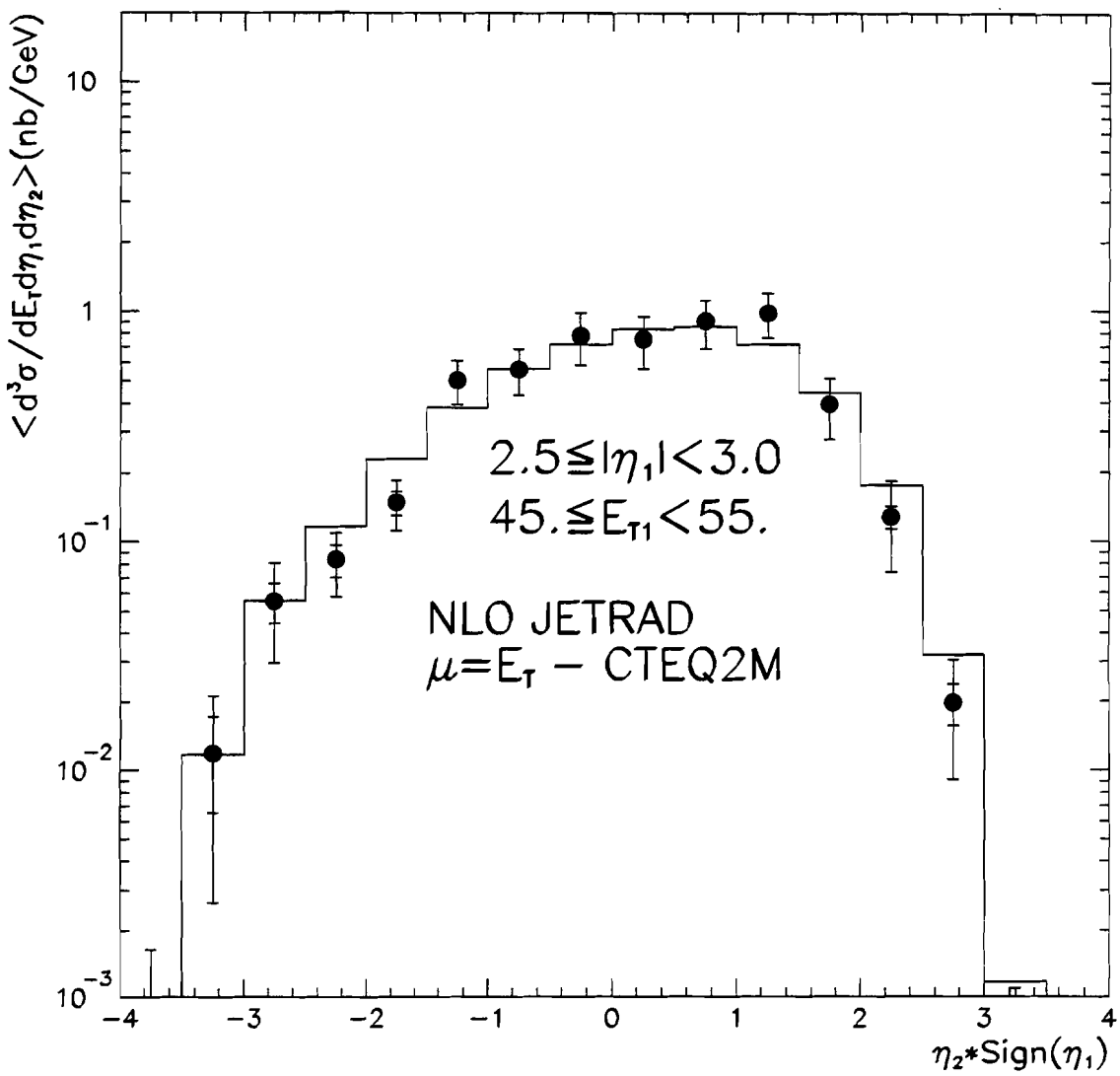

Figure 6.20: The unsmeared inclusive triple differential dijet cross section, $d^3\sigma/dE_T d\eta_1 d\eta_2$ vs. $\eta_2 \times sign(\eta_1)$ for $2.5 \leq |\eta_1| < 3.0$. The 5.4% luminosity uncertainty has not been included.

$\eta_2 \times sign(\eta_1)$	Cross Section (nb/GeV)	Statistical Error (nb/GeV)(%)	Systematic Error (nb/GeV)(%)
-3.75	0.01	0.24E-02 (28.0)	0.23E-02 (26.7)
-3.25	0.13	0.02 (12.7)	0.05 (35.7)
-2.75	0.70	0.04 (6.0)	0.16 (23.1)
-2.25	1.86	0.07 (4.0)	0.37 (20.0)
-1.75	3.80	0.11 (3.0)	0.64 (16.9)
-1.25	5.87	0.14 (2.4)	1.08 (18.4)
-0.75	6.69	0.15 (2.3)	1.13 (16.8)
-0.25	6.80	0.15 (2.3)	1.04 (15.3)
0.25	6.53	0.15 (2.3)	1.02 (15.6)
0.75	6.16	0.14 (2.3)	0.97 (15.8)
1.25	5.81	0.14 (2.4)	1.07 (18.4)
1.75	4.24	0.12 (2.8)	0.75 (17.7)
2.25	2.40	0.09 (3.6)	0.50 (20.9)
2.75	1.11	0.05 (4.7)	0.24 (21.6)
3.25	0.17	0.02 (9.4)	0.05 (27.1)
3.75	0.01	0.53E-02 (28.7)	0.16E-02 (29.9)

Table 6.21: Unsmeared cross section as a function of $\eta_2 \times sign(\eta_1)$ for $0.5 \leq |\eta_1| < 1.0$.

$\eta_2 \times sign(\eta_1)$	Cross Section (nb/GeV)	Statistical Error (nb/GeV)(%)	Systematic Error (nb/GeV)(%)
-3.75	0.01	0.20E-02 (35.4)	0.59E-03 (10.6)
-3.25	0.10	0.01 (14.0)	0.02 (24.1)
-2.75	0.48	0.04 (7.5)	0.07 (14.3)
-2.25	1.26	0.06 (4.9)	0.22 (17.5)
-1.75	2.78	0.10 (3.5)	0.40 (14.5)
-1.25	4.27	0.12 (2.8)	0.58 (13.5)
-0.75	5.91	0.14 (2.4)	0.76 (12.9)
-0.25	6.23	0.15 (2.4)	0.80 (12.8)
0.25	6.24	0.15 (2.3)	0.85 (13.6)
0.75	5.75	0.14 (2.4)	0.76 (13.2)
1.25	4.90	0.13 (2.6)	0.68 (13.9)
1.75	3.69	0.11 (2.9)	0.63 (17.1)
2.25	2.15	0.08 (3.7)	0.32 (15.0)
2.75	0.96	0.05 (4.9)	0.16 (16.3)
3.25	0.13	0.01 (9.8)	0.04 (27.0)
3.75	0.13E-02	0.76E-03 (58.5)	0.11E-02 (85.4)

Table 6.22: Unsmeared cross section as a function of $\eta_2 \times sign(\eta_1)$ for $1.0 \leq |\eta_1| < 1.5$.

$\eta_2 \times sign(\eta_1)$	Cross Section (nb/GeV)	Statistical Error (nb/GeV)(%)	Systematic Error (nb/GeV)(%)
-3.75	0.40E-02	0.19E-02 (46.4)	0.11E-02 (27.2)
-3.25	0.06	0.01 (17.0)	0.01 (21.9)
-2.75	0.20	0.02 (10.5)	0.03 (15.0)
-2.25	0.68	0.04 (6.5)	0.11 (15.6)
-1.75	1.31	0.06 (4.8)	0.26 (19.9)
-1.25	2.53	0.09 (3.5)	0.39 (15.5)
-0.75	3.27	0.10 (3.1)	0.53 (16.1)
-0.25	3.83	0.11 (2.9)	0.52 (13.5)
0.25	4.07	0.11 (2.8)	0.67 (16.4)
0.75	4.08	0.11 (2.8)	0.65 (15.9)
1.25	3.58	0.10 (2.9)	0.56 (15.5)
1.75	2.14	0.08 (3.7)	0.35 (16.4)
2.25	1.08	0.05 (4.8)	0.23 (21.0)
2.75	0.42	0.03 (6.7)	0.12 (28.6)
3.25	0.03	0.01 (15.7)	0.01 (27.1)
3.75	0.63E-03	0.36E-03 (57.7)	0.13E-03 (21.2)

Table 6.23: Unsmeared cross section as a function of $\eta_2 \times sign(\eta_1)$ for $1.5 \leq |\eta_1| < 2.0$.

$\eta_2 \times sign(\eta_1)$	Cross Section (nb/GeV)	Statistical Error (nb/GeV)(%)	Systematic Error (nb/GeV)(%)
-3.75	0.19E-02	0.12E-02 (65.6)	0.19E-02 (100.)
-3.25	0.02	0.01 (27.0)	0.01 (30.6)
-2.75	0.11	0.02 (14.9)	0.02 (18.3)
-2.25	0.24	0.02 (10.2)	0.06 (26.6)
-1.75	0.61	0.04 (6.9)	0.10 (17.0)
-1.25	1.18	0.06 (5.1)	0.22 (18.9)
-0.75	1.47	0.07 (4.5)	0.28 (19.1)
-0.25	1.90	0.08 (4.0)	0.38 (19.9)
0.25	2.12	0.08 (3.8)	0.34 (16.0)
0.75	2.05	0.08 (3.9)	0.37 (18.0)
1.25	2.06	0.08 (3.8)	0.32 (15.7)
1.75	1.10	0.05 (4.9)	0.17 (15.8)
2.25	0.57	0.04 (6.5)	0.12 (21.1)
2.75	0.15	0.02 (10.5)	0.05 (30.0)
3.25	0.01	0.24E-02 (27.8)	0.01 (60.4)
3.75	0.85E-04	0.78E-04 (92.0)	0.85E-04 (100.)

Table 6.24: Unsmeared cross section as a function of $\eta_2 \times sign(\eta_1)$ for $2.0 \leq |\eta_1| < 2.5$.

$\eta_2 \times sign(\eta_1)$	Cross Section (nb/GeV)	Statistical Error (nb/GeV)(%)	Systematic Error (nb/GeV)(%)
-3.75	0.85E-03	0.79E-03 (93.6)	0.85E-03 (100.)
-3.25	0.01	0.01 (45.1)	0.01 (63.3)
-2.75	0.06	0.01 (19.9)	0.02 (42.3)
-2.25	0.08	0.01 (15.6)	0.02 (26.5)
-1.75	0.15	0.02 (11.9)	0.03 (21.6)
-1.25	0.50	0.04 (7.4)	0.10 (20.1)
-0.75	0.56	0.04 (6.9)	0.12 (21.8)
-0.25	0.78	0.04 (5.7)	0.19 (24.7)
0.25	0.75	0.04 (5.8)	0.19 (24.8)
0.75	0.90	0.05 (5.2)	0.21 (23.2)
1.25	0.98	0.05 (5.0)	0.21 (21.7)
1.75	0.39	0.03 (7.1)	0.11 (28.5)
2.25	0.13	0.01 (11.2)	0.05 (40.8)
2.75	0.02	0.41E-02 (20.6)	0.01 (49.8)
3.25	0.65E-03	0.30E-03 (46.2)	0.33E-03 (50.8)
3.75	-	--	--

Table 6.25: Unsmeared cross section as a function of $\eta_2 \times sign(\eta_1)$ for $2.5 \leq |\eta_1| < 3.0$.

CHAPTER 7

Comparisons to Parton Distribution Functions

7.1 χ^2 Fits of Data and Theory

In this chapter, we will explore the sensitivity of the triple differential cross section, $d^3\sigma/dE_T d\eta_1 d\eta_2$, to the differences among the available parton distribution functions. The overall strategy is to generate NLO predictions using different pdf's and compare them to the experimental results. The comparisons are made with the signed-η distributions since there is a clear mapping back to the x-values of the events. For the comparisons, we construct a χ^2 that measures the agreement of the data to theoretical predictions with the different pdf's using a minimization package called MINUIT to vary parameters in the fit [53].

The dominant systematic error for the experimental cross section is due to the jet energy scale. As stated in the previous chapter, the standard jet correction is given by the NOMINAL choice but the HIGH and LOW choices lead to different cross sections because, for the signed-η distributions, we require the leading jet to be within $45 \leq E_T < 55$ GeV. Similarly, the dominant error for the theoretical predictions is the variation of the renormalization/factorization scale, μ. The typical choices for renormalization/factorization scale are $\mu = 2E_T$, $\mu = E_T$, and $\mu = E_T/2$. The differences between the LO and the NLO calculations are small indicating that the predictions are reliable for these choices of renormalization/factorization scale [54]. We assume that the jet energy scale and renormalization/factorization scale errors are fully correlated. In order to deal with these correlations, we adopt the following scheme:

- We determine the experimental results for the three different jet energy scale corrections: HIGH, NOMINAL, and LOW.
- We generate the theoretical predictions with three choices of renormalization/factorization scale: $\mu = 2E_T$, $\mu = E_T$, and $\mu = E_T/2$ for each pdf.
- We choose two families of current pdf's. The CTEQ [9] family (CTEQ2M, CTEQ2MF, CTEQ2MS, and CTEQ2ML) and the MRS [55, 56] family (MRSD-′ and MRSD0′.)
- We only consider data points for $|\eta_{1,2}| \leq 3.0$ because we understand the systematics within this region very well. At larger values of η there may be effects due to beam halo and pile-up.
- In order to account for the different choices of the jet energy scale, we interpolate the three cross sections using a quadratic polynomial based on one parameter, α:

$$F(\alpha) = F(0) + \frac{\alpha}{2}[F(1) - F(-1)] + \frac{\alpha^2}{2}[F(1) + F(-1) - 2F(0)] \quad (7.1)$$

  where $F(1)$ corresponds to the cross section with the HIGH correction, $F(0)$ corresponds to the cross section with the NOMINAL correction, and $F(-1)$ corresponds to the cross section with the LOW correction. One can show that $F(\alpha = 1)$ returns $F(1)$, $F(\alpha = 0)$ returns $F(0)$, and $F(\alpha = -1)$ returns $F(-1)$. After obtaining the value for the parameter α using MINUIT, we construct the experimental cross sections using equation 7.1.
- We handle the three choices of the renormalization/factorization scale for the theoretical predictions in the same manner. We interpolate the three theoretical predictions using a quadratic polynomial based on one parameter, β:

$$G(\beta) = G(0) + \frac{\beta}{2}[G(1) - G(-1)] + \frac{\beta^2}{2}[G(1) + G(-1) - 2G(0)] \quad (7.2)$$

  where $G(1)$ corresponds to the prediction with $\mu = E_T/2$, $G(0)$ corresponds to the prediction with $\mu = E_T$, and $G(-1)$ corresponds to the prediction with $\mu = 2E_T$. One can show that $G(\beta = 1)$ returns $G(1)$, $G(\beta = 0)$ returns $G(0)$, and $G(\beta = -1)$ returns $G(-1)$. After obtaining the value for the parameter β using MINUIT, we construct the theoretical predictions using equation 7.2.
- The statistical errors for both data and theoretical predictions are obtained using the same interpolation method.

Finally, we minimize the χ^2 using MINUIT using the following formula:

$$\chi^2 = \sum_{i=1}^{n} \frac{(t_i - \gamma \times d_i)^2}{\sigma_{ti}^2 + (\gamma \times \sigma_{di})^2} + \frac{(\gamma - 1)^2}{\sigma_{lum}^2} + \alpha^2 + \beta^2 \tag{7.3}$$

where i runs over all the data points. d_i and σ_{di} are the experimental cross section and associated statistical error respectively obtained using equation 7.1. t_i and σ_{ti} are the theoretical prediction and associated statistical error respectively obtained using equation 7.2. γ is the overall normalization determined by MINUIT, and $\frac{(\gamma-1)^2}{\sigma_{lum}^2}$ limits the normalization range allowed on the theoretical prediction where σ_{lum} is the 5.4% normalization error due to the luminosity uncertainty. α and β are the two interpolation parameters described in equations 7.1 and 7.2 and are determined by MINUIT. The statistical errors due to the theory is much smaller than the experimental errors and are included in the formula for completeness.

Tables 7.1-7.6 contain the cross sections and statistical errors for the three different choices of jet energy scale correction.

$\eta_2 \times sign(\eta_1)$	HIGH correction(nb/GeV)	NOMINAL correction(nb/GeV)	LOW correction(nb/GeV)
-2.75	1.08 ± 0.05	0.91 ± 0.05	0.70 ± 0.04
-2.25	2.30 ± 0.08	1.85 ± 0.07	1.51 ± 0.07
-1.75	4.41 ± 0.12	3.69 ± 0.11	3.05 ± 0.10
-1.25	6.94 ± 0.15	5.91 ± 0.14	5.05 ± 0.13
-0.75	7.32 ± 0.16	6.10 ± 0.14	5.22 ± 0.13
-0.25	7.73 ± 0.16	6.61 ± 0.15	5.67 ± 0.14
0.25	7.41 ± 0.16	6.28 ± 0.15	5.37 ± 0.14
0.75	7.43 ± 0.16	6.37 ± 0.15	5.33 ± 0.13
1.25	7.07 ± 0.15	5.82 ± 0.14	4.89 ± 0.13
1.75	4.84 ± 0.12	4.07 ± 0.11	3.38 ± 0.10
2.25	2.76 ± 0.09	2.25 ± 0.08	1.86 ± 0.07
2.75	1.33 ± 0.06	1.09 ± 0.05	0.85 ± 0.05

Table 7.1: Unsmeared cross section and statistical error as a function of $\eta_2 \times sign(\eta_1)$ for $0.0 \leq |\eta_1| < 0.5$ and $45 \leq E_T < 55$ GeV for the three choices of jet energy scale correction: HIGH, NOMINAL, and LOW.

$\eta_2 \times sign(\eta_1)$	HIGH correction(nb/GeV)	NOMINAL correction(nb/GeV)	LOW correction(nb/GeV)
-2.75	0.88 ± 0.05	0.70 ± 0.04	0.55 ± 0.04
-2.25	2.24 ± 0.08	1.86 ± 0.07	1.50 ± 0.07
-1.75	4.44 ± 0.12	3.80 ± 0.11	3.16 ± 0.10
-1.25	7.13 ± 0.15	5.87 ± 0.14	4.97 ± 0.13
-0.75	7.94 ± 0.17	6.69 ± 0.15	5.69 ± 0.14
-0.25	7.91 ± 0.17	6.80 ± 0.15	5.83 ± 0.14
0.25	7.64 ± 0.16	6.53 ± 0.15	5.61 ± 0.14
0.75	7.21 ± 0.16	6.16 ± 0.14	5.27 ± 0.13
1.25	7.00 ± 0.15	5.81 ± 0.14	4.87 ± 0.13
1.75	5.08 ± 0.13	4.24 ± 0.12	3.58 ± 0.11
2.25	2.92 ± 0.09	2.40 ± 0.09	1.92 ± 0.08
2.75	1.38 ± 0.06	1.11 ± 0.05	0.90 ± 0.05

Table 7.2: Unsmeared cross section and statistical error as a function of $\eta_2 \times sign(\eta_1)$ for $0.5 \leq |\eta_1| < 1.0$ and $45 \leq E_T < 55$ GeV for the three choices of jet energy scale correction: HIGH, NOMINAL, and LOW.

$\eta_2 \times sign(\eta_1)$	HIGH correction(nb/GeV)	NOMINAL correction(nb/GeV)	LOW correction(nb/GeV)
-2.75	0.58 ± 0.04	0.48 ± 0.04	0.44 ± 0.03
-2.25	1.44 ± 0.07	1.26 ± 0.06	1.00 ± 0.06
-1.75	3.22 ± 0.10	2.78 ± 0.10	2.41 ± 0.09
-1.25	4.90 ± 0.13	4.27 ± 0.12	3.74 ± 0.11
-0.75	6.70 ± 0.15	5.91 ± 0.14	5.18 ± 0.13
-0.25	7.15 ± 0.16	6.23 ± 0.15	5.56 ± 0.14
0.25	7.18 ± 0.16	6.24 ± 0.15	5.48 ± 0.14
0.75	6.48 ± 0.15	5.75 ± 0.14	4.96 ± 0.13
1.25	5.78 ± 0.14	4.90 ± 0.13	4.41 ± 0.12
1.75	4.41 ± 0.12	3.69 ± 0.11	3.14 ± 0.10
2.25	2.48 ± 0.08	2.15 ± 0.08	1.83 ± 0.07
2.75	1.14 ± 0.05	0.96 ± 0.05	0.82 ± 0.04

Table 7.3: Unsmeared cross section and statistical error as a function of $\eta_2 \times sign(\eta_1)$ for $1.0 \leq |\eta_1| < 1.5$ and $45 \leq E_T < 55$ GeV for the three choices of jet energy scale correction: HIGH, NOMINAL, and LOW.

$\eta_2 \times sign(\eta_1)$	HIGH correction(nb/GeV)	NOMINAL correction(nb/GeV)	LOW correction(nb/GeV)
-2.75	0.23 ± 0.02	0.20 ± 0.02	0.17 ± 0.02
-2.25	0.79 ± 0.05	0.68 ± 0.04	0.58 ± 0.04
-1.75	1.61 ± 0.07	1.31 ± 0.06	1.09 ± 0.06
-1.25	3.00 ± 0.10	2.53 ± 0.09	2.22 ± 0.08
-0.75	3.74 ± 0.11	3.27 ± 0.10	2.69 ± 0.09
-0.25	4.36 ± 0.12	3.83 ± 0.11	3.33 ± 0.10
0.25	4.88 ± 0.12	4.07 ± 0.11	3.54 ± 0.11
0.75	4.81 ± 0.12	4.08 ± 0.11	3.51 ± 0.10
1.25	4.22 ± 0.11	3.58 ± 0.10	3.11 ± 0.10
1.75	2.54 ± 0.09	2.14 ± 0.08	1.84 ± 0.07
2.25	1.35 ± 0.06	1.08 ± 0.05	0.89 ± 0.05
2.75	0.57 ± 0.03	0.42 ± 0.03	0.33 ± 0.03

Table 7.4: Unsmeared cross section and statistical error as a function of $\eta_2 \times sign(\eta_1)$ for $1.5 \leq |\eta_1| < 2.0$ and $45 \leq E_T < 55$ GeV for the three choices of jet energy scale correction: HIGH, NOMINAL, and LOW.

$\eta_2 \times sign(\eta_1)$	HIGH correction(nb/GeV)	NOMINAL correction(nb/GeV)	LOW correction(nb/GeV)
-2.75	0.14 ± 0.02	0.11 ± 0.02	0.10 ± 0.02
-2.25	0.31 ± 0.03	0.24 ± 0.02	0.18 ± 0.02
-1.75	0.72 ± 0.05	0.61 ± 0.04	0.52 ± 0.04
-1.25	1.38 ± 0.06	1.18 ± 0.06	0.94 ± 0.05
-0.75	1.72 ± 0.07	1.47 ± 0.07	1.15 ± 0.06
-0.25	2.34 ± 0.08	1.90 ± 0.08	1.58 ± 0.07
0.25	2.48 ± 0.09	2.12 ± 0.08	1.80 ± 0.07
0.75	2.49 ± 0.09	2.05 ± 0.08	1.75 ± 0.07
1.25	2.39 ± 0.08	2.06 ± 0.08	1.74 ± 0.07
1.75	1.28 ± 0.06	1.10 ± 0.05	0.93 ± 0.05
2.25	0.67 ± 0.04	0.57 ± 0.04	0.43 ± 0.03
2.75	0.21 ± 0.02	0.15 ± 0.02	0.12 ± 0.01

Table 7.5: Unsmeared cross section and statistical error as a function of $\eta_2 \times sign(\eta_1)$ for $2.0 \leq |\eta_1| < 2.5$ and $45 \leq E_T < 55$ GeV for the three choices of jet energy scale correction: HIGH, NOMINAL, and LOW.

$\eta_2 \times sign(\eta_1)$	HIGH correction(nb/GeV)	NOMINAL correction(nb/GeV)	LOW correction(nb/GeV)
-2.75	0.07 ± 0.01	0.06 ± 0.01	0.03 ± 0.01
-2.25	0.10 ± 0.01	0.08 ± 0.01	0.06 ± 0.01
-1.75	0.20 ± 0.02	0.15 ± 0.02	0.14 ± 0.02
-1.25	0.61 ± 0.04	0.50 ± 0.04	0.41 ± 0.03
-0.75	0.71 ± 0.04	0.56 ± 0.04	0.47 ± 0.04
-0.25	0.98 ± 0.05	0.78 ± 0.04	0.59 ± 0.04
0.25	0.99 ± 0.05	0.75 ± 0.04	0.62 ± 0.04
0.75	1.18 ± 0.05	0.90 ± 0.05	0.76 ± 0.04
1.25	1.20 ± 0.05	0.98 ± 0.05	0.78 ± 0.04
1.75	0.55 ± 0.03	0.39 ± 0.03	0.33 ± 0.03
2.25	0.19 ± 0.02	0.13 ± 0.01	0.08 ± 0.01
2.75	0.03 ± 0.01	0.020 ± 0.004	0.012 ± 0.003

Table 7.6: Unsmeared cross section and statistical error as a function of $\eta_2 \times sign(\eta_1)$ for $2.5 \leq |\eta_1| < 3.0$ and $45 \leq E_T < 55$ GeV for the three choices of jet energy scale correction: HIGH, NOMINAL, and LOW.

After using MINUIT to minimize the χ^2, we have tabulated the results in Table 6.7. The first column indicates the pdf being tested, the second column indicates the total χ^2 value, the following three columns show the values for α, β, and γ that minimized the χ^2 value.

pdf	χ^2	α	β	γ
CTEQ2M	970	0.79 ± 0.10	1.56 ± 0.11	0.90 ± 0.02
CTEQ2MF	701	0.67 ± 0.10	0.93 ± 0.13	0.91 ± 0.02
CTEQ2MS	1081	0.88 ± 0.10	1.21 ± 0.10	0.84 ± 0.01
CTEQ2ML	1008	0.07 ± 0.15	-2.03 ± 0.04	0.80 ± 0.02
MRSD0′	691	0.50 ± 0.11	1.07 ± 0.13	1.00 ± 0.02
MRSD-′	1016	0.79 ± 0.10	1.08 ± 0.10	0.84 ± 0.01

Table 7.7: Total χ^2 and fit parameters for the two families for pdf's tested. The number of data points used was 72.

From Table 6.7, we see that none of the pdf's give theoretical predictions consistent with our measured cross sections. The fact that all the pdf's behave similarly is understood given that they agree within 5% of each other in their gluon content,

which is the quantity being tested. The test is over several decades in x value, while most of the experimental data used to derive the gluon distribution was performed at $x \sim 0.3$ and very low Q^2 ($Q^2 \sim 5\ GeV^2$) [57].

In order to visualize these results, we show in Figs. 7.1-7.6 the interpolated experimental points with the interpolated theoretical cross sections for the case of MRSD0′ since this pdf resulted in the lowest χ^2 value. The 5.4% error due to the luminosity uncertainty is not included.

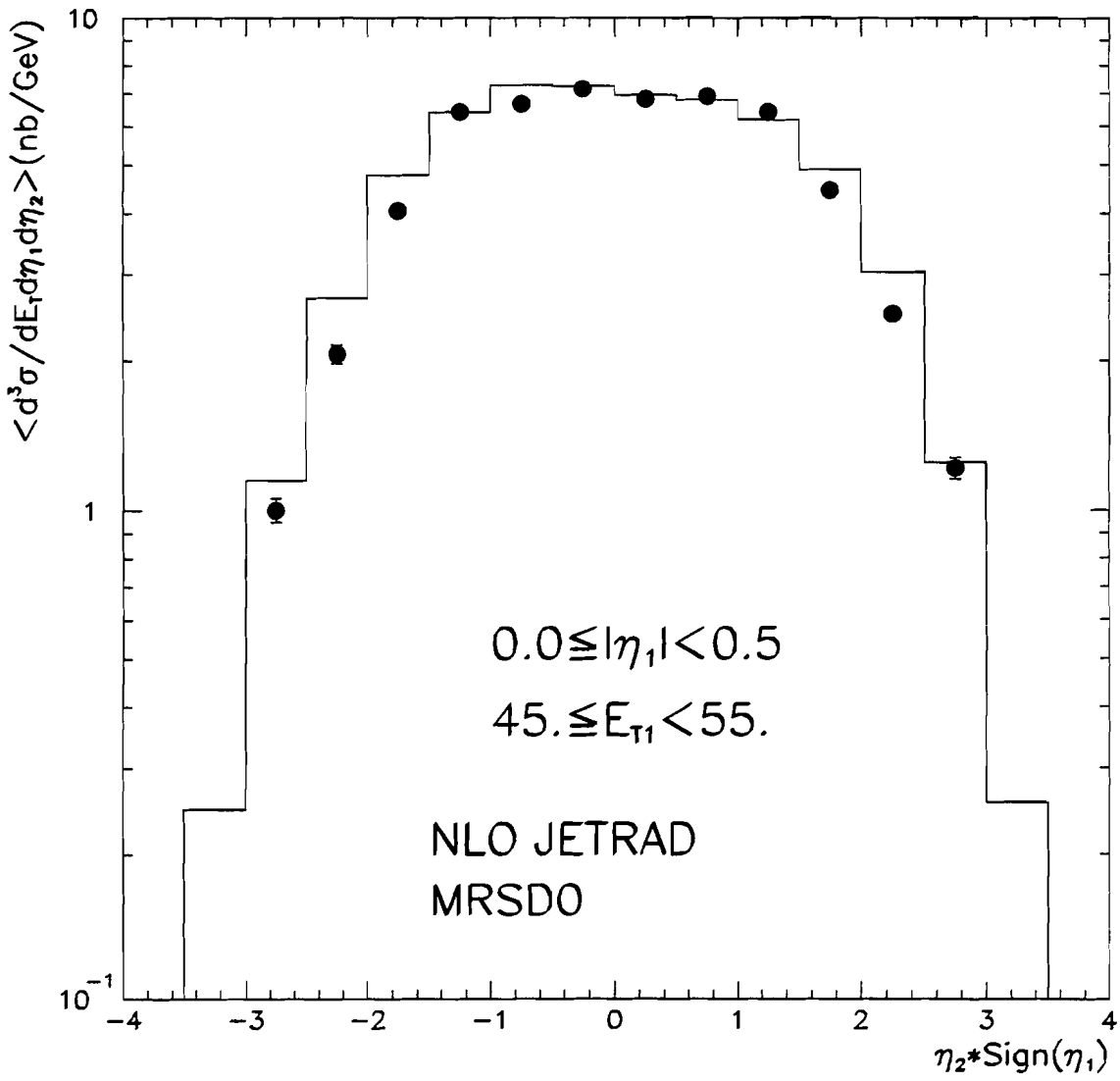

Figure 7.1: The interpolated triple differential dijet cross section, $d^3\sigma/dE_T d\eta_1 d\eta_2$ vs. $\eta_2 \times sign(\eta_1)$ for $0.0 \leq |\eta_1| < 0.5$. The 5.4% luminosity uncertainty has not been included.

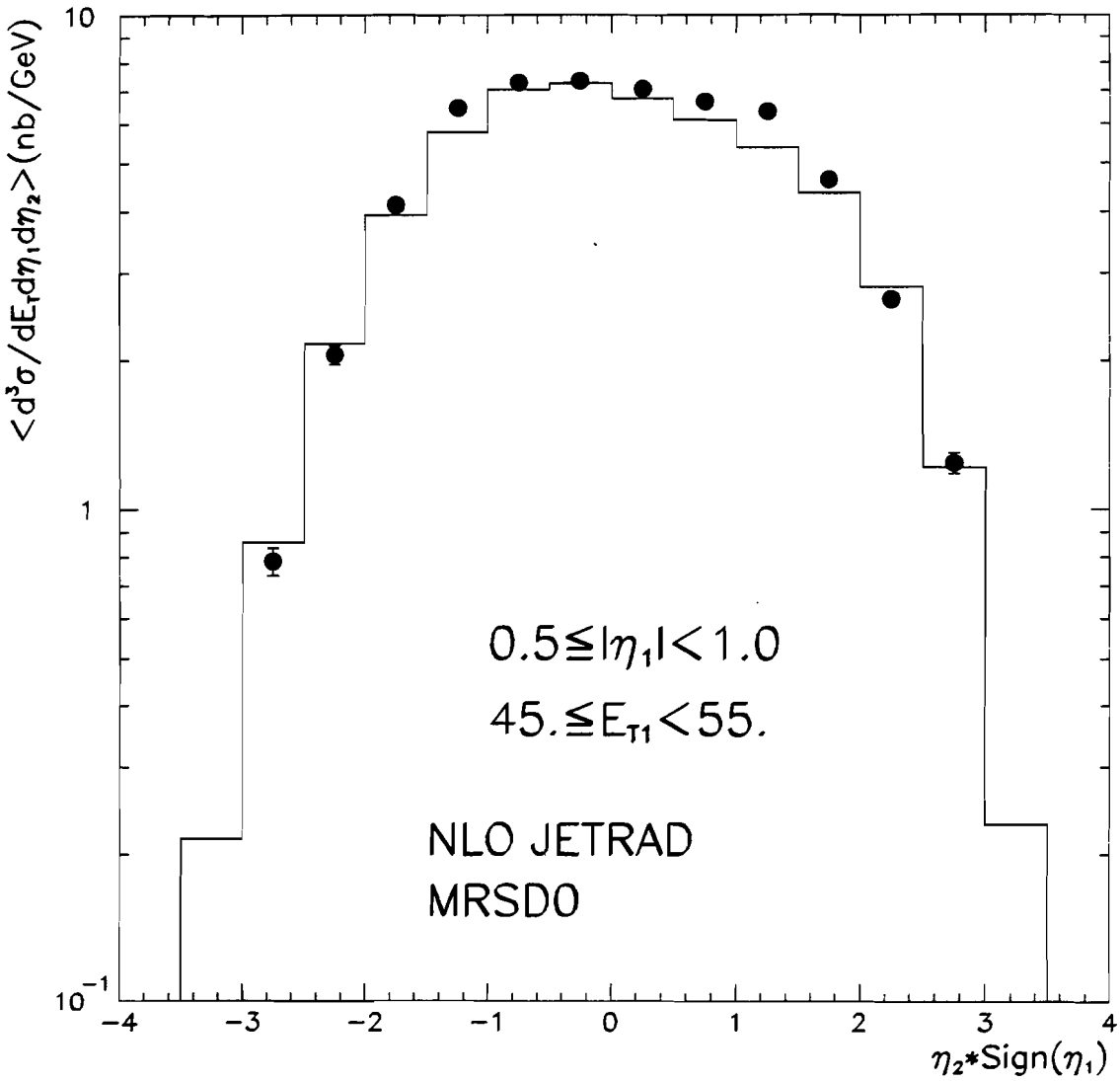

Figure 7.2: The interpolated triple differential dijet cross section, $d^3\sigma/dE_T d\eta_1 d\eta_2$ vs. $\eta_2 \times sign(\eta_1)$ for $0.5 \leq |\eta_1| < 1.0$. The 5.4% luminosity uncertainty has not been included.

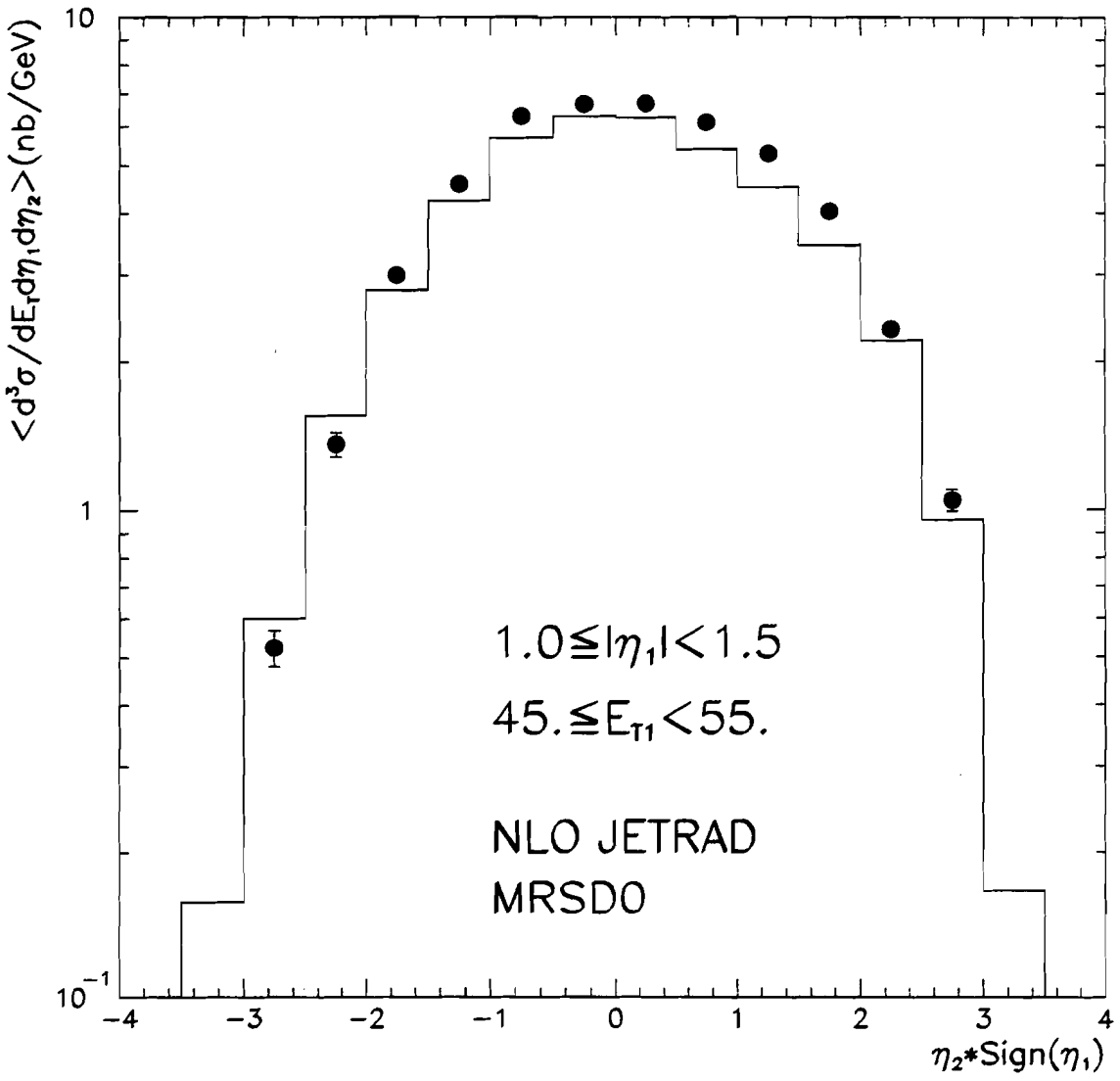

Figure 7.3: The interpolated triple differential dijet cross section, $d^3\sigma/dE_T d\eta_1 d\eta_2$ vs. $\eta_2 \times sign(\eta_1)$ for $1.0 \leq |\eta_1| < 1.5$. The 5.4% luminosity uncertainty has not been included.

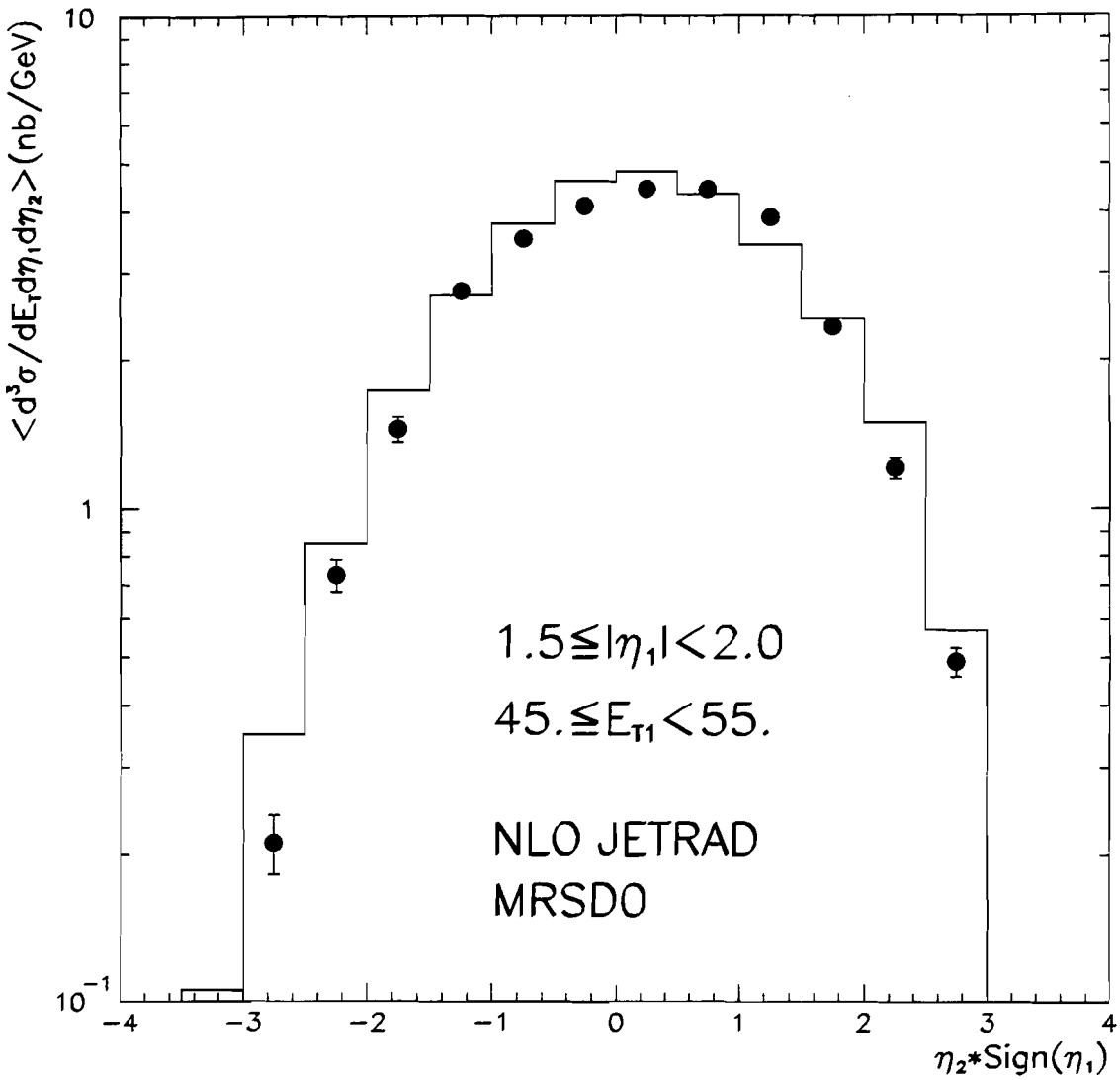

Figure 7.4: The interpolated triple differential dijet cross section, $d^3\sigma/dE_T d\eta_1 d\eta_2$ vs. $\eta_2 \times sign(\eta_1)$ for $1.5 \leq |\eta_1| < 2.0$. The 5.4% luminosity uncertainty has not been included.

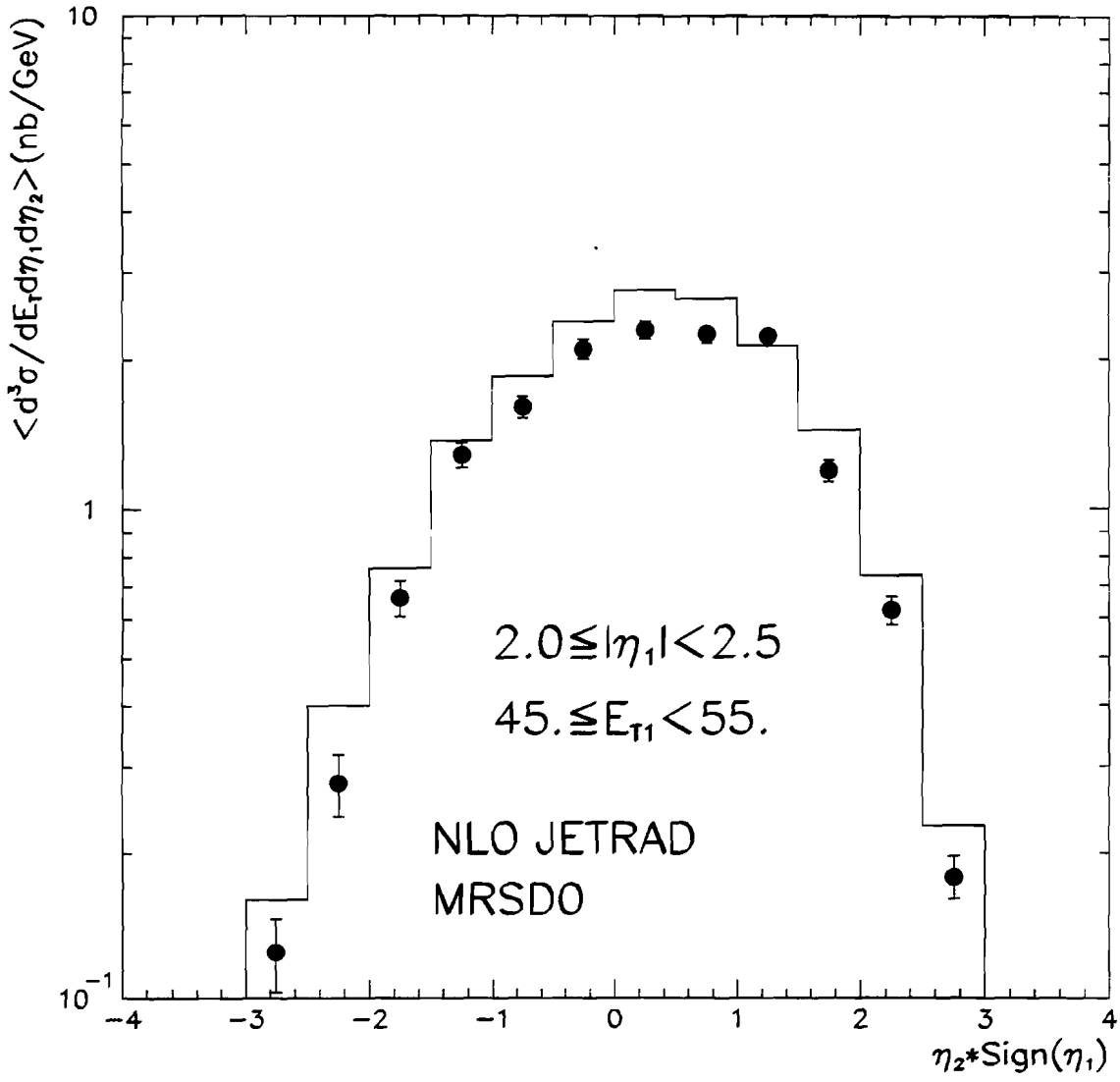

Figure 7.5: The interpolated triple differential dijet cross section, $d^3\sigma/dE_T d\eta_1 d\eta_2$ vs. $\eta_2 \times sign(\eta_1)$ for $2.0 \leq |\eta_1| < 2.5$. The 5.4% luminosity uncertainty has been included.

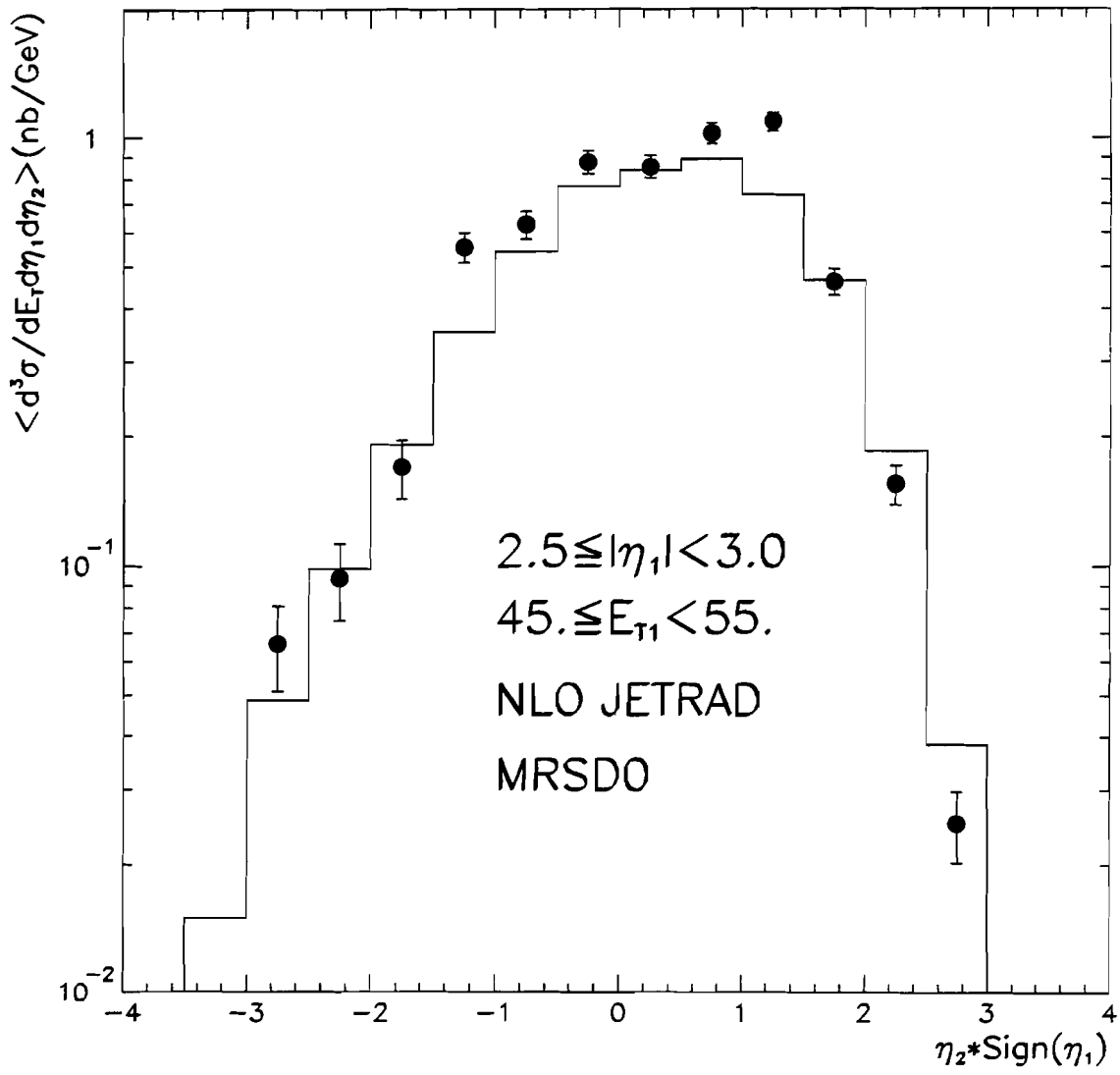

Figure 7.6: The interpolated triple differential dijet cross section, $d^3\sigma/dE_T d\eta_1 d\eta_2$ vs. $\eta_2 \times sign(\eta_1)$ for $2.5 \leq |\eta_1| < 3.0$. The 5.4% luminosity uncertainty has not been included.

In an attempt to understand the poorness of the fits, we have divided the data in subsets. The criteria used was the corresponding pair of x-values of each data point. Based in Figs. 2.7 and 2.8, we have chosen a subset where both partons have $x < 0.1$, another subset where both partons have $x \geq 0.1$, and the final case is the "mixed" case: one parton has $x < 0.1$ and the other parton has $x \geq 0.1$. As is clear from these figures, the pdf's have very similar gluon contribution at $x = 0.1$ for $Q = 50\ GeV$.

The data points where both partons have $x < 0.1$ are shown in Table 7.8 and the results from the MINUIT fit are in Table 7.9. From Table 7.9, we see that for data points where both partons have $x < 0.1$, none of the pdf's give a good fit to the data.

η_1	η_2	x_1	x_2
0.0-0.5	-1.25	0.044	0.119
0.0-0.5	-0.75	0.049	0.080
0.0-0.5	-0.25	0.057	0.057
0.0-0.5	0.25	0.071	0.043
0.0-0.5	0.75	0.094	0.035
0.5-1.0	-1.25	0.067	0.110
0.5-1.0	-0.75	0.072	0.072
0.5-1.0	-0.25	0.080	0.049
0.5-1.0	0.25	0.094	0.035
1.0-1.5	-0.75	0.110	0.067
1.0-1.5	-0.25	0.119	0.044

Table 7.8: Data points where both partons have $x < 0.1$.

The data points where both partons have $x \geq 0.1$ are given in Table 7.10 and the results from the MINUIT fit are shown in Table 7.11. For the case where both partons have $x \geq 0.1$, none of the pdf's give a good fit to the data.

Finally for the mixed case, the results are tabulated in Table 7.12. In the mixed case, no pdf's give a good fit to the data.

pdf	χ^2	α	β	γ
CTEQ2M	42	0.33 ± 0.37	0.47 ± 0.39	0.95 ± 0.05
CTEQ2MF	81	0.02 ± 0.33	0.77 ± 0.47	0.99 ± 0.05
CTEQ2MS	49	-0.52 ± 0.38	0.60 ± 0.48	0.95 ± 0.05
CTEQ2ML	39	-0.03 ± 0.41	-0.06 ± 0.59	0.99 ± 0.05
MRSD0′	56	0.41 ± 0.30	0.68 ± 0.47	0.98 ± 0.04
MRSD-′	48	-0.28 ± 0.36	1.60 ± 0.38	0.93 ± 0.05

Table 7.9: Total χ^2 and fit parameters where both partons have $x < 0.1$. The number of data points is 11.

η_1	η_2	x_1	x_2
1.0-1.5	-2.75	0.099	0.442
1.0-1.5	-2.25	0.100	0.272
1.0-1.5	-1.75	0.102	0.168
1.0-1.5	-1.25	0.105	0.105
1.5-2.0	-2.75	0.162	0.439
1.5-2.0	-2.25	0.163	0.268
1.5-2.0	-1.75	0.165	0.165
1.5-2.0	-1.25	0.168	0.102
2.0-2.5	-2.75	0.265	0.437
2.0-2.5	-2.25	0.266	0.266
2.0-2.5	-1.75	0.268	0.163
2.0-2.5	-1.25	0.272	0.100
2.5-3.0	-2.75	0.436	0.436
2.5-3.0	-2.25	0.437	0.265
2.5-3.0	-1.75	0.439	0.162
2.5-3.0	-1.25	0.442	0.099

Table 7.10: Data points where both partons have $x \geq 0.1$.

pdf	χ^2	α	β	γ
CTEQ2M	134	0.43 ± 0.29	1.01 ± 0.25	1.00 ± 0.05
CTEQ2MF	67	-0.01 ± 0.25	1.43 ± 0.17	0.96 ± 0.04
CTEQ2MS	96	-0.13 ± 0.32	1.72 ± 0.16	0.99 ± 0.05
CTEQ2ML	165	0.22 ± 0.33	-1.71 ± 0.09	0.90 ± 0.05
MRSD0′	94	0.47 ± 0.29	1.34 ± 0.37	1.02 ± 0.04
MRSD-′	104	-0.02 ± 0.26	1.53 ± 0.17	0.96 ± 0.04

Table 7.11: Total χ^2 and fit parameters where both partons have $x \geq 0.1$. The number of data points is 16.

pdf	χ^2	α	β	γ
CTEQ2M	621	0.75 ± 0.11	1.77 ± 0.15	0.95 ± 0.02
CTEQ2MF	530	0.64 ± 0.12	1.02 ± 0.22	0.93 ± 0.02
CTEQ2MS	632	-0.20 ± 0.24	-2.11 ± 0.10	0.73 ± 0.03
CTEQ2ML	616	-0.60 ± 0.18	-2.14 ± 0.08	0.91 ± 0.02
MRSD0′	527	0.38 ± 0.13	0.85 ± 0.21	1.02 ± 0.02
MRSD-′	568	-0.51 ± 0.19	-2.01 ± 0.08	0.77 ± 0.02

Table 7.12: Total χ^2 and fit parameters where one parton has $x \geq 0.1$ and the other parton has $x < 0.1$. The number of data points is 45.

7.2 Conclusions

We have shown that the dijet triple differential cross section, when shown as a lego plot as a functions of the pseudorapidities of the two leading jets, supports the statement that there is an increase in cross sections in areas of phase space allowed at NLO but prohibited at LO.

When the cross sections are shown as a function of the transverse energy of the leading jet, they can be used to test QCD predictions. Furthermore, in areas of large pseudorapidity, the data clearly favor the NLO predictions over the LO predictions.

Finally, when the cross sections are shown as a function $\eta_2 \times Sign(\eta_1)$, we can probe the shape of the gluon content of the currently available pdf's. The difficulty in drawing conclusions here is the incomplete understand of the uncertainties due to the jet energy scale correction. We have assumed that they are completely correlated in our extrapolation. If we proceed after making this assumption, we find that the shape of the data is not described by any of the pdf's tested. Even after we have segmented the comparisons based on the different combinations of x-values of the event, we cannot find any pdf that would describe our data.

APPENDICES

APPENDIX A

Trigger Logic Tables

For completeness, we show the trigger efficiencies for trigger requirement of 3 and 4 towers at L1. Assume that the trigger requirement is 3 towers above m GeV. Define p_i as the probability of having three towers or more above m GeV, s_i as the probability of having two and ONLY two towers above m GeV, t_1 as the probability of having one and ONLY one tower above m GeV and q_i as the probability of none $(p + s + t + q = 1)$.

The event fails L1 with probability:

$$\begin{aligned}
\epsilon_{fail}^{L1} &= q_1 * q_2 * q_3 + \\
& t_1 * q_2 * q_3 + t_2 * q_1 * q_3 + t_3 * q_1 * q_2 + \\
& s_1 * q_2 * q_3 + s_2 * q_1 * q_3 + s_3 * q_1 * q_2 \\
& q_1 * t_2 * t_3 + q_2 * t_1 * t_3 + q_3 * t_1 * t_2.
\end{aligned}$$

J1	J2	J3	TOPOLOGY	COMMENTS
|||	|||	|||	$p_1 * p_2 * p_3$	event passes
|||	|||	||	$p_1 * p_2 * s_3$	event passes
|||	|||			$p_1 * p_2 * t_3$	event passes
|||	|||	0	$p_1 * p_2 * q_3$	event passes
|||	||	|||	$p_1 * s_2 * p_3$	event passes
|||	||	||	$p_1 * s_2 * s_3$	event passes
|||	||			$p_1 * s_2 * t_3$	event passes
|||	||	0	$p_1 * s_2 * q_3$	event passes
|||			|||	$p_1 * t_2 * p_3$	event passes
|||			||	$p_1 * t_2 * s_3$	event passes
|||					$p_1 * t_2 * t_3$	event passes
|||			0	$p_1 * t_2 * q_3$	event passes
|||	0	|||	$p_1 * q_2 * p_3$	event passes
|||	0	||	$p_1 * q_2 * s_3$	event passes
|||	0			$p_1 * q_2 * t_3$	event passes
|||	0	0	$p_1 * q_2 * q_3$	event passes

Table A.1: First set of combinations for the case of requiring 3 towers above m GeV.

J1	J2	J3	TOPOLOGY	COMMENTS
||	|||	|||	$s_1 * p_2 * p_3$	event passes
||	|||	||	$s_1 * p_2 * s_3$	event passes
||	|||			$s_1 * p_2 * t_3$	event passes
||	|||	0	$s_1 * p_2 * q_3$	event passes
||	||	|||	$s_1 * s_2 * p_3$	event passes
||	||	||	$s_1 * s_2 * s_3$	event passes
||	||			$s_1 * s_2 * t_3$	event passes
||	||	0	$s_1 * s_2 * q_3$	event passes
||			|||	$s_1 * t_2 * p_3$	event passes
||			||	$s_1 * t_2 * s_3$	event passes
||					$s_1 * t_2 * t_3$	event passes
||			0	$s_1 * t_2 * q_3$	event passes
||	0	|||	$s_1 * q_2 * p_3$	event passes
||	0	||	$s_1 * q_2 * s_3$	event passes
||	0			$s_1 * q_2 * t_3$	event passes
||	0	0	$s_1 * q_2 * q_3$	event FAILS

Table A.2: Second set of combinations for the case of requiring 3 towers above m GeV.

J1	J2	J3	TOPOLOGY	COMMENTS
|	|||	|||	$t_1 * p_2 * p_3$	event passes
|	|||	||	$t_1 * p_2 * s_3$	event passes
|	|||	|	$t_1 * p_2 * t_3$	event passes
|	|||	0	$t_1 * p_2 * q_3$	event passes
|	||	|||	$t_1 * s_2 * p_3$	event passes
|	||	||	$t_1 * s_2 * s_3$	event passes
|	||	|	$t_1 * s_2 * t_3$	event passes
|	||	0	$t_1 * s_2 * q_3$	event passes
|	|	|||	$t_1 * t_2 * p_3$	event passes
|	|	||	$t_1 * t_2 * s_3$	event passes
|	|	|	$t_1 * t_2 * t_3$	event passes
|	|	0	$t_1 * t_2 * q_3$	event FAILS
|	0	|||	$t_1 * q_2 * p_3$	event passes
|	0	||	$t_1 * q_2 * s_3$	event passes
|	0	|	$t_1 * q_2 * t_3$	event FAILS
|	0	0	$t_1 * q_2 * q_3$	event FAILS

Table A.3: Third set of combinations for the case of requiring 3 towers above m GeV.

J1	J2	J3	TOPOLOGY	COMMENTS
0	|||	|||	$q_1 * p_2 * p_3$	event passes
0	|||	||	$q_1 * p_2 * s_3$	event passes
0	|||	|	$q_1 * p_2 * t_3$	event passes
0	|||	0	$q_1 * p_2 * q_3$	event passes
0	||	|||	$q_1 * s_2 * p_3$	event passes
0	||	||	$q_1 * s_2 * s_3$	event passes
0	||	|	$q_1 * s_2 * t_3$	event passes
0	||	0	$q_1 * s_2 * q_3$	event FAILS
0	|	|||	$q_1 * t_2 * p_3$	event passes
0	|	||	$q_1 * t_2 * s_3$	event passes
0	|	|	$q_1 * t_2 * t_3$	event FAILS
0	|	0	$q_1 * t_2 * q_3$	event FAILS
0	0	|||	$q_1 * q_2 * p_3$	event passes
0	0	||	$q_1 * q_2 * s_3$	event FAILS
0	0	|	$q_1 * q_2 * t_3$	event FAILS
0	0	0	$q_1 * q_2 * q_3$	event FAILS

Table A.4: Last set of combinations for the case of requiring 3 towers above m GeV.

Assume now that the trigger requirement is 4 towers above m GeV. Define p_i as the probability of having four or more towers above m GeV, r_i as the probability of having three and ONLY three towers above m GeV, s_i as the probability of having two and ONLY two towers above m GeV, t_i as the probability of having one and ONLY one towers above m GeV and q_i as the probability of having none $(p + r + s + t + q = 1)$.

The event fails L1 with probability:

$$
\begin{aligned}
\epsilon_{fail}^{L1} \quad = \quad & q_1 * q_2 * q_3 + \\
& t_1 * q_2 * q_3 + t_2 * q_1 * q_3 + t_3 * q_1 * q_2 + \\
& s_1 * q_2 * q_3 + s_2 * q_1 * q_3 + s_3 * q_1 * q_2 \\
& q_1 * t_2 * t_3 + q_2 * t_1 * t_3 + q_3 * t_1 * t_2 \\
& r_1 * q_2 * q_3 + r_2 * q_1 * q_3 + r_3 * q_1 * q_2 \\
& t_1 * t_2 * t_3 \\
& s_1 * t_2 * q_3 + s_1 * t_3 * q_2 + s_2 * t_1 * q_3 + s_2 * t_3 * q_1 + s_3 * t_1 * q_2 + s_3 * t_2 * q_1.
\end{aligned}
$$

J1	J2	J3	TOPOLOGY	COMMENTS
IIII	IIII	IIII	$p_1 * p_2 * p_3$	event passes
IIII	IIII	III	$p_1 * p_2 * r_3$	event passes
IIII	IIII	II	$p_1 * p_2 * s_3$	event passes
IIII	IIII	I	$p_1 * p_2 * t_3$	event passes
IIII	IIII	0	$p_1 * p_2 * q_3$	event passes
IIII	III	IIII	$p_1 * r_2 * p_3$	event passes
IIII	III	III	$p_1 * r_2 * r_3$	event passes
IIII	III	II	$p_1 * r_2 * s_3$	event passes
IIII	III	I	$p_1 * r_2 * t_3$	event passes
IIII	III	0	$p_1 * r_2 * q_3$	event passes
IIII	II	IIII	$p_1 * s_2 * p_3$	event passes
IIII	II	III	$p_1 * s_2 * r_3$	event passes
IIII	II	II	$p_1 * s_2 * s_3$	event passes
IIII	II	I	$p_1 * s_2 * t_3$	event passes
IIII	II	0	$p_1 * s_2 * q_3$	event passes
IIII	I	IIII	$p_1 * t_2 * p_3$	event passes
IIII	I	III	$p_1 * t_2 * r_3$	event passes
IIII	I	II	$p_1 * t_2 * s_3$	event passes
IIII	I	I	$p_1 * t_2 * t_3$	event passes
IIII	I	0	$p_1 * t_2 * q_3$	event passes
IIII	0	IIII	$p_1 * q_2 * p_3$	event passes
IIII	0	III	$p_1 * q_2 * r_3$	event passes
IIII	0	II	$p_1 * q_2 * s_3$	event passes
IIII	0	I	$p_1 * q_2 * t_3$	event passes
IIII	0	0	$p_1 * q_2 * q_3$	event passes

Table A.5: First set of combinations for the case of requiring 4 towers above m GeV.

J1	J2	J3	TOPOLOGY	COMMENTS
|||	||||	||||	$r_1 * p_2 * p_3$	event passes
|||	||||	|||	$r_1 * p_2 * r_3$	event passes
|||	||||	||	$r_1 * p_2 * s_3$	event passes
|||	||||			$r_1 * p_2 * t_3$	event passes
|||	||||	0	$r_1 * p_2 * q_3$	event passes
|||	|||	||||	$r_1 * r_2 * p_3$	event passes
|||	|||	|||	$r_1 * r_2 * r_3$	event passes
|||	|||	||	$r_1 * r_2 * s_3$	event passes
|||	|||			$r_1 * r_2 * t_3$	event passes
|||	|||	0	$r_1 * r_2 * q_3$	event passes
|||	||	||||	$r_1 * s_2 * p_3$	event passes
|||	||	|||	$r_1 * s_2 * r_3$	event passes
|||	||	||	$r_1 * s_2 * s_3$	event passes
|||	||			$r_1 * s_2 * t_3$	event passes
|||	||	0	$r_1 * s_2 * q_3$	event passes
|||			||||	$r_1 * t_2 * p_3$	event passes
|||			|||	$r_1 * t_2 * r_3$	event passes
|||			||	$r_1 * t_2 * s_3$	event passes
|||					$r_1 * t_2 * t_3$	event passes
|||			0	$r_1 * t_2 * q_3$	event passes
|||	0	||||	$r_1 * q_2 * p_3$	event passes
|||	0	|||	$r_1 * q_2 * r_3$	event passes
|||	0	||	$r_1 * q_2 * s_3$	event passes
|||	0			$r_1 * q_2 * t_3$	event passes
|||	0	0	$r_1 * q_2 * q_3$	event FAILS

Table A.6: Second set of combinations for the case of requiring 4 towers above m GeV.

J1	J2	J3	TOPOLOGY	COMMENTS
||	||||	||||	$s_1 * p_2 * p_3$	event passes
||	||||	|||	$s_1 * p_2 * r_3$	event passes
||	||||	||	$s_1 * p_2 * s_3$	event passes
||	||||	|	$s_1 * p_2 * t_3$	event passes
||	||||	0	$s_1 * p_2 * q_3$	event passes
||	|||	||||	$s_1 * r_2 * p_3$	event passes
||	|||	|||	$s_1 * r_2 * r_3$	event passes
||	|||	||	$s_1 * r_2 * s_3$	event passes
||	|||	|	$s_1 * r_2 * t_3$	event passes
||	|||	0	$s_1 * r_2 * q_3$	event passes
||	||	||||	$s_1 * s_2 * p_3$	event passes
||	||	|||	$s_1 * s_2 * r_3$	event passes
||	||	||	$s_1 * s_2 * s_3$	event passes
||	||	|	$s_1 * s_2 * t_3$	event passes
||	||	0	$s_1 * s_2 * q_3$	event passes
||	|	||||	$s_1 * t_2 * p_3$	event passes
||	|	|||	$s_1 * t_2 * r_3$	event passes
||	|	||	$s_1 * t_2 * s_3$	event passes
||	|	|	$s_1 * t_2 * t_3$	event passes
||	|	0	$s_1 * t_2 * q_3$	event FAILS
||	0	||||	$s_1 * q_2 * p_3$	event passes
||	0	|||	$s_1 * q_2 * r_3$	event passes
||	0	||	$s_1 * q_2 * s_3$	event passes
||	0	|	$s_1 * q_2 * t_3$	event FAILS
||	0	0	$s_1 * q_2 * q_3$	event FAILS

Table A.7: Third set of combinations for the case of requiring 4 towers above m GeV.

J1	J2	J3	TOPOLOGY	COMMENTS
|	||||	||||	$t_1 * p_2 * p_3$	event passes
|	||||	|||	$t_1 * p_2 * r_3$	event passes
|	||||	||	$t_1 * p_2 * s_3$	event passes
|	||||	|	$t_1 * p_2 * t_3$	event passes
|	||||	0	$t_1 * p_2 * q_3$	event passes
|	|||	||||	$t_1 * r_2 * p_3$	event passes
|	|||	|||	$t_1 * r_2 * r_3$	event passes
|	|||	||	$t_1 * r_2 * s_3$	event passes
|	|||	|	$t_1 * r_2 * t_3$	event passes
|	|||	0	$t_1 * r_2 * q_3$	event passes
|	||	||||	$t_1 * s_2 * p_3$	event passes
|	||	|||	$t_1 * s_2 * r_3$	event passes
|	||	||	$t_1 * s_2 * s_3$	event passes
|	||	|	$t_1 * s_2 * t_3$	event passes
|	||	0	$t_1 * s_2 * q_3$	event FAILS
|	|	||||	$t_1 * t_2 * p_3$	event passes
|	|	|||	$t_1 * t_2 * r_3$	event passes
|	|	||	$t_1 * t_2 * s_3$	event passes
|	|	|	$t_1 * t_2 * t_3$	event FAILS
|	|	0	$t_1 * t_2 * q_3$	event FAILS
|	0	||||	$t_1 * q_2 * p_3$	event passes
|	0	|||	$t_1 * q_2 * r_3$	event passes
|	0	||	$t_1 * q_2 * s_3$	event FAILS
|	0	|	$t_1 * q_2 * t_3$	event FAILS
|	0	0	$t_1 * q_2 * q_3$	event FAILS

Table A.8: Fourth set of combinations for the case of requiring 4 towers above m GeV.

J1	J2	J3	TOPOLOGY	COMMENTS
0	IIII	IIII	$q_1 * p_2 * p_3$	event passes
0	IIII	III	$q_1 * p_2 * r_3$	event passes
0	IIII	II	$q_1 * p_2 * s_3$	event passes
0	IIII	I	$q_1 * p_2 * t_3$	event passes
0	IIII	0	$q_1 * p_2 * q_3$	event passes
0	III	IIII	$q_1 * r_2 * p_3$	event passes
0	III	III	$q_1 * r_2 * r_3$	event passes
0	III	II	$q_1 * r_2 * s_3$	event passes
0	III	I	$q_1 * r_2 * t_3$	event passes
0	III	0	$q_1 * r_2 * q_3$	event FAILS
0	II	IIII	$q_1 * s_2 * p_3$	event passes
0	II	III	$q_1 * s_2 * r_3$	event passes
0	II	II	$q_1 * s_2 * s_3$	event passes
0	II	I	$q_1 * s_2 * t_3$	event FAILS
0	II	0	$q_1 * s_2 * q_3$	event FAILS
0	I	IIII	$q_1 * t_2 * p_3$	event passes
0	I	III	$q_1 * t_2 * r_3$	event passes
0	I	II	$q_1 * t_2 * s_3$	event FAILS
0	I	I	$q_1 * t_2 * t_3$	event FAILS
0	I	0	$q_1 * t_2 * q_3$	event FAILS
0	0	IIII	$q_1 * q_2 * p_3$	event passes
0	0	III	$q_1 * q_2 * r_3$	event FAILS
0	0	II	$q_1 * q_2 * s_3$	event FAILS
0	0	I	$q_1 * q_2 * t_3$	event FAILS
0	0	0	$q_1 * q_2 * q_3$	event FAILS

Table A.9: Last set of combinations for the case of requiring 4 towers above m GeV.

APPENDIX B

Unsmearing Factors

The unsmearing factors corresponding to the four η slices in the dijet E_T distribution are shown below. We also show the unsmearing factors corresponding to the six η slices of the signed η distribution.

E_T (GeV)	Unsmearing Factor
40.- 50.	0.757
50.- 60.	0.760
60.- 70.	0.799
70.- 80.	0.818
80.- 90.	0.841
90.- 100.	0.872
100.- 110.	0.870
110.- 120.	0.879
120.- 130.	0.901
130.- 140.	0.889
140.- 150.	0.915
150.- 170.	0.904
170.- 190.	0.910
190.- 210.	0.916
210.- 230.	0.917
230.- 250.	0.907
250.- 270.	0.914
270.- 300.	0.914
300.- 330.	0.906
330.- 360.	0.900
360.- 390.	0.889
390.- 430.	0.886

Table B.1: Unsmearing factors for the dijet E_T spectra when the second jet is in the range $0.0 \leq |\eta| < 1.0$.

E_T (GeV)	Unsmearing Factor
40.- 50.	0.736
50.- 60.	0.726
60.- 70.	0.767
70.- 80.	0.777
80.- 90.	0.813
90.- 100.	0.845
100.- 110.	0.845
110.- 120.	0.840
120.- 130.	0.846
130.- 140.	0.851
140.- 150.	0.872
150.- 170.	0.867
170.- 190.	0.856
190.- 210.	0.859
210.- 230.	0.850
230.- 250.	0.846
250.- 270.	0.841
270.- 300.	0.824
300.- 330.	0.801
330.- 360.	0.764
360.- 390.	0.707
390.- 430.	0.690

Table B.2: Unsmearing factors for the dijet E_T spectra when the second jet is in the range $1.0 \leq |\eta| < 2.0$.

E_T (GeV)	Unsmearing Factor
40.- 50.	0.648
50.- 60.	0.627
60.- 70.	0.669
70.- 80.	0.655
80.- 90.	0.698
90.- 100.	0.701
100.- 110.	0.684
110.- 120.	0.661
120.- 130.	0.691
130.- 140.	0.640
140.- 150.	0.648
150.- 170.	0.605
170.- 190.	0.571
190.- 210.	0.545

Table B.3: Unsmearing factors for the dijet E_T spectra when the second jet is in the range $2.0 \leq |\eta| < 3.0$.

E_T (GeV)	Unsmearing Factor
40.- 50.	0.374
50.- 60.	0.329
60.- 70.	0.308
70.- 80.	0.254
80.- 90.	0.214
90.- 100.	0.203
100.- 110.	0.181

Table B.4: Unsmearing factors for the dijet E_T spectra when the second jet is in the range $3.0 \leq |\eta| < 4.0$.

$\eta_2 \times sign(\eta_1)$	Unsmearing Factor
-3.75	0.183
-3.25	0.397
-2.75	0.529
-2.25	0.649
-1.75	0.696
-1.25	0.715
-0.75	0.730
-0.25	0.732
0.25	0.732
0.75	0.733
1.25	0.707
1.75	0.693
2.25	0.636
2.75	0.567
3.25	0.364
3.75	0.118

Table B.5: Unsmearing factors for the signed η distribution when the leading jet is in the range $0.0 \leq |\eta| < 0.5$.

$\eta_2 \times sign(\eta_1)$	Unsmearing Factor
-3.75	0.146
-3.25	0.445
-2.75	0.539
-2.25	0.649
-1.75	0.726
-1.25	0.720
-0.75	0.739
-0.25	0.743
0.25	0.718
0.75	0.726
1.25	0.714
1.75	0.700
2.25	0.654
2.75	0.535
3.25	0.331
3.75	0.094

Table B.6: Unsmearing factors for the signed η distribution when the leading jet is in the range $0.5 \leq |\eta| < 1.0$.

$\eta_2 \times sign(\eta_1)$	Unsmearing Factor
-3.75	0.150
-3.25	0.408
-2.75	0.590
-2.25	0.656
-1.75	0.719
-1.25	0.724
-0.75	0.747
-0.25	0.745
0.25	0.732
0.75	0.736
1.25	0.727
1.75	0.676
2.25	0.619
2.75	0.499
3.25	0.278
3.75	0.095

Table B.7: Unsmearing factors for the signed η distribution when the leading jet is in the range $1.0 \leq |\eta| < 1.5$.

$\eta_2 \times sign(\eta_1)$	Unsmearing Factor
-3.75	0.185
-3.25	0.379
-2.75	0.465
-2.25	0.612
-1.75	0.652
-1.25	0.669
-0.75	0.686
-0.25	0.678
0.25	0.688
0.75	0.673
1.25	0.648
1.75	0.618
2.25	0.539
2.75	0.411
3.25	0.184
3.75	0.045

Table B.8: Unsmearing factors for the signed η distribution when the leading jet is in the range $1.5 \leq |\eta| < 2.0$.

$\eta_2 \times sign(\eta_1)$	Unsmearing Factor
-3.75	0.173
-3.25	0.348
-2.75	0.537
-2.25	0.550
-1.75	0.625
-1.25	0.652
-0.75	0.638
-0.25	0.660
0.25	0.666
0.75	0.667
1.25	0.636
1.75	0.581
2.25	0.514
2.75	0.361
3.25	0.146
3.75	0.016

Table B.9: Unsmearing factors for the signed η distribution when the leading jet is in the range $2.0 \leq |\eta| < 2.5$.

$\eta_2 \times sign(\eta_1)$	Unsmearing Factor
-3.75	0.160
-3.25	0.520
-2.75	0.470
-2.25	0.440
-1.75	0.451
-1.25	0.591
-0.75	0.568
-0.25	0.540
0.25	0.536
0.75	0.532
1.25	0.535
1.75	0.431
2.25	0.344
2.75	0.180
3.25	0.030
3.75	—

Table B.10: Unsmearing factors for the signed η distribution when the leading jet is in the range $2.5 \leq |\eta| < 3.0$.

REFERENCES

[1] CDF Collaboration, F. Abe *et al.*, Phys. Rev. Lett. **74**, 2626 (1995).
DØ Collaboration, S. Abachi *et al.*, Phys. Rev. Lett. **74**, 2632 (1995).

[2] V.D. Barger and R.J.N. Phillips, *Collider Physics*, p. 134, Addison-Wesley Publishing Co. (1987).

[3] J. Collins, D. Soper and G. Sterman, *Perturbative QCD*, World Scientific (1989).

[4] A. Vogt, "Dynamical Parton Distributions for α_s Determinations", DESY 95-068 (1995).

[5] B. Anderson *et al.*, Z. Phys. **C20**, 317 (1983); Phys. Rep. **97**, 33 (1983); Phys. Lett. **B94**, 211 (1980).

[6] G. Altarelli, "Partons in QCD", Phys. Rep. **81**, 1 (1982).
G. Altarelli, "New Phenomena in Lepton-Hadron Physics", NATO Advanced Study Series, Series B, Vol. 49. Plenum Press, New York (1978).

[7] BCDMS Collaboration, A. C. Benvenuti *et al.* Phys. Lett. B **223**, 485 (1989); Phys. Lett. B **237**, 592 (1990) and Phys. Lett. B **237**, 599 (1990);
EMC Collaboration, M. Arneodo *et al.*, Nucl. Phys. **B333**, 1 (1990);
NMC Collaboration, D. Allasia *et al.*, Phys. Lett. B **249**, 366 (1990);
NMC Collaboration, P. Amaudruz *et al.*, Nucl. Phys. **B371**, 3 (1992) and Phys. Lett. B **295**, 159 (1992).

[8] W. T. Giele, E. W. N. Glover, and D. A. Kosower, "The Inclusive Two Jet Triply Differential Cross Section", Fermilab-Pub-94/382-T (1994).

[9] CTEQ Collaboration, J. Botts, *et al.*, "CTEQ Parton Distributions and Flavor Dependence of Sea Quarks", Phys. Lett. B **304**, 159-166, (1993).

[10] A.D. Martin, W.J. Stirling, R.G. Roberts, "Two-Jet Hadroproduction as a Measure of the Gluon at Small x", Preprint RAL-93-047 (1993); Phys. Lett. B **306**, 145 (1993); Erratum-*ibid.* B **309**, 492 (1993).

[11] M. Gluck, E. Reya, A. Vogt, Z. Phys. **C53**, 127 (1993).

[12] H1 Collaboration: K. Müller, Proc. of 29th Rencontre de Moriond, (1994).
ZEUS Collaboration: G. Wolf, Proc. of International Workshop on Deep Inelastic Scattering, Eilat, Israel, Feb. 1994; M. Roco, Proc. of 29th Rencontre de Moriond, (1994).

[13] W. T. Giele, E. W. N. Glover, and D. A. Kosower, Phys. Rev. Lett. **73**, 2019 (1994).

[14] M. Abolins *et al.*, "Design Report, The DØ Experiment at the Fermilab Antiproton-Proton Collider", (November 1984).

[15] CDF Collaboration, Abe *et al.*, Nucl. Instrum. Methods Phys. Res., Sect. A **271**, 387 (1988).

[16] UA2 Collaboration, A. Beer *et al.*, Nucl. Instrum. Methods Phys. Res., Sect. A **224**, 360 (1984).
R. Ansari *et al.*, Nucl. Instrum. Methods Phys. Res., Sect. A **263**, 51 (1988); Nucl. Instrum. Methods Phys. Res., Sect. A **279**, 388 (1989).
F. Bosi *et al.*, Nucl. Instrum. Methods Phys. Res., Sect. A **283**, 532 (1989).
R. E. Ansorge *et al.*, Nucl. Instrum. Methods Phys. Res., Sect. A **265**, 33 (1988).
J. Alitti *et al.*, Nucl. Instrum. Methods Phys. Res., Sect. A **279**, 364 (1989).
K. Borer *et al.*, Nucl. Instrum. Methods Phys. Res., Sect. A **286**, 128 (1990).

[17] J. Thompson, "Introduction to Colliding Beams at Fermilab", Fermilab-TM-1909 (1994).
"Design Report, Tevatron 1 Project," Fermi National Accelerator Lab internal note, (unpublished, 1984).
P. Emma, "Tevatron Introduction" National Accelerator Lab internal note, (unpublished, 1984).
F. T. Cole, M. R. Donaldson, D. A. Edwards, H. T. Edwards, and P. F. M. Koehler, "Design Report, Superconducting Accelerator," Fermi National Accelerator Lab internal note, (unpublished, 1979).

[18] Leon M. Lederman, Scientific American, pp. 48, March (1991).

[19] Thomas Ferbel, *Experimental Techniques in High energy Physics*, pp. 79, Addison-Wesley Publishing Co. (1987).

[20] R. Fernow, *Introduction to Experimental Particle Physics*, Cambridge University Press (1986).

[21] Adrian C. Melissinos, *Experiments in Modern Physics*, p.194-196, Academic Press College (1966).

[22] Thomas Ferbel, *Experimental Techniques in High energy Physics*, pp. 371, Addison-Wesley Publishing Co. (1987).

[23] Dave Anderson, "Principles of EM Calorimetry" given in an Academic Lecture Series at FNAL DØ Note 1713 (unpublished) (4/1993).
Dave Anderson, "Some Calorimetry Techniques" given in an Academic Lecture Series at FNAL DØ Note 1714 (unpublished) (4/1993).
Dave Anderson, "Principles of Hadron Calorimetry" given in an Academic Lecture Series at FNAL DØ Note 1715 (unpublished) (4/1993).

[24] A. R. Clark *et al.*, Nucl. Instrum. Methods Phys. Res., Sect. A **279**, pp. 243 (1989).

[25] DØ Collaboration, S. Abachi *et al.*, Nucl. Instrum. Methods Phys. Res., Sect. A **338**, pp. 190-192 (1994).
A. R. Clark, "The DØ Vertex Chamber Status Report", DØ Note 776 (unpublished) (11/1988).

[26] Y. Ducros *et al.*, Nucl. Instrum. Methods Phys. Res., Sect. A **277** (1989).

[27] T. Behnke, Ph. D. Thesis, SUNY at Stony Brook, *The Central Drift Chamber for the DØ Experiment: Design, Construction, and Test* August 1989 (unpublished).

[28] S. Rajagopalan, Ph. D. Thesis, Nothwestern University, *The dE/dx capabilities of the DØ Tracking System*, June 1992 (unpublished).

[29] J. Bantly Ph. D. Thesis, Nothwestern University, *The DØ Detector Forward Drift Chamber Performance and Physics Capability in the 1990 FNAL Testbeam Run*, June 1992 (unpublished).

[30] C. Brown *et al.*, Nucl. Instrum. Methods Phys. Res., Sect. A **279** (1989).

[31] J. M. Butler *et al.*, Nucl. Instrum. Methods Phys. Res., Sect. A **290** (1990).

[32] DØ Collaboration, S. Abachi *et al.*, Nucl. Instrum. Methods Phys. Res., Sect. A **338**, p. 188 (1994).

[33] Zachary Wolf, James Walker, and Andrew White, DØ Note 795 (1989) (unpublished).

[34] J. Bantly *et al.*, **IEEE41**:1274 (1994).

[35] CDF Collaboration, F. Abe *et al.*, "Measurement of the $p\bar{p}$ Total Cross Section at $\sqrt{s} = 546$ and 1800 GeV", FERMILAB-Pub-93/234-E (1993), submitted to Phys. Rev. D.

[36] P. Aurenche *et al.*, Phys. Rev. **D45** (1992) 92. See also F. W. Bopp *et al.*, Z. Phys. **C51** (1991) 99.

[37] N. Amos *et al.*, "Change to the DØ Luminosity Monitor Constant", DØ Note 2186 (4/1995).

[38] J. Bantly *et al.*, "Improvement to the DØ Luminosity Monitor Constant", Fermilab-TM-1930, DØ Note 2544 (4/1995).

[39] DØ Collaboration, S. Abachi *et al.*, Nucl. Instrum. Methods Phys. Res., Sect. A **338**, p. 227-234(1994).

[40] UA2 Collaboration, M. Banner *et al.*, Phys. Lett. B**118**, 203 (1982).

[41] UA1 Collaboration, G. Arnison *et al.*, Phys. Lett. B**123**, 115 (1983).

[42] CDF Collaboration, F. Abe *et al.*, Phys. Rev. Lett. **62**, 613 (1989).

[43] B. Flaugher and K. Meier, article in Reseach Directions for the Decade Snowmass 1990,pp. 128-133, edited by Edmond L. Berger (World Scientific, Singapore 1990).

[44] N. J. Hadley, DØ Note #904 (unpublished) (11/1989).

[45] John E. Huth *et al.*, article in Reseach Directions for the Decade Snowmass 1990, pp. 134-136, edited by Edmond L. Berger (World Scientific, Singapore 1990).

[46] V. D. Elvira, G. Blazey, and R. Astur, DØ Note #1763 (unpublished) (6/1993).

[47] S. Abachi, *et al.* NIM **A324**:52 (1993).
A. Milder and R. Astur. DØ Note #1595 (unpublished) (12/1992).
B. Kehoe, DØ Note #2052 (unpublished) (2/1994). B. Kehoe, DØ Note #2053 (unpublished) (3/1994).

[48] M. Bhattacharjee, G. Blazey, and R. Hirosky DØ Note #2557 (unpublished).
D. Elvira, Ph.D. Dissertation, University of Buenos Aires, Argentina (1994) (unpublished).

[49] D. Elvira, DØ Note #2173 (unpublished) (6/1994).

[50] D. Elvira, J. Blazey, and R. Astur, DØ Note #1763 (unpublished) (6/1993).

[51] W. T. Giele, E. W. .N. Glover, and D. A. Kosower, Fermilab preprint FERMILAB-PUB-94-382-T.

[52] D. Elvira, Ph.D. Dissertation, University of Buenos Aires, Argentina (1994) (unpublished).

[53] *Minuit CERN Reference Manual Version 92.1* (March 92).

[54] W. T. Giele, E. W. N. Glover, and David A. Kosower, "Jet Physics at $P\bar{P}$-colliders", FERMILAB-CONF-94/350-T.

[55] A.D. Martin, W.J. Stirling, R.G. Roberts, "Two-Jet Hadroproduction as a Measure of the Gluon at Small x", Preprint RAL-93-047 (1993).

[56] A.D. Martin, W.J. Stirling, R.G. Roberts, Phys. Lett. **B306**, 145 (1993); Erratum-*ibid.***B309**, 492 (1993).

[57] A. D. Martin, W. J. Stirling and R. G. Roberts, "Pinning down the Glue in the Proton".